Dark matter phenomenology

Andrew James Robert Williams

Department of Physics

Royal Holloway, University of London

A thesis submitted to the University of London for the

Degree of Doctor of Philosophy

September 17, 2013

DECLARATION

I confirm that the work presented in this thesis is my own. Where information has been derived from other sources, I confirm that this has been indicated in the document.

Andrew J R Williams

Abstract

In this thesis we present some phenomenological investigations of freeze-in models of dark matter and also a numerical calculation of the particle flux produced by dark matter annihilations around a rotating black hole.

Freeze-in is an alternative dark matter production mechanism in which an out of equilibrium very weakly coupled particle is produced in the early universe. We consider the Minimal Supersymmetric Standard Model (MSSM) extended by an additional singlet superfield feebly coupled to the other particles. This feeble coupling leads to a long lifetime for the next to lightest superpartner which can only decay via this coupling. The long lifetime of this decaying particles could lead to displaced vertices which provide a prominent signal for beyond the standard model physics. The phenomenology of the signals from this simple Feebly Interacting Massive Particle (FIMP) model is investigated and compared to some experimental searches.

The freeze-in mechanism may also constitute an alternative for generating the correct relic density for dark matter candidates whose predicted freeze-out abundance is too low due to a large total annihilation cross section. We show that although such a mechanism could explain why a dark matter candidate has the correct relic density, some candidates may still be ruled out because they would lead to a large gamma ray flux in dwarf spheroidal galaxies or a large elastic scattering rate in direct detection experiments. To investigate this scenario we examine neutralino dark matter in the MSSM.

Collisions around black holes may provide a window onto very high energy physics. The geodesics of massless particles produced in collisions near a rotating black hole are solved numerically and a Monte Carlo integration of the momentum distribution of the massless particles is performed to calculate the fraction that escape the black hole to infinity. A distribution of in falling dark matter particles, which are assumed to annihilate to massless particles, is considered and an estimate of the emergent flux from the collisions is made. The energy spectrum of the emergent particles is found to contain two Lorentz shifted peaks centred on the mass of the dark matter. The separation of the peaks is found to depend on the density profile of the dark matter and could provide information about the size of the annihilation plateau around a black hole and the mass of the dark matter particle.

Acknowledgements

I would firstly like to thank my supervisor Dr Stephen West whose support and guidance have made this thesis possible.

I am also grateful to SEPNET for funding my PhD as well as the NexT Institute whose graduate courses and workshops have helped enormously.

I extend, of course, my thanks to friends and family for feigning interest in my research for the last four years, especially my mother to whom I owe a great deal. I am particularly grateful to Bertie for showing me how to relax. Finally I am grateful to Anna, whose love, kindness and baking prowess continue to keep me fed and happy.

Contents

List of Figures

List of Tables

Chapter 1

Introduction

Establishing the identity of dark matter (DM) is one of the fundamental problems in particle physics today. There is overwhelming evidence for the existence of non-baryonic particle dark matter requiring physics beyond the standard model. This comes from a variety of sources at the scales of galaxies, galaxy clusters and cosmological scales. The observations of colliding galaxy clusters such as the Bullet cluster have provided unambiguous evidence of the particle nature of DM [11]. Despite this little is known about the properties of the particle or particles that make up the DM since so far only the gravitational effects of DM have been observed.

For any proposed candidate to explain the DM it is important that the theory predicts the correct relic abundance of DM that has been measured with great accuracy by the Planck satellite [12]. One mechanism by which DM can be produced in the early universe is by thermal freeze-out, where the particle initially in thermal equilibrium decouples from the plasma as the universe expands. This is an attractive proposal particularly in the case of Weakly Interacting Massive Particles (WIMPs) whose couplings and mass conspire to produce the correct relic abundance. Many proposed models for DM have consisted of WIMPs and much of the experimental effort to detect DM is tailored to the discovery of WIMPs although alternative candidates do exist.

The main topic of this thesis is one such alternative to the WIMP paradigm of DM. The theory presents an alternative thermal production mechanism to freeze-out called freeze-in which in turn allows alternative candidates for the DM to be considered. The basic principle of freeze-in is that the DM called a FIMP (Frozen-In/Feebly Interacting Massive Particle) has such feeble couplings to the standard model particle that it is out of thermal equilibrium in the early universe, decays of heavy particles occasionally produce DM particles the interactions of which are

so weak that they do not annihilate with each other and thus the number density increases. It is this very small coupling to the other particles which drives the phenomenology around FIMPs.

In this thesis two phenomenological aspects of freeze-in are presented. Firstly the prospect of long lived states occurring at particle colliders due to the very weak coupling of the FIMP. Secondly the possibility that the freeze-in production of DM can be used to regenerate a relic abundance of DM in theories where the predicted abundance of DM is too small.

In addition to freeze-in another alternative way to study DM is the study of DM collisions around black holes. In particular the novel signals that may exist due to the acceleration of DM around rotating black holes. The possibility of very energetic collisions between DM particles close to a black hole and the effect of the black hole on the escaping flux of particles produced in DM collisions is the other topic of this thesis.

This thesis is structured as follows, In chapter 2 the topic of DM is introduced including the production of DM through thermal freeze-out and the existing search strategies for DM. In chapter 3 the topic of freeze-in production is introduced along with a description of the associated phenomenology. Chapter 4 briefly introduces supersymmetry and the Minimal Supersymmetric Standard Model (MSSM), this model forms the basis of the freeze-in models used in the following chapters. The original work in this thesis is presented in the subsequent three chapters and these are, chapter 5 which presents work investigating the possible production of long lived particles produced at the LHC leading to displaced vertices. Chapter 6 explores the phenomenology associated with the regeneration of under-abundant WIMPs in the MSSM. Chapter 7 presents a numerical calculation of the escaping flux of particles from a rotating black hole and the energy spectrum associated with DM annihilations close to the black hole.

Chapter 2

Dark matter

In this chapter the topic of dark matter is introduced. There is a great deal of evidence for the existence of a DM component of the universe and the identity of this DM is an open problem. This introduction gives a brief outline of the DM problem and some of the proposed candidates from particle physics. The issue of detecting DM and the standard production mechanism of freeze-out is also covered.

In section **??** we introduce the standard cosmology of the ΛCDM model of the universe to provide the background for the DM problem. Section 2.1 outlines the evidence for particle DM at the various length scales and how the size of the DM component is estimated. In section 2.2 we give a brief outline of some of the candidates for DM that have been proposed. Section 2.3 is devoted to the production of DM through thermal freeze-out which has been the standard explanation for DM production in many of the models proposed. This will be compared to an alternative mechanism called "freeze-in" in chapter 3. In section 2.4 we outline the experimental methods that have been employed to attempt to detect DM.

2.1 Introduction to cosmology

To describe the universe we specify its geometry via a metric and the dynamics of the metric are described by the Einstein equation that links the geometry to the matter and energy content. We therefore need three ingredients to define the standard cosmological model, a metric, the solution the Einstein equation and the equation of state of the matter and energy in the universe.

The observation that the universe is both isotropic and homogeneous at the largest scales

restricts the form that the metric can take to that of the Robertson-Walker metric [13]

$$ds^2 = dt^2 - a(t)^2 \left(\frac{dr^2}{1-kr^2} + r^2 d\Omega^2 \right), \tag{2.1}$$

where k is a constant describing the spatial curvature and can take the values $k = -1, 0, +1$ with $k = 0$ corresponding to flat space. The scale factor $a(t)$ describes the expansion of space as observed in Hubble's law. Solving the Einstein equation for this metric leads to the Friedmann equation

$$\left(\frac{\dot{a}}{a} \right)^2 + \frac{k}{a^2} = \frac{8\pi G_N}{3} \rho_{tot}, \tag{2.2}$$

where G_N is Newtons constant and ρ_{tot} is the total energy density of the universe. The Hubble parameter is defined as $H(t) = \frac{\dot{a}(t)}{a(t)}$ and the Hubble constant H_0 is the present day value of the Hubble parameter. If the universe is flat, $k = 0$, then we have the following relation between the critical energy density and Hubble parameter.

$$\rho_c = \frac{3H^2}{8\pi G_N}. \tag{2.3}$$

This defines the critical density ρ_c as the energy density required to have a flat universe. It is useful to express the energy densities of the various components of the universe in terms of this critical density and we define the quantity Ω_i as

$$\Omega_i = \frac{\rho_i}{\rho_c}, \tag{2.4}$$

where i represents the ith component of the energy density. The total energy density is then described by

$$\Omega = \sum_i \Omega_i. \tag{2.5}$$

The curvature of the universe can then be re-expressed in terms of Ω by

$$\Omega - 1 = \frac{k}{H^2 a^2}. \tag{2.6}$$

Which makes clear that the value of Ω sets the sign of k. If $\Omega < 1$ then k is negative and the universe is open, $\Omega > 1$ has positive k and a closed universe and $\Omega = 1$ gives $k = 0$, a flat universe.

To describe the evolution of the universe we need to know how the energy density behaves in response to the scale factor. This is described by the equation of state leading to the relationship [13]

$$\rho_i \propto a^{-3(1+\omega_i)}. \tag{2.7}$$

We identify three components to the energy density of the universe described by three values of ω_i. $\omega = 1/3$ corresponding to radiation with $\rho_r \propto a^{-4}$. Matter is described by $\omega = 0$ and $\rho_M \propto a^{-3}$. Vacuum or dark energy given by $\omega = -1$ and $\rho_\Lambda = \text{constant}$. At current times the universe is dominated by the matter and dark energy components while the early universe will have been radiation dominated.

The fact that the universe is expanding now implies that the early universe was hot and dense. The behaviour of the radiation energy density with the scale factor implies that the early universe was radiation dominated and can be described as a relativistic plasma. We can extrapolate our known physics back to give a history of the universe in terms of the temperature [14].

- $T \sim 10^{16}$GeV - This is potentially the scale of Grand Unification where some larger symmetry group breaks down to the standard model gauge groups. Inflation may also occur at this transition.
- $T \sim 10^{2}$GeV - Electroweak symmetry breaking occurs.
- $T \sim 10^{1} - 10^{3}$GeV - The temperature at which a weakly interacting massive particle would undergo freeze-out potentially producing DM.
- $T \sim 0.3$GeV - The QCD phase transition occurs confining quarks and gluons into hadrons.
- $T \sim 1$MeV - Neutrons undergo freeze-out.
- $T \sim 100$KeV - Big bang nucleosynthesis (BBN) occurs with protons and neutrons forming the light elements. The primordial abundances of these light elements agree well with the predictions from BBN.
- $T \sim 1$eV - The matter dominated epoch begins and structure formation can start to occur.
- $T \sim 0.4$eV - Recombination occurs and the photons decouple. The decoupled photons will become the cosmic microwave background radiation (CMB).
- $T \sim 10^{-4}$eV - The current temperature corresponding to $2.7K$.

2.2 Evidence for dark matter

The evidence for the existence of DM has built up over time and comes from a large range of sources. The evidence for DM appears at different scales in the universe from rotation curves of galaxies to the total energy density of matter in the universe. The combination of all of the data provides overwhelming evidence that the majority of the matter in the universe is made up of non-luminous non-baryonic matter which can not be explained by the current standard model of particle physics. Precision measurements of the CMB have allowed the DM component of the universe to be measured with a great deal of accuracy. Despite this achievement DM has still only been detected by its gravitational effects and this leaves the question of identifying and measuring the other properties of the DM and open question.

2.2.1 Galactic scale dark matter and rotation curves

Galaxy rotation curves present compelling direct evidence for the existence of DM at galactic scales. Plotting the circular velocity of stars and gas in a galaxy produces a graph that is incompatible with the prediction obtained when only the luminous matter in the galaxy is considered. At large distances beyond the edge of the visible disk the circular velocity remains flat indicating the presence of matter in addition to the luminous matter in the disk [15, 16, 1].

The circular velocity is given by Newtonian dynamics

$$v(r) = \sqrt{\frac{GM(r)}{r}}, \tag{2.8}$$

where $M(r)$ is the mass contained within the volume up to radius r given by $M(r) \equiv 4\pi \int \rho(r) r^2 dr$. Where $\rho(r)$ is the mass density profile. The observed behaviour of $v(r)$ is that it is approximately constant beyond the disk implying the existence of a halo of matter with $M(r) \propto r$ corresponding to a density profile $\rho(r) \propto 1/r^2$.

Figure **??** shows the rotation curve for the galaxy NGC 6503 along with the contributions of the gas, disk and DM halo. This shows clearly the need for extra DM to explain the shape of the roation curve.

The same method can be applied to the rotation velocities in the interior of the disk to estimate the density profile of the DM within the visible disk and the core of the galaxy which is of importance to both direct and indirect detection of DM. The behaviour of the density profile

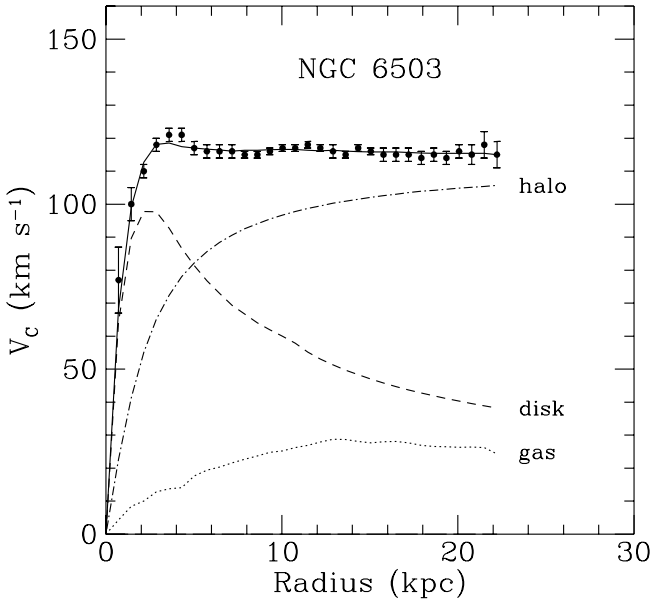

Figure 2.1: Rotation curve of NGC 6503. The dotted, dashed and dash-dotted lines are the contributions of gas, disk and dark matter, respectively. [1]

at the centre of galaxies is unknown, the innermost regions could exhibit either shallow or cuspy profiles. Some observations suggest the presence of shallow or flat cores in the DM density [17, 18] which is in tension with results from N-body simulations of DM halos which predict significantly steeper profiles [19]. The measurement of the local DM density at our location in the galaxy is less uncertain since the estimates depend much less on the unknown inner profile [20, 21].

Galactic rotation curves are not the only evidence for DM within galaxies. Modulations in the gravitational lensing around galaxies provides evidence for dark substructure within the halos of the galaxies which is expected in models with cold DM [22, 23, 24]. The weak gravitational lensing of distant galaxies by foreground structure also indicates the presence of DM [25]. The velocity dispersions within the dwarf satellites of the milkyway implies a mass to light ratio that indicates that they are DM dominated [26, 27].

2.2.2 Dark matter in galaxy clusters

The first evidence for DM came from observation of galaxy clusters. When the mass inferred by the velocity dispersion of the Coma cluster indicated a ratio of mass to luminosity around 400

times that of the sun [28] showing that the majority of the mass was not contained in stars. More recent dynamical estimates of the mass contained in galaxy cluster suggest values that require DM to be explained [29, 30].

Another method of estimating the mass of a galaxy cluster is to measure the temperature of the hot gas in rich clusters by X-ray emission. For a gas in hydrostatic equilibrium the temperature can be related to the total mass enclosed. The disparity between the measured temperature from X-ray emission and the predicted temperature when considering the baryonic mass in the clusters indicates the presence of DM.

This can be compared to an independent measurement of the mass of the cluster from gravitational lensing. By measuring the distortion of objects behind the cluster the gravitational well produced by the cluster can be mapped allowing the mass of the cluster to be measured.

It is important to measure the baryonic mass of the cluster so that this can be compared to the total gravitational mass since this will show the separate contributions of the ordinary baryonic matter and DM in the cluster. The bayronic mass can measured by the Sunyaev-Zeldovich effect [31]. The Sunyaev-Zeldovich effect occurs when the CMB photons undergo compton scattering with hot electrons, this causes the apparent brightness of the CMB in the direction of galaxy clusters to change. This change can be used to infer the density of gas along the line of sight in the cluster and thus measure the baryonic mass of the cluster.

2.2.3 Dark matter at cosmological scales

We have seen that DM is necessary to explain the dynamics of galaxies and galaxy clusters but this does not provide a precise observation of the total amount of DM in the universe. The total DM content of the universe can however be measured with great accuracy due to precision measurements of the CMB. WMAP and more recently the Planck satellite have measured the anisotropies of the CMB radiation with incredible precision allowing the cosmological parameters of the universe to be measured in detail [2, 32, 33].

The CMB is isotropic to the 10^{-5} level and corresponds precisely to the black body spectrum at $T = 2.726$K. The tiny anisotropies in the CMB put stringent constraints on cosmological parameters, in particular we can extract $\Omega_b h^2$ the abundance of baryons in the universe and $\Omega_M h^2$ the total abundance of matter.

The observed temperature fluctuations in the CMB can be expanded in terms of the spherical

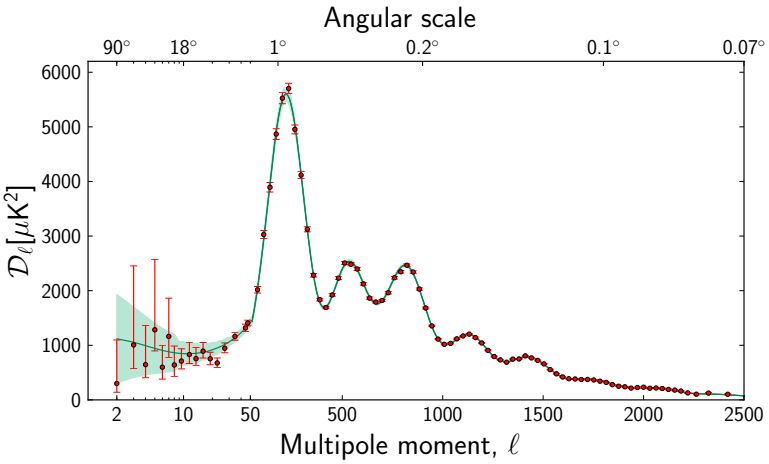

Figure 2.2: The temperature angular power spectrum of the primary CMB from Planck, showing a precise measurement of seven acoustic peaks, that are well fit by a simple six-parameter ΛCDM theoretical model. The shaded area around the best-fit curve represents cosmic variance, including the sky cut used. The error bars on individual points also include cosmic variance. The horizontal axis is logarithmic up to $l = 50$, and linear beyond. The vertical scale is $l(l+1)C_l/2\pi$ [2].

harmonics

$$\frac{\delta T}{T} = \sum_{l=2}^{\infty} \sum_{m=-l}^{+l} a_{lm} Y_{lm}(\theta, \phi), \tag{2.9}$$

where Y_{lm} are the spherical harmonic functions of order l and degree m, θ and ϕ are the spherical polar coordinates of the point on the last scattering surface and a_{lm} are the coefficients. The power spectrum is then defined in terms of

$$C_l \equiv \langle |a_{lm}|^2 \rangle \equiv \frac{1}{2l+1} \sum_{m=-l}^{+l} |a_{lm}|^2, \tag{2.10}$$

where the power spectrum is given by the behaviour of C_l as a function of l. The resulting power spectrum as measured by Planck [2, 33] is shown in figure 2.1.

In the early universe baryons and dark matter behave differently. The baryons will undergo gravitational in fall enhancing perturbations but this will be resisted by photon pressure leading to acoustic oscillations. Unlike the baryons the dark matter is decoupled from the photons and feels no radiation pressure. In the CMB this is realised in the ratio of the heights between the even and odd acoustic peaks relating these to the ratio between the baryon and dark matter densities [3].

The cosmological parameters are extracted from the CMB anisotropy data by taking a simple cosmological model with a fixed number of parameters including the matter and baryon com-

ponents then finding the peak of the likelihood given the observed data. This can be performed using the data from a single experiment such as Planck [12] and WMAP [34] or by a global fit to all the cosmological data from many different observations [35, 36, 37].

The most stringent constraints on the DM abundance come from measurements of the CMB by Planck in combination with the higher resolution CMB experiments ACT and SPT which measure the anisotropies for larger values of l. This is combined with data on the baryon acustic oscilations (BAO) from the Sloane Digital Sky Survey (SDSS) and WMAP polarisation data at low l. This gives a measurement of the baryon density $\Omega_b h^2$ and the DM density $\Omega_{DM} h^2$ as [12]

$$\begin{aligned} \Omega_b h^2 &= 0.02214 \pm 0.00024, \\ \Omega_{DM} h^2 &= 0.1187 \pm 0.0017. \end{aligned}$$

2.2.4 Large scale structure as evidence for DM

The formation of large scale structure also provides evidence for DM. The large scale structure of the universe has been observed via the Sloan Digital Sky Survey [38]. This can be compared with the structures generated in N-body simulations such as the MS-II simulation [39]. Simulations without DM fail to generate the filament and void structures that are observed. We can also consider the scenario in which the DM is relativistic during structure formation in which case the relativistic DM washes out the formation of structure [40, 41], this indicates that the DM must be non-relativistic or "cold" during structure formation.

2.2.5 The Bullet cluster

Recently the study of merging galaxy clusters has provided a direct observation of DM in the Bullet cluster [11]. This observation hinges on the disentanglement of the three components of the galaxy cluster the luminous galaxies, the hot baryonic gas and the DM. When the clusters collide the DM and stars are essentially non-interacting and pass by, the gas behaves like a fluid and friction between the plasma in the two clusters slows its passage. The stars can be imaged in the visible spectrum, while the position of the plasma can be traced by its X-ray emission. Finally the distribution of matter can be inferred by gravitational lensing. Strikingly the matter distribution does not follow the distribution of the plasma providing evidence that the majority of the mass is contained in the non-interacting DM.

2.3 Dark matter candidates

In the previous section the need for DM was illustrated and it was shown that this DM must be non-baryonic. The non-baryonic and non-luminous nature of DM already constrains the properties of the DM enough to exclude all the standard model particles except for the neutrinos. However standard model neutrinos can not account for all of the DM and so we require a new particle (or particles) beyond the standard model to explain the DM.

In order for a particle to be a good candidate for the DM it should satisfy the following conditions [42]

1. Reproduce the correct relic density of DM.
2. Be cold.
3. Be electromagentically neutral.
4. Be consistent with BBN.
5. Have self interactions that are compatible with constraints from structure formation.
6. Be compatible with direct DM searches.
7. Be compatible with indirect gamma ray and neutrino searches.

The requirement that the DM is cold here refers to the kinetic energy of the DM when it decouples if it is relativistic it is described as hot DM and its free streaming length will smooth out small scale structure. The constraints from BBN place limits on DM that is produced with decays during the BBN epoch. The direct and indirect searches will be discused in section 2.4 while we describe one of the methods of producing the correct relic density in section 2.3.

We briefly describe here some of the proposed DM candidates from particle physics. One important distinction is between candidates that are Weakly Interacting Massive Particles (WIMPs) and those that are not. WIMPs have received a great deal of attention as they have the attraction of correctly reproducing the relic density of DM (see section 2.3) but are also beginning to be in tension with DM detection experiments as they probe the natural cross section for WIMPs. At the same time the LHC is sensitive to many of the proposed WIMP models.

2.3.1 WIMP Candidates

- *Neutralinos*:

  In supersymmetric theories the lightest neutralino is a WIMP and makes a good DM candidate. In supersymmetry every standard model particle has a corresponding superpartner with spin differing by 1/2. The lightest of these superpartners must be stable to forbid fast proton decay. The neutralinos are combinations of the superpartners of the neutral gauge bosons and higgs particles, they naturally have weak scale masses and interactions which can reproduce the correct relic abundance of DM. See chapter 4 for an introduction to the Minimal Supersymmetric standard model.

- *Kaluza-Klein Dark Matter*:

  In models with compactified extra dimensions a WIMP candidate can emerge due to the tower of Kaluza-Klein (KK) states. Universal extra-dimension (UED) models have a new spatial dimension in which all the standard model particles can propagate [43]. In the simplest UED models the extra dimension is compactified on a circle and momentum in the new dimension is therefore quantized. Particles with quantized momentum in the extra dimension appear as heavier copies of standard model particle in 4-dimensions creating a Kaluza-Klein tower of states. The lightest of these KK-states is stabilized by KK-parity arising from the conservation of momentum in the extra dimensions and is thus a DM candidate [44, 45]. The lightest KK-state is often the KK-partner of the hypercharge gauge boson to reproduce the correct relic abundance the mass is typically between 600 GeV and 1.5 TeV [46].

- *Little Higgs models*:

  Little Higgs models have been developed to stabilize the Higgs mass by making the Higgs boson the pseudo-Goldstone boson whose mass is protected by approximate global symmetries [47, 48, 49]. Little Higgs models produce effective theories valid up to $\sim$ 10TeV and can produce WIMP DM candidates typically in the form of a heavy partner of the hypercharge gauge boson [50, 51, 52]. Stable DM candidates in little Higgs models require the introduction of a discrete unbroken symmetry that is fundamental and not broken in the high energy theory.

2.3.2 Non-WIMP Candidates

- *SuperWIMPs*:

  SuperWIMPs are DM candidates with interaction strength smaller than that of a WIMP. In the SuperWIMP frame work a WIMP decouples from the thermal bath with some relic abundance and then decays to the SuperWIMP [53]. The relic density of superWIMPs is then given by

  $$\Omega_{SWIMP} = \frac{m_{WIMP}}{m_{SWIMP}} \Omega_{WIMP}. \tag{2.11}$$

  There are a number of models with particles that are SuperWIMP candidates such as the gravitino in supersymmetric models [54, 55, 56, 57, 58, 59] or the KK-mode graviton in extra dimension models [60, 53, 55]. Because of the suppressed interactions of the SuperWIMP the WIMP may be long lived enough to have signals for BBN.

- *WIMPless hidden sectors*:

  Another category of DM occurs in models with hidden sectors. In a hidden sector model the DM belongs to an extension of the standard model that has no standard model gauge couplings [61]. This increases the freedom available in creating a hidden sector but typically comes with the cost of the hidden sector no longer being connected to the other outstanding particle physics problems such as the hierarchy problem. While the WIMP miracle is generally absent for a hidden sector theory there exists the so called WIMPless miracle which allows non-WIMP DM to reproduce the correct abundance of DM. This occurs by noting that the thermal relic density is governed by (see section 2.3)

  $$\Omega_X \sim \langle \sigma_A v \rangle^{-1} \sim \frac{m_X^2}{g_X^4}. \tag{2.12}$$

  Where X is the DM particle with mass m_X, coupling g_X and $\langle \sigma_A v \rangle$ is the thermally averaged annihilation cross section. For $m_X \approx m_{weak}$ and $g_X \approx g_{weak}$ the WIMP miracle is fulfilled and the correct abundance of DM is generated. However it is clear that the correct relic abundance can also be satisfied for other combinations of m_X and g_X expanding the class of models for which the correct relic abundance is obtained through thermal freeze-out.

  A number of hidden sector models have been proposed, notably in Gauge Mediated Su-

persymmetry Breaking models (GMSB) [62, 63] but WIMPless models for DM also occur in other contexts [64].

- *Axions*:

  Axions are a potential solution to the strong CP problem in the standard model [65, 66, 67, 68]. As DM candidates axions are constrained to be very light by observations of stellar cooling [69, 70, 71, 72, 73] and interact very weakly with the standard model particles. Thermal production of axions is insufficient to produce the correct abundance of DM and would imply a mass of the axion that leads to too rapid decay of axions to photons to be a DM candidate. Several non-thermal production mechanisms for axions have been proposed [74, 75, 76, 77, 78].

- *Sterile Neutrinos*:

  Sterile neutrinos are similar to the standard model neutrinos but lacking the standard model gauge couplings. They gain their couplings to the other particles via mixing with the standard model neutrinos. They can arise in models to explain the neutrino masses in the standard model. Sterile neutrinos can be produced via oscillation with the standard model neutrinos [79, 80] or can be produced at high temperatures by the decays of new heavy particles in the thermal bath [81, 82, 83]. Sterile neutrinos will decay to the standard model neutrinos and so must have a life time longer than the age of the universe to be a good DM candidate. An interesting astrophysical signal for sterile neutrino DM is the possibility of a gamma ray line produced by the decays of the sterile neutrino [82, 84].

- *Technicolor*:

  Technicolor models solve the hierarchy problem by breaking the electroweak symmetry dynamically without introducing an elementary scalar [85, 86, 87, 88]. Technicolor introduces a new strongly coupled gauge group. In analogy with QCD this leads to composite states including a light composite Higgs boson which is responsible for the EWSB. Technicolor also introduces a new technibaryon quantum number which is conserved making the lightest technibaryon composite state stable. If the lightest technibaryon is electrically neutral then it can be a DM candidate [89, 90, 91, 92, 93].

2.4 Dark matter production

For many DM candidates the relic abundance of DM is governed by the decoupling of the DM from the thermal bath in the early universe. This process is known as thermal freeze-out and plays a role for any stable or meta-stable particle that is in thermal equilibrium at some point during the evolution of the universe. The abundance of DM is generated by the decoupling of the DM from the thermal bath. At early times the DM is in thermal equilibrium and its number density tracks the equilibrium density given by the Boltzmann distribution. As the universe expands and cools the equilibrium number density will decrease rapidly as the temperature drops bellow the mass of the DM. This is due to annihilations of the DM while the production of the DM is Boltzmann suppressed. As the universe expands at some point the interaction rate of the DM will drop below the Hubble expansion rate of the universe at this point the DM decouples from the thermal bath and annihilation process cease to occur. The left over number density at this time then becomes the DM relic. A key feature of thermal freeze-out is that the larger the annihilation cross section of the DM the longer the DM is able to stay in equilibrium and the smaller the DM relic becomes. Figure **??** shows the evolution of the co-moving number density of the DM as it decouples, as the annihilation cross section increases the DM decouples at latter times and with a smaller relic abundance. To calculate the relic abundance of DM from freeze-out we need to solve the Boltzmann equations that govern the number density of the particles in the thermal bath. The evolution of the number density n of a particle species is given by

$$\frac{dn}{dt} + 3Hn = -\langle \sigma v \rangle \left(n^2 - (n^{eq})^2 \right), \tag{2.13}$$

where H is the Hubble expansion rate, $\langle \sigma v \rangle$ is the thermally averaged annihilation cross-section multiplied by the velocity and n^{eq} is the equilibrium number density of the particle species. The second term on the left hand side accounts for the dilution of the number density by the expansion of the universe while the right hand side is the collision term and accounts for the scattering processes that produce or annihilate the particles. The effect of the right hand side can be understood by noting that when the number density deviates from the equilibrium density the collision term acts to bring the particle species back to the equilibrium density. It is clear then that when the annihilation rate $\langle \sigma v \rangle$ dominates over the expansion rate H the particle will remain in equilibrium. When H is much larger than the annihilation rate then the right hand side can be

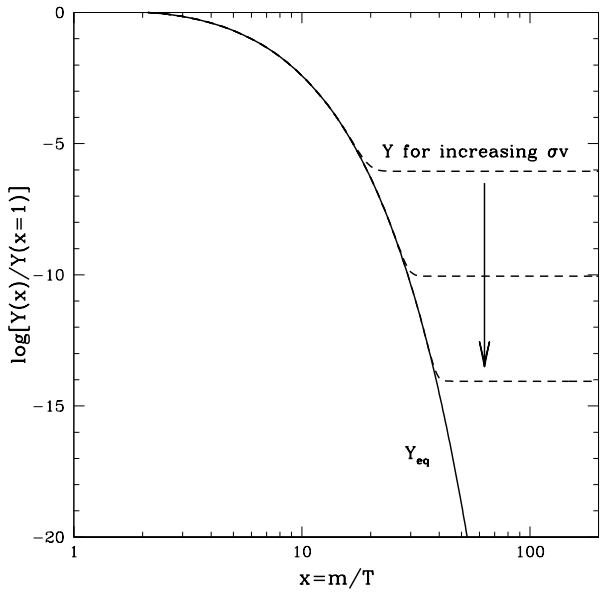

Figure 2.3: The evolution of $Y(x)/Y(x=1)$ versus $x = m/T$ where $Y = n/s$ [3]

neglected and the only effect is the dilution due to expansion.

It is usual [94] to introduce the number density per co-moving volume Y defined by

$$Y \equiv \frac{n}{s}, \tag{2.14}$$

where s is the entropy density given by $s = 2\pi^2 g_* T^3/45$. The conservation of entropy means that sa^3 is a constant which leads to

$$\frac{dn}{dt} + 3Hn = s\frac{dY}{dt}. \tag{2.15}$$

Eq. **??** can then be rewritten as

$$\frac{dY}{dt} = -\langle \sigma v \rangle s \left(Y^2 - (Y^{eq})^2 \right), \tag{2.16}$$

where $Y^{eq} \equiv n^{eq}/s$. Since the right hand side depends only on the temperature it is then useful to make a change of variables from t to $x \equiv m/T$ where m is the mass of particle. We then have

$$\frac{dY}{dx} = \frac{m}{x^2}\frac{s}{\dot{T}}\langle\sigma v\rangle\left(Y^2 - (Y^{eq})^2\right). \tag{2.17}$$

The time derivative of the temperature $\dot{T}$ can be written in terms of the entropy by

$$\frac{1}{\dot{T}} = \frac{1}{\dot{s}}\frac{ds}{dT} = -\frac{1}{3Hs}\frac{ds}{dT}. \tag{2.18}$$

From the Friedmann equation (eq. 2.2) we have that the Hubble expansion rate is given by

$$H^2 = \frac{8\pi}{3M_{\rm P}^2}\rho, \tag{2.19}$$

where $M_{\rm P}$ is the Planck mass and ρ is the total energy density of the universe. For a radiation dominated universe ρ is given by

$$\rho = \frac{\pi^2}{30}g_{\rm eff}(T)T^4, \tag{2.20}$$

where $g_{\rm eff}(T)$ is the effective number of degrees of freedom for the energy density. The entropy density of the radiation dominated universe is given by

$$s = \frac{2\pi^2}{45}h_{\rm eff}(T)T^3, \tag{2.21}$$

where $h_{\rm eff}(T)$ is the entropy effective number of degrees of freedom. We then introduce the degrees of freedom parameter $g_*^{1/2}$ given by

$$g_*^{1/2} = \frac{h_{\rm eff}}{\sqrt{g_{\rm eff}}}\left(1 + \frac{T}{3h_{\rm eff}}\frac{dh_{\rm eff}}{dT}\right). \tag{2.22}$$

We can then substitute in the definitions of H and $\frac{ds}{dT}$ into the Boltzmann equation to give

$$\frac{dY}{dx} = \left(\frac{45\pi}{M_{\rm P}^2}\right)^{-1/2} g_*^{1/2}\frac{m}{x^2}\langle\sigma v\rangle\left(Y^2 - (Y^{eq})^2\right). \tag{2.23}$$

This equation can then be solved numerically to give the present day DM yield. An approximate solution can be obtained in the following way, we first introduce a new variable which tracks the departure of the species from equilibrium $\Delta = Y - Y^{eq}$ and approximate the annihilation cross

section in the non-relativistic limit by expanding in terms of v

$$\langle \sigma v \rangle \ = a + b\langle v^2 \rangle + O(v^4) \approx a + \frac{6b}{x}. \tag{2.24}$$

We then have for the Boltzmann equation

$$\frac{d\Delta}{dx} = -\frac{dY^{eq}}{dx} - f(x)\Delta\left(2Y^{eq} + \Delta\right), \tag{2.25}$$

where $f(x)$ is given by

$$f(x) = \sqrt{\frac{\pi g_*}{45}} M_{\rm P} \left(a + \frac{6b}{x}\right) x^{-2}. \tag{2.26}$$

We call the temperature at which the particle decouples T_F and define $x_F \equiv m/T_F$. At late times and low temperatures we have $x \gg x_F$ and in this region the Boltzmann equation simplifies to

$$\frac{d\Delta}{dx} = -f(x)\Delta^2 \qquad \text{for} \quad x \gg x_F. \tag{2.27}$$

This can be integrated between x_F and x_∞ to give

$$Y_\infty^{-1} = \sqrt{\frac{\pi g_*}{45}} M_{\rm P}\, m\, x_F^{-1} \left(a + \frac{6b}{x_F}\right). \tag{2.28}$$

The relic abundance of DM can then be calculated from the yield by $\rho = mn = ms_0 Y_\infty$ where s_0 is the present day value of the entropy density $s_0 = 2889.2cm^3$. The relic density is then usually expressed in terms of the critical density

$$\Omega h^2 \approx \frac{1.07 \times 10^{-9}\text{GeV}}{M_{\rm P}} \frac{x_F}{\sqrt{g_*}} \frac{1}{(a + 3b/x_F)}. \tag{2.29}$$

The problem is then reduced to calculating thermally averaged annihilation cross section, extracting a and b and finding the value of x_F.

x_F is defined as the time at which the particle decouples from the thermal bath. We can express this by stating

$$\Delta(x_F) = cY^{eq}(x_F). \tag{2.30}$$

That is x_F is the temperature at which Δ becomes comparable to Y^{eq} up to some order one numerical constant c. We then take the limit $x \ll x_F$ and again solve the Boltzmann equation

giving,

$$\Delta = -\frac{dY^{eq}}{dx}\frac{1}{2f(x)Y^{eq}}. \tag{2.31}$$

The final result being [95]

$$x_F = \ln\left[c(c+1)\sqrt{\frac{45}{8}}\frac{g}{2\pi^3}\frac{mM_P(a+6b/x_F)}{g_*^{1/2}x_F^{1/2}}\right], \tag{2.32}$$

where g is the number of internal degrees of freedom of the particle species and we have used the Boltzmann equilibrium distribution

$$n^{eq} = g\left(\frac{mT}{2\pi}\right)^{3/2} e^{-m/T}. \tag{2.33}$$

x_F is then found by iterative solution of equation. 2.15 and the numerical value of c is found by comparison to numerical solutions or by matching of the early and late time solutions of the Boltzmann equation.

It is often useful to make an approximate solution that captures the behaviour of Ωh^2 that is

$$\Omega h^2 \approx \frac{3\times 10^{-27} cm^3 s^{-1}}{\langle\sigma v\rangle}. \tag{2.34}$$

Which will often provide an order of magnitude estimate of the relic density.

The relic density calculation can be dramatically altered by the presence of co-annihilations [94]. Co-annihilations occur when there is one or more particles charged under the same symmetry as the DM that are similar in mass to the DM particle, for example in supersymmetry all of the superpartners have odd R-parity and the DM candidate is the lightest R-parity odd particle.

Numerical tools now exist to automate the calculation of the relic density including co-annihilations. `micrOMEGAs` [96, 97, 98] calculates the relic density numerically including co-annihilations when required for many different models while the `DarkSusy` [99] numerical code performs the calculation for supersymmetric models.

2.5 Detecting dark matter

So far the only evidence for DM comes from its gravitational interactions. A key step in identifying the nature of the DM is to measure its other couplings to the standard model particles

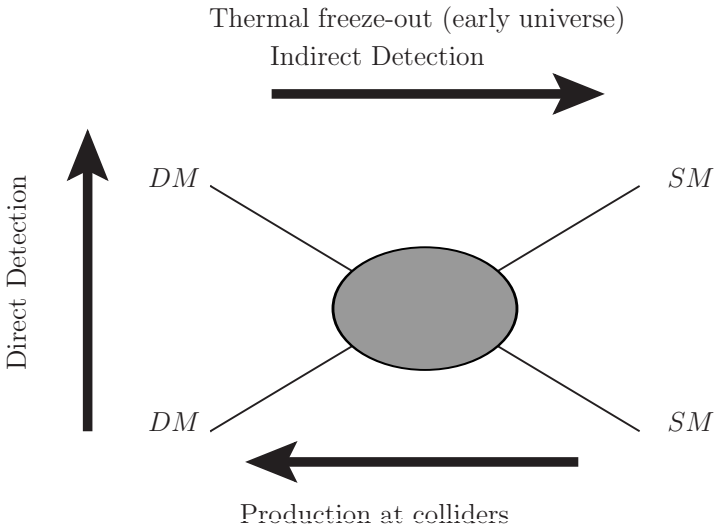

Figure 2.4: Relation between detection methods and production of DM by thermal freeze-out

should they exist. There are a number of methods that have been proposed to detect DM and these depend on the type of DM candidate and its expected interactions. Generally the type of DM detection experiment can be split into three categories, direct detection, indirect detection and production at colliders. Direct detection involves measuring an interaction between the DM thought to be passing through the earth all the time and the target material of the detector. Indirect detection aims to detect the astrophysical signal of photons, neutrinos or antiparticles produced by annihilating or decaying DM in the galaxy. The production of DM at colliders such as the LHC can also occur, in this case the DM is either produced directly from annihilating standard model particles or appears at the end of a decay chain produced from new heavy particle.

For particles produced by thermal freeze-out the detection methods and production mechanism can all be related as shown in figure 2.2. Freeze-out involves the process of DM pair annihilating to standard model states, DM DM $\rightarrow$ SM SM and the same process can occur today in the galaxy producing a signal for indirect detection. The opposite process SM SM $\rightarrow$ DM DM corresponds to the production of DM at colliders. The final direction is DM SM $\rightarrow$ DM SM the elastic scattering of DM off a SM particle which can be observed in direct detection experiments.

2.5.1 Collider searches

The weakness of the interactions between DM and the standard model particles means that if DM is produced in a particle accelerator then it will leave the detector without interacting. DM therefore appears as missing energy and momentum in collisions rather than being detected directly. There have been many searches for new physics at LEP, the Tevatron and the LHC that have constrained DM candidates. The limits depend on the type of DM candidate for example searches for supersymmetry will constrain neutralino DM. Typically these searches look for the pair production of new heavy particles that then decay producing standard model particles and a pair of DM particles. The searches then put limits on the production of the standard model particles in association with missing transverse energy.

Another method of searching for DM at colliders is to look for its direct production, if only a pair of DM particles is produced then there is no detectable signal however if a photon or gluon is radiated from the initial state then DM production is signalled by events with a single photon or gluon. These searches constrain the effective coupling of the DM to the standard model quarks and can be compared directly to direct detection experiments [100, 101, 102, 103].

Despite not showing up in the detectors it may still be possible to measure the parameters of the DM if it can be produced at the LHC. In particular its mass can be measured using event variables calculated from the visible part of the event and the missing transverse energy and momentum. With enough events these variables can be used to infer the mass of the invisible particles [104, 105, 106, 107].

2.5.2 Direct detection dark matter searches

The general idea of a direct detection experiment is to set up a sensitive device filled with a target element that is able to measure energy deposited in the target from an interaction with a DM particle. Since DM in the galaxy is passing through the earth all the time even with a small interaction cross section the DM will interact with the nucleus of atoms in the target material from time to time. The detector must then measure the recoil of the target nucleus from the DM interaction.

Direct detection of DM is challenging as the kinetic energy of the DM is set by the relative velocity of the earth to the galaxy at around $220 km/s$. The kinetic energy of the DM then depends on its mass but for a WIMP candidate it will be of the order of keV. The energy

deposited in the detector by the DM is then much less than the energy from naturally occurring radioactive decay. Direct detection experiments must therefore be shielded from radioactivity and cosmic rays that would swamp any signal from DM.

To show evidence for DM interactions the experiment must measure a number of nuclear recoils above the background rate. The expected number of nuclear recoils within a range of recoil energy (E_1, E_2) is given by [3]

$$N_{E_1-E_2} = \sum_i \int_{E_1}^{E_2} \frac{dR_i}{dE} \varepsilon_i(E) dE, \tag{2.35}$$

where i runs over the different nuclear species in the target material, $\frac{dR_i}{dE}$ is the differential count rate per unit mass of i. $\varepsilon_i(E)$ is the effective exposure of i. The differential count rate is given by

$$\frac{dR_i}{dE} = \frac{\rho \sigma_i |F_i(E)|^2}{2m\mu_i^2} \int_{v>\sqrt{M_i E/2\mu_i^2}} \frac{f(\vec{v},t)}{v} d^3v, \tag{2.36}$$

where ρ is the local DM density, σ_i is the DM-nucleus cross section, $F_i(E)$ is the nuclear form factor which accounts for the finite size of the nucleus. m is the DM mass and μ_i is the reduced mass of the DM and nucleus system. v is the velocity of the DM relative to the detector and M_i is the mass of the target nucleus so that the integration over the velocity begins at the minimum velocity required to produce a recoil of energy E. $f(\vec{v},t)$ is the DM velocity distribution in the detector reference frame. The velocity distribution and local density of DM contain all of the astrophysical uncertainties in the expected count rate.

The effective exposure of the target is given by

$$\varepsilon_i(E) = \mathcal{M}_i T_i \xi_i(E), \tag{2.37}$$

where $\mathcal{M}_i$ is the total mass of target species i, T_i is time that the detector is active and $\xi_i(E)$ is the efficiency of the detector for counting nuclear recoils with energy E.

To maximize the sensitivity of the direct detection experiment the expected count rate should be made as large as possible which can be achieved with large target masses and exposure times. The background count rate needs to be minimized with shielding and background rejection. Upper limits on the scattering cross-section of the DM with the nucleus can be found by comparing the expected count rate with observation. The absence of a signal can therefore constrain DM

candidates that predict a cross-section above the limit.

The scattering of DM off the target nucleus can be classified by two characteristics of the interaction. Whether the interaction is spin-dependent or spin-independent and whether the scattering is elastic or inelastic.

The coupling of the DM to the quarks can be either scalar or axial-vector, for scalar couplings the cross-section is independent of the spin of the nucleus and is thus constrained by spin-independent interactions. In this case the DM couples coherently to the whole nucleus and the cross section is proportional to the atomic mass. For axial-vector couplings the DM couples to the overall spin of the nucleus so there is no gain from using heavier elements.

Elastic scattering occurs when the DM interacts with the nucleus as a whole causing the nucleus to recoil. If the kinetic energy of the recoiling energy is large enough for the detector to measure then the DM interaction can be recorded. In inelastic scattering the DM scatters off the target and either the nucleus or an electron is put into an excited state. The subsequent radiation due to the relaxation can then be detected. Inelastic scattering can also occur when there is another particle close enough in mass to the DM that there is enough energy for the new particle to be produced in the final state such that the scattering with the quark in the nucleus becomes $DM\ q \rightarrow NP\ q$, where NP is the new particle and q is a quark in the nucleus.

2.5.3 Indirect detection dark matter searches

Indirect detection of DM searches look for DM pair annihilations producing visible particles. DM decaying to lighter particles can also produce visible particles that can be detected. The rate at which DM annihilates is proportional to the square of the local density of DM it is therefore natural to search for DM annihilations in regions with a large expected density such as the centre of the galaxy. Dwarf spheroidal galaxies are also good targets as they are suspected to be DM dominated and so would have a large signal to background ratio. DM annihilations could also occur where DM gathers at the centre of large gravitational bodies such as the sun.

Indirect detection can be categorised by the visible messenger particle that is produced in the annihilation or decay and then detected by the experiment. Indirect detection can be achieved through the detection of the gamma rays, neutrinos, positrons or anti-protons and the nature of the signal from each of these varies considerably.

- *Gamma rays*:

Gamma rays can be produced from DM annihilation or decays in two ways. Firstly the DM can annihilate to form standard model particles such as gauge bosons or fermions the decays of these particles and the production of jets from quarks produced a continuous spectrum of gamma rays. The second type of gamma ray signal is the emission of a fixed energy gamma ray line. This occurs when the DM annihilates directly to a pair of gamma rays or a $Z\,\gamma$ pair. The energy of the gamma rays in this case will be proportional to the mass of the DM which could be of the order of 100GeV. Although the flux of gamma rays would be small the observation of a gamma ray line at this high energy would be a strong signal for DM and also indicate the mass. Decaying DM can also produce a gamma ray line for example sterile neutrinos can decay to produce a keV gamma ray line. One advantage of gamma rays is that their propagation through the galaxy is well understood and can be pointed back to their origin. This allows indirect detection experiments to mask known sources of gamma rays and to perform observations in regions thought to be rich in DM.

- *Neutrinos*:

  Neutrinos can also be produced in DM annihilations giving rise to another source of indirect detection. Neutrinos are able to pass through matter without interacting this means that unlike other particles neutrinos produced at the centre of the sun can pass freely to be detected by neutrino telescopes on earth. DM may have become bound due to scatterings off particles in the sun increasing the density of making the centre of the sun a possible point source of neutrinos arising from DM annihilations. There is a neutrino background coming from the fusion processes occurring in the sun however DM annihilations typically produce neutrinos from decays of Z and W bosons with much larger energy allowing them to be discriminated from the background.

- *Antimatter*:

  DM annihilations that produce standard model particles will necessarily produce equal numbers of particles and anti-particles. These can be produced directly in the form of fermion anti-fermion pairs or from decays of heavier particles. In particular stable positrons will be produced and stable anti-protons will form from the hadronisation of anti-quarks. The observation of a flux of positrons or anti-protons above the expected

background is therefore evidence of DM annihilations. The observation of anti-particles is complicated since they are charged and are thus deflected by magnetic fields in the galaxy. This makes the propagation of the anti-particles uncertain and the source of any excess of anti-particles can not be determined. Searches for anti-particle excesses from DM annihilation must instead estimate the expected flux of anti-particles from annihilation throughout the DM halo and their subsequent propagation. This also means that local astrophysical sources of anti-particles cannot be excluded as the cause of an excess.

Chapter 3

Freeze-in production of dark matter

In the previous chapters the dark matter problem was introduced and the standard freeze-out production of a WIMP was described. In this chapter an alternative production mechanism of DM known as freeze-in [4] is introduced. This alternative method of producing the DM leads to new DM candidates known as FIMPs (Feebley Interacting/Frozen-In Massive Particles) and new experimental signatures for the detection of DM which vary considerably from the detection of WIMPs. In Section. **??** the basic mechanism of freeze-in and the properties of frozen-in particles are described. Section. 3.1 describes the experimental signatures associated with freeze-in and FIMP DM and how freeze-in can be differentiated from freeze-out experimentally. Section. 3.2 outlines the calculation of the relic abundance of DM due to freeze-in from different processes in the early universe.

3.1 Basics of freeze-in

We first recall the process of thermal freeze-out [108, 109, 110] in which the DM particle begins in thermal equilibrium with the hot plasma and its number density is set by the equilibrium number density. As the temperature of the universe drops below the mass of the DM the processes that create DM particles become Boltzmann suppressed and annihilations of DM particles begin to dilute the number density of the DM. At some point the expansion rate of the universe becomes larger than the annihilation rate and the DM co-moving number density becomes fixed. A key feature of this processes is that the longer the DM stays in thermal equilibrium the more DM is annihilated away and the freeze-out abundance of DM is reduced. That is the later the

decoupling time of the DM the more Boltzmann suppressed the equilibrium number density of the DM becomes and smaller the final yield of DM. Since the decoupling typically occurs at a factor of 25-30 below the DM mass the production of DM is entirely infrared (IR) dominated, this means that the production is dominated by interactions described by the low energy theory and does not depend on any unknown high energy physics.

Freeze-in represents an alternative to this picture that retains the attractive feature of IR-dominance. In freeze-in we consider a FIMP labelled X that is thermally decoupled from the thermal bath. This is achieved by restricting the couplings that connect the FIMP to the thermal bath particles to be $\ll 1$. The number density of X is assumed to be negligible due to some early process such as inflation. Even though the interactions between X and the bath are extremely weak some X particles will still be produced by interactions in the thermal bath. As in freeze-out these interactions will eventually become Boltzmann suppressed when the temperature of the bath drops below the masses of the particles involved in the process. This freezes-in an abundance of FIMP particles. The amount of particles produced by this process increases with the coupling between the bath and FIMP. In contrast to freeze-out the FIMP never reaches thermal equilibrium and annihilation of FIMP particles does not occur since the annihilation rate is too small[1].

It can be seen from the above description that freeze-in is essentially the opposite process to freeze-out. In freeze-out a particle species is initially in thermal equilibrium and as the temperature decreases below its mass it decouples from thermal bath. In freeze-in the particle species is initially out of thermal equilibrium and its number density is increasing as the temperature drops below its mass. In freeze-in the particle is approaching thermal equilibrium from its initial out of equilibrium state while in freeze-out the particle is departing from thermal equilibrium. The dependence of the freeze-in and freeze-out yields on the coupling of the WIMP or FIMP is also inverted. In freeze-out increasing the coupling keeps the WIMP in thermal equilibrium for longer decreasing the freeze-out relic abundance. In freeze-in increasing the coupling increases the rate at which the FIMP is approaching equilibrium and increases the relic abundance of the FIMP.

The basic mechanism of freeze-in can be considered for a FIMP particle X of mass m coupled to the thermal bath via a yukawa interaction with coupling constant $\lambda \ll 1$. At $T >> m$ the yield

[1] Assuming there are no extra states in the hidden sector that the FIMP can annihilate to

of X particles during a Hubble doubling time is given by [4],

$$Y_X(T) \sim \lambda^2 \frac{M_{\rm PL}}{m} \frac{m^2}{T^2}, \tag{3.1}$$

where $Y_X = n_X/S$, with n_X the number density of X and S the entropy density of the thermal bath and M_{PL} is the planck mass. The process is IR dominated due to the factors of T and will be dominated by production at $T \approx m$ due to the Boltzmann suppression at temperatures below m. The yield of FIMPs frozen-in can then be approximated by

$$Y_X \sim \lambda^2 \frac{M_{\rm PL}}{m}. \tag{3.2}$$

This can be compared to the result from freeze-out,

$$Y_{FO} \sim \frac{1}{\sigma v M_{\rm PL} m'} \sim \frac{1}{\lambda'^2} \frac{m'}{M_{\rm PL}}. \tag{3.3}$$

For a DM particle of mass m' and coupling λ', where we have used $\sigma v \sim \lambda'^2/m'^2$. This illustrates the opposite nature of the freeze-in and freeze-out processes in their dependence on the mass and coupling of the particle. Despite this both processes are independent of unknown high temperature physics and can be completely described by the IR physics and initial state of the bath particles in thermal equilibrium.

The DM is the lightest particle transforming under some unbroken symmetry such as R-parity in super symmetry. In a normal freeze-out scenario the DM is a WIMP that undergoes freeze-out. In freeze-in the FIMP need not be lightest particle that carries charge under the symmetry. In freeze-in there are two particles which are important when considering the phenomenology. The FIMP and the lightest ordinary particle in the thermal bath carrying the DM stabilising symmetry called the LOSP. If the LOSP is lighter than the FIMP then the FIMP will be unstable and decay after freeze-in leading to LOSP DM. If the FIMP is lighter than the LOSP then the FIMP will be stable and is the DM candidate. In both cases the small coupling associated with the FIMP will automatically lead to some long lived particle. In the first case when the FIMP is heavier than the LOSP the FIMP can only decay via the small coupling to the LOSP which is thermal bath particle. Due to the small size of the coupling the life time of the FIMP will be long. In the second scenario the LOSP will be long lived since the symmetry that sta-

bilises the FIMP will require that the only allowed decays of the LOSP will have a FIMP in the final state. This can again only occur via the small coupling giving the LOSP a long life time. In the next section the consequences of these long decay lifetimes of either the FIMP or LOSP will be discussed.

Finally we can infer the size of the coupling λ which is required for freeeze-in to produce the correct relic abundance of DM compatible with observation. The relic abundance of FIMPs is dominated in some scenarios by the decays of the heavier LOSP to the FIMP particle (see Section. 3.2). In this case the relic abundance of FIMPs will be given by [4],

$$\Omega_X h^2 = \frac{1.09 \times 10^{27}}{g_*^S \sqrt{g_*^\rho}} \frac{m_X \Gamma_{B1}}{m_{B1}^2}, \tag{3.4}$$

where $B1$ is the LOSP. For a LOSP decay rate given by $\Gamma_{B1} = \lambda^2 m_{B1}/(8\pi)$ and using $g_*^S \approx g_*^\rho$ the correct abundance of DM $\Omega h^2 \simeq 0.11$ occurs for a coupling of,

$$\lambda \simeq 1 \times 10^{-12} \sqrt{\frac{m_{B1}}{m_X}} \left(\frac{g_*(m_{B1})}{100} \right)^{3/4}. \tag{3.5}$$

The effect of multiple particles of similar masses decaying to the FIMP will reduce the coupling required and the yield from scattering processes and inverse decays will give different required couplings. This gives an approximate figure however for the size of the coupling required for freeze-in to be successful in producing the required amount of DM.

3.2 Experimental signatures

Since the FIMP couples only very weakly to the other particles directly detecting a FIMP through present day cosmological annihilations or DM direct detection experiments is not possible. There are however other experimental signatures that could allow the freeze-in mechanism to be tested. The main feature of freeze-in that can be probed is the existence of a particle either then FIMP or LOSP that has a long decay lifetime. This generally leads to either long lived particles decaying in the early universe or particles produced in particle colliders such as the LHC with long lifetimes.

Which experimental signatures are relevant for freeze-in depends on the hierarchy of the LOSP and FIMP masses and which process either freeze-in or freeze-out contributes to the DM

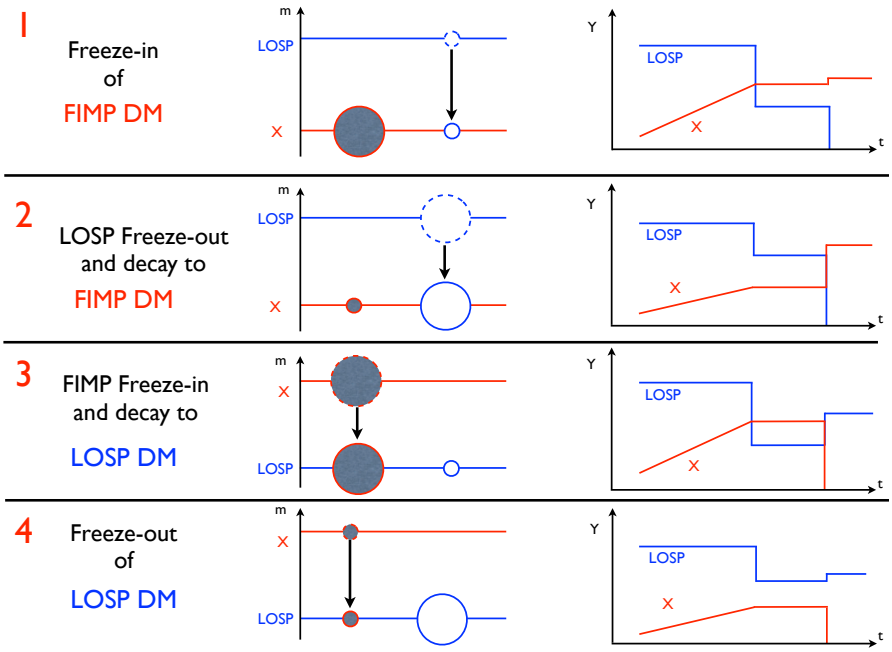

Figure 3.1: Figure from [4]. Schematic representation of the four possible scenarios involving the freeze-in mechanism. The left-hand figures show the LOSP/FIMP spectrum with circles representing cosmologically produced abundances. The large (small) circles represent the dominant (sub-dominant) mechanism for producing the DM relic abundance, a dotted (solid) circle signifies that the particle is unstable (stable), and a filled (open) circle corresponds to production by freeze-in (freeze-out). The right-hand figures show the LOSP and FIMP abundances as a function of time. The initial era has a thermal abundance of LOSPs and a growing FIMP abundance from freeze-in. The LOSP and FIMP are taken to have masses of the same order, so that FIMP freeze-in ends around the same time as LOSP freeze-out. Considerably later, the heavier of the LOSP and FIMP decays to the lighter.

relic. For a general model there will be both freeze-in of the FIMP and freeze-out of the LOSP. This gives four scenarios shown in Figure. 3.1. This shows the time evolution of the FIMP and LOSP as they undergo freeze-in and freeze-out respectively and their subsequent decays if they are unstable. The scenarios are differentiated by either having LOSP DM as in scenarios 3 and 4 or FIMP DM as in 1 and 2. They are also split according to whether freeze-in dominates the production of the DM as in scenarios 1 and 3 or the cases where freeze-out dominates the production in scenarios 2 and 4. The evolution for each case is described as follows.

1. Freeze-in dominated production of FIMP DM. In this case $m_X < m_{B1}$ such that the FIMP is stable and is the DM. The FIMP abundance is produced by freeze-in. The LOSP undergoes freeze-out and subsequently decays to FIMP but the relic abundance of FIMPs from these decays is small.

2. Freeze-out dominated production of FIMP DM. The FIMP is again stable but freeze-in

production is too weak to produce the correct relic abundance. The LOSP is produced by freeze-out and then decays to the FIMP. The LOSP decays dominate the FIMP relic abundance.

3. Freeze-in dominated production of LOSP DM. In this case $m_X > m_{B1}$ and the LOSP is stable. The FIMP is produced via freeze-in and subsequently decays at a time after the LOSP has frozen-out. The relic abundance of the LOSP from freeze-out is small.

4. Freeze-out dominated production of LOSP DM. The LOSP again makes up the DM but is produced in this case by freeze-out. The freeze-in of the FIMP and subsequent decay contributes only a small amount. This is scenario represents the standard freeze-out production of DM as the freeze-in component goes to zero.

From this we see that in the case of scenarios 2 and 3 the dominant contribution to the DM comes from late decays in the early universe while scenario 1 has an unstable LOSP that could be produced at the LHC. Scenario 4 reproduces the standard freeze-out result and does not present freeze-in experimental signatures. We now describe the five main ways in which freeze-in can be tested experimentally and classify them according to which scenario the signal may correspond to.

3.2.1 Long lived decays at colliders

The cross section to directly produce FIMPs at a particle collider will be very small so in scenarios 3 and 4 there will be no FIMP related collider signatures. In scenarios 1 and 2 however the FIMP may be produced as the end point of a decay chain. The LOSP can be produced at the LHC if its mass is within the reach and its production cross section is large enough. If the LOSP is unstable then it will decay to the FIMP which can only occur via the small coupling responsible for freeze-in. This will give the LOSP a long lifetime with the possibility of decaying within the detector. In an ideal scenario the life time of the LOSP could be measured at the LHC by measuring the distance from the interaction point to the decay, however this only occurs over a narrow range of lifetimes. Life times that are too small will decay at the interaction point while longer lifetimes will leave the detector entirely before decaying.

If the life time of the LOSP, τ can be measured then it may be possible to connect the life time to the freeze-in mechanism. In general if there are multiple small couplings that connect

the FIMP to different bath particles then only one of the couplings can be found via the life time of the LOSP and the connection to the freeze-in abundance is lost. If the model is particularly simple then it is possible to predict the life time from the required relic abundance in scenario 1 [4]. Consider the case when the FIMP is coupled to 2 bath particles via a small yukawa interaction $\lambda X B_1 B_2$. Where B_1 is the LOSP and $m_{B2} + m_X < m_{B1}$ so that freeze-in is dominated by the process $B_1 \to X B_2$. Applying the condition that the DM abundance is produced entirely be freeze-in yields a prediction of the life time of [4],

$$\tau_{B_1} = 7.7 \times 10^{-3} \text{sec}\, g_{B_1} \left(\frac{m_X}{100\,\text{GeV}}\right) \left(\frac{300\,\text{GeV}}{m_{B_1}}\right)^2 \left(\frac{10^2}{g_*(m_{B_1})}\right)^{3/2}. \tag{3.6}$$

In scenario 2 the life time will be increased due to the component of DM abundance coming from freeze-out which reduced the required coupling λ for the freeze-in component.

This scenario has been investigated in the context of freeze-in in the MSSM [111] and this is examined in Chapter. 5. Freeze-in signatures at the LHC is also considered in terms of general hidden sectors in [112].

3.2.2 Measurement of LOSP parameters at the LHC

Accurate measurement of LOSP parameters at the LHC may allow its annihilation cross section in the early universe to be reconstructed. This essentially allows a measurement of the freeze-out abundance of the LOSP. If the dominant contribution to the DM relic comes from freeze-in as in scenarios 1 and 3 then the annihilation cross section of the LOSP can deviate from the value predicted by freeze-out. This implies that another mechanism must be responsible for the production of DM such as freeze-in.

It is particularly clear in the case where the LOSP is charged or coloured which is possible in scenarios 1 and 2. In this case the detection of a charged or coloured LOSP rules out scenarios 3 and 4 since the LOSP can not be the DM. It then becomes important to measure the lifetime of the LOSP as in the previous section.

3.2.3 Enhanced detection of LOSP DM

FIMP DM is essentially undetectable in direct or indirect DM detection experiments due to its very small annihilation cross section and small scattering cross section with nucleons. Scenarios

3 and 4 however predicts a LOSP DM that would be detectable by DM experiments. In scenario 3 the DM relic is produced mainly by freeze-in this requires that the freeze-out relic of the LOSP be smaller than the measure DM density. This implies an annihilation cross section for the LOSP at freeze-out with $\sigma v > 3 \times 10^{-26} cm^3 s^{-1}$.

This can lead to an enhanced signal from present day LOSP annihilations and also from direct detection experiments depending on LOSP properties and how suppressed the freeze-out relic is. We present this scenario in the context of the MSSM in Chapter. 6 [113].

3.2.4 Cosmological decays and BBN

It is a general feature of all the freeze-in in scenarios that there is a meta-stable particle produced in the early universe that then decays. The long lived particle can be either the FIMP or the LOSP produced by freeze-in or freeze-out respectively and the decay life time will be controlled by the small coupling between the FIMP and bath particles. Meta-stable particles that decay producing hadrons in the early universe may perturb big bang nucleosynthesis by injecting non-thermal hadronically or electromagnetically interacting particles into the plasma [114].

For freeze-in the typical decay time of the FIMP or LOSP in the early universe is $\sim 10^{-2} s$ [4] while significant deviations to BBN occur for lifetimes $\gtrsim 0.3 s$. However the small coupling λ can be reduced thus increasing the lifetime in the case where the FIMP couples to multiple bath particles and many process contribute to the freeze-in relic. Even greater lifetimes become possible when the 2-body decays of the FIMP or LOSP are forbidden kinematically, this allows lifetimes or the order of up to $1000 s$ which can correspond to dramatic changes in BBN.

3.2.5 Warm dark matter component

DM produced in decays can be warm or hot since the particles produced in the decay carry the kinetic energy released. This leads to the DM produced in the decays having a free streaming velocity that can erase small density perturbations and so effect structure formation. In the case of freeze-in at least some of the DM component will come from decays. How warm the produced DM is depends on the life time and mass difference between the DM and decaying particle. Varying the LOSP and FIMP parameters in the above scenarios allows different combinations of warm and cold DM to be generated.

3.3 Calculation of Freeze-in abundance

In this section we present the calculation of the DM relic density from freeze-in governed by the Boltzmann equations for the FIMP number density. The results presented here are as obtained in [4] which concludes that the freeze-in yield is dominated by decays or inverse decays to the FIMP particle (depending on the relative mass of the FIMP to the bath particles) with $2 \to 2$ scattering process being sub dominant. The thermal corrections to the decay processes have also been considered [115, 116]. It should be noted that although the $2 \to 2$ processes from 4-point interactions are indeed sub-dominant to decays in models with a large number of possible $2 \to 2$ processes the sum of all the scatterings can be dominant and resonance effects in scattering diagrams can boost the freeze-in yield [117].

3.3.1 Freeze-in from direct decays

We consider that case where the FIMP particle X is coupled to two bath particles B_1 and B_2 via the term $\lambda X B_1 B_2$ with masses such that $m_{B_1} > m_{B_2} + m_X$. The dominant freeze-in process is then decays of $B_1 \to X B_2$. The Boltzmann equation for the number density of X is then given by.

$$\dot{n}_X + 3Hn_X = \int d\Pi_X d\Pi_{B_1} d\Pi_{B_2} (2\pi)^4 \delta^4(p_X + p_{B_2} - p_{B_1}) \times \left[|M|^2_{B_1 \to B_2 + X} f_{B_1}(1 \pm f_{B_2})(1 \pm f_X) - |M|^2_{B_2 + X \to B_1} f_{B_2} f_X (1 \pm f_{B_1}) \right], \quad (3.7)$$

where $d\Pi_i = d^3 p_i / (2\pi)^3 2E_i$ is the usual integral over the phase space and f_i is the Boltzmann phase space factor. $|M|^2$ is the matrix element squared where the outgoing spins are summed over but with no averaging over the initial spin states. The delta function ensures that this process is kinematically allowed. We then make the important assumption that the initial density of X is negligible and set $f_X \approx 0$ which allows the inverse decay term in eq. 3.5 to be dropped.

We write the partial decay width of $B_1 \to X B_2$ as Γ_{B_1} then neglecting Pauli-blocking/stimulated emission we set $(1 \pm f_{B_2}) \approx 1$ this allows eq. 3.5 to be written as,

$$\dot{n}_X + 3Hn_X \approx 2 g_{B_1} \int d\Pi_{B_1} \Gamma_{B_1} m_{B_1} f_{B_1} = g_{B_1} \int \frac{d^3 p_{B_1}}{(2\pi)^3} \frac{f_{B_1} m_{B_1} \Gamma_{B_1}}{E_{B_1}}. \quad (3.8)$$

The bath particle B_1 is assume to be in thermal equilibrium and we can approximate its phase space density $f_{B_1} = (e^{E_{B_1}/T} \pm 1)^{-1}$ by $e^{-E_{B_1}/T}$. The Boltzmann equation can be rewritten as a

one dimensional integral over the energy giving,

$$\begin{aligned} \dot{n}_X + 3n_X H &\approx g_{B_1} \int \frac{d^3 p_{B_1}}{(2\pi)^3} \frac{f_{B_1}\Gamma_{B_1}}{\gamma_{B_1}} \\ &= g_{B_1} \int_{m_{B_1}}^{\infty} \frac{m_{B_1}\Gamma_{B_1}}{2\pi^2} (E_{B_1}^2 - m_{B_1}^2)^{1/2} e^{-E_{B_1}/T} dE_{B_1} \\ &= \frac{g_{B_1} m_{B_1}^2 \Gamma_{B_1}}{2\pi^2} T K_1(m_{B_1}/T), \end{aligned} \tag{3.9}$$

where K_1 is the first modified Bessel Function of the 2nd kind. It is useful to rewrite this in terms of the number density per comoving volume, the yield $Y_X \equiv n_X/S$. We convert from an integral over time to temperature using $\dot{T} \approx -HT$, which is valid when the variation of total plasma statistical degrees of freedom with temperature $\mathrm{d}g/\mathrm{d}T \approx 0$.

$$Y_X \approx \int_{T_{min}}^{T_{max}} \frac{g_{B_1} m_{B_1}^2 \Gamma_{B_1}}{2\pi^2} \frac{K_1(m_{B_1}/T)}{SH} dT, \tag{3.10}$$

where we can write $S = 2\pi^2 g_*^S T^3/45$ and $H = 1.66\sqrt{g_*^\rho} T^2/M_{Pl}$ with M_{Pl} the Planck mass and g_*^S and g_*^ρ the effective number of degrees of freedom in the thermal bath for entropy S and density ρ. The usual replacement of $x \equiv m/T$ gives the integral,

$$Y_X \approx \frac{45}{(1.66)4\pi^4} \frac{g_{B_1} M_{Pl} \Gamma_{B_1}}{m_{B_1}^2 g_*^s \sqrt{g_*^\rho}} \int_{x_{min}}^{x_{max}} K_1(x) x^3 dx, \tag{3.11}$$

where we have evaluated g_*^s and $\sqrt{g_*^\rho}$ at the freeze-in temperature $T \sim m_{B_1}$ and made the approximation that m_{B_1} and Γ_{B_1} are independent of temperature which may not be the case once thermal corrections are taken into account. The x integral can be evaluated for $x_{min} = 0$ and $x_{max} = \infty$ to give.

$$Y_{1\to 2} \approx \frac{135\, g_{B_1}}{8\pi^3 (1.66) g_*^S \sqrt{g_*^\rho}} \left(\frac{M_{\mathrm{Pl}} \Gamma_{B_1}}{m_{B_1}^2} \right), \tag{3.12}$$

The yield can be converted to the relic abundance of FIMP DM giving.

$$\Omega_X h^2 \approx \frac{1.09 \times 10^{27} g_{B_1}}{g_*^S \sqrt{g_*^\rho}} \frac{m_X \Gamma_{B_1}}{m_{B_1}^2}. \tag{3.13}$$

This form holds for a single freeze-in process but a realistic model may have the FIMP coupling to multiple heavy bath particles and the yield will gain contributions from the decays of all the particles. Each bath particle that can decay will contribute with the same dependence on its mass

and partial width as in eq.**??**. The partial contributions to freeze-in can be approximated by an effective mass m_B and effective number of degrees of freedom g_{bath}. Making the substitution $\Gamma_B = \lambda^2 m_B/(8\pi)$ for the effective partial width allows the coupling required to produce the correct relic abundance to be calculated [4]

$$\lambda \simeq 1.5 \times 10^{-13} \left(\frac{m_B}{m_X}\right)^{1/2} \left(\frac{g_*(m_B)}{10^2}\right)^{3/4} \left(\frac{g_{bath}}{10^2}\right)^{-1/2}. \tag{3.14}$$

So allowing the FIMP to couple to many bath particles increases the yield and decreases the coupling required below the value that is expected for freeze-in from a single decaying particle.

3.3.2 Freeze-in from inverse decays

We now consider freeze-in production of DM when the FIMP is unstable. This corresponds to the scenario 3 of the previous section where an abundance of FIMPs is produced by freeze-in which then decay at a later time to produce the LOSP DM. The simplest case is where there is a single interaction responsible for both freeze-in and the subsequent decay process. The Lagrangian term is the same as in the previous case $\lambda X B_1 B_2$ but the masses now satisfy $m_X > m_{B_1} + m_{B_2}$. In the thermal bath X particles are produced by the process $B_1 B_2 \to X$ and the decay of FIMPs is the reverse process.

The Boltzmann equation for X under the assumption that $f_X = 0$ can be written as,

$$\dot{n}_X + 3Hn_X \approx \int d\Pi_X d\Pi_{B_1} d\Pi_{B_2} (2\pi)^4 \delta^4(p_X - p_{B_1} - p_{B_2}) \, |M|^2_{B_1+B_2\to X} \, f_{B_1} f_{B_2}. \tag{3.15}$$

We can rearrange this by making the substitution $|M|^2_{B_1+B_2\to X} = |M|^2_{X\to B_1+B_2}$ which is valid assuming CP-invariance and applying the condition of detailed balance for the equilibrium distributions of the particles we have.

$$\dot{n}_X + 3n_X H \approx \int d\Pi_X d\Pi_{B_1} d\Pi_{B_2} (2\pi)^4 \delta^4(p_X - p_{B_1} - p_{B_2}) \, |M|^2_{X\to B_1+B_2} \, f_X^{eq}, \tag{3.16}$$

where f_X^{eq} is the equilibrium density of X which we can approximate by $f_X^{eq} \approx e^{-E_X/T}$. Eq. 3.8 is then of the same form as eq. 3.5 and applying the same steps allows the yield to be calculated as,

$$Y_{2\to 1} \approx \frac{135}{8\pi^3 (1.66) g_*^S \sqrt{g_*^\rho}} \left(\frac{M_{\rm Pl}\Gamma_X}{m_X^2}\right), \tag{3.17}$$

where the dependence is now on Γ_X the partial width of $X \to B_1 B_2$. Now in contrast to the previous calculation the X particle is not the DM so we are interested in the relic abundance of B_1 which is the DM particle in this example. B_1 will undergo freeze-out and if X decays before B_1 freezes-out then the effect of freeze-in will be annihilated away by the B_1 annihilations. Instead we assume now that X has a long enough life time that the decays occur after the freeze-out of B_1 and that the freeze-out abundance of B_1 is negligible. The relic abundance of B_1 from freeze-in can then be written as.

$$\Omega_{B_1} h^2 \approx \frac{1.09 \times 10^{27}}{g_*^S \sqrt{g_*^\rho}} \frac{m_{B_1} \Gamma_X}{m_X^2}. \tag{3.18}$$

Again assuming the standard form for the decay width $\Gamma_X = \lambda^2 m_X / 8\pi$ the coupling required to fix the relic abundance to the correct value can be determined to be [4].

$$\lambda \simeq 1.5 \times 10^{-12} \left(\frac{m_X}{m_{B_1}} \right)^{1/2} \left(\frac{g_*(m_X)}{10^2} \right)^{3/4}. \tag{3.19}$$

3.3.3 Freeze-in from scattering processes

We now consider the case where the FIMP is produced by a $2 \to 2$ scattering via a 4-point interaction with 3 bath particles. The interaction term is $\lambda X B_1 B_2 B_3$ where all the particles are scalars. The corresponding Boltzmann equation is

$$\dot{n}_X + 3 n_X H \approx 3 \int d\Pi_{B_1} d\Pi_{B_2} d\Pi_{B_3} d\Pi_X (2\pi)^4 \delta^4 (p_{B_1} + p_{B_2} - p_{B_3} - p_X) \, |M|^2_{B_1 B_2 \to B_3 X} \, f_{B_1} f_{B_2}, \tag{3.20}$$

where we have set $f_X = 0$ again and the factor 3 appears since we have the processes $B_1 B_2 \to B_3 X$, $B_1 B_3 \to B_2 X$ and $B_2 B_3 \to B_1 X$ occurring at the same rate. We rewrite the Boltzmann equation as a one dimensional integral following [94].

$$\dot{n}_X + 3 n_X H \approx \frac{3T}{512\pi^6} \int_{m_X^2}^{\infty} ds \, d\Omega P_{B_1 B_2} P_{B_3 X} \, |M|^2_{B_1 B_2 \to B_3 X} \, K_1(\sqrt{s}/T) / \sqrt{s}, \tag{3.21}$$

where s is the center of mass energy of the collision and $P_{B_1 B_2}$ is the momentum of the incoming particles B_1 and B_2. $P_{B_3 X}$ is the outgoing momentum of B_3 and X. The momenta of the particles

in the center of mass frame can be written in terms of their masses and s as.

$$P_{ij} \equiv \frac{[s-(m_i+m_j)^2]^{1/2}[s-(m_i-m_j)^2]^{1/2}}{2\sqrt{s}}. \tag{3.22}$$

We make the simplifying assumption that the masses of the bath particles are negligible compared to the mass of the FIMP so that $P_{B_1B_2} \approx \frac{\sqrt{s}}{2}$ and $P_{B_3X} \approx \frac{(s-m_X^2)}{2\sqrt{s}}$. The matrix element is simply $|M|^2_{B_1B_2\to B_3X} = \lambda^2$. The integral is then

$$\dot{n}_X + 3n_X H \approx \frac{3T\lambda^2}{512\pi^5}\int_{m_X^2}^{\infty} ds\,(s-m_X^2)K_1(\sqrt{s}/T)/\sqrt{s}. \tag{3.23}$$

The s integration can be completed and converting from the number density to the yield gives

$$\frac{dY_X}{dT} \approx \frac{3\lambda^2 K_1(m_X/T)}{1.66\,T^3 g_*^S\sqrt{g_*^\rho}}\frac{45M_{\rm Pl}m_X}{256\pi^7}. \tag{3.24}$$

Applying the same steps as before we change variables from T to $x \equiv m_X/T$ and note that the x integral can be completed for $x_{min} = 0$ and $x_{max} = \infty$ giving.

$$Y_X \approx \frac{135\lambda^2 M_{\rm Pl}}{256\pi^7 g_*^S\sqrt{g_*^\rho}(1.66)m_X}\int_0^{\infty} xK_1(x)dx = \frac{135M_{\rm Pl}\lambda^2}{512\pi^6 g_*^S\sqrt{g_*^\rho}(1.66)m_X}. \tag{3.25}$$

Which is equivalent to a relic density of FIMPs of,

$$\Omega h_X^2 \approx \frac{2m_X Y_X}{3.6\times10^{-9}\,\text{GeV}} = \frac{1.01\times10^{24}}{g_*^S\sqrt{g_*^\rho}}\lambda^2. \tag{3.26}$$

Finally the coupling required to produce an abundance of FIMPs compatible with the DM relic abundance is [4]

$$\lambda \simeq 1\times10^{-11}\left(\frac{g_*(m_X)}{10^2}\right)^{3/4}. \tag{3.27}$$

Thus the required coupling for freeze-in through a 4-point interaction is larger than the coupling required for decays or inverse decays. It should be noted that yield from scattering processes can be enhanced when there are many scattering processes that contribute and when the scatting process arises from 3-point interactions with a particle exchanged in either the t or s channels. In this case individual scattering diagrams can become large due to resonance effects.

Chapter 4

The MSSM

In the previous chapter the freeze-in mechanism of dark matter production was introduced. In the following chapters 5 and 6 some aspects of the phenomenology of freeze-in are investigated. While freeze-in itself is quite general and can apply to a wide range of models providing that they contain a feebly coupled sector we will look at the phenomenology in terms of a few concrete models. In particular we will look at possible freeze-in extensions of the minimal supersymmetric standard model (MSSM). In section **??** we will briefly introduce the topic of supersymmetry (SUSY) and section **??** will define the MSSM and describe some of its properties.

4.1 Supersymmetry

4.1.1 Motivation

The standard model consists of both fermions and bosons, while fermions make up the matter bosons are responsible for transmitting forces between particles. There is therefore a distinction between the particles that mediate interactions and the matter particles. This raises the question of whether there can be any symmetry that relates the boson and fermion components of the standard model. A symmetry that relates bosons to fermions called a supersymmetry.

One main motivation for such a symmetry is the hierarchy problem. The hierarchy problem emerges in the standard model due to the large difference between the electroweak and the Planck energy scales. This leads to difficulties when considering the radiative corrections to the Higgs boson mass. Scalar particles receive radiative corrections that increase quadratically with

energy, the one-loop correction to the Higgs boson mass from a fermion has the form,

$$\Delta m_h^2 \sim -\frac{\left|\lambda_f^2\right|}{8\pi^2}\Lambda_{UV}^2, \tag{4.1}$$

where λ_f is the coupling between the Higgs and the fermion and Λ_{UV} is the energy cut-off introduced to regulate the loop integral. Λ_{UV} can be interpreted as the energy scale at which new physics alters the high-energy behaviour of the theory. In the standard model the largest contribution of this form comes from the top quark which has $\lambda_f \approx 1$. The hierarchy problem occurs when we take Λ_{UV} to be of the order of the Planck mass (M_P) this implies very large corrections to the Higgs mass many orders of magnitude larger than the required mass of the Higgs boson. One solution to the hierarchy problem is to introduce new particles to the loops with the same couplings but with spin differing by a half. So for all the fermions in the standard model introduce a corresponding boson and for each boson a corresponding fermion. The contributions to Δm_h^2 from fermion loops differ by a sign to those from boson loops so for each fermion boson pair we get a correction to the Higgs mass of,

$$\Delta m_h^2 \sim \frac{\left|\lambda^2\right|}{8\pi^2}(\Lambda_{UV}^2 + m_B^2) - \frac{\left|\lambda^2\right|}{8\pi^2}(\Lambda_{UV}^2 + m_F^2) = \frac{\left|\lambda^2\right|}{8\pi^2}(m_B^2 - m_F^2), \tag{4.2}$$

where λ is the coupling shared by the fermion and boson, m_B and m_F are the boson and fermion mass respectively. Supersymmetry guaranties the existence of new particles with the same coupling and differing spin and the structure of supersymmetry ensures that the quadratic divergences cancel at all orders of perturbation theory.

Another feature that has motivated the study of supersymmetry is the unification of the gauge couplings. Extrapolation of the energy dependence of the gauge couplings in the standard model fails to reach a point at which all 3 couplings are unified. If supersymmetric state appear at the TeV order then the change to running of couplings causes them to unify a scale $M_U \sim 2 \times 10^{16}$GeV [118]. This effect is shown in figure 4.1.

4.1.2 Supersymmetry basics

Supersymmtry is an extension of the symmetries of the Lagrangian that relates boson and fermions. SUSY introduces a generators that change fermion states into bosons and bosons into

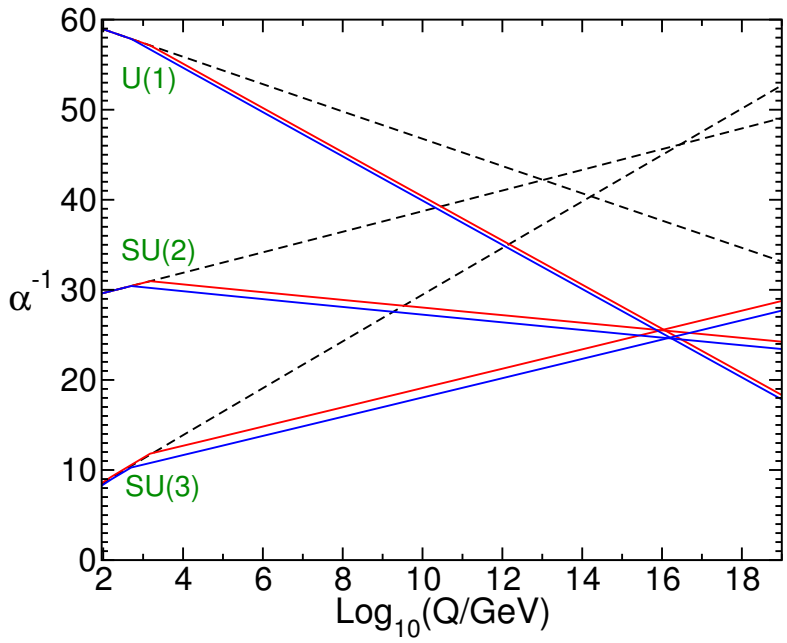

Figure 4.1: Two-loop renormalization group evolution of the inverse gauge couplings $\alpha_a^{-1}(Q)$ in the Standard Model (dashed lines) and the MSSM (solid lines). In the MSSM case, the sparticle masses are treated as a common threshold varied between 500 GeV and 1.5 TeV, and $\alpha_3(m_Z)$ is varied between 0.117 and 0.121. [5]

fermions. The operator Q that generates the transformation must itself be an anti-commuting spinor with,

$$Q|Boson\rangle = |Fermion\rangle, \qquad Q|Fermion\rangle = |Boson\rangle. \tag{4.3}$$

Since Q carries spin 1/2 the symmetry must be a spacetime symmetry. The structure of a symmetry that extends the Poincaré group for an interacting quantum field theory is highly restricted by highly restricted by the Haag-Lopuszanski-Sohnius extension [119] of the Coleman-Mandula theorem [120]. For theories with chiral fermions this implies that the supersymmetry has the structure,

$$\left\{Q, Q^\dagger\right\} = P^\mu, \tag{4.4}$$

$$\left\{Q, Q\right\} = \left\{Q^\dagger, Q^\dagger\right\} = 0, \tag{4.5}$$

$$\left[P^\mu, Q\right] = \left[P^\mu, Q^\dagger\right] = 0, \tag{4.6}$$

where P^μ is the 4-momentum generator of spacetime translations. The particles in the theory come in supermultiplets which are representations of the supersymmetry. Each supermultiplet

contains fermion and boson states which are called superpartners. The components of the supermultiplet transform between each other under supersymmetric transformations so that for a supermultiplet containing states Ω and Ω', Ω' is proportional to some combination of Q and $Q^\dagger$ acting on Ω. In addition since the squared-mass operator $-P^2$ commutes with Q and $Q^\dagger$ particles in the same supermultiplet must have equal masses [5]. Q and $Q^\dagger$ also commute with the generators of gauge transformations and thus superpartners must also be in the same gauge representations and carry the same electric charge, weak isospin and colour quantum numbers. In the MSSM we have two types of supermultiplets, Chiral or matter multiplets which consist of a Weyl fermion and a complex scalar and Vector multiplets consisting of a vector boson and a Weyl fermion.

Supersymmetry can be made manifest by writing the theory in the superspace formalism. Superfields are defined on the set of coordinates that is the superspace $x^\mu, \theta, \overline{\theta}$ where x^μ is the usual coordinate in Minkowski-space and θ, $\overline{\theta}$ are anti-commuting Weyl-spinors. The components of the supermultiplets are then represented by a single superfield that is function in superspace.

For a renormalizable supersymmetric theory the interactions and masses of all the particles are determined by their gauge transformation properties and the superpotential [5]. The superpotential W is a holomorphic function of the complex scalar fields of the theory. Equivalently in the superspace formalism the superpotential is written as a holomorphic function of the chiral superfields. The general form of the superpotential is

$$W = L^i\Phi_i + \frac{1}{2}M^{ij}\Phi_i\Phi_j + \frac{1}{6}y^{ijk}\Phi_i\Phi_j\Phi_k, \tag{4.7}$$

for chiral superfields Φ_i. The superpotential leads to a supersymmetric Lagrangian in terms of the component fields given by

$$\mathcal{L}_{SUSY} = -\frac{1}{2}\left(W^{ij}\psi_i\psi_j + W^*_{ij}\right) - W^iW^*_i, \tag{4.8}$$

where $W^i \equiv \partial W/\partial\phi_i$, $W^*_i \equiv \partial W/\partial\phi^{i*}$ and $W^{ij} \equiv \partial\partial W/\partial\phi_j\partial\phi_i$. ϕ and ψ are the scalar and fermion components of the chiral superfields.

4.1.3 Supersymmetry breaking

If supersymmetry is unbroken then there would be for every particle in the standard model a superpartner with the same quantum numbers and mass. For example there would be a scalar copy of the electron with mass 0.511MeV. These superpartners would have been easily detected in past experiments and so it is clear that supersymmetry must be be broken. We would like supersymmetry to be an exact symmetry of the Lagrangian but be broken spontaneously by the vacuum state of the theory in analogy with electroweak symmetry breaking the standard model. Supersymmetry breaking in the MSSM requires extending the theory to include new particles and interactions at a high energy scale and there have been many proposals for the mechanism by which supersymmetry is broken and the interaction between the SUSY breaking sector and MSSM which transmits the SUSY breaking.

For our purposes we can parametrize our lack of knowledge of the exact mechanism for SUSY breaking and instead introduce a set of terms in the Lagrangian that explicitly break SUSY to form an effective MSSM Lagrangian where SUSY is broken. The form of these SUSY breaking terms is constrained by the requirement that the hierarchy problem does not reappear after SUSY breaking. That is we want to maintain the cancellation of the quadratic divergences in the Higgs mass even in the theory where SUSY is broken. To this end we note that the cancellation that occurs in eq.4.2 requires that the superpartners have dimensionless couplings that are related eg. $|\lambda_F| = \lambda_S$. If SUSY breaking came in a form that disrupted this relation then we would reintroduce divergent terms of the form.

$$\Delta m_h^2 \sim \frac{1}{8\pi^2}\left(\lambda_S^2 - |\lambda_F|^2\right)\Lambda_{UV}^2. \tag{4.9}$$

We therefore only include SUSY breaking terms that have positive mass dimension which is referred to as soft supersymmetry breaking. The full Lagrangian can the be written as,

$$\mathcal{L} = \mathcal{L}_{SUSY} + \mathcal{L}_{soft}, \tag{4.10}$$

where $\mathcal{L}_{SUSY}$ is the part of the Lagrangian that respects SUSY while $\mathcal{L}_{soft}$ contains the additional soft SUSY breaking terms. The possible terms for $\mathcal{L}_{soft}$ are

$$\mathcal{L}_{soft} = -\left(\frac{1}{2}M_a\lambda^a\lambda^a + \frac{1}{6}a^{ijk}\phi_i\phi_j\phi_k + \frac{1}{2}b^{ij}\phi_i\phi_j + t^i\phi^i\right) + \text{c.c.} - \left(m^2\right)^i_{\ j}\phi^{j*}\phi_i. \tag{4.11}$$

These terms are, masses M_a for the fermion components of vector supermultiplets, these fermions are referred to as gauginos as they are the superpartners of gauge bosons and these are then gaugino mass terms. The next term is trilinear couplings a^{ijk} for the scalar fields, scalar mass squared terms b^{ij} and $\left(m^2\right)^i_j$ for the scalars and tadpole couplings t^i. The tadpole terms can only occur for scalars which gauge singlets and so do not appear in the MSSM. Mass terms for the fermion components of the chiral supermultiplets do not appear as these can be absorbed by redefinitions $\mathcal{L}_{SUSY}$. The allowed terms in $\mathcal{L}_{soft}$ will always allow masses to be given to all the gauginos and scalars of the theory, the remaining terms may or may not be allowed due to other symmetries of the theory.

4.2 Defining the MSSM

4.2.1 The field content of the MSSM

The Minimal Supersymmetric Standard Model (MSSM) is the supersymmetric extension of the standard model that contains the only the superfields necessary to reproduce the fields of the standard model. This means associating every field in the standard model with a superfield, i.e every particle in the standard model acquires a superpartner with spin differing by 1/2. The question that arises is for each particle in the standard model does it belong to a chiral or vector multiplet. For the Higgs and gauge bosons the answer is clear and they must belong to chiral and vector multiplets respectively. For the standard model fermions we note that in supersymmetry only chiral multiplets can contain fermions that have left handed components that transform differently from their right handed components under gauge transformations. Since this is true for the standard model fermions they must all belong to chiral multiplets.

So for each fermion in the standard model we have an associated scalar superpartner which are collectively refered to as sfermions. The left and right handed components of the standard model fermions are separate Weyl fermions and so there is a a corresponding left and right handed sfermion. For example the electron is composed of a left and a right handed Weyl fermion leading to two complex scalar superpartners, $\tilde{e}_R$ and $\tilde{e}_L$ referred to as selectrons (scalar-electron). The sfermions are generally denoted by the same symbol as their stanadrd model superpartner but with tilde (̃). The naming convention for the sfermions continues in a similar fashion by prepending an “s” to the corresponding standard model names. The standard model

Superfield	Standard model particles	Spin	Superpartner	Spin	$SU(3)_C$, $SU(2)_L$, $U(1)_Y$
Q	$\begin{pmatrix} u_L \\ d_L \end{pmatrix}$	1/2	$\begin{pmatrix} \tilde{u}_L \\ \tilde{d}_L \end{pmatrix}$	0	$\left(\mathbf{3},\mathbf{2},\frac{1}{6}\right)$
U	$\overline{u}_R$	1/2	$\tilde{u}_R^*$	0	$\left(\overline{\mathbf{3}},\mathbf{1},-\frac{2}{3}\right)$
D	$\overline{d}_R$	1/2	$\tilde{d}_R^*$	0	$\left(\overline{\mathbf{3}},\mathbf{1},-\frac{1}{3}\right)$
L	$\begin{pmatrix} \nu_L \\ e_L \end{pmatrix}$	1/2	$\begin{pmatrix} \tilde{\nu}_L \\ \tilde{e}_L \end{pmatrix}$	0	$\left(\mathbf{1},\mathbf{2},-\frac{1}{2}\right)$
E	$\overline{e}_R$	1/2	$\tilde{e}_R^*$	0	$(\mathbf{1},\mathbf{1},1)$
H_u	$\begin{pmatrix} H_u^+ \\ H_u^0 \end{pmatrix}$	0	$\begin{pmatrix} \tilde{H}_u^+ \\ \tilde{H}_u^0 \end{pmatrix}$	1/2	$\left(\mathbf{1},\mathbf{2},\frac{1}{2}\right)$
H_d	$\begin{pmatrix} H_d^0 \\ H_d^- \end{pmatrix}$	0	$\begin{pmatrix} \tilde{H}_d^0 \\ \tilde{H}_d^- \end{pmatrix}$	1/2	$\left(\mathbf{1},\mathbf{2},-\frac{1}{2}\right)$
G	g	1	$\tilde{g}$	1/2	$(\mathbf{8},\mathbf{1},0)$
W	$W^\pm, W^0$	1	$\tilde{W}^\pm, \tilde{W}^0$	1/2	$(\mathbf{1},\mathbf{3},0)$
B	B^0	1	$\tilde{B}^0$	1/2	$(\mathbf{1},\mathbf{1},0)$

Table 4.1: Field content of the MSSM.

leptons have superpartner sleptons called the selectron, smuon, stau and sneutrino. The standard model quarks have corresponding squarks with the superpartner of the top quark referred to as a stop. The gauge interactions of the sfermions are the same as their standard model partners i.e $\tilde{e}_L$ and $\tilde{\nu}$ couple to the W bosons while $\tilde{e}_R$ does not.

As mention earlier the Higgs boson must reside in a chiral multiplet however due to the structure of supersymmetry there must be two Higgs chiral superfields in order to avoid a guage anomaly. A second Higgs multiplet is also required due to the structure of the superpotential, since the conjugate Higgs field can not be included in the superpotential (it is a holomorphic function of the superfields) different Higgs fields are required to give masses to the up and down type quarks. As such we two Higgs doublets H_u with components (H_u^+, H_u^0) and H_d with components (H_d^0, H_d^-). The standard model Higgs boson is then a linear combination of H_u^0 and H_d^0 and there will be additional scalar states including an electrically charged Higgs boson. The spin 1/2 superpartners are named by appending "-ino" to the standard model names, so the spin 1/2 superpartners of the Higgs particles are called higgsinos and there will be in total four higgsinos, two charged and two neutral.

Finally each of the standard model gauge bosons will get a corresponding superpartner, the gluon gets a gluino, the W-bosons have superpartners called winos and the B boson gets a superpartner called the bino.

The complete field content of the MSSM is shown in table **??**, where the family and colour

indices of the particles have been suppressed. This is the field content in terms of the guage eigenstates and the mass eigenstates will differ as in the standard model where the B and W^0 bosons mix to form the Z and photon. If supersymmetry was unbroken then a similar mixing would occur for the neutral wino and bino states however since supersymmetry is broken the superpartner mass eigenstates will not coincide with the standard model mass states.

The only remaining specification to make for the supersymmetric part of the theory is the superpotential. The terms allowed in the MSSM superpotential are dictated by the gauge symmetries of the standard model and renormalizability and is given by

$$W_{MSSM} = \mathbf{y_u} UQH_u - \mathbf{y_d} DQH_d - \mathbf{y_e} ELH_d + \mu H_u H_d, \tag{4.12}$$

where the first 3 terms correspond to the standard model yukawa terms with $\mathbf{y}$ the yukawa couplings. This also makes clear why two Higgs fields are required since we can not include a term like $\mathbf{y_u} UQH_d^*$ to account for the masses up the up type quarks since the superpotential is holomorphic.

There are other possible terms for the superpotential allowed by the symmetries of the standard model these are

$$W_{\Delta L=1} = \frac{1}{2}\lambda^{ijk} L_i L_j E_k + \lambda'^{ijk} L_i Q_j D_k + \mu'^i L_i H_u, \tag{4.13}$$

$$W_{\Delta B=1} = \frac{1}{2}\lambda''^{ijk} U_i D_j D_k, \tag{4.14}$$

where i, j, k run over the family indices. These terms violate lepton number and baryon number and can lead to proton decay. To avoid this a new symmetry is introduced in the MSSM that forbids these terms from the superpotential known as R-parity. R-parity is a multiplicative quantum number defined by

$$R \equiv (-1)^{(3B-L+2s)}. \tag{4.15}$$

The result being that standard model particles all have R-parity $R = 1$ while the superpartners have $R = -1$. As a consequence of this the lightest supersymmetric particles (LSP) is automatically stable and can only be destroyed via pair annihilation with itself or another SUSY particle.

4.2.2 Soft SUSY breaking in the MSSM

As previously argued SUSY must be broken in the MSSM so that the superpartners are not degenerate in mass with the standard model particles. The SUSY breaking in the MSSM is parametrised by the set of soft SUSY breaking terms allowed by the gauge symmetries and R-parity of the MSSM. These are

$$\begin{aligned}
\mathcal{L}_{soft}^{MSSM} &= -\frac{1}{2}\left(M_3\tilde{g}\tilde{g} + M_2\tilde{W}\tilde{W} + M_1\tilde{B}\tilde{B} + c.c.\right) \\
&\quad -\frac{1}{2}\left(\mathbf{a_u}\tilde{u}_R^*\tilde{Q}H_u - \mathbf{a_d}\tilde{d}_R^*\tilde{Q}H_d - \mathbf{a_e}\tilde{e}_R^*\tilde{L}H_d + c.c.\right) \\
&\quad -\mathbf{m_Q^2}\tilde{Q}^\dagger\tilde{Q} - \mathbf{m_L^2}\tilde{L}^\dagger\tilde{L} - \mathbf{m_u^2}\tilde{u}_R\tilde{u}_R^\dagger - \mathbf{m_d^2}\tilde{d}_R\tilde{d}_R^\dagger - \mathbf{m_e^2}\tilde{e}_R\tilde{e}_R^\dagger \\
&\quad -m_{H_u}^2 H_u^* H_u - m_{H_d}^2 H_d^* H_d - (bH_uH_d + c.c.). \qquad (4.16)
\end{aligned}$$

Here we have M_3, M_2, M_1 the gaugino masses. $\mathbf{a_e}$, $\mathbf{a_u}$ and $\mathbf{a_d}$ are the trilinear scalar couplings and correspond with the allowed yukawa couplings in the superpotential. $\mathbf{m_Q^2}$, $\mathbf{m_L^2}$, $\mathbf{m_u^2}$, $\mathbf{m_d^2}$ and $\mathbf{m_e^2}$ are squared mass terms for all of the sfermions and in general these are 3x3 matrices with family indices which could in principle include off diagonal and complex terms. The final line of eq. 4.13 are the SUSY breaking contributions to the higgs potential. Note that it is these soft terms that introduces all the new parameters into the MSSM and for the most general case there are 105 masses, mixing angles and phases that have no corresponding parameter in the standard model [121].

Despite this large number of free parameters there is already strong experimental evidence of structure in the soft SUSY breaking Lagrangian. Namely that most of the new parameters imply CP violation or flavour mixing that is heavily constrained by existing experiments. These effects are effectively removed by taking the squared mass terms to be proportional to the identity matrix multiplied by some flavour blind mass squared and similarly for trilinear couplings but proportional to the associated yukawa couplings rather than the identity matrix. The problem of CP violations is avoided by having all the soft breaking parameters be real. The flavour mixing and CP violating effects are generally suppressed as the masses of the superpartners increase, this leads to the possibility of non-flavour blind soft terms. Depending on the assumptions made about the soft terms we arrive at different MSSM models. For our purposes we mention two important models the constrained MSSM (CMSSM) [122] and the phenomenological MSSM (pMSSM).

The CMSSM imposes the following boundary conditions at the grand unification scale (GUT scale) M_U. Gauge coupling unification

$$\alpha_1(M_U) = \alpha_2(M_U) = \alpha_3(M_U), \tag{4.17}$$

common gaugino masses

$$M_1(U) = M_2(U) = M_3(U) \equiv m_{1/2}, \tag{4.18}$$

universal scalar masses

$$M_Q(M_U) = M_u(M_U) = M_d(M_U) = M_L(M_U) = M_e(M_U) = M_{H_d}(M_U) = M_{H_u}(M_U) \equiv m_0, \tag{4.19}$$

universal trilinear couplings

$$A_u(M_U) = A_d(M_U) = A_e(M_U) \equiv A_0. \tag{4.20}$$

By requiring Electroweak symmetry breaking to occur the number of parameters is reduced to 4 continuous parameters and one discrete. These are the universal gaugino masses, sfermion masses and trilinear couplings $m_{1/2}, m_0, A_0$, the ratio of the vacuum expectation values of the two Higgs vevs $\tan\beta$ and the sign of μ parameters appearing in the superpotential.

The pMSSM is not a single model and is not necessarily theoretically motivated but rather is a useful way of reducing the number of free parameters and parametrising the theory in a way that is relevant for phenomenology. In the pMSSM the soft breaking terms are specified at the EWSB scale. Typically the soft terms are then taken to be flavour diagonal and real. The number of parameters can be reduced further by assuming universality between the first 2 generations or that only the 3rd generation trilinear terms are non-zero. Different scenarios can be constructed in this way with varying motivation. Some examples of pMSSM models can be found in [123, 124, 125, 126, 127, 128]

4.2.3 The particle content of the MSSM

After specifying the field content of the MSSM, specifying the superpotential and introducing the soft SUSY breaking terms of the MSSM the remaining question is what are the mass eigen-

states of the MSSM following SUSY breaking and how are they constructed from the gauge eigenstates. A summary of the new particles in the MSSM is shown in table 4.1.

The Higgs sector of the MSSM differs from the standard model as there are now two Higgs doublets H_u and H_d leading to a total of 8 real scalar degrees of freedom. After electroweak symmetry breaking the Naumbu-Goldstone modes become the longitudinal degrees of freedom of the Z and $W^{\pm}$ bosons leaving 5 scalar mass eigenstates these consist of two CP-even neutral scalars h^0 and H^0, a CP-odd pseudo scalar A^0 and a positively charged Higgs boson H^+ and its conjugate H^-. Note that H^0, A^0 and $H^{\pm}$ depend on the soft SUSY breaking parameters m_{H_d}, m_{H_u}, b and so can become arbitrarily large while the lightest Higgs is bounded from above at tree level by $m_Z |\cos 2\beta|$ but receives relatively large loop corrections with the largest contributions typically coming from top quark and stop loops.

The spin 1/2 superpartners of the higgs and gauge bosons mix due to the effects of EWSB. In particular the neutral higgsino states $\tilde{H}_u^0$ and $\tilde{H}_d^0$ mix with the gauginos $\tilde{W}^0$ and $\tilde{B}$ to form four mass eigenstates called neutralinos $\tilde{\chi}^0$. While the charged higgsinos $\tilde{H}^{\pm}$ and charged winos $\tilde{W}^{\pm}$ form two mass eigenstates called charginos $\tilde{\chi}^{\pm}$. The lightest of the neutralinos is particularly important as it provides a good DM candidate since it is weakly interacting and will be stable if it is the LSP. The remaining guagino is the gluino which can not mix with any of the other fermions and so the mass eigenstate is the same as a gauge eigenstate.

There can be mixing between any sfermions with same electric charge and colour quantum numbers this means that for the squarks there can in principle be mixing between all 6 of the up-type squarks and amongst all 6 of the down-type squarks and also for the 6 charged sleptons. The 3 sneutrinos can also mix giving a total of 3 6x6 mixing matrices and one 3x3 mixing matrix. However as we previously argued completely generic soft masses are not allowed and so mixing between families is very small. Mixing between the left and right handed squarks and sleptons is generally only large in the 3rd generation due to the negligible yukawa couplings of the first two generations. For this reason the first two generations of squarks and sleptons have mass eigenstates that correspond closely with the gauge eigenstates with the same being true for all of the sneutrinos. The sbottoms, staus and stops have larger mixing between the left and right guage states and the mass eigenstates are labeled $\tilde{b}_1, \tilde{b}_2$ for the bottom squarks, $\tilde{\tau}_1, \tilde{\tau}_2$ for the staus and $\tilde{t}_1, \tilde{t}_2$ for the stops.

Names	Spin	R-parity	Gauge eigenstates	Mass eigenstates
Higgs bosons	0	+1	$H_u^0\ H_d^0\ H_u^+\ H_d^-$	$h^0\ H^0\ A^0\ H^\pm$
Squarks	0	-1	$\tilde{u}_L\ \tilde{u}_R\ \tilde{d}_L\ \tilde{d}_R$ $\tilde{s}_L\ \tilde{s}_R\ \tilde{c}_L\ \tilde{c}_R$ $\tilde{t}_L\ \tilde{t}_R\ \tilde{b}_L\ \tilde{b}_R$	(same) (same) $\tilde{t}_1\ \tilde{t}_2\ \tilde{b}_1\ \tilde{b}_2$
Sleptons	0	-1	$\tilde{e}_L\ \tilde{e}_R\ \tilde{\nu}_e$ $\tilde{\mu}_L\ \tilde{\mu}_R\ \tilde{\nu}_\mu$ $\tilde{\tau}_L\ \tilde{\tau}_R\ \tilde{\nu}_\tau$	(same) (same) $\tilde{\tau}_1\ \tilde{\tau}_2\ \tilde{\nu}_\tau$
Neutralinos	1/2	-1	$\tilde{B}^0\ \tilde{W}^0\ \tilde{H}_u^0\ \tilde{H}_d^0$	$\tilde{\chi}_1^0\ \tilde{\chi}_2^0\ \tilde{\chi}_3^0\ \tilde{\chi}_4^0$
Charginos	1/2	-1	$\tilde{W}^\pm\ \tilde{H}_u^+\ \tilde{H}_d^-$	$\tilde{\chi}_1^\pm\ \tilde{\chi}_2^\pm$
Gluino	1/2	-1	$\tilde{g}$	(same)

Table 4.2: New particle content of the MSSM [5].

Chapter 5

Long Lived particles at the LHC

In this chapter the consequences of the freeze-in mechanism on collider signals is investigated. We consider the case where the FIMP particle is the dark matter leading to a long lived LOSP which can be produced at the LHC. Since the decay lifetime of the LOSP is tied to the freeze-in mechanism via the feeble coupling the lifetime is large and can possibly lead to displaced vertex signatures at the LHC. Parts of this work were originally published as part of [111].

We consider a model created by extending the MSSM by the addition of a singlet superfield, which is feebly coupled to the usual MSSM states. This extra superfield is assumed to contain the Lightest Supersymmetric Particle (LSP), and consequently the Next to Lightest Supersymmetric Particle (NLSP) will only be able to decay to the LSP via the feeble coupling leading to long-lived NLSPs. We investigate one example of this type of model with a number of benchmark parameter choices. In section **??** the model and benchmark points are described. The method of implementing the model and generating the Monte Carlo events is described in section 5.1. In section 5.2 the phenomenology of the model is discussed and the benchmarks are compared to experimental constraints in section **??**.

5.1 Model and benchmarks

Consider a connection between hidden sector FIMP states and the MSSM in the form of a SUSY particle, Y, decaying to the hidden sector state, X via $Y \to X + \ldots$, where the ellipses represent some SM sector states. Here we assume that both Y and X are odd under R-parity. The relic abundance of X states generated by the freeze-in mechanism reads $\Omega h^2 \sim 10^{24} \Gamma_Y m_X / m_Y^2$ [4],

where Γ_Y is the decay rate of Y with X final state. For all particle masses of interest, in order to get $\Omega h^2 \sim 0.1109 \pm 0.0056$ [129], Γ_Y is required to be very small. A consequence of which is that if we produce the particle Y in a detector it will travel a significant distance (greater than a few mm) before decaying. Moreover, the decay width of this state, which could be reconstructed from measurements of a number of such decays, could have a direct link to the relic abundance of DM as frozen-in via the decays of Y in the early Universe. Finally, it may also be possible to determine the masses of Y and X using kinematical techniques and therefore test the freeze-in expression for the relic abundance.

Beyond this simple picture, more complicated scenarios are possible and the exact predictions for the decay length and the mass of the X DM state can vary [112]. Therefore, in this analysis we take a range of decay lengths for the lightest visible sector particle Y (in this analysis, Y is either the MSSM neutralino or chargino) and a range of masses for X that do not necessarily reconstruct the correct relic abundance. As a result we consider a range of parameters and masses to remain as general as possible with this study being easily applied to a specific picture of a visible and hidden sector feebly coupled with the the DM living in the hidden sector. Going beyond the freeze-in mechanism such a scenario can occur in a number of different theories, for example in the context of asymmetric DM (see e.g. [130, 131]).

Given this motivation, we consider a supersymmetric model with a LOSP that has a small decay width to some hidden sector state. This means that in every event where a pair of supersymmetric particles are produced, there will be two long-lived LOSPs that will decay into the hidden sector state. In this analysis, we take a phenomenological approach and optimise the signal by choosing by hand the decay length such that the majority of the decays occur in the tracker thereby allowing for better reconstruction and maximise the sensitivity of the search. In this way we are looking for the best possible scenario from a detector point of view, which will allow for a better idea of what could be achieved in less ideal scenarios.

We follow the basic set up outlined in both [132] and [112] where a singlet superfield is added to the MSSM and a survey of the potential operators that can be written down is made. We take our lead from this analysis and look in more detail at one of the operators.

We assume that this extra singlet superfield is even under R-parity and consider only renormalisable operators. Under these assumptions we choose to analyse the superpotential Higgs portal operator $\Delta\mathcal{W} = \lambda X H_u H_d$. This choice has been made in order to initiate the study rather

than fully cover all possibilities. An immediate extension of this work is to consider all other operators, including non-renormalisable operators and where the extra singlet superfield is also allowed to be odd under R-parity. The consequences of this operator has also been previously studied in [133], where an additional singlet superfield was added to the MSSM in order to solve the "μ-problem". The low energy theory studied in [133] has many features in common with the set-up we consider here.

In order for this operator to give rise to a long lived LOSP, the coupling λ has to be small. At order λ this term induces the interactions $\widetilde{\chi}_i^- X_f W^+$ and $\widetilde{\chi}_i^0 X_f Z$ (and the Hermitian conjugates), where $\widetilde{\chi}_i^-$ and $\widetilde{\chi}_i^0$ are the MSSM charginos and neutralinos, respectively and X_f is the fermionic component of the X superfield. These interaction terms are induced by the mixing between the neutralinos $\tilde{\chi}^0$ and the FIMP field X_f. The mixing comes from the yukawa terms between the higgsinos, X_f and scalar higgs field. This leads to off diagonal mass terms due the higgs vacumm expectation value. The new mass terms in the Lagrangian are,

$$-\mathcal{L}_m \supset \lambda v s_\beta \widetilde{H}_{d_L}^{0^T} X_f + \lambda v c_\beta \widetilde{H}_{u_L}^{0^T} X_f + \lambda^* v s_\beta^* \overline{X_f}\, \overline{\widetilde{H}_{d_L}^0}^T + \lambda^* v c_\beta^* \overline{X_f}\, \overline{\widetilde{H}_{u_L}^0}^T + m_X X_f X_f + m_X^* \overline{X_f X_f}, \tag{5.1}$$

where λ is the small coupling, v is the SM vev, s_β is $\sin\beta$, c_β is $\cos\beta$ for β the ratio of the two vevs. $\widetilde{H}_{d_L}^0$ and $\widetilde{H}_{u_L}^0$ are the two higgsinos. We can write the full mass matrix in the gauge eigenstate basis in terms of a vector of the gauge states $\Psi_0^T = (\widetilde{B}_0, \widetilde{W}_L^{0^T}, \widetilde{H}_{d_L}^0 \widetilde{H}_{u_L}^0, X_f)$. The mass terms of the Lagrangian can then be written as $-\mathcal{L}_m = \frac{1}{2}\Psi_0^T M_N \Psi_0 + \text{h.c.}$ with

$$M_N = \begin{bmatrix} m_1 & 0 & -c_\beta s_w m_Z & s_\beta s_w m_Z & 0 \\ 0 & m_2 & c_\beta c_w m_Z & -s_\beta c_w m_Z & 0 \\ -c_\beta s_w m_Z & c_\beta c_w m_Z & 0 & -\mu & -\lambda v c_\beta \\ s_\beta s_w m_Z & -s_\beta c_w m_Z & -\mu & 0 & -\lambda v s_\beta \\ 0 & 0 & -\lambda v c_\beta & -\lambda v s_\beta & m_X \end{bmatrix},$$

where the upper left 4x4 matrix is just the usual neutralino mass mixing matrix of the MSSM. Since the coupling λ is small we can apply perturbation theory and split the mixing matrix into a

part that is zero order in λ the unperturbed matrix and a part that is order 1 in λ the perturbation.

$$M_N = \begin{bmatrix} M_N(4) & 0 \\ 0 & m_X \end{bmatrix} + \begin{bmatrix} 0 & 0 & 0 & 0 & 0 \\ 0 & 0 & 0 & 0 & 0 \\ 0 & 0 & 0 & 0 & -\lambda v c_\beta \\ 0 & 0 & 0 & 0 & -\lambda v s_\beta \\ 0 & 0 & -\lambda v c_\beta & -\lambda v s_\beta & 0 \end{bmatrix} = M_N^0 + \lambda v M_N^1,$$

where M_N^0 is 0th order in λ and $\lambda v M_N^1$ is 1st oder in λ and M_N^1 is just a function of c_β and s_β. The matrix $M_N(4)$ is the usual 4×4 neutralino mass mixing matrix which can be diagonalised by

$$U_N^* M_N(4) U_N^\dagger = \text{ diagonal},$$

With U_N the normal neutralino mixing matrix which can be calculated using standard SUSY spectrum calculators. The full zeroth order matrix can then be diagonalised by,

$$\begin{bmatrix} U_N^* & 0 \\ 0 & 1 \end{bmatrix} M_N^0 \begin{bmatrix} U_N^\dagger & 0 \\ 0 & 1 \end{bmatrix} = X^T M_N^0 X = \text{ diagonal},$$

where X is the 5x5 matrix that diagonalizes the unperturbed mass matrix. We can write X in terms of 5 5-d vectors which express the mass eigenstates in terms of the gauge states. Where each vector is an eigenvector of the mass matrix.

$$X = (\underline{X}_1, \underline{X}_2, \underline{X}_3, \underline{X}_4, \underline{X}_5),$$

the first four vectors $i = 1,2,3,4$ will read,

$$\underline{X}_i^T = (U_{i1}^*, U_{i2}^*, U_{i3}^*, U_{i4}^*, 0). \tag{5.2}$$

The last vector is given by will read

$$\underline{X}_5^T = (0,0,0,0,1). \tag{5.3}$$

We now apply perturbation theory to find the first order corrections to these vectors, the perturbed components of the eigenvectors are given by

$$\underline{X}_i' = \underline{X}_i + \lambda v \sum_j \left(\frac{\underline{X}_j^T . M_N^1 . \underline{X}_i}{M_i - M_j} \right) \ \underline{X}_j,$$

where M_i, M_j are the unperturbed mass eigenvalues where we have assumed that $M_i \neq M_j$ for $i \neq j$. Applying this gives

$$\underline{X}_i = \begin{bmatrix} \\ U_{i1}^* \\ U_{i2}^* \\ U_{i3}^* \\ U_{i4}^* \\ -\frac{\lambda v}{M_i - M_X} \left(c_\beta U_{i3}^* + s_\beta U_{i4}^* \right) \end{bmatrix} \quad \text{and} \quad \underline{X}_5 = \begin{bmatrix} \sum_k A_k U_{k1}^* \\ \sum_k A_k U_{k2}^* \\ \sum_k A_k U_{k3}^* \\ \sum_k A_k U_{k4}^* \\ 1 \end{bmatrix},$$

where $A_k = \frac{\lambda v}{M_k - M_X} \left(c_\beta U_{k3}^* + s_\beta U_{k4}^* \right)$. These vectors then specify the full mixing matrix in terms of the standard unperturbed MSSM neutralino mixing matrix and the FIMP parameters.

The parameter space of the model can be split into two parts. Firstly there is the parameter space of the MSSM which defines the mass spectrum of all the usual SUSY particles. Specifying a point in the parameter space of the MSSM will set the dominant production mechanisms for the SUSY particles and the properties of the prompt decay chain at the primary vertex. The second part of the parameter space is the FIMP sector the two parameters of interest are the mass of the fermionic R-partiy odd FIMP field X_f and the small coupling λ. λ along with the masses of the NLSP and X_f will define the lifetime of the NLSP and thus the decay length that characterises the displacement of the secondary vertex.

The coupling λ is chosen to produce decay lengths that are relevant for the LHC rather than a coupling that would correctly produce the relic abundance of DM from freeze-in. The size of the coupling can still be consistent with the DM density if X_f is itself unstable and decays down to a lighter state outside of the detector. The ATLAS and CMS detectors are most sensitive to displaced vertices in the range of around 1cm to 50cm [134, 135]. To produce a proper decay length of $c\tau \approx 25cm$ we require a coupling of $\lambda \approx 1 \times 10^{-10}$ depending on the MSSM parameter point chosen and the FIMP mass. Conversely $\lambda \lesssim 1 \times 10^{-11}$ would lead to a proper decay length larger than the inner detector sizes of ATLAS and CMS. A larger decay length would lead to

Sample	Hard process	Prompt objects	Proper decay length /cm	M_{FIMP} /GeV	σ/pb
FIMP Benchmark 1		2 hard Ws	25	1	0.103
Neutralino LOSP	$M_{\tilde{\chi}_1^+} = 235$ GeV		50	1	
	$M_{\tilde{\chi}_1^0} = 123$ GeV		100	1	
			50	0.1	
			50	25	
FIMP Benchmark 2	Chargino	2 soft Ws	25	1	1.21
Neutralino LOSP	pair production		50	1	
	$M_{\tilde{\chi}_1^+} = 133$ GeV		100	1	
	$M_{\tilde{\chi}_1^0} = 123$ GeV				
FIMP Benchmark 3	Chargino	None	25	1	0.677
Chargino LOSP	pair production		50	1	
	$M_{\tilde{\chi}_1^+} = 193$ GeV		100	1	
SM sample 1	$W\mu\nu$	$W\mu\nu$	0		10.46
SM sample 1	$Z\mu\mu$	$Z\mu\mu$	0		1.07
SM sample 2	QCD multijet	QCD multijet	0		1×10^7

Table 5.1: Description of Monte Carlo samples used in the analysis. The cross sections quoted for the FIMP benchmarks are for the chargino pair production only, see text for more details.

most of the displaced vertices occurring outside of the sensitive region of the detector reducing the strength of the signal.

We choose to look for final state muons coming from a displaced vertex as this is a particularly powerful way to search for displaced vertices due to low backgrounds. In each event, we require only one cascade, resulting from the production and decay of a SUSY particle, to yield a displaced muon(s).

The benchmark points are fixed points in the parameter space of the MSSM, the three benchmarks are chosen to give different prompt objects at the primary vertex. For each benchmark λ is varied to give a selection of decay lengths for the NLSP. We have chosen to look at events where the dominant SUSY production channel is the production of chargino pairs. In order for this to be the dominant production channel, we have chosen a spectrum where the squarks and gluinos are heavy. This choice has been made in order to remove the complication of applying existing limits on squarks and gluinos and also to leave the events as clean as possible.

Some details of the benchmarks we choose are listed in table 5.1. Benchmark 1 (BM1) looks at a possible point in the MSSM parameter space with a neutralino LOSP. The production cross section for the chargino pairs for this parameter point is calculated using both `MadGraph5` [136] and `CalcHep` [137] to be ~ 0.1 pb. The diagrams for the production of a pair of charginos are

depicted in figure 5.1. Due to the large masses of the squarks, the t-channel process is sub-dominant compared with the s-channel diagrams. The chargino will decay to a neutralino via a W, and with the large mass difference between the chargino and neutralino in BM1, this W can be produced on shell leading to hard jets or a hard single charged lepton. In the sample we allow the W to decay to all possible final states. The neutralino, as the LOSP, has two possible decay modes, both yielding an X_f in the final state. In the sample we only include events where the neutralino decays to an X_f and an on-shell Z, with the Z decaying to muons as shown in figure 5.1. The other decay mode is to the light Higgs plus X_f and has a small branching ratio for the chosen benchmark points.

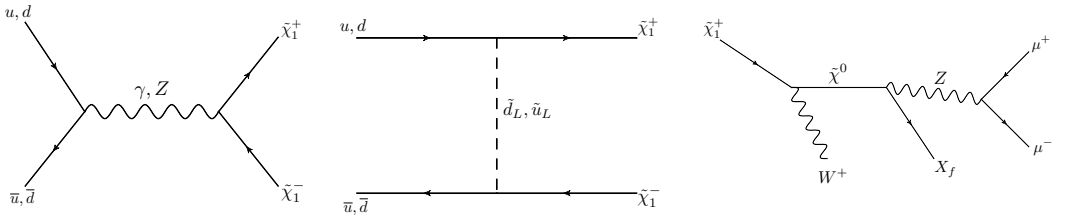

Figure 5.1: Production for all benchmarks with the cascade decays for BM1 and BM2.

The mass for the X_f state has been chosen to be 1 GeV for the majority of the benchmark scenarios. The reason for this is twofold but ultimately arbitrary. One motivation comes from the fact that we want to produce an on-shell Z in the decay of the neutralino so that we can reconstruct its mass. The other is that in the majority of asymmetric DM models the mass needed for the DM state is around a 1 GeV. In BM1 we also vary the mass of the X_f state to cover more scenarios and to investigate what effect this has on the kinematics and whether we can use this variation to determine the mass of the hidden sector state and of the LOSP.

As stated above, we only generate Monte Carlo events where both SUSY cascades end with a pair of oppositely charged muons produced in a displaced vertex. We determine what fraction of these will pass cuts imposed on the displaced vertex (and other aspects of the event) in section **??**. Ultimately in an analysis of real data, it may be the case that we only require events with one displaced pair of oppositely charged muons passing these cuts rather than two and therefore a further analysis is required to accurately estimate the efficiency (in terms of passing cuts) of identifying events with one pair of muons coming from a displaced vertex. In this analysis, we have simply asked for how many of the total number of displaced muon pairs pass the cuts. As there are two of these displaced muon pairs per event there will be a correlation between the

displaced muons produced in the same event but as a first pass this estimate gives us a good ball park figure with which to work.

Given $BR(Z \to \mu\mu) \sim 0.034$, an estimate, with the chargino pair production cross section of 0.1 pb, of the number of events with at least one displaced pair of oppositely charged muons is $N \sim 8\,(\sigma/0.1\text{pb})\left(L/1\text{fb}^{-1}\right)$, where L is the integrated Luminosity, which we have set at a value of 1 fb^{-1}.

Benchmark 2 (BM2) contains a lighter chargino and the resulting production cross section is larger, 1.21 pb. Due to the lower chargino mass, the W produced in the decay from the chargino to the neutralino will be soft. Otherwise, BM2 is the same as BM1 and with the increased cross section we expect over 80 events with at least one pair of oppositely charged muons from a displaced vertex.

It is possible to have the lightest chargino lighter than the lightest neutralino if for low $\tan\beta$; $\text{sign}(M_1) \neq \text{sign}(M_2) = \text{sign}(\mu)$, see e.g. [138]. In Benchmark 3 (BM3) the chargino still delivers the dominant SUSY production cross section (as our squarks are still heavy), but now is the LOSP and is long-lived and will decay directly to X_f plus a W. We then decay the W to a muon plus muon neutrino thereby producing a displaced muon. The obvious difference in this case is that the LOSP will have a charged track, which will produce a kink when it decays to the muon. The number of events expected in this case is much higher due to the $W \to \mu\nu_\mu$ branching ratio being larger than the $Z \to \mu^+\mu^-$ branching ratio ($BR(W \to \mu\nu_\mu) \sim 0.11$). An estimate for the number of events with at least one displaced muon is close to 150 for 1 fb^{-1}.

5.2 Tools

A `MadGraph5` [136] model file was produced using `FeynRules` [139] based on the existing MSSM model file [140]. The widths and branching ratios of the SUSY particles were calculated using `BRIDGE` [141] and passed to `Pythia8` [142, 143] via the SLHA [144] decay tables. Although `BRIDGE` is capable of decaying the events in full, it forces all particles in a decay chain to be exactly on-shell (i.e. `BRIDGE` does not sample widths from the full Breit-Wigner distribution) so we decayed the events using `Pythia8` instead. For benchmark 3 the initial scattering is performed in `Pythia8` using the `MadGraph5` matrix element as a semi-internal process. This was done to counteract a problem with passing events between `MadGraph5` and `Pythia8` where

long-lived states are produced in the initial scattering, see section 5.1.2 for more details. The subsequent decay chain and showering was performed in `Pythia8` using the decay tables obtained from `BRIDGE` for the chargino and neutralino decays. For comparison, Standard Model samples were also produced and these were generated using only `Pythia8`.

5.2.1 Model implementation in `FeynRules`

The model file was developed by extending the existing MSSM implementation in `FeynRules`, since the extension of the MSSM is in the form of a new superpotential term the superspace module of `FeynRules` was used [140]. This module allows the Lagrangian to be written in terms of superfields, a superpotential and the soft SUSY breaking terms. This makes the implementation of the extension of the MSSM very easy as only one new superfield and superpotential term need to be added and all the relevant vertices will be calculated automatically.

The only remaining work is to specify the mixing of the gauge states to form the mass states of the model. Since the Lagrangian is written in terms of the gauge superfields the model file must also specify the transformation between the component particles of the superfields and the mass states. For the MSSM particles this has already been included in the model file via the definitions of the mixing matrices that are read from an SLHA file. When putting new particles into the model any mixing between the existing MSSM particles and the new states must be included in the model file. This can involve extending the mixing matrices so care must be taken concerning the dimensions of the matrices and vectors of particles. For the model in question the case is simplified since the mixing between states occurs due to terms in the Lagrangian that come with a power of the small freeze-in coupling. This is generic to freeze-in models since any large mixing terms would bring the FIMP into thermal equilibrium quickly and ruin freeze-in. This means that any mixing between the new FIMP states and existing MSSM states can be treated as a perturbation to the MSSM mixing and mass matrices. This gives a simple formula for the new mixing terms, in contrast to the normal MSSM mixing matrices which can be complicated. The mixing between the MSSM states does not need to be recalculated then and the existing implementation of the mixing and results from the spectrum calculators can be used. The relevant mixing for the model occurs between the fermion FIMP field X_f and the neutralinos $\tilde{\chi}^0$ was implemented as discussed in section **??**.

5.2.2 Displaced vertices in `pythia`

The following steps were used to generate the signal events.

1. The `FeynRules` model file was exported to both the `MadGraph4` and `MadGraph5` formats.
2. Using `MadGraph5` a set of events for the production process was produced for a set of benchmark points as an LHE file.
3. The decay rates and branching ratios for $\tilde{\chi}_1^+$ and $\tilde{\chi}_1^0$ were produced for the benchmark points using `BRIDGE` via the `MadGraph4` model files.
4. The full parton showered events are generated by `pythia` using the decay table from `BRIDGE` and events from `MadGraph5`.

For this study version 8.153 of `pythia` was used which did not handle displaced vertices correctly in this context. A number of problems had to be overcome to generate displaced vertices correctly using `Pythia`. For particle widths specified in the SLHA header of the event file the calculation of the decay lifetime τ from the particle width seems not to be performed automatically. As a solution, the lifetime of the long-lived particles can be set by hand during initialisation. After setting the particle lifetime and decaying the event in `Pythia` we found that all particles have their production coordinates set at the interaction point. Outputting events in the Les Houches Event (LHE) format [145] is not affected, as only the particles lifetime and momentum is recorded, but outputting events to `HepMC` [146] format or as root trees will generate events with incorrect production vertices.

This problem can be overcome by producing the hard process in the LHE format and running the event file through `Pythia` a second time, since, with this method, the production vertices are calculated correctly from the information in the LHE file. However, producing fully showered events including final state radiation (FSR) seems to be problematic with this procedure as displaced particles in the final state that emit a photon are moved back to the interaction point. A solution is to calculate the production vertices for each displaced particle and set them after the full event has been generated by `Pythia`.

This was done by writing a recursive function to navigate the event record finding all the daughter particles from each displaced vertex before writing the event to disk. The event record is essentially an array containing all the particles that make up the event. Each particle record

contains (along with other variables) the production coordinates of the particle and the locations in the event record of any daughter particles. Where daughter particles are particles produced from the decay of the first particle or radiation from the particle. Schematically the function works as follows and is initially called with the particle id of the displaced W or Z and the position of the displaced vertex.

1. Set particle production location to displaced vertex location.
2. Check if particle has any daughter particles in the event record.
3. Call function for each daughter particle.

In this way the function is called recursively and sets the correct location for the initial displaced vertex and also all the subsequent particles produced in decays or as final state radiation.

A further complication arises in handling event files where the long-lived particle is produced in the initial scattering process. For example, in benchmark 3 for the FIMP model, the charginos are long lived and are produced directly via $pp \to \widetilde{\chi}_1^+ \widetilde{\chi}_1^-$. If this event is generated by `MadGraph5` and then passed to `Pythia` to decay, it always decays the charginos at the interaction point even if the lifetime has been correctly set. To avoid this for benchmark 3 the scattering process was calculated entirely in `Pythia`.

5.3 Phenomenology

5.3.1 Displaced vertex searches

For this analysis we consider the following searches for displaced vertices at the Tevatron and an early displaced vertex searches from CMS.

CMS displaced vertex study. In Ref. [147], a search in 1.1 fb^{-1} of integrated luminosity collected in 2011 with the CMS detector for displaced vertices is presented. The search is for Higgs bosons decaying to two long-lived, massive, neutral particles. The analysis searches for these long-lived particles via their decay to dileptons (both electron and muon) within the volume of the CMS tracker. No significant excess was observed above the Standard Model background and upper limits were placed typically in the range $0.003 - 0.03$ pb, for X bosons whose lifetime is such their mean transverse decay length is less than 1 m.

CDF displaced vertex study. In Ref. [148], the results of a search for new particles with long lifetime that decay to a Z boson were presented in 163 pb^{-1} of data recorded with the CDF detector. Dimuons with invariant mass near the Z peak are vertexed and the decay length distribution studied. No evidence of a long-lived component was found, and cross section limits were presented on a fourth generation quark model. For a long-lived particle of mass 150 GeV, limits were set at 95% C.L. in the range $3-50$ pb for a decay length between 1 mm and 1 m.

D0 displaced vertex study. In Ref. [149], a search for a neutral particle, pair produced in $p\overline{p}$ collisions at a centre-of-mass energy $\sqrt{s} = 1.96$ TeV, which decays into two muons and lives long enough to travel at least 5 cm before decaying, was presented. The analysis used 380 pb^{-1} of data recorded with the D0 detector. No candidates were observed, and limits were set on the pair-production cross section times branching fraction into dimuons+X for such particles. For a mass of 10 GeV and lifetime of 4×10^{11}s , values greater than 0.14 pb were excluded at 95% C.L.

.

5.3.2 Phenomenology of the model

This section describes the properties of the benchmarks described in section **??**. All benchmarks considered predict a long-lived particle decaying into a fermionic DM particle in addition to a W or Z boson. In this analysis we consider the subsequent decay of the boson in the muon decay channel.

Figure 5.2 shows the transverse momenta and angular separation (if applicable) of the muons originating from the heavy boson decay in all three benchmarks. That from Standard Model Drell-Yan background is also shown by way of comparison. The kinematic constraints imposed by existing detector searches are marked on the plot.

In the interests of maximising acceptance, the optimal lepton P_T requirement should be as low as possible. A single or di-muon trigger is envisaged to record the events studied here and, due to the muon displacement, the trigger is expected not to rely on inner detector tracking information.

Some cut on angular separation between the muons – either transverse or otherwise – would be necessary to avoid background contamination from cosmic rays falling on top of a collision, but the tighter this is the more sensitivity the analysis will have to these models. The D0, and to a lesser extent the CMS, analyses will have reduced sensitivity as their requirements on angular

separation are sufficiently tight that they would remove many candidates.

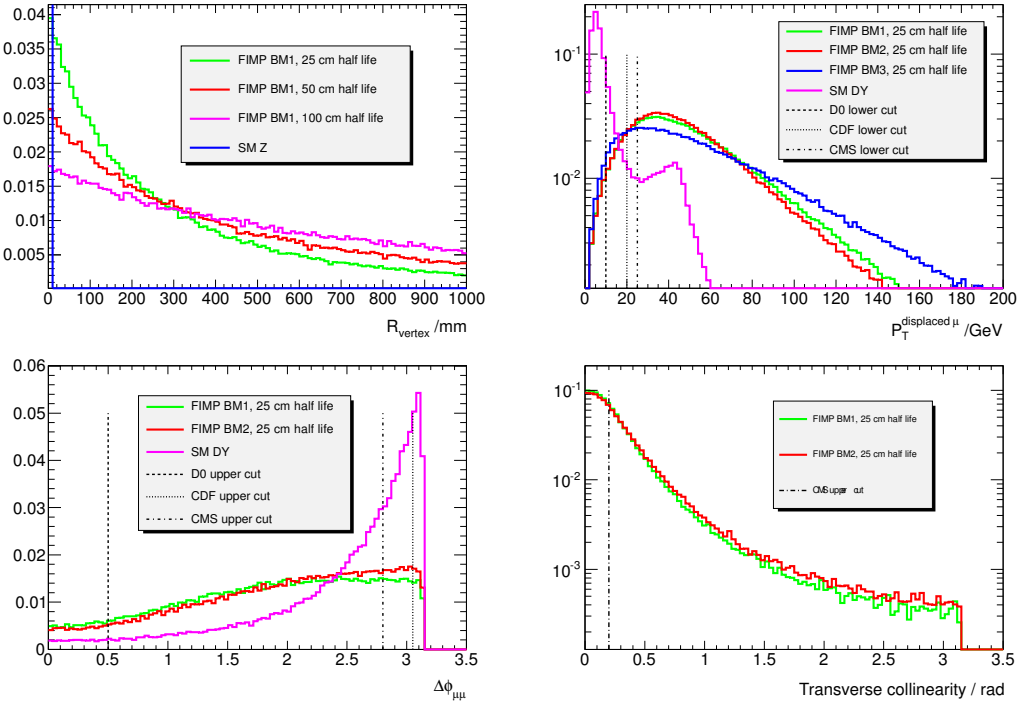

Figure 5.2: Radial displacement (top left), transverse muon momenta (top right), transverse angular muon separation (bottom left) and transverse collinearity (bottom right) of displaced Z decay. Standard Model Drell-Yan kinematics from a prompt Z decay are also shown by way of comparison. Existing cuts on these variables in displaced vertex searches are shown on the plot.

Searching for a muon pair displaced from the interaction point is a powerful way of discriminating these models from Standard Model background signatures. Figure 5.2 shows the typical R displacement predicted by the FIMP models when the mean lifetime is set at 25, 50 and 100 cm in BM1. A measured R displacement represents the lifetime of the chargino lifetime and thus its coupling to the FIMP. For any displaced particle, the most likely point of decay is (0, 0, 0) and then an exponential decay from that point is observed, its mean lifetime governed by the decay length of the particle. It can be seen in the CMS and ATLAS studies that the efficiency for reconstructing these vertices also drops sharply as the displacement is increased.

The displaced vertex represents a decay into a Z boson and a fermionic DM particle which will be observed as missing transverse energy in the detector. The invariant mass of muon pairs, observed at a radial displacement R seen in the distribution in figure 5.2, will follow the same distribution as the invariant mass in Standard Model Z decays. A cut around the Z mass peak

of the vertex could prove powerful in the proposed analysis, as there are no Standard Model physics backgrounds in which a high mass displaced $\mu\mu$ vertex would be seen in the detector.

The transverse collinearity angle between the reconstructed momentum vector of the Z boson and the vector from the primary to the secondary vertex – the neutralino direction of flight – is also shown in figure 5.2. It is seen that the most likely direction of the Z is collinear to the neutralino although there is a significant proportion of events in which this is not the case. The collinearity cut imposed in the CMS analysis – an upper limit of 0.2 radians – would be likely to remove a significant number of FIMP decays, should they be present, from their selected events.

The presence of missing transverse energy in the event is also considered. Figure **??** shows the total missing transverse energy from, firstly, both neutrinos and FIMPs, and secondly, only FIMPs in the event. All benchmarks are shown (with 25 cm mean life) as well as Standard Model $W \to \mu\nu$ events. Only the BM3 benchmark, due to the additional contribution from the displaced W decay, predicts larger missing transverse energy than the Standard Model W sample. This implies that the transverse missing energy contribution provided by a 1 GeV FIMP is comparable to that from the neutrino in a $W \to \mu\nu$ decay, and for this reason a cut on transverse missing energy may not be a powerful discriminant for these models. Generally the extra step in the decay chain introduced by the FIMP will decrease the amount of the missing energy in the event compared to the SUSY decay chain without the FIMP. There can be significant instrumental uncertainty in the low missing transverse energy region. The benchmarks predicting small amounts of missing energy will therefore suffer from this background reducing the power of missing transverse energy as a discriminant between signal and background. This is not considered in this parton level analysis and would require simulation of the full event and detector response.

5.4 Experimental Constraints

In the current searches for displaced vertex signatures at hadron colliders, the CMS search has the most sensitivity to the model under consideration. The D0 analysis would have limited sensitivity to the model due to the cut on the angular separation between the muons, and the limits set by the CDF analysis (limited by the luminosity available) do not reach the cross sections for the range of FIMP models considered.

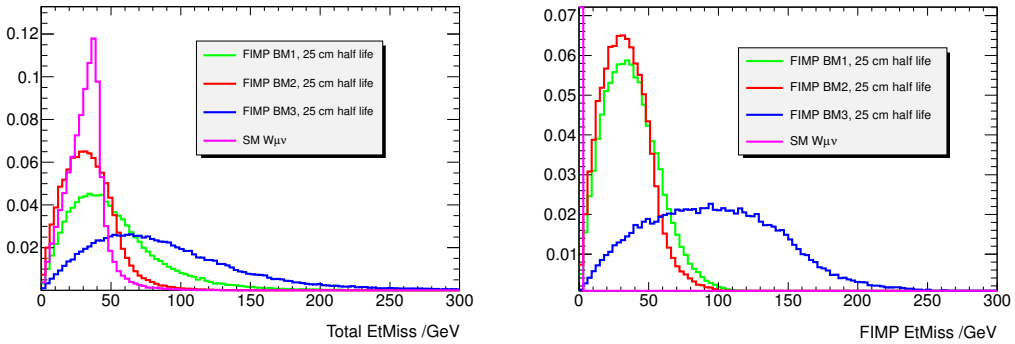

Figure 5.3: Missing transverse energy from combination of neutrinos and FIMPS (left), and from FIMPS only (right) in all 3 benchmarks. The distribution expected from Standard Model $W\mu\nu$ is shown for comparison.

To estimate the potential sensitivity of a CMS-like search for FIMP decays, a similar event selection is run – at truth level – for the benchmarks. The requirement applied is two energetic (transverse momenta > 25 GeV) and fiducial ($|\eta| < 2.4$) muons associated with the same vertex. A veto is applied to muons that are back-to-back (transverse angular separation < 2.8). The transverse collinearity cut employed by the CMS analysis, which would remove many FIMP events, is not applied. The expected yields per fb of data for each benchmark is summarised in table 5.2, having taken into account the branching ratio, $\Gamma(\mu)$, for having at least one of the legs decaying muonically. No physics background was seen to pass the proposed event selection, and it is assumed that there is zero machine or detector background given the high mass of the displaced vertex.

There will be additional losses to the number of events seen to pass the fiducial selection at truth level, due to imperfect detector reconstruction of the event. As has been discussed, the largest losses will be in triggering and reconstructing the displaced vertex. A functional form of efficiency – although it must be noted this is very detector dependent – to reconstruct a muon as a function of radial displacement was assumed from studying the publicly-available CMS efficiency plots. The form was taken as linear fall off from unity at zero displacement to zero at 40 cm displacement. As would be expected, the more long-lived the particle, the more events are lost due to imperfect efficiency modelling in the detector. The results here suggest that certain models (BM2) may very well already be ruled out by existing displaced vertex searches,

but others (BM1) may not yet be visible with the current detector limitations and integrated luminosity available.

Selection	$N_{BM1} \times \Gamma(\mu)$	$N_{BM2} \times \Gamma(\mu)$	$N_{BM3} \times \Gamma(\mu)$	$N_{SM} \times \Gamma(\mu)$
W	1	0	0	$\simeq 5000000$
Z	0.05	0	0	$\simeq 100000$
Displaced Vertex	4	42	0.01	$\simeq 0$

Table 5.2: Expected yield of FIMP events per for 1 fb^{-1} of luminosity passing Standard Model and CMS-style displaced vertex selections at truth level.

Due to the cascade decays inherent in the FIMP models, such events can be quite noisy with many hard leptons and jets produced at the interaction point. Standard W and Z event topology selections were applied to the samples. It was found that the expected contribution from the models considered here would be well below the current fractional uncertainty on measured W and Z cross sections [150]. This suggests that if these events were produced at the LHC, they would not be detected in ATLAS or CMS Standard Model analyses if event yields or basic kinematics alone are considered.

Chapter 6

Regenerating WIMPs

6.1 Introduction

For several decades, the vast majority of dark matter (DM) models have assumed that DM exists in the form of annihilating particles whose relic density is determined by the freeze-out mechanism [108, 109, 110]. This mechanism intimately links the total DM annihilation (or co-annihilation) cross section to the DM relic abundance and leads to the prediction that the total annihilation cross section must be of order the weak scale.

In some models, nevertheless, the total annihilation cross section at chemical decoupling can be so large (notably if it involves annihilations through resonant channels) that the predicted abundance for the DM candidate is well below the observed value [151], ruling it out as the dominant contribution to the DM relic abundance. However as discussed in chapter 3 a new mechanism, such as the the freeze-in scenario [4], provides a viable alternative to restore the relic density of such candidates to the required value.

The scenario in mind here is where the annihilation cross section of the DM is large enough that the predicted abundance from freeze-out is incompatibly small compared to the observed value. The relic abundance of DM is regenerated by the decay of a heavy FIMP particle which has undergone freeze-in. If the FIMP transforms under the same stabilising symmetry that keeps the DM particle stable and has a larger mass, then decays of the FIMP states will generically produce an abundance of DM particles. Due to their small coupling the FIMPs will have a sufficiently long lifetime such that they will decay after the DM freezes-out and regenerate the DM abundance.

The story in the early universe is that a feebly coupled particle the FIMP undergoes freeze-in as the temperature of the universe drops below its mass. The FIMP has a sufficiently long life time that it does not decay immediately. As the temperature of the universe drops further the DM particle undergoes freeze-out. The cross section at freeze-out of the DM is large enough that almost all of the DM annihilates away leaving only a very small abundance. Some time after the DM freezes-out the population of FIMPs will decay. Since the FIMPs and DM are charged under the same symmetry each decaying FIMP will produce a DM particle. The late decays of the FIMPs thus regenerate the abundance of DM. We recall that the abundane of DM produced by such a freeze-in scenario depends on the ratio of masses of the FIMP and DM and the feeble coupling between the FIMP and thermal bath particles. We assume here that the mass of the FIMP and the coupling are free parameters and can be chosen in such a way that the abundance of DM produced by this mechanism will agree with the observed value. This can always be achieved given any value of the residual abundance of DM freeze-out.

The question that we wish to address is whether such a mechanism can both explain the observed DM abundance in models where the DM annihilation (or co-annihilation [152, 153]) rate at freeze-out is too large, and be simultaneously compatible with the latest results from direct and indirect detection experiments. In particular, for direct detection constraints, we apply limits on the DM-nucleon spin-independent elastic cross section as derived from the XENON100 experiment [6]. The indirect detection limits that we apply come from the latest observations of the dwarf spheroidal galaxies (dSphs) by FERMI-LAT [154], which place an upper limit on the gamma flux emerging from DM annihilations.

Although we have described the freeze-in mechanism as the method of regenerating the relic abundance of DM the DM physics itself is related only to the cross section at freeze-out and is not necessarily related to the regeneration mechanism. The results therefore do not depend on the mechanism of regeneration and will hold for any process that can regenerate the abundance of DM. There could however by restrictions to the scenario coming from the regeneration mechanism which are not considered here. For example in freeze-in the feeble coupling is related to the life time of the FIMP which is constrained due to the fact that it must not decay before the DM has undergone freeze-out while too large a lifetime can be constrained by big bang nucleosynthesis. Whether such constraints can rule out a regeneration scenario will depend on the particular regeneration mechanism.

We consider as our DM candidate the neutralino of the MSSM and assume that one can add an extra term or terms to the MSSM Lagrangian in order to implement the freeze-in scenario. The use of Supersymmetry enables us to explore very different types of configurations in terms of resonances and co-annihilations. However, similar conclusions will also hold for other types of DM candidates where the freeze-out relic density is too low due to a large annihilation cross section. Previous supersymmetric parameter scans either looked for scenarios with the correct relic density (e.g.[155, 156, 157, 158, 159, 160, 161, 162, 163, 164]) or relaxed the constraint on the relic density, allowing for very small $\Omega_{\rm FO}h^2$, and did not assume the presence of regeneration mechanism [165, 166]. Here we will both relax the lower bound on the relic density and assume that the freeze-in mechanism can regenerate the relic density to the observed value. The main results of this chapter were presented in [113].

6.2 Bayesian inference

We wish to find the high probability regions in the MSSM that are compatible with a regeneration scenario. We want to discover if such a scenario is possible and then find the properties of the regions that allow the scenario. In particular we want to find regions in which regeneration is necessary to fix the relic abundance of DM but are compatible with all other constraints.

We proceed via the method of Bayesian inference of the parameters of the model given a set the set of experimental constraints on the MSSM. In this section we present the Bayesian framework for this inference and the methods used to generate the results. A general introduction to Bayesian methods can be found in [167, 168] and applications to cosmology and astrophysics in [169] and to supersymmetry in [170].

Bayes' theorem is the starting point of bayesian parameter inference. We begin with the statement that probabilities must sum to unity.

$$p\left(A|I\right)+p\left(\overline{A}|I\right)=1, \tag{6.1}$$

where $p\left(A|I\right)$ is the probability of A given I and $p\left(\overline{A}|I\right)$ is the probability of not A given I. I here represents any relevant information which may effect the probability of A and is assumed to be true. The notation here is that $p\left(A|I\right)$ represents the conditional probability of A given that

I is true. The product rule of probabilities is written in this notation as.

$$\begin{aligned} p(A,B|I) &= p(A|B,I)\,p(B|I)\,, \\ &= p(B|A,I)\,p(A|I)\,. \end{aligned} \tag{6.2}$$

In words that the joint probability of A and B is the probability of A given B multiplied by the probability of B independent of A. If A and B are independent of each other then this reduces to the simple rule that the probability of two events is the product of their individual probabilities. Likewise the probability of B and A is the probability of B given A multiplied by the probability of A. Rewriting the product rule gives Bayes' theorem,

$$p(A|B,I) = \frac{p(B|A,I)\,p(A|I)}{p(B|I)}. \tag{6.3}$$

The usual form for Bayes' theorem which makes clear its value for assessing a hypothesis is written as,

$$p(H|D,I) = \frac{p(H|I)\,p(D|H,I)}{p(D|I)}. \tag{6.4}$$

Where we have the following definitions,

$$\begin{aligned} H &\equiv \text{The hypothesis we want to evaluate,} \\ I &\equiv \text{Represents our prior knowledge,} \\ D &\equiv \text{Represents the data which is used to update our belief in the hypothesis,} \\ p(D|H,I) &= \text{Is the likelihood function, the probability of obtaining } D \text{ if } H \text{ and } I \text{ are true} \\ &\quad \text{often abbreviated to } \mathcal{L}(H), \\ p(H|I) &= \text{The prior probability of } H \text{ before considering } D, \\ p(H|D,I) &= \text{The posterior probability of } H, \\ p(D|I) &= \text{A normalisation factor.} \end{aligned}$$

Written in this way Bayes' theorem gives a prescription for how to update the degree of belief in H given the accumulation of new data D. The normalisation factor $p(D|I)$ can be rewritten

via the sum rule for probabilities,

$$p(D|I) = \sum_H p(H|I)\, p(D|H,I)\,, \tag{6.5}$$

where the sum runs over all the possible different hypothesis H. $p(D|I)$ is called the Bayesian evidence and is vital for comparing different models while the posterior probability $p(H|D,I)$ is the target of Bayesian parameter inference.

A key element of Bayesian statistics is in the inclusion of the prior $p(H|I)$. The prior can not be removed from Bayes' theorem but there is not specification in the theorem as to how the prior should be selected. It has been argued that this is a deficiency in Bayesian statistics since the prior depends on our degree of belief in H before considering the data which may be subjective. In fact the inclusion of the prior can be of value to Bayesian inference when there is external evidence that can govern the choice of a prior. The prior then gives a way of including this knowledge in the inference. We will return to the problem of priors with respect to Bayesian parameter inference shortly.

Bayesian parameter inference is the application of Bayes' theorem to a model specified by a set of parameters and gives a method to estimate the values of the parameters of the model given some observed data. We specify the model by a vector of parameters θ. We must also specify a prior associated with each component of θ which contains our knowledge of the parameters of the model before considering the data. The posterior for θ is then defined by Bayes' theorem as,

$$p(\theta|D) = \frac{\mathcal{L}(\theta)p(\theta)}{p(D)}, \tag{6.6}$$

where $\mathcal{L}(\theta)$ is the likelihood function, $p(\theta)$ is the prior and $p(D)$ is the Bayesian evidence. The evidence is not required for parameter inference. The likelihood function should be constructed to reflect how the data was obtained and may introduce nuisance parameters. In general the parameters θ will include both physically relevant parameters of interest and nuisance parameters which we are not interested in. Nuisance parameters are handled by first calculating the posterior distributions for all the parameters including nuisance parameters and then marginalising over the nuisance parameters. For a set of parameters θ including the relevant physical parameters ϕ and a number of nuisance parameters ψ such that $\theta = (\phi, \psi)$. The marginalised distribution for

ϕ is obtained by,

$$p(\phi|D) \propto \int d\psi \mathcal{L}(\phi,\psi)p(\phi,\psi) = \int d\psi p(\phi,\psi|D). \tag{6.7}$$

Generally the posterior distribution of ϕ is then given for each component by marginalising over all the other components of ϕ or two dimensional distributions of pairs of components in ϕ can be generated.

We also have to consider the prior $p(\theta)$ in terms of parameter inference. The prior probability that a parameter in θ takes on a certain value is essentially arbitrary but care should be taken as the choice of prior can effect the posterior distributions. The first consideration is that where possible information that is known about a parameter can be used to inform the prior. For example if the parameter to be determined is the mass of some particle then the prior can enforce that the mass be positive by setting $p(m) = 0$ for $m < 0$. When the data D is very constraining then the choice of prior becomes less important. So long as the prior is non-zero in regions where the likelihood is large then repeating the application of Bayes' theorem with more data will cause distributions constructed using different priors to converge. Essentially the choice of prior is overridden by the information contained in the data. This is not always the case however and the effect of the choice of prior on the posterior distribution should be taken into account. There are a number of choices for the prior distributions, the simplest is a flat prior which takes the form of $p(\theta) = \frac{1}{\theta_{max}-\theta_{min}}$ where θ_{max} and θ_{min} are the maximum and minimum values that specify the range θ can take. Such a prior is constant in that range so that all values of θ between θ_{max} and θ_{min} have equal probability. For a suitable choice of θ_{max} and θ_{min} a flat prior would appear to be a good choice in the absence of any other information about θ as it does nothing to inform the posterior distribution except bound it within that range. There is a danger to using flat priors however since the prior of some function $f(\theta)$ will not be flat. The prior distributions of θ and $f(\theta)$ are related by,

$$p(f(\theta)) = p(\theta)\left|\frac{d\theta}{df}\right| \tag{6.8}$$

This means that a flat prior for θ may be strongly informative for $f(\theta)$. If the likelihood depends on $f(\theta)$ this raises the question as to whether our prior belief is flat in θ or $f(\theta)$. In the case where scale of the quantity θ is unknown then the correct prior to use is one that is flat in $\ln\theta$ so that the prior probability of θ is given by $p(\theta) = \theta^{-1}$.

6.3 Markov Chain Monte Carlo

One method to draw samples from the posterior distribution is Markov Chain Monte Carlo (MCMC). See [171] for an introduction to MCMC methods. We describe here the basics of Markov chain Monte Carlo and the metropolis algorithm that we use to explore the parameter space. Alternatives to the metropolis algorithm include Gibbs sampling [171], hybrid Monte Carlo methods [171] and slice sampling [172]. In some situations simulated annealing and parallel tempering [171] can be used when traditional metropolis methods are not effective. One alternative to MCMC methods for bayesian parameter estimation is nested sampling [173] which has also been applied to the MSSM [174]. For our exploration of the pMSSM a standard metropolis algorithm is sufficient to explore the relevant parameter space.

MCMC works by producing a series of points in the parameter space with a density that is proportional to the posterior. A Markov chain is defined as a sequence of random variables where each variable in the sequence depends only on the variable preceding it. That is for a series of variables $X^0, X^1, ...$, the probability distribution for X^{n+1} depends only on X^n. We assume here that the X^n can take a finite number of discrete values although the results will generalise to continuous variables. The Markov chain is entirely defined by two distributions, the marginal or initial probability distribution for the fist variable in the chain X^0 and the transition probabilities which give the probability of a state to follow from the preceding state. The initial probabilities are written as $p_0(x)$ that is the probability that $X^0 = x$ as a function of x and the transition probabilities can be written as $T(x,x')$ for the probability that $X^{n+1} = x'$ will follow $X^n = x$ in the chain. For our purposes the transition probabilities will be independent of n this makes the Markov chain homogeneous. From this it is clear that the probability of state x occurring at position $n+1$ in the chain $p_{n+1}(x)$ can be written as,

$$p_{n+1}(x) \sum_{x'} p_n(x') T(x', x). \tag{6.9}$$

Along with $p_0(x)$ this defines the behaviour of the chain completely.

We are interested in invariant distributions, invariant distributions have the property that once the Markov chain has reached a distribution over x of $\pi(x)$ that distribution will persist for all

future n. In terms of the transition probabilities we can write this as,

$$\pi(x) = \sum_{x'} \pi(x') T(x', x). \tag{6.10}$$

The goal is then to construct a Markov chain where the invariant distribution of the chain is given by the posterior distribution we are interested in. Once this distribution is reached each successive variable in the chain is then a sample drawn from the posterior distribution. A sufficient condition for invariance of the distribution is detailed balance. That is that the probability of transitioning from state x' to x is equal to the probability to transition from state x to x'.

$$\pi(x) T(x, x') = \pi(x') T(x', x). \tag{6.11}$$

The invariance of $\pi(x)$ can be shown by considering,

$$\begin{aligned} \sum_{x'} \pi(x') T(x', x) &= \sum_{x'} \pi(x) T(x, x'), \\ &= \pi(x) \sum_{x'} T(x, x'), \\ &= \pi(x). \end{aligned} \tag{6.12}$$

Where we have made use of the fact the the transition probabilities must sum to unity. The final property that the Markov chain must posses is ergodicity, that is that the stationary distribution will be reached from any initial distribution of the states. Such a chain admits only one stationary distribution and has the property that at large times the distribution of the chain will be close to the stationary distribution regardless of $p_0(x)$. For an ergodic chain we also have that the state of the chain at time m will be independent of the state at time n for $m \gg n$. Since for an starting state of the chain at time n we will reach the equilibrium distribution such that that the probability distribution of states at time m will be the equilibrium distribution which does not depend on the choice of starting state at time n.

There are several algorithms available to produce Markov chains with a desired stationary distribution. One such algorithm is the metropolis algorithm which can be applied to a wide range of problems. The metropolis algorithm works by finding the next state in the Markov chain by generating a proposed step from a proposal distribution then either accepting the proposed state based on some probability that is a function of the current and proposed state. If the state is

accepted then it becomes the next state in the Markov chain if it is rejected then the current state is repeated as the next state in the chain. We call the proposal distribution for a candidate state x' to follow state x, $S(x,x')$. The acceptance probability is then called $A(x,x')$. The metropolis algorithm is then defined by follow steps.

1. Select a candidate x' from the proposal distribution $S(x_n,x')$.
2. Calculate the acceptance probability for the new state $A(x_n,x')$.
3. Generate a random number $r \in [0,1)$.
4. The new state is given by,

$$x_{n+1} = \begin{cases} x' & \text{if } r < A(x_n,x') \\ x_n & \text{otherwise} \end{cases} \tag{6.13}$$

5. Return to step 1.

For a particular realisation of the algorithm both $S(x_n,x')$ and $A(x_n,x')$ must be defined. $S(x_n,x')$ Should be chosen in such a way that the produced Markov chain is ergodic and also should be chosen to minimise the time taken for the chain to converge and minimise the decorrelation time. The acceptance probability should ensure that detailed balance is satisfied and that the Markov chain has the required stationary distribution. For the purposes of parameter inference an appropriate acceptance probability is given by.

$$A(x_n,x') = \min\left(1, \frac{p(x'|D)}{p(x_n|D)}\right). \tag{6.14}$$

Where $p(x'|D)$ is the posterior probability of x' given the data D. Where x now represents a point in the parameter space of the model. Note that since we are taking the ratio of the posterior probabilities this does not depend on the overall normalisation factor $p(D)$ and we can write the acceptance probability just in terms of the prior probabilities and likelihood function.

$$A(x_n,x') = \min\left(1, \frac{\mathcal{L}(x')p(x')}{\mathcal{L}(x_n)p(x_n)}\right). \tag{6.15}$$

In the case of flat priors this simplifies further to just the ratios of the likelihoods of the two points in parameter space.

There are a number of choices for the proposal distribution the simplest of which is a uniform distribution centred on the current state x_n with a characteristic width s. Such a proposal distribution will be ergodic since although not all values of x are accessible on each step any point in the range of x can be reached eventually after some number of steps. One key choice is the form of the proposal distribution when each state has several components, in our problem of parameter inference the model is defined by a choice of parameters θ that is a vector of components. The metropolis algorithm can then either be global where all the components are updated at the same time or local where only a single component of θ is changed. A local algorithm has the advantage that the performance of the random walk in parameter space may be improved by having a different proposal distribution for each component.

One consideration when using the metropolis algorithm is that successive samples generated by the chain will exhibit correlation. The number of Monte Carlo steps between independent samples will depend on the proposal distribution and the rate of acceptance. Choosing these so that the correlation time between samples is reduced will improve the exploration of the parameter space and reduce the time required to the chain to converge to the stationary distribution.

The representation of θ in terms of its components may not be optimal for exploring the parameter space. In particular if certain components are correlated in their posterior distributions then the random walk may proceed more easily in these flat directions of posterior probability. The correlation between samples can then be reduced by proposing steps aligned along these directions. This was performed by generating an initial sample of the parameter space then using the results of that sample to produce the covariance matrix of the posterior distributions of the parameters. The eigenvectors of the covariance matrix were then found. Proposals are then made along these directions in parameter space either by updating in each direction in turn which constitutes a local algorithm. The equivalent global update is achieved by considering a random rotation projected onto the eigenvectors. A random direction is chosen and then projected onto the eigenvectors by,

$$\mathbf{e}\lambda x'. \tag{6.16}$$

Where $\mathbf{e}$ is the matrix of the eigenvectors of the covariance matrix, λ is the diagonal matrix of eigenvalues and v is the vector pointing in the direction generated by the random rotation. This aligns the proposals along directions of correlation between parameters and along the direction with greatest variance.

The result is easiest to see with a simple example. Consider the problem of generating a Markov chain using the metropolis algorithm that converges to the bivariate distribution shown in figure 6.1a. The distribution is a bi-normal distribution with standard deviations of 1 and 6 that has been rotated by $\pi/4$ so that the distribution is no longer aligned with the axes. The sample of points used to generate figure 6.1a can be used to generate the covariance matrix which represents the step of generating a preliminary Markov chain. The covariance matrix is found and the eigenvectors and eigenvalues found. For this example these are,

$$\begin{aligned} \Sigma &= \begin{pmatrix} 18.5 & -17.5 \\ -17.5 & 18.5 \end{pmatrix}, \\ Q &= \begin{pmatrix} -1/\sqrt{2} & -1/\sqrt{2} \\ 1/\sqrt{2} & -1/\sqrt{2} \end{pmatrix}, \\ \Lambda &= \begin{pmatrix} 6 & 0 \\ 0 & 1 \end{pmatrix}, \end{aligned} \tag{6.17}$$

where Σ is the covariance matrix, Q is the matrix of eigenvectors and Λ is the diagonal matrix of the square root of the eigenvalues. A proposal step is then made by taking a random direction generated by a rotation matrix which we label $\mathbf{v}$. we choose size of the step to be given by a uniform distribution between zero and three which in practise would be chosen to maximise exploration of the parameter space. Proposed steps are then generated by,

$$x' = x_n + Q\Lambda\mathbf{v}r, \tag{6.18}$$

where r is the size of the step uniformly distributed between zero and three. The distribution of proposals centred on the origin is shown in figure 6.1 and shows how the proposed steps are directed towards the flat directions in the target distribution.

In choosing the proposal distribution using the covariance matrix we are still free to choose the distribution that governs the size of the step. There are a number of choices for the distribution to ensure detailed balance holds the direction and step size distribution should not depend on the current state of the Markov chain. So any distribution that does not depend on current or past θ is suitable. The simple choice of a uniform distribution of some width is one such choice. Another choice would be a half Gaussian centred at zero. We utilize a more complicated

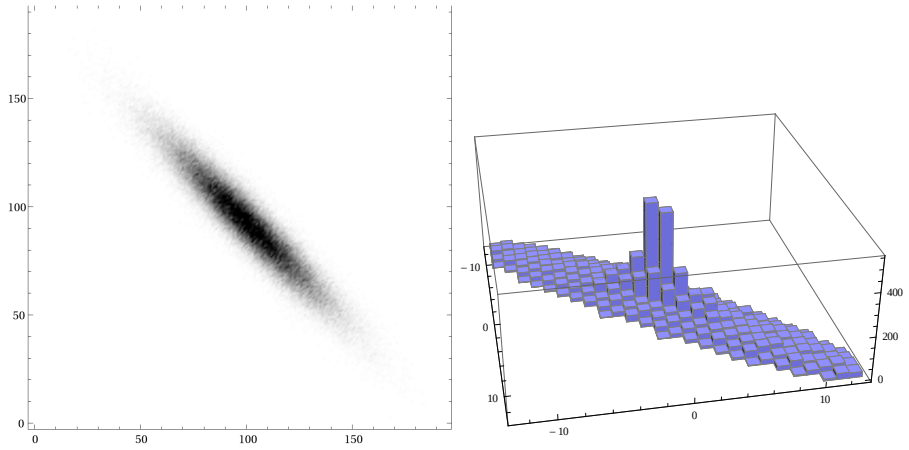

(a) Target distribution (b) Distribution of step proposals

Figure 6.1: Bi-normal target distribution and distribution of proposal steps using a random rotation matrix projected onto the eigenvectors of the covariance matrix.

distribution favoured by [170] of.

$$p(r) \propto \frac{2}{3} r^{n-1} \exp\left(\frac{-nr^2}{2}\right) + \frac{1}{3}\exp(-r), \tag{6.19}$$

where n is a free parameter chosen to be 4. The first term of this distribution pushes proposed steps away from $r = 0$ encouraging the Markov chain to move through the parameter space. The second term reduces the probability of very large steps that are more likely to be rejected. The actual proposed step is multiplied by a scaling factor which we label s. Previous studies of the CMSSM favour a value of $s = 2.4$ with this distribution [170].

A suitable value of s is usually found by trial and error by running several different chains with varying values of s and monitoring the properties of each chain such as convergence time and the time taken to full traverse the parameter space. It would be useful to automate this procedure, one such method would be to monitor some property of the chain such as the probability that a new step is accepted and adjust s during the run to achieve an optimal value of acceptance. By varying s however detailed balance is broken and the chain may not converge to the correct stationary distribution. This method can still be of some use however since if s is fixed at some point so that it no longer varies. The subsequent Markov chain with the preceding values discarded will satisfy detailed balance, the remaining question is whether the value of s obtained by this method is in fact optimal and how long the chain will take to converge to the stationary distribution.

We make use of this method to bootstrap a suitable value for s, an initial run using a local update procedure for each parameter is used. During a burn-in phase s is varied to achieve a target acceptance between 10% and 30%. The acceptance is calculated only after a reasonably large number of proposed steps for each dimension in the parameter space and s is held fixed between these times. By choosing a reasonable value of s to start and allowing enough Monte Carlo proposals between updates of s the chain is able to converge for each new value of s and the states of the chain are essentially decorrelated over these times. Once s has been updated a set number of times it is fixed and the subsequent Markov chain recorded. This is performed for several chains in parallel and convergence of each chain is checked. This initial run is used to estimate the covariance matrix for subsequent runs. The process is repeated using the global update method described above to find the new optimal value of s. The value of s generated by parallel runs agreed well and is then used to generate a final set of Markov chains used for the inference. For the final run s is held constant so that detailed balance is ensured and standard convergence checks are used to ensure that the parameter space is traversed well.

Since calculation of the likelihood can be computationally intensive growing a single Markov chain can take a long time. To improve the statistics we want to draw as many samples as possible from the target distribution. The process can be improved by constructing several chains in parallel and splitting the computation between many computers. This has the advantage the chains can have independent starting positions and by checking the agreement between chains the independence of the stationary distribution from the starting point can be checked. The value of s arrived at by the above method can also be checked between chains to ensure that it does not depend on the initial parameters.

When combining parallel chains the convergence of the total sample is checked by Gelman & Rubin R-statistics [175]. The statistic is defined in terms of the variance of the means between the different chains compared to the mean of variance within each chain. For m chains of length n we define,

$$\begin{aligned} B/n &= \sum_{i=1}^{m} \frac{(\overline{x_i} - \overline{x})^2}{m-1}, \\ W &= \sum_{i=1}^{m} \frac{s_i^2}{m}, \end{aligned} \tag{6.20}$$

where $\overline{x_i}$ is the mean for parameter x for chain i and $\overline{x}$ is the average value of x over all the chains.

s_i is the variance of x for chain i. In this way B/n is the variance of the means between chains and W is the mean of the variance between chains. The R-statistic is defined as,

$$\sqrt{\hat{R}} = \sqrt{\left(\frac{n-1}{n} + \frac{m+1}{nm}\frac{B}{W}\right)\frac{\mathrm{df}}{\mathrm{df}-2}}, \tag{6.21}$$

where df is the degrees of freedom and the term $\frac{\mathrm{df}}{\mathrm{df}-2}$ can be ignored in most cases. If $\sqrt{\hat{R}}$ is close to 1 then we can conclude that each of the m chains is converged and can be safely combined.

Once the Markov Chain has been created it can be used to infer the properties of the posterior distribution. In simple terms we replace integrations over the posterior distribution to sums over the MCMC sample. Expectation values are given by,

$$\langle\theta\rangle \approx \int p(\theta|D)\theta \mathrm{d}\theta = \frac{1}{M}\sum_{t=0}^{M-1}\theta_t, \tag{6.22}$$

where M is the total number of samples in the Markov chain. We generate marginal probabilities of the parameters by integrating over all the other parameters in the model.

$$p(\theta_1|D) = \int p(\theta|D)\mathrm{d}\theta_2 ... \mathrm{d}\theta_j, \tag{6.23}$$

where we have integrated over the other $j-1$ parameters of the model. We can generate the distribution from the Markov chain by dividing the range of θ_1 into bins and then counting the number samples that fall into each bin. The other parameters $\theta_2 ... \theta_j$ are ignored during the binning so that for each bin in θ_1 the other parameters are essentially integrated out. Nuisance parameters are dealt with in the same fashion. 2-dimensional distributions are generated in the same way but with a 2-dimensional grid of bins.

6.4 The pMSSM and prior probabilities

We use the phenomenological MSSM (pMSSM) as our model. The pMSSM is defined by specifying all of the soft SUSY breaking terms in the Lagrangian ($\mathcal{L}_{soft}$) at the weak scale. In total there are 105 free parameters in $\mathcal{L}_{soft}$ however many of these are tightly constrained by limits on CP-violation and flavour changing neutral currents (FCNC). These constraints can be satisfied by taking the soft terms to be real and setting all the off diagonal trilinear coupling and sfermion

Scan A	Scan B
$2\ \text{GeV} < M_1 < 120\ \text{GeV}$	$90\ \text{GeV} < M_1 < 2000\ \text{GeV}$
$90\ \text{GeV} < M_2 < 2000\ \text{GeV}$	
$200\ \text{GeV} < M_3 < 6000\ \text{GeV}$	
$2\ \text{GeV} < \mu < 2000\ \text{GeV}$	
$0.1 < \tan\beta < 75$	
$-4000\ \text{GeV} < A_t < 4000\ \text{GeV}$	
$A_b = A_\tau = 0$	
$100\ \text{GeV} < m_{A^0} < 1500\ \text{GeV}$	$100\ \text{GeV} < m_{A^0} < 4000\ \text{GeV}$
$100\ \text{GeV} < m_{\tilde{l}_L} < 4000\ \text{GeV}$	
$100\ \text{GeV} < m_{\tilde{l}_R} < 4000\ \text{GeV}$	
$100\ \text{GeV} < m_{\tilde{q}_{1,2}} = m_{\tilde{u}_{1,2}} = m_{\tilde{d}_{1,2}} < 4000\ \text{GeV}$	
$100\ \text{GeV} < m_{\tilde{q}_3} = m_{\tilde{u}_3} = m_{\tilde{d}_3} < 4000\ \text{GeV}$	

Table 6.1: Allowed ranges of the parameters.

masses to zero suppresses FCNC. This reduces the number of free parameters considerably. In this way the pMSSM parameter space has been explored using further constraints on the soft parameters to reduce the number of free parameters to 25 [176] or 19 [128]. We use 11 parameters to specify the model namely the gaugino masses, M_1, M_2, M_3, the Higgs-Higgsino mass parameter, μ, the ratio of the Higgs vacuum expectation values, $\tan\beta$, the stop trilinear coupling, A_t, (all other trilinear couplings are set to zero $A_b = A_\tau = 0$), the mass of the CP-odd Higgs, m_{A^0}, and finally the parameters $m_{\tilde{q}_{1,2}}$, $m_{\tilde{q}_3}$ and $m_{\tilde{l}_{L,R}}$, which represent the squark masses for the first two generations, the third generation squark masses, and all generations of the "left" and "right" sleptons respectively. So that for the squarks we have the soft masses equal for the up and down type quarks for both the left and right handed fields $m_{\tilde{q}_i} = m_{\tilde{u}_i} = m_{\tilde{d}_i}$.

The choice of $m_{\tilde{q}_1} = m_{\tilde{q}_2} \neq m_{\tilde{q}_3}$ is particularly relevant since stops can be lighter than the first two generations and can be relevant for enhancing neutralino annihilations (cf e.g. [177]). Separating the "left" and "right" slepton masses also allows for a light slepton (mostly in the case of "left" sleptons) that can play a significant role in neutralino co-annihilations [178, 179].

We perform two Markov Chain Monte Carlo (MCMC) scans labelled Scan A and Scan B. Scan A is dedicated to low neutralino masses (below 100 GeV) while Scan B is dedicated to heavier candidates (above 100 GeV). This choice of two separate scans above and below 100 GeV is purely arbitrary but it turns out to be a useful division. The reason being that the neutralino candidates found in each scan represent different freeze-out scenarios and are most

Standard model parameter	Mean value	Experimental uncertainty
m_t	172.9 GeV	1.5
$m_b(m_b)^{\overline{MS}}$	4.19 GeV	$^{+0.18}_{-0.06}$
$\alpha_s(m_Z)^{\overline{MS}}$	0.1184	0.0007
$\alpha_{EM}^{-1}(m_Z)^{\overline{MS}}$	127.916	0.015

Table 6.2: Constraints used to calculate likelihoods for standard model parameters, from Ref. [10].

sensitive to different experimental searches. Scan A features s-channel resonant effects while Scan B shows a greater number of t-channel exchange and co-annihilation processes. Table 6.1 shows the allowed range of the parameters for the two scans. We use flat priors for the parameters.

In addition to the parameters of the model coming from the soft SUSY breaking terms we include a number of standard model parameters as nuisance parameters. The nuisance parameters are included as part of the random walk and then marginalised over to produce the final inferences for the SUSY parameters. The mean values and uncertainties of the nuisance parameters are shown in table 6.2.

6.5 Likelihood Function

We construct the total likelihood function as the product of likelihood functions corresponding to each constraint. For the partial likelihoods we use one type of function for upper and lower limits and another form for observables with a preferred value. Following Ref. [166] we use a Gaussian distribution for preferred values,

$$F_2(x,\mu,\sigma) = e^{-\frac{(x-\mu)^2}{2\sigma^2}}, \tag{6.24}$$

where μ is the preferred value of the observable and σ is the tolerance. For observables with only an upper or lower limit a distribution of the form,

$$F_3(x,\mu,\sigma) = \frac{1}{1+e^{-\frac{(x-\mu)}{\sigma}}}, \tag{6.25}$$

Constraint	Value	Tolerance
$\Omega_{\rm FO}h^2$	< 0.1123 [180]	none
$\delta\,(g-2)_\mu$	28.7×10^{-10}	stat: 6.3×10^{-10} sys: 4.9×10^{-10}
$\Delta\rho$	≤ 0.002	0.0001
BF$(b\to s\gamma)$	3.55×10^{-4} [181]	exp: 0.24×10^{-4}
BF$(B_s\to\mu^+\mu^-)$	$\leq 4.5\times10^{-9}$ [182]	4.5×10^{-11}
R$(B\to\tau\nu_\tau)$	1.36 [181]	0.23
$\Gamma(Z\to\tilde{\chi}_1^0\tilde{\chi}_1^0)$	≤ 1.7 MeV	0.3 MeV
$\sigma(e^+e^-\to\tilde{\chi}_1^0\tilde{\chi}_{2,3}^0)$	≤ 0.1 pb [183]	0.001pb

Table 6.3: Constraints used to calculate likelihoods, from Ref. [10] unless stated. Here $\Omega_{\rm FO}h^2$ is the relic abundance of neutralino DM from freeze-out, $\Delta\rho$ is the contribution to the electro-weak precision variable ρ, R$(B\to\tau\nu_\tau)$ is the ratio of the MSSM to SM branching fraction of $B^+\to\tau^+\nu_\tau$.

is used. Here σ is positive for lower bounds and negative for upper bounds. The tolerance is given by the experimental or theoretical uncertainty for the observable.

Table 6.3 shows the different constraints used to create the likelihood. These are:

6.5.1 $\Omega_{\rm FO}h^2$

$\Omega_{\rm FO}h^2$ is the DM relic density calculated from the freeze-out of the lightest neutralino. Since we are interested in regeneration scenarios we take the best value of $\Omega_{\rm DM}h^2 = 0.1123\pm0.0035$ from the 7-year Wilkinson Microwave Anisotropy Probe (WMAP) fits to the ΛCDM model [180] as an upper limit. The tolerance is given by zero for this partial likelihood as we only consider those models that require some regeneration.

Recent results from the PLANCK satellite have observed a larger value for the relic abundance of $\Omega_{\rm DM}h^2 = 0.1192\pm0.0024$ [184]. This shift in the preferred value of $\Omega_{\rm DM}h^2$ has a minimal effect on the results of the scan since we are interested in the parameter space where the relic abundance from freeze-out significantly deviates from the upper limit.

The calculation of $\Omega_{\rm FO}h^2$ is performed using the program `micrOMEGAss` which takes into account the direct annihilations and co-annihilations that contribute to the freeze-out abundance.

6.5.2 Muon Anomalous Magnetic Moment

The muon anomalous magnetic moment has been measured in collisions at Brookhaven [185] to be $a_\mu^{exp} = (g-2)_\mu = 11659208.9\pm5.4\pm3.3\times10^{-10}$. The standard model calculation gives

a value of $a_\mu^{SM} = 11659180.2(2)(42)(26) \times 10^{-10}$ [10]. The discrepancy between these values gives,

$$\delta a_\mu = a_\mu^{exp} - a_\mu^{SM} = 28.7(6.3)(4.9) \times 10^{-10}. \tag{6.26}$$

This difference can be accounted for by corrections from SUSY, for sparticles of universal mass M_{SUSY} their contribution is of order [186],

$$a_\mu^{SUSY} = 13 \times 10^{-10} \left(\frac{100\text{GeV}}{M_{SUSY}} \right) \tan\beta \, \text{sign}(\mu). \tag{6.27}$$

A routine in `micrOMEGAs` is used to calculate the SUSY contribution to a_μ [187]. The result depends on the smuon properites as well as the chargino and neutralino sector.

6.5.3 $\Delta\rho$

$\Delta\rho$ describes the corrections to electroweak observable ρ due to virtual particles. The ρ parameter measures the relative strength of the charged and neutral currents at zero momentum transfer and is sensitive to new particles in the self energy diagrams of the W and Z bosons [188]. In SUSY the extended Higgs sector, neutralinos and charginos and also the sfermions can contribute to $\Delta\rho$ when there is a mass splitting between particles in isospin doublets. $\Delta\rho$ is calculated in `micrOMEGAs` via a call to `SUSPECT` [189] which calculates $\Delta\rho$ including the contribution from 3rd generation sfermions as well as 2-loop corrections from gluon exchange and gluino exchange in the heavy gluino limit.

6.5.4 BF$(b \to s\gamma)$

The rare decay $(b \to s\gamma)$ proceeds at the loop level in the standard model, new SUSY particles appearing in loops can enhance the rate of this decay. The process $(b \to s\gamma)$ can not be measured directly as the underlying quarks form hadrons due to the strong interaction. Instead experiments must measure the inclusive decay rate of a B meson to photon plus a strange hadronic state X_s where X_s is any hadronic state that carries the strange quantum number $s = +1$ [190]. The inclusive rate $b \to X_s\gamma$ has been measured at the B-factories to be [181] BF$(b \to s\gamma) = (3.55 \pm 0.24) \times 10^{-4}$. This is in good agreement with the SM calculation BR$(B \to X_s\gamma)_{SM} = (3.70 \pm 0.30) \times 10^{-4}$ [191]. This agreement constrains any new particles that could appear in loop diagrams contributing to this process. In the MSSM contributions from the charged higgs and

chargino/squark loops could enhance the decay rate.

The calculation of both the SM and SUSY contributions to $(b \to s\gamma)$ are calculated by a routine in `micrOMEGAs`.

6.5.5 BF$(B_s \to \mu^+\mu^-)$

The rare decay $B_s \to \mu^+\mu^-$ proceeds via a FCNC and is therefore suppressed in the standard model. The contribution from SUSY particles in loops is calculated by `micrOMEGAs` and includes the loop contributions from chargino, sneutrino, stop and higgs exchange.

For the likelihood the result published by the LHCb collaboration placing an 95%CL upper limit on $B_s \to \mu^+\mu^-$ is used [182].

$$\mathrm{BF}(B_s \to \mu^+\mu^-) \leq 4.5 \times 10^{-9}. \tag{6.28}$$

More recently $\mathrm{BF}(B_s \to \mu^+\mu^-)$ has been positively observed at a rate of [192]

$$\mathrm{BR}(B_s \to \mu^+\mu^-) = (3.2^{+1.5}_{-1.2}) \times 10^{-9}. \tag{6.29}$$

The possible effect of this updated measurement on the scan will be discussed latter.

6.5.6 R$(B \to \tau\nu_\tau)$

The decay of a B meson to a τ and ν_τ proceeds in the standard model via the W boson. In SUSY the charged higgs particle can also mediate this decay and so if SUSY is present the measured value of $\mathrm{BR}(B \to \tau\nu_\tau)$ may deviate from the predicted standard model value. The measured value of $\mathrm{BR}(B \to \tau\nu_\tau)$ used was [181]

$$\mathrm{BR}(B \to \tau\nu_\tau) = (1.67 \pm 0.3) \times 10^{-4}. \tag{6.30}$$

Which is in agreement with the standard model prediction of

$$\mathrm{BR}(B \to \tau\nu_\tau)^{SM} = (1.20 \pm 0.25) \times 10^{-4}. \tag{6.31}$$

Which constrains any new physics that can mediate this decay. We use `micrOMEGAs` to calculate the ratio of the decay rate in the MSSM to the SM value.

6.5.7 $\Gamma(Z \to \tilde{\chi}_1^0 \tilde{\chi}_1^0)$

For light neutralinos bellow half the mass of the Z boson there are strong constraints from the invisible branching ratio of the Z measured at LEP.

$$\Gamma(Z \to \tilde{\chi}_1^0 \tilde{\chi}_1^0) \leq 1.7 \text{ MeV} \tag{6.32}$$

This limit constrains the mixing of the lightest neutralino and restricts its coupling to the Z boson when the decay is kinematically allowed. The partial width of this decay is calculated using the `micrOMEGAs` interface to `calcHEP`.

6.5.8 $\sigma(e^+e^- \to \tilde{\chi}_1^0 \tilde{\chi}_{2,3}^0)$

Light neutralinos are also constrained by the SUSY searches at LEP and a limit was placed on the production rate of the lightest neutralino in association with a heavier neutralino. This leads to a limit of [183]

$$\sigma(e^+e^- \to \tilde{\chi}_1^0 \tilde{\chi}_{2,3}^0) \leq 0.1 \text{ pb}. \tag{6.33}$$

The cross section is calculated at the tree level using the `micrOMEGAs` interface to `calcHEP`.

6.5.9 Sparticle mass limits

There have been many searches for supersymmetry at colliders that set bounds on the masses of sparticles. For the likelihood calculation we include the limits on sleptons and charginos implemented in `micrOMEGAs` coming from LEP which are relevant up to about 100GeV. The sparticle mass limit is implemented as a step function for the likelihood. This means the partial likelihood is 1 when the constraints are met and 0 otherwise.

We do not apply limits on the squark and gluino masses coming from the latest CMS and ATLAS data. The limits form LHC searches are more difficult to interpret in the pMSSM, in particular when the mass splitting between SUSY particles is very small the limits become very poor. The effect of these limits could be considered by simulating events for a converged sub set of the Markov chains as described in [125], however, we consider this beyond the scope of this

particular work. Our focus here is to examine the possibility of regenerating the DM density in under-abundant DM scenarios in the light of DM experiments. We discuss the possible effects of including these limits on the two different scans later (see section 6.9).

6.5.10 Constraints on the higgs sector

The higgs sector of the MSSM consists of the two CP-even higgs bosons h^0 and H^0 where h^0 is the lighter of the two, a CP-odd pseudoscalar A^0 and a charged higgs $H^{\pm}$. Higgs searches at LEP, the Tevatron and the LHC have all sought to discover or constrain both the SM higgs and also the MSSM higgs sector. In particular the light higgs h^0 can be similar in properties to the standard model higgs for much of the MSSM parameter space. In calculating the likelihood we use the `HiggsBounds` program [193] [194] to test if the entire higgs sector passes the experimental constraints. We use version 3.7.0 which contains experimental data released up to 20.03.12 including searches from Atlas and CMS. Higgs bounds returns a binary result that either the higgs sector passes all constraints or that it does not we use this returned value as a step function partial likelihood, rejecting any points that do not pass the higgs sector constraints.

Both Atlas and CMS have updated their searches for the higgs boson since the results presented here [195] [196]. This has further constrained the masses of the heavier higgs particles and lead to the discovery of a particle compatible with the SM (or lightest MSSM) higgs boson with mass around 126GeV [197, 198, 199, 200]. The updated constraints have been included in the new versions of `HiggsBounds` while the positive signal is included in the new program `HiggsSignal` [201]. We discuss the effects of these results on the two different scans in a latter section.

6.6 Computational Tools

In this section the numerical tools used to calculate the likelihood function are described. The driving code responsible for carrying out the metropolis algorithm was written in C. The code has to interface with several different programs that perform different parts of the calculation. Much of the interface takes advantage of the SUSY Les Houches Accord (`SLHA`) [144, 202] which is a standard for specifying a SUSY model.

The driving code works as follows

- A set of proposed coordinates in the parameter and nuisance parameter space is generated by the Metropolis algorithm.
- The input parameters are written to an `SLHA` file and `SoftSusy` is used to calculate the particle spectrum.
- `micrOMEGAs` reads the `SLHA` file containing the SUSY parameters, checks that `SoftSusy` has not raised any issues with the spectrum then uses the SUSY parameters to calculate the relic abundance and other observables.
- `SUSYHIT` is then called on the `SLHA` file to calculate the higgs decay modes.
- `micrOMEGAs` uses the `SUSYHIT` output to write the set of parameters needed by `HiggsBounds`.
- `HiggsBounds` is called to evaluate the constraints on the higgs sector.
- The total likelihood is computed and the step accepted or rejected based on the Metropolis algorithm.
- If the step is accepted the spin independent nucleon cross section and indirect detection photon flux are calculated using `micrOMEGAs`.

6.6.1 `micrOMEGAs`

`micrOMEGAs` is a code to calculate the properties of the DM in a general particle physics model under a set of assumptions, namely that the DM is stabilised by some discrete symmetry and that the relic abundance is described by freeze-out. It also contains subroutines specifically for the MSSM which are used to compute the flavour physics and electro weak precision observables mentioned in the previous section.

The relic abundance is calculated by solving the differential equations numerically using the Runge Kutta method to find the freeze-out temperature. The thermally averaged cross section is calculated by generating all of scattering processes involving two LSPs, an LSP co-annihilating SUSY particle and processes involving two co-annihilating SUSY particles. Since the total number of processes is large co-annihilation processes are neglected when the particles involved are heavier than the LSP due to their Boltzmann suppression.

The method for calculating the WIMP-nucleon cross section is described in [203]. It can be briefly summarised as follows. The WIMP-quark squared matrix element can be written in terms of effective operators, the coefficients of the effective operators are found numerically by adding the effective vertices to the model file and using these to project the matrix elements calculated from the full theory onto the effective vertices to extract the coefficients. The implementation of the new model file including the auxiliary effective vertices is done automatically without user intervention. The quark-nucleon matrix elements squared calculated from the effective theory are scaled to find the WIMP-nucleon cross section by nuclear form factors.

The indirect detection flux of photons is calculated in `micrOMEGAs` and is described by [204]. The cross section for the annihilation of WIMPs to standard model final states is calculated via the interface to `CalcHEP`. Standard tables of the photon spectrum from the production of pairs of standard model particles generated using `pythia` are used for the produced photon spectrum. The tables are calculated from $A\overline{A}$ final states, for AB final states the spectrum is averaged between the $A\overline{A}$ and $B\overline{B}$ spectrums. In addition `micrOMEGAs` can take into account gauge boson polarisation and photon radiation from intermediate state radiation (ISR) and final state radiation (FSR) which can have dramatic effects on the cross section if the emitted photon lifts a chiral suppression in the final state.

6.6.2 `SoftSusy`

The SUSY particle spectrum, couplings and mixing matrices are calculated from the input parameters by `SoftSusy` [205]. `SoftSusy` computes the full set of SUSY parameters and pole masses from the SUSY breaking terms fixed at some high scale and the SM parameters fixed at the low energy scale along with the conditions for electroweak symmetry breaking. It performs this by way of an iterative solution. The low scale yukawa and gauge couplings are run up to the high scale and the SUSY breaking terms fixed by the input parameters. All the parameters are run down to the EWSB scale and the EWSB conditions are used to fix μ and m_3. The full set of MSSM parameters is then used to calculate the mass spectrum and mixing matrices. This processes is repeated until the spectrum converges with the first iteration is special as there is initially no SUSY spectrum to use in running the parameters up to the high scale. Subsequent iterations include the loop effects from the SUSY spectrum. `SoftSusy` performs the RGE calculations using the 2-loop MSSM beta functions.

The calculation can fail for a variety of reasons, firstly the iterative procedure can fail to converge in which case the result is considered unreliable. A coupling can encounter a Landau pole during it's evolution in which case the evolution can not be continued and the spectrum can not be calculated. If the EWSB can not be satisfied because $\mu^2 < 0$ or the electroweak minimum is in fact a saddle point of the potential then the parameter point can be ruled out as it is not physical. A Tachyonic mass $m^2 < 0$ for a particle in the model will also rule out that set of input parameters. In all of these cases `SoftSusy` will place flags in the `SLHA` file indicating how the calculation failed and we use these to discard points where the calculation fails.

6.6.3 `SUSYHIT`

`SUSYHIT` combines the `SuSpect` spectrum calculator, `SDECAY` and `HDECAY` packages. In order to constrain the higgs sector the branching fractions of various decay modes of the Higgs particles must be found. `micrOMEGAs` is able to calculate $1 \to 2$ and 3 body decays at tree level but some of the important decay modes $h \to gg$ and $h \to \gamma\gamma$ appear at the loop level. `HDECAY` includes code to calculate these loop decays as well as doubly off shell-decays to 4 fermions via 2 off-shell gauge bosons.

6.6.4 `HiggsBounds`

`HiggsBounds` uses a large collection of experimental limits from Higgs boson searches from LEP, the Tevatron and the LHC to attempt to constrain any arbitrary Higgs sector. The limits are applied by taking each applicable search to each Higgs boson in Higgs sector. For each combination of limit and Higgs boson called an analysis application X [194] there is predicted cross section for the production of that Higgs boson on which the experimental search places a limit. `HiggsBounds` uses the input provided to calculate the prediction of the model of $Q(X)_{model}$ which is the prediction for the quantity that the limit places a bound on, for example this will ordinarily be a cross section multiplied by branching fraction.

The correct statistical interpretation only one observed limit applied to a Higgs boson should be considered that is one analysis application X should be chosen from all possible X that can be constructed. To do this the list of constraints includes the expected sensitivity $Q_{expected}$, the analysis application, X that has the largest ratio of $Q(X)_{model}$ to $Q_{expected}$ is then used to constrain the model. `HiggsBounds` will also calculate a 'SM-likeness' for a Higgs boson to

check if searches carried out under SM assumptions can be applied.

The input to `HiggsBounds` is via the `SLHA` format and was given in terms of the masses, total widths and branching fractions (as calculated in `HDECAY` and the ratios of the effective couplings of the Higgs particles to bosons and fermions to the standard model values. `HiggsBounds` then uses the effective coupling approximation to calculate production cross sections at the colliders.

6.7 Results: Contribution to freeze-out

Before presenting the results of the scan the procedure for plotting is mentioned here. One and two dimensional Posterior probability distributions are presented as "Blue" plots produced using the `Pippi` package with 64% and 95% preferred region contours [206]. Plots of the contributions to freeze-out the points found by the random walk are plotted as semi-transparent dots, faint regions therefore correspond to a low density of points while regions of strong colour correspond to denser regions. For the multi-coloured plots presenting the effects of regeneration the transparency of the colours follows the density of points and 64% and 95% confidence level contours are overlaid. Details of the plotting procedure are found in appendix A.

6.7.1 Scan A: $m_{\tilde{\chi}_1^0} < 100$GeV

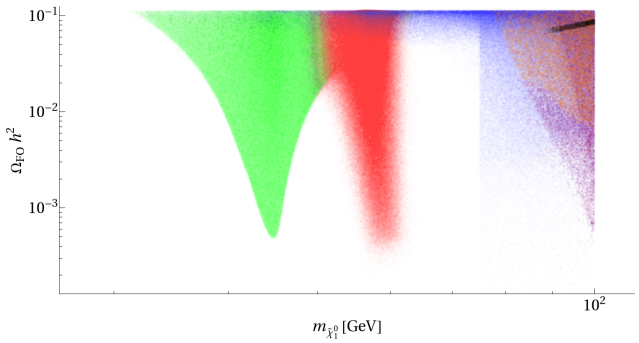

Figure 6.2: Plot of $\Omega_{\rm FO}h^2$ against $m_{\tilde{\chi}_1^0}$. The colour coding represents the process with the largest contribution to the neutralino annihilation rate, which determines the freeze-out relic abundance. Green points correspond to resonant annihilation via Z, red points to resonant annihilation via the light Higgs boson (h^0), orange points to resonant annihilation via the pseudo-scalar Higgs (A^0), blue points to stau co-annihilation or annihilation via stau exchange, violet points to chargino co-annihilations or chargino exchange, black points to squark co-annihilation (all squark flavours).

In figure **??**, we show the relic density versus DM mass for candidates found by the MCMC. In most scenarios more than one process will contribute to the freeze-out relic abundance but

in figure **??** the largest single contribution to the annihilation rate, which in the majority of scenarios dominates the others, is indicated. As expected there are two visible resonance regions [152], corresponding to Z gauge boson and light CP-even Higgs (h^0) s-channel resonances. In addition there are the usual points corresponding to heavier neutralinos that can annihilate via s-channel exchange of the CP-odd Higgs (A^0) [158], as is well known from traditional freeze-out scenarios. These points appear as a smeared out region due to the large variation in the value of m_{A^0}.

In addition to the s-channel processes the well known t-channel exchange and co-annihilations processes involving charginos, staus and squarks are also found by the MCMC. It is likely that the majority of the points corresponding to squark exchange and co-annihilation will be excluded by the LHC or Tevatron. However, we still include these points as our focus here is to examine the effect of regeneration and the resulting DM detection constraints on the possible regions of the parameter space.

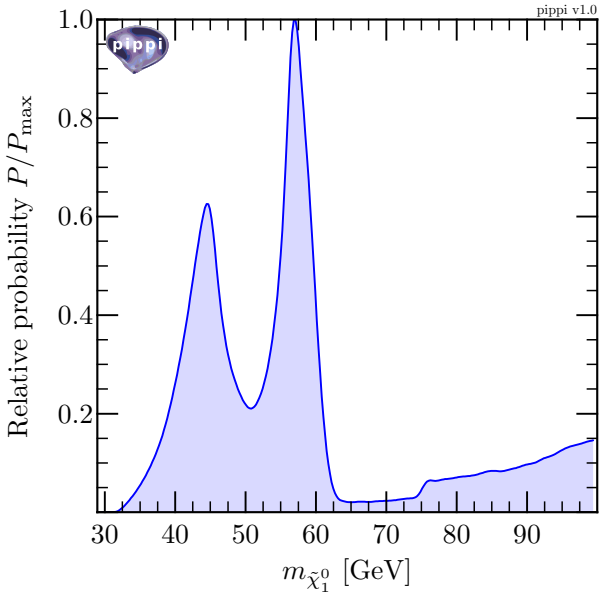

Figure 6.3: Marginalised posterior distribution for the mass of the lightest neutralino for scan A

Figure 6.2 shows the posterior distribution for the mass of the lightest neutralino. Projected onto this observable the relative amount of prior mass in the two resonance regions and the co-annihilation regions can be seen. This shows that the Higgs resonance processes are favoured followed by the Z resonance. It can also be seen that the co-annihilation region is favouring neutralinos with masses close to the boundary of the scan.

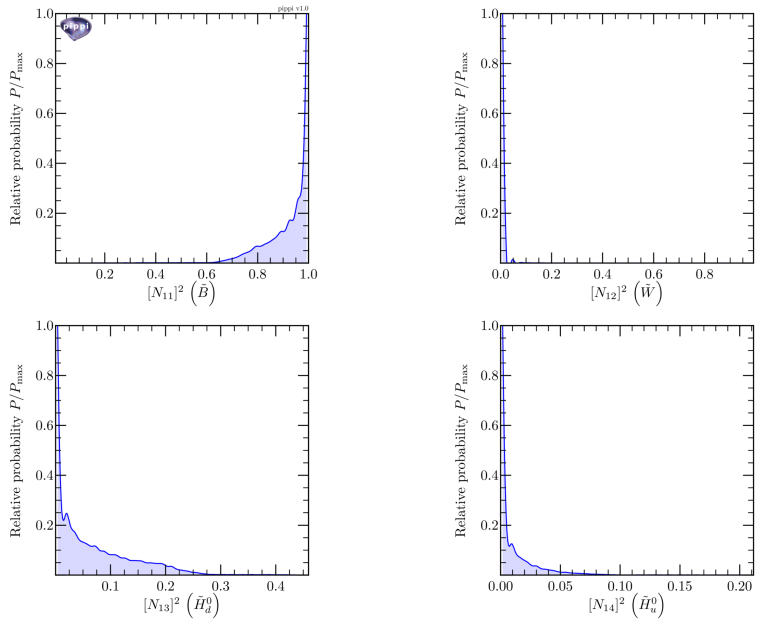

Figure 6.4: Marginalised posterior distributions of the composition of the lightest neutralino in terms of the Gaugino and Higgsino components for $m_{\tilde{\chi}_1^0} < 100$GeV.

Figure 6.3 shows the composition of the neutralino LSP in terms of the weak eigenstates, the Bino, Higgsinos and Wino. The mixing of the states differs slightly for the various regions displayed in figure **??**. In general we see that most of the posterior mass is located where the neutralino is almost entirely Bino but regions with a sizeable Higgsino contribution are also found. The neutarlino contains almost no contribution from the Wino in this scan.

For the Z and h^0 resonance regions the neutralino is mostly Bino with a small Higgsino component. As is well known, (see for example [207, 208]), the size of the Higgsino component will play a central role in determining the cross section for DM annihilations via s-channel Z and h^0. This Higgsino component will also lead to the dominant contributions to the spin-independent elastic scattering cross section in direct detection experiments, where the main process is the t-channel exchange of a Higgs. This connection is important for what follows in the later sections.

In the cases where t-channel exchange and co-annihilation processes, involving light SUSY squarks and sleptons, dominate the freeze-out dynamics, the neutralino can have a much smaller Higgsino component. This is because, in contrast to the s-channel annihilation processes, the t-channel annihilation and co-annihilation diagrams can occur for pure Bino neutralinos.

Figure 6.4 shows the posterior distributions for SUSY input parameters. It can be seen that the distribution for the Gaugino input parameter M_1 follows the same distribution as the mass

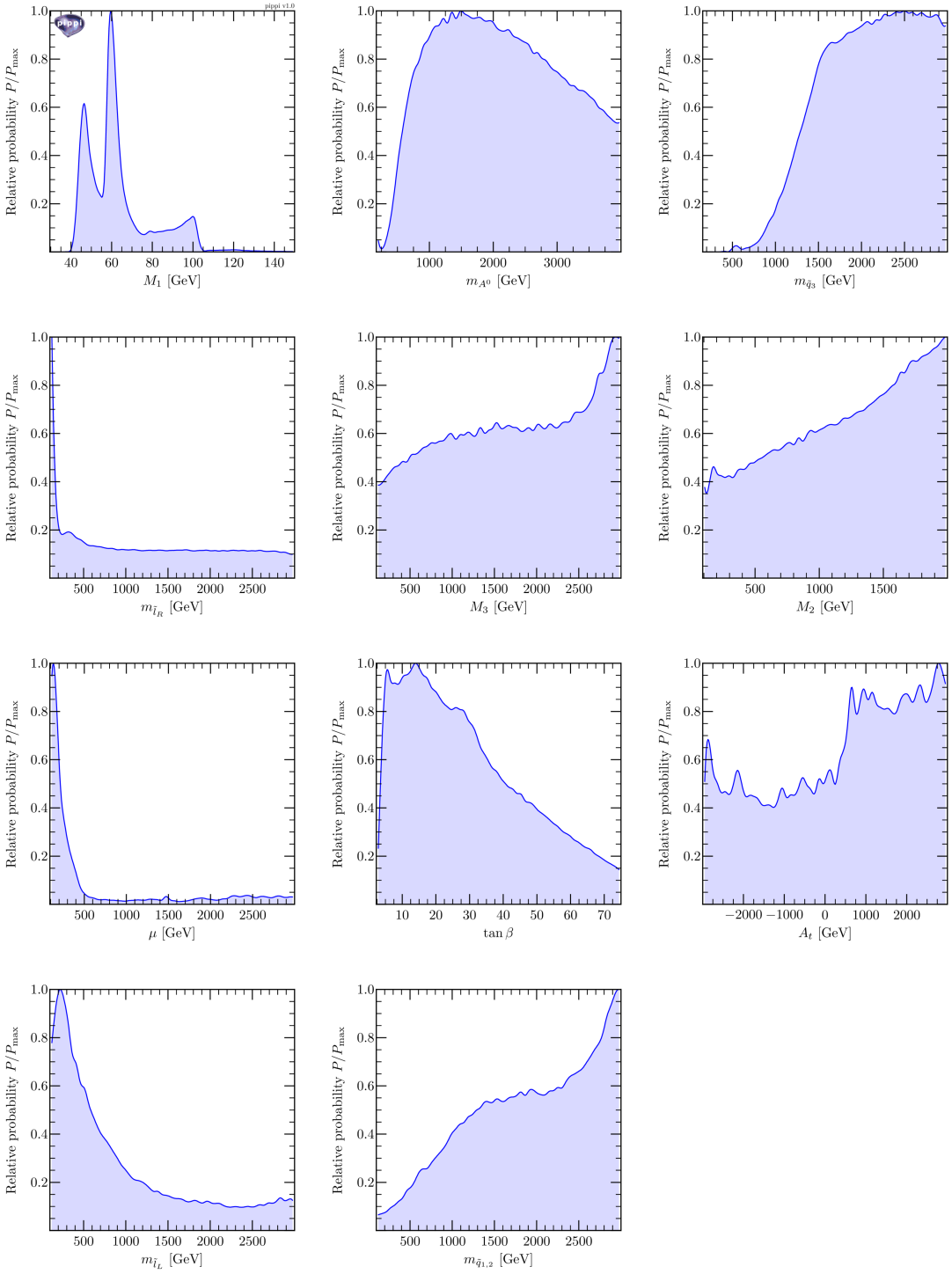

Figure 6.5: Marginalised posterior distributions for the SUSY input parameters for $m_{\tilde{\chi}_1^0} < 100$GeV.

of the neutralino this is because of the small amount of mixing between the Bino with the Wino and Higgsino states leaving a lightest neutralino that is dominantly Bino. In contrast the M_2

parameter is largely unconstrained at high values but must be large enough that the lightest chargino is above the LEP limits. There is a small dip and peak in the probability at low masses near 100GeV where the value of M_2 allows a light chargino contributing to co-annihilation. The preferred values of μ and $\tan\beta$ are likely to be driven by the required mixing between the Higgsino and Bino states in the resonance regions as well as the limits on the Higgs sector and charginos. The gluino mass parameter M_3 and the various squark mass parameters are relatively unconstrained in the absence of the direct sparticle searches. Larger values of these parameters are favoured here which will act to suppress the gluino and squark loop corrections to the flavour physics observables. The choice of priors for the squark and gluino mass parameters can be important as log priors would reduce the prior probability of these high mass regions. The distribution of the right-handed slepton mass parameter $m_{\tilde{l}_R}$ contains a peak at low values. Figure 6.5 shows the 2-dimensional distribution of $m_{\tilde{l}_R}$ against M_1, here we can see that values of $m_{\tilde{l}_R}$ fall into two regions. At small M_1 corresponding to the resonance region $m_{\tilde{l}_R}$ is unconstrained and can take on large values. In the region where M_1 is close to 100GeV corresponding to the co-annihilation region $m_{\tilde{l}_R}$ also takes on values close to 100GeV. From this it is clear that the co-annihilation region is largely controlled by the right-handed slepton mass parameter. The mass of the pseudo-scalar Higgs shows that direct searches for the Higgs particles constrain this parameter driving it to larger values. There is however a small region in which the pseudo-scalar Higgs is light which allows for resonant annihilation through the pseudo-scalar. Figure 6.6 shows that this region occurs for small values of $\tan\beta$ which accounts for the pseudo-scalar escaping detection in the Higgs searches.

6.7.2 Scan B: $m_{\tilde{\chi}_1^0} > 100$GeV

In the case of neutralinos heavier than 100 GeV, one does not expect any resonance structure in the $(m_{\tilde{\chi}_1^0}, \Omega_{\rm FO}h^2)$ plane since there are no fixed mass neutral particles (such as the light CP-even Higgs[1] or Z boson) that can be produced in an s-channel resonance. Instead resonant annihilation through A^0 will appear over a range of different neutralino masses. Non-resonant annihilation via the h^0 and Z bosons can still produce a large enough cross section to reduce the relic abundance for masses above 200 GeV. Chargino or squark t-channel exchange and co-annihilations also lead to an enhanced cross section but this does not appear as a fixed mass

[1] Although the h^0 mass is not fixed, it is restricted to a narrow range in the MSSM.

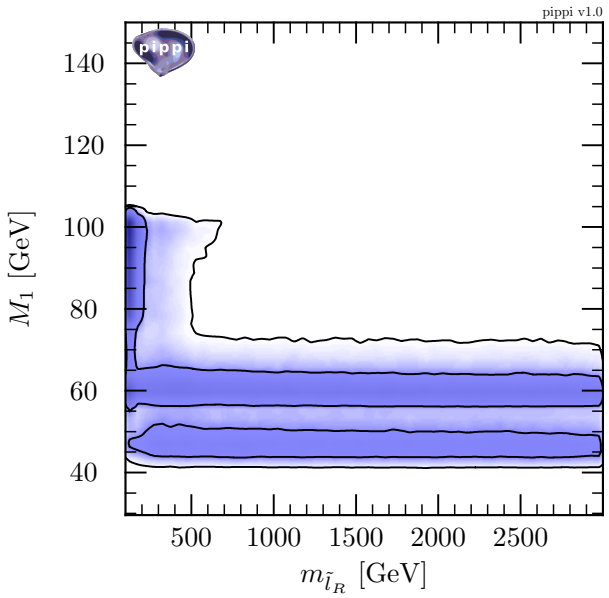

Figure 6.6: Marginalised 2D posterior distribution for the SUSY input parameters $m_{\tilde{l}_R}$ and M_1 (Scan A $m_{\tilde{\chi}_1^0} < 100$GeV).

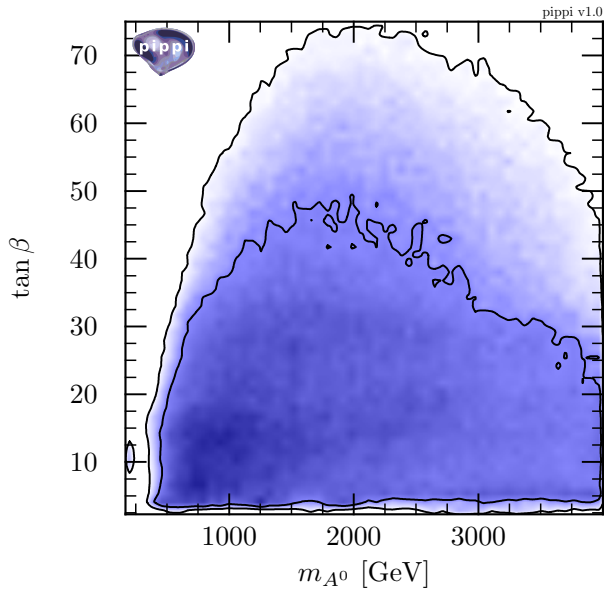

Figure 6.7: Marginalised 2D posterior distribution for the SUSY input parameters $\tan\beta$ and M_{A^0} (Scan A $m_{\tilde{\chi}_1^0} < 100$GeV).

resonance. As a result, we find a smooth homogeneous distribution of points in the $(m_{\tilde{\chi}_1^0}, \Omega_{\rm FO}h^2)$ plane, as shown in figure 6.7.

The most visible trend in figure 6.7 is that the minimum relic abundance found by the MCMC

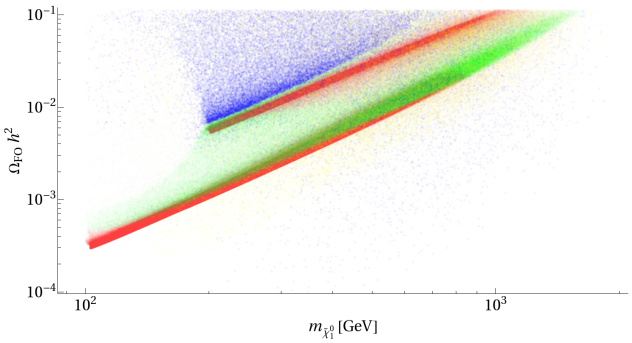

Figure 6.8: Plot of $\Omega_{\rm FO}h^2$ against $m_{\tilde{\chi}_1^0}$. Colour coded for the process with the largest contribution to the total neutralino annihilation rate, which determines the freeze-out relic abundance. Red points correspond to chargino co-annihilation, green points to annihilation via chargino t-channel exchange, blue points to annihilation via s-channel Higgs (roughly speaking the blue points above the green band correspond to annihilation via an s-channel h^0 into $t\bar{t}$ and $b\bar{b}$, the few below are s-channel annihilation via A^0), yellow points correspond to a either squark co-annihilation or gluino-gluino annihilations (the latter in the case where the gluino is approximately mass degenerate with the neutralino DM and its freeze-out sets the neutralino relic abundance).

increases quadratically as a function of mass. This dependence of the relic abundance on the mass of the neutralino DM arises due to the fact that the relic abundance scales as the inverse of the thermally averaged cross section, which in turn scales approximately as the inverse of the neutralino mass squared. As a result the minimum relic abundance will increase quadratically with the mass of the neutralino. Co-annihilation with light stops is expected to add a few more points (below the "quadratic" limit) when there is a large fine-tuning between the neutralino and the stop mass. However, the stop and neutralino self-annihilation cross sections both decrease with the mass of these particles and an increase in the fine tuning becomes less and less effective in compensating for the lack of efficiency of the co-annihilation process when the neutralino mass increases. Besides, these points become more difficult to find by the MCMC as they require smaller variance (i.e. more dedicated searches).

Figure 6.8 is the posterior distribution for the mass of the neutralino. The "quadratic" limit can be seen clearly here as well as the two peaks corresponding to the main co-annihilation regions.

Figure 6.9 shows the composition of the neutralino in terms of the weak eigenstates. The compositions of the higher mass neutralinos is more varied than the lower mass states. For points whose freeze-out annihilation is dominated by s-channel Higgs processes, the Higgsino component of these neutralinos can be much larger (even dominating the composition) than that for neutralino DM with masses below 100GeV. The chargino co-annihilation region is split into

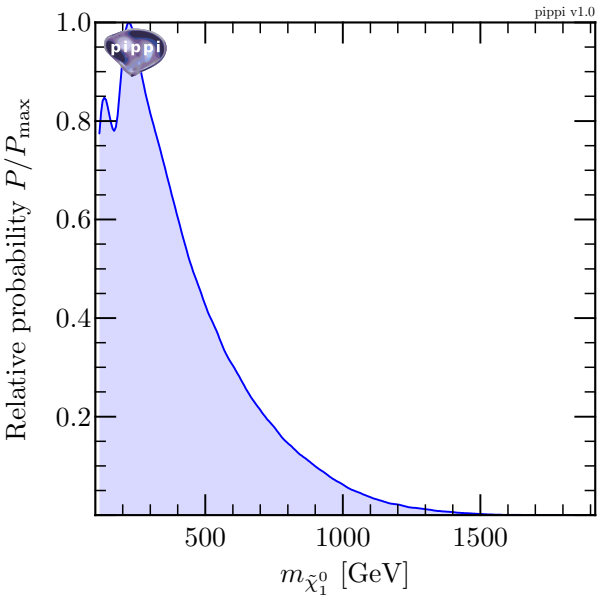

Figure 6.9: Marginalised posterior distribution for the mass of the lightest neutralino for scan B

two branches in the lower branch the composition is dominated by the Wino component and the degeneracy of the chargino and neutralino is driven by the Wino mass parameter. In the upper branch the composition is a mixture of the two Higgsino states and the co-annihilating chargino is Higgsino dominated. In terms of the relic abundance the Wino dominated neutralino annihilates with greater efficiency and extends to smaller values of $\Omega_{FO}h^2$ as well as lighter neutralinos extending down to the boundary at 100GeV while the Higgsino dominated neutralino appears only for $m_{\tilde{\chi}_1^0} > 200$GeV.

Figure 6.10 shows the posterior distributions for SUSY input parameters for scan B. In contrast to scan A M_1 is now pushed to higher values and the lightest neutralino has almost zero Bino component. M_2 now tracks the neutralino mass for the Wino dominated co-annihilation region while μ has a large peak towards smaller masses corresponding to the Higgsino dominated co-annihilation region. The rest of the Higgs sector parameters also differ from scan A with m_{A^0} pushed towards higher masses by the direct searches but also in step with the rising neutralino mass to allow for some resonant annihilation. $\tan\beta$ favours larger values in this region, which is allowed by the Higgs searches as the mass of the pseudo-scalar increases. Squark co-annihilation leads to $m_{\tilde{q}_{1,2}}$ being pushed towards 1500GeV although the chargino co-annihilation regions dominate over squark co-annihilation so this effect is small and $m_{\tilde{q}_{1,2}}$ is pushed towards its maximum value in those regions.

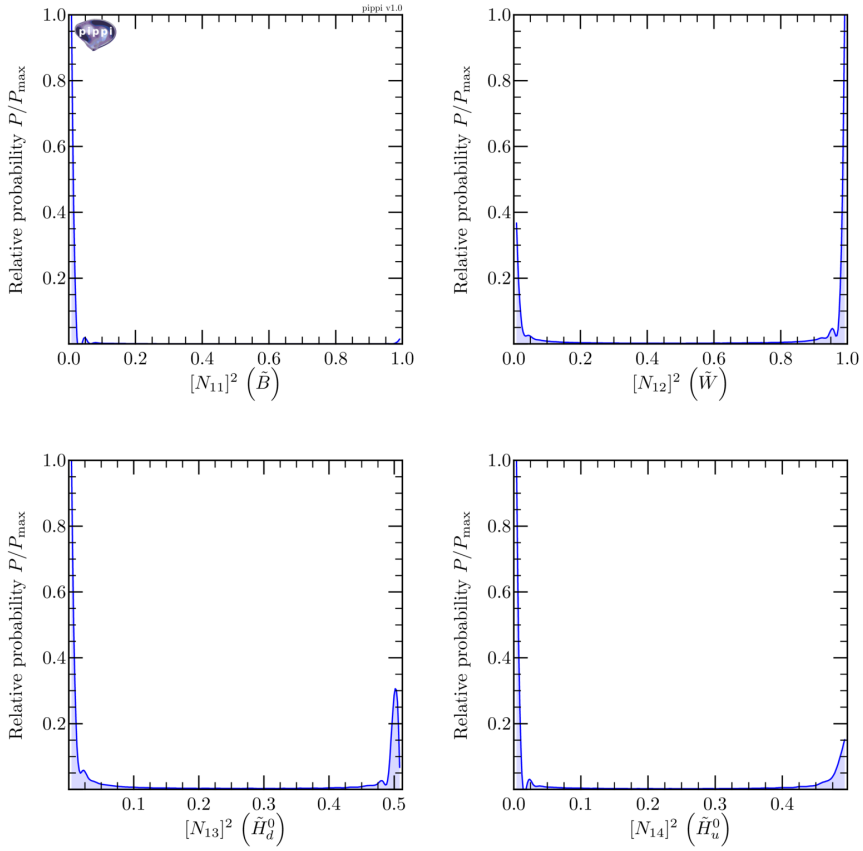

Figure 6.10: Marginalised posterior distributions of the composition of the lightest neutralino in terms of the Gaugino and Higgsino components for $m_{\tilde{\chi}_1^0} > 100$GeV.

6.8 DM regeneration in the light of FERMI-LAT and XENON100 limits

To examine the impact of a possible regeneration mechanism we apply limits arising in direct and indirect detection experiments to the points found by the MCMC. We do so in two cases. The first where there is no regeneration and the DM density is set by the value determined by freeze-out. The second where regeneration of the DM density has taken place after freeze-out and has been regenerated to the WMAP observed value. The limits for direct and indirect detection are applied as 95% confidence level exclusions to the points found by the MCMC after the scans have completed rather than including these limits in the likelihood calculations. This allows the two scenarios to be compared directly using the same set of points.

We look at the effect of regeneration in the planes $(\sigma_{\rm SI}, m_{\tilde{\chi}_1^0})$, $(\sigma_{\rm SI}, \Omega_{\rm FO}h^2)$, $(\Phi_{\rm PP}, m_{\tilde{\chi}_1^0})$ and

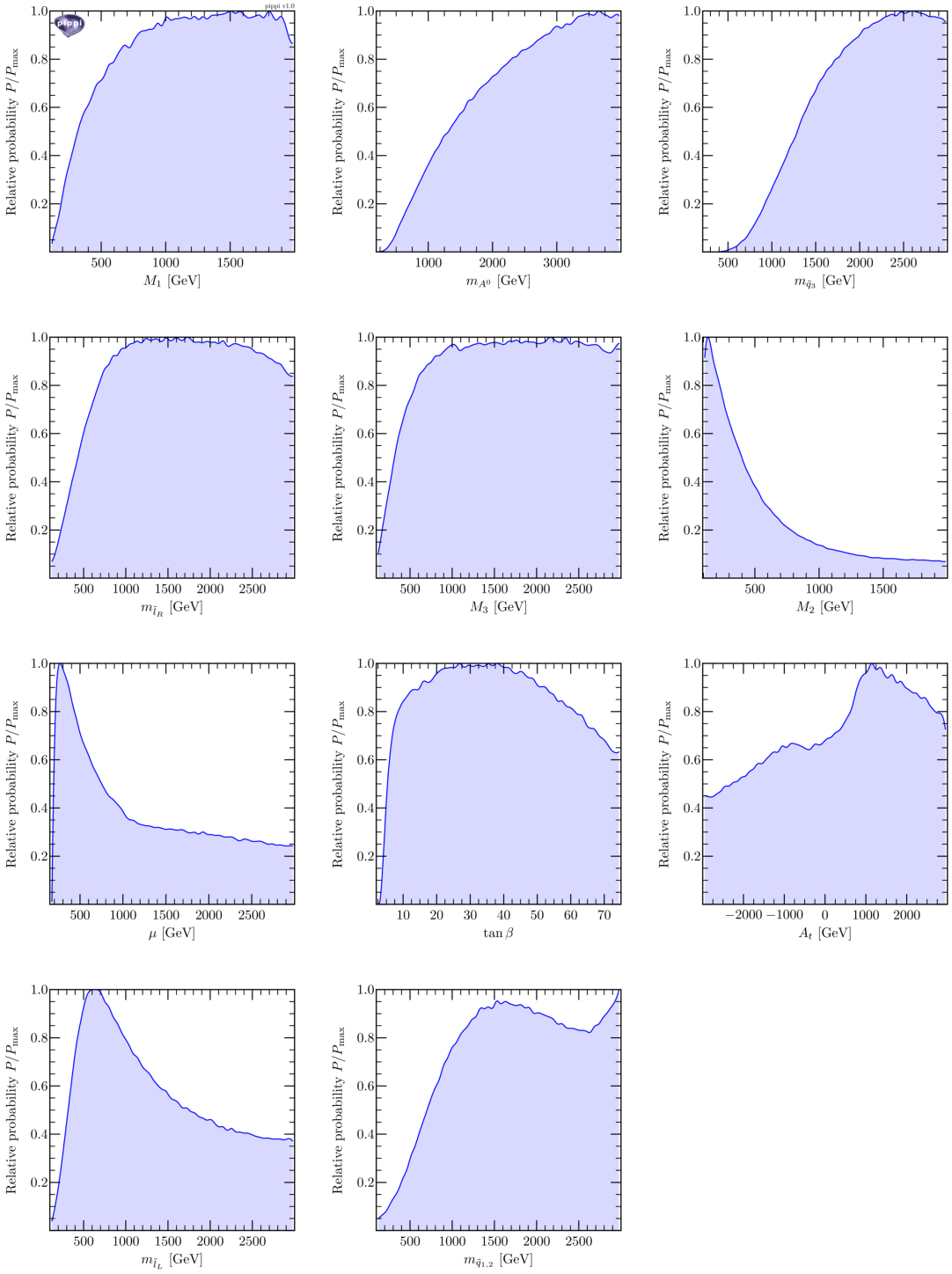

Figure 6.11: Marginalised posterior distributions for the SUSY input parameters for $m_{\tilde{\chi}_1^0} > 100$GeV.

(Φ_{PP}, σ_{SI}), where σ_{SI} is the spin-independent elastic scattering rate, $\Omega_{FO}h^2$ is the relic abundance generated by freeze-out only and Φ_{PP}, which encodes the "particle physics input" to the total

flux of gamma rays from annihilating DM in the dSphs. The quantity Φ_{PP} is defined as

$$\Phi_{PP} = \frac{\langle \sigma v \rangle}{8\pi m^2_{\tilde{\chi}^0_1}} \int_{E_0}^{E_{max}} \frac{dN}{dE} dE, \tag{6.34}$$

where $\langle \sigma v \rangle$ is the thermally averaged cross section for DM annihilation, E_0 is the minimum threshold energy considered, E_{max} is the maximum photon energy the limit is sensitive to and $\frac{dN}{dE}$ is the gamma ray spectrum averaged over all of the different annihilation channels. Neglecting propagation the expected flux of gamma rays from a given source reads as

$$\Phi_\gamma = \Phi_{PP} \times J, \tag{6.35}$$

where J is the DM density integrated along the line of sight and over the solid angle and sensitivity of the observation.

An upper limit on the flux and a particular choice of J then set an upper limit on Φ_{PP}. In general the upper limit on the flux depends on assumptions about the spectral shape of the gamma ray source. Choosing the hardest power-law model from [154] gives an upper bound on the photon flux which can be divided by J to give a conservative upper bound of $\Phi_{PP} < 7.5 \times 10^{-30} \mathrm{cm}^3 \mathrm{s}^{-1} \mathrm{GeV}^{-2}$ from observations of the Draco dSph by FERMI-LAT [154]. However, using a combined analysis of several dSphs places a stronger limit of $\Phi_{PP} < 5.0 \times 10^{-30} \mathrm{cm}^3 \mathrm{s}^{-1} \mathrm{GeV}^{-2}$[7]. In this case there is no single limit on the gamma ray flux and corresponding J value, instead the limit on Φ_{PP} is found by Neyman construction [209, 210] where each dSph is weighted by its J value. We use this combined limit in what follows.

For each point found by the MCMC the gamma ray spectrum $\frac{dN}{dE}$ is calculated using micrOMEGAs and integrated from 1 GeV to 100 GeV in order to obtain Φ_{PP}.

In addition to applying constraints from indirect detection, we also apply constraints coming from direct detection experiments. In particular we apply the limits on the spin-independent elastic cross section coming from XENON100 [6]. The spin-independent cross section for each point is calculated automatically in micOMEGAs and we refer the reader to [96] for details. One important point we do note here is that we use the default values for the scalar form factors of the proton and neutron as set in micOMEGAs [96]. In particular we use the default value for the strange quark scalar form factors as given in [96] as $f_s^{n,p} = 0.2594$. It is well known that this is a source of a large uncertainty in direct detection rates, see for example [211, 159, 212]

and can lead to a significant change in the predicted cross sections. Astrophysical uncertainties can also have an impact on the limits applied, see [213, 214] but again we do not allow for these uncertainties.

Finally, for $m_{\tilde{\chi}_1^0} < 50$ GeV, the uncertainties on the exclusion curve, due to the lack of physical knowledge on the energy behaviour of the relative scintillation efficiency, are important. The latter do not appear in [6] because the XENON100 collaboration assumed that the uncertainties on the relative scintillation efficiency can be well modelled by a Gaussian likelihood centred on the $\mathcal{L}_{\rm eff}$ mean value. It was not realised that maximising the global likelihood gives more weight to the mean (but not necessarily the physical) value of $\mathcal{L}_{\rm eff}$ and does not allow the real (physical) uncertainties on $\mathcal{L}_{\rm eff}$ to be taken properly into account [215]. Here we continue to use the exclusion curve obtained in [6] as a guideline to understand the effect of regeneration but a more detailed study would require the implementation of all these sources of uncertainties in the derivation of the direct detection exclusion limit.

In the following subsections we present a series of double panel figures. The plots corresponding to no regeneration (freeze-out only contributions to the DM relic density) are displayed in the left panels. The same points are plotted in the right panels but now with the DM density regenerated to the WMAP observed value. Note that these scenarios are strictly identical in the pairs of plots apart from the DM densities used to calculate the limits. It should be noted that in the calculations for the indirect detection rates, micrOMEGAS [96] uses by default the value of the DM density determined by WMAP [151] not the value predicted by freeze-out, which in the majority of our cases will be below the WMAP value. In order to calculate the gamma ray flux for the under-abundant scenarios, the square of the scaling factor, η, needs to be applied, where $\eta = \Omega_{\rm FO}/\Omega_{\rm WMAP}$. Similarly, for the under-abundant scenarios, the limits on the elastic scattering cross section from direct detection need to be scaled by η.

6.8.1 Scan A: $m_{\tilde{\chi}_1^0} < 100$GeV

In figure 6.11 plots of the spin-independent elastic scattering cross section against neutralino mass are shown for Scan A. In these plots the red points are excluded by the constraints from the FERMI-LAT gamma ray limits from dSphs, yellow points are ruled out by XENON100 direct detection searches, grey points are ruled out by both and the green points are those that survive the constraints applied.

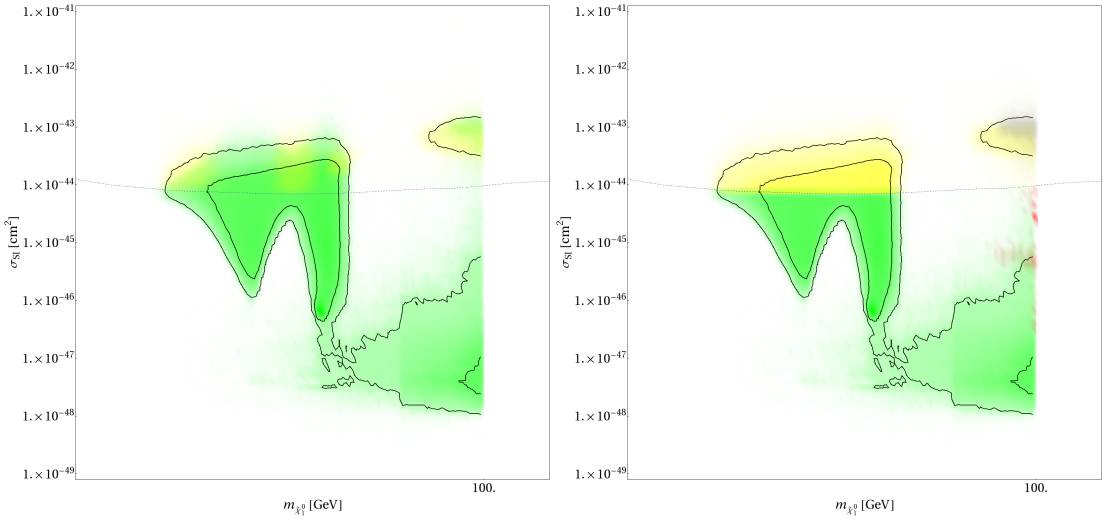

Figure 6.12: Spin-independent cross section versus neutralino mass. The right panel shows the case with the regeneration of the DM relic density to the correct value, the left panel shows the case without. The limit from XENON100 [6] as a limits on the spin-independent cross section of a DM species with the WMAP observed relic density is shown as a blue dashed line. The yellow points are excluded by XENON100, the red points are excluded by indirect detection, grey points are excluded by both and green points survive all constraints applied.

In the left panel of figure 6.11 no regeneration of the DM density is assumed; hence η can be small. The result is that for points with a low freeze-out relic abundance, like those in the Z and h^0 resonance regions, the elastic scattering cross section can be large, i.e. above the XENON100 limit as evaluated for a DM species with the WMAP observed density, and still predict a sufficiently low event rate in a direct detection experiment to evade the exclusion limits.

Also visible is a region around and just below $m_{\tilde{\chi}_1^0} \sim 100$ GeV. Comparing with figure **??**, this region corresponds to the scenarios in which chargino co-annihilations and t-channel exchange diagrams dominate during freeze-out.

If we now assume that the DM density is regenerated after freeze-out to the observed value, all points above the XENON100 limit are now ruled out, as shown in the right panel of figure 6.11. There are a number of points that are still allowed, in particular those that appear in the Z and h^0 resonance regions. The reason for this is that if the neutralino DM can annihilate via an on-shell s-channel resonance, the size of the couplings needed to give a large enough annihilation cross section at freeze-out to reduce the DM relic abundance below the WMAP measured value, can be smaller.

The size of the couplings between the neutralino and both the Z and h^0 is determined by the

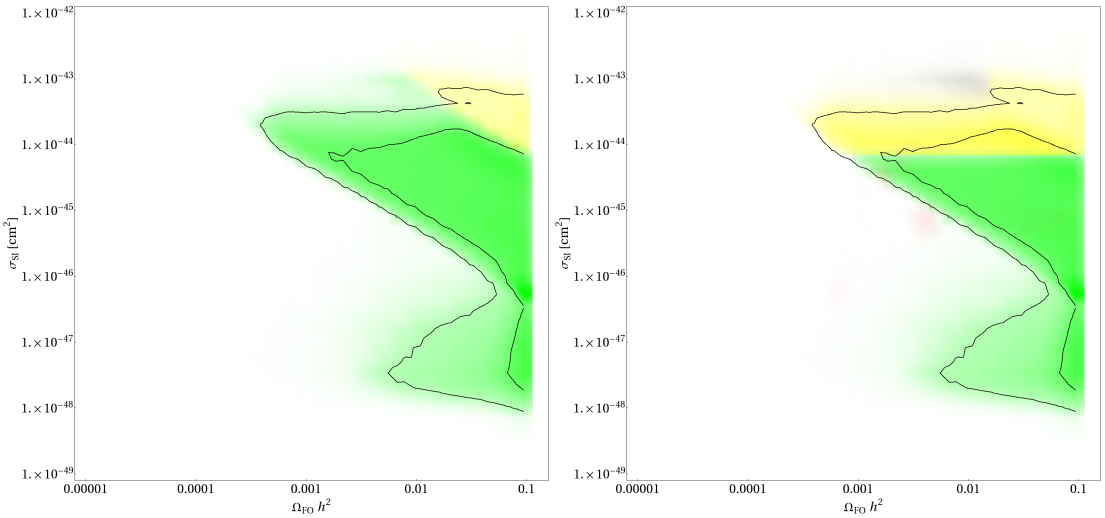

Figure 6.13: Spin-independent cross section versus the neutralino freeze-out relic density for $m_{\tilde{\chi}_1^0} < 100$ GeV. The right panel shows the case with the regeneration of the DM relic density to the correct value, the left panel shows the case without. Colour coding is the same as in figure 6.11.

size of the Higgsino component in the neutralino, which in turn determines the size of the spin-independent elastic scattering cross section. This reduction in the couplings will therefore allow some of the points in the resonance regions to avoid the direct detection limit, provided they correspond to points with close to on-shell freeze-out annihilations. Despite this, a significant number of points are ruled out by direct detection.

In figure 6.12 we present plots of the distribution of points found by the MCMC in the $(\sigma_{SI}, \Omega_{FO}h^2)$ plane. Once again, in the left panel of figure 6.12 the DM relic density is kept at the value predicted by freeze-out and in the right the DM density is assumed to have been regenerated to the observed value but is plotted as a function of the relic density generated by freeze-out for each point.

Different regions of the plots in figure 6.12 can be identified and explained in terms of the connection between the annihilation cross section in the early universe and the spin-independent elastic scattering cross section. There are two main regions of points corresponding to different types of process that dominate the DM annihilation cross section at freeze-out, they are, DM annihilation via s-channel Z or h^0 and DM co-annihilation with another SUSY particle (usually the chargino). With reference to the left panel of figure 6.12, the points corresponding to s-channel processes are roughly contained within the green diagonal band and the yellow points above. The co-annihilation points are those below the green diagonal band.

Moving from small to large freeze-out abundances (left to right in both panels of figure 6.12 but remaining at a constant spin-independent scattering rate, corresponds to moving off-shell for the s-channel annihilation rate at freeze-out. That is, the mass of the neutralino DM is moving away from either $m_Z/2$ or $m_{h^0}/2$. This reduces the overall annihilation rate and therefore increases the freeze-out relic abundance.

Moving down the plots in figure 6.12 we move to smaller spin-independent elastic scattering cross sections with the size of the Higgsino component in the mostly Bino neutralino decreasing, which results in smaller couplings to h^0. The DM s-channel annihilation cross section at freeze-out also decreases with the decreasing couplings and that effect translates into the diagonal slope that can be seen in both plots of figure 6.12. The maximum size of the annihilation cross section at freeze-out, when the s-channel resonance is on shell, decreases with decreasing Higgsino component. Consequently the smallest possible value of the freeze-out relic abundance gets larger as we decrease the spin-independent elastic scattering cross section leading to the diagonal edge clearly visible in the distribution of points.

The second region corresponding to DM co-annihilations in figure 6.12) has generically lower spin-independent scattering cross sections but can have a range of relic abundances. The majority of points in this region correspond to situations where the freeze-out process is unrelated to the spin-independent cross section as is the case for stau co-annihilations and exchange and so no discernible pattern emerges.

In the left hand panel of figure 6.12 the relic abundance is kept at the freeze-out value and the resulting relaxation of the elastic scattering cross section bound is once again apparent due to the reduction of the DM relic density compared to the WMAP observed value. In this scenario the limits from dSphs also play no role due to the suppression in the DM relic density.

In the right hand panel of figure 6.12, with the DM density regenerated to the WMAP observed value, a significant number of points are excluded by direct detection. The effect of the limits from dSphs is quite minimal, only a handful of points (red points in figure 6.12) are ruled out exclusively by this indirect constraint and they are the ones with very low freeze-out relic abundance and hence a large DM annihilation cross section. In particular, these points represent on-shell annihilation through A^0.

Figure 6.12 is particularly interesting as it shows that unless the cross section is very sup-

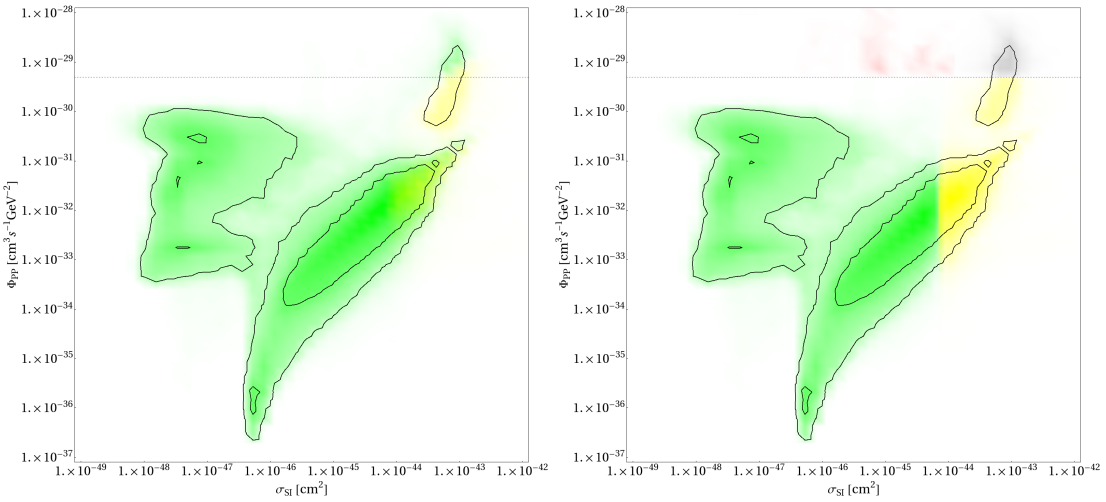

Figure 6.14: Φ_{PP} vs the spin-independent cross section for $m_{\tilde{\chi}_1^0} < 100$ GeV. The right panel shows the case with the regeneration of the DM relic density to the correct value, the left panel shows the case without. The limit on Φ_{PP} shown as a blue dashed line is from the combined analysis of FERMI-LAT observations of dSphs [7]. Colour coding is the same as in figure 6.11.

pressed[2] ($\sigma_{SI} \ll 10^{-44}$cm^2), neutralinos with a freeze-out relic density that exceeds one percent of the WMAP upper limit are the only possible type of DM candidates that can be saved via a regeneration mechanism.

In figure 6.13 the same points are shown on plots in the (Φ_{PP}, σ_{SI}) plane. These plots give a useful demonstration of the relative importance of the two constraints, with the majority of points being ruled out by direct detection. We also see that the co-annhilation region is slightly more sensitive to the indirect detection limit.

Figure 6.14 shows the final result of applying both direct and indirect detection constraints in the ($m_{\tilde{\chi}_1^0}$, $\Omega_{FO}h^2$) plane assuming the regeneration of the DM relic abundance to the WMAP observed value. It can be seen that indirect detection limits do not constrain the resonant Z and h^0 freeze-out annihilation scenarios. Spin-independent direct detection excludes the most under abundant scenarios particularly in the case of resonant annihilation via h^0. The interplay between the spin-independent coupling and resonant effects during freeze-out discussed earlier can again be seen in the thin strip of points excluded around the edges of the Z and h^0 resonance regions. It is clear that points further from the resonance regions require larger couplings in order to reduce the freeze-out relic abundance below the WMAP observed value. This generates a larger

[2]Even with this suppression the number of points in this region is very low.

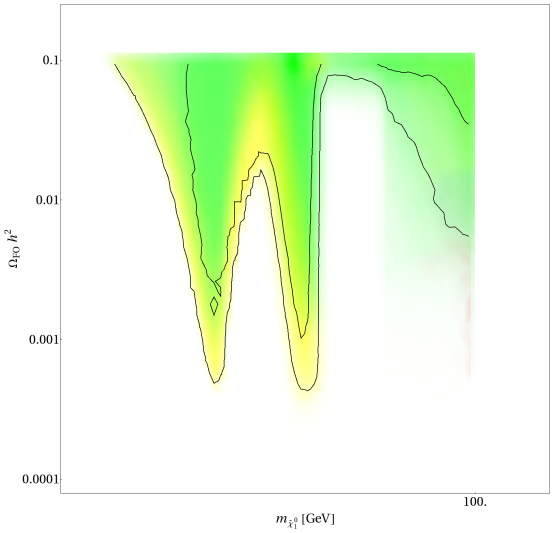

Figure 6.15: A plot of $m_{\tilde{\chi}_1^0}$ versus the freeze-out neutralino relic density where regeneration is assumed. Colour coding is the same as in figure 6.11.

spin-independent cross-section leading to the exclusion of these points by direct detection.

6.8.2 Scan B: $m_{\tilde{\chi}_1^0} > 100$GeV

Turning now to the heavier candidates of Scan B. Figure 6.15 displays the distribution of MCMC points found in the $(\Phi_{PP}, m_{\tilde{\chi}_1^0})$ plane. The colour scheme is identical to the earlier figures with red points ruled out by the dSph limits, yellow points ruled out by the XENON100, grey points ruled out by both and green points are not constrained by either.

The left panel of figure 6.15, with no regeneration, has no points that are ruled out by the dSph limits. As with neutralinos with masses below 100 GeV, the dSph limits plays no significant role in restricting the under-abundant scenarios due to the reduced relic density suppressing the DM annihilation rate into photons.

Regenerating the DM density to the WMAP observed value, the dSph limits now play a significant role in constraining the allowed parameter space as demonstrated in the right panel of figure 6.15. The points ruled out by the dSph limits correspond to the most under-abundant scenarios, which can be seen clearly in figure 6.16, which contains plots of points in the $(\sigma_{SI}, \Omega_{FO}h^2)$ plane. In the case of regeneration (right panel of figure 6.16) the impact of the dSph limits is restricted to the most under-abundant scenarios with abundances up to just below 3% of the WMAP observed value being constrained.

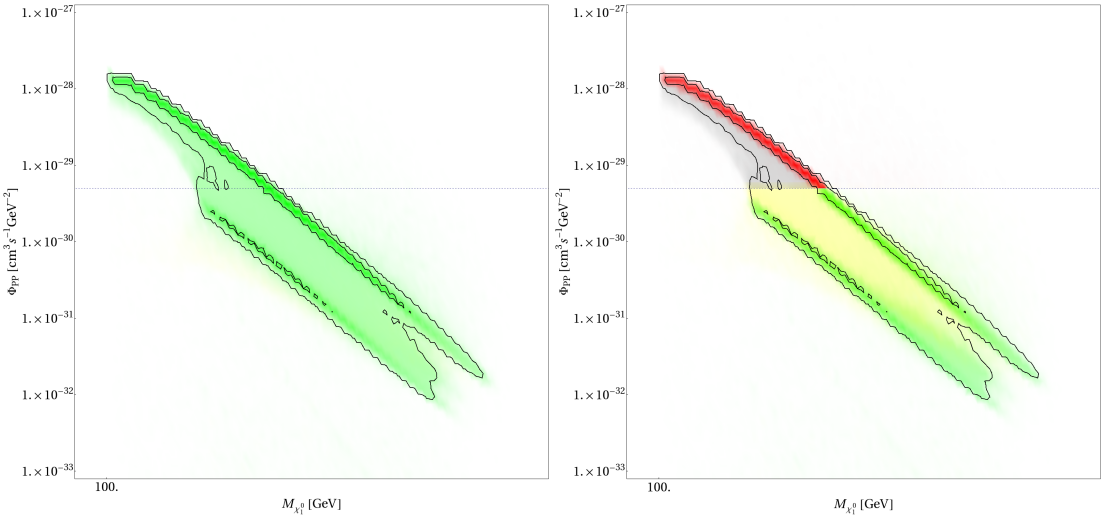

Figure 6.16: Φ_{PP} vs the neutralino mass for Scan B. The limit shown is from FERMI-LAT observations of dSphs [7]. The right panel shows the case with the regeneration of the DM relic density to the correct value, the left panel shows the case without. Colour coding is the same as in figure 6.11.

In addition, figure 6.16 shows that direct detection still plays an important role in constraining neutralino DM with masses above 100 GeV. In particular, it constrains points with a large range of freeze-out abundances and consequently provides a useful complementary constraint to the dSph limits.

6.9 New Results from the LHC

New results from the LHC published after the scans presented here have updated our knowledge of the Higgs sector, the $B_s \to \mu\mu$ branching fraction and have also included various direct searches for supersymmetry. To fully account for these new results the Likelihood function should be changed to include the limits and measurements of the new observables and a new MCMC generated. In the case of the direct SUSY searches and observation of the Higgs boson the implementation of the likelihood function is itself challenging while for the latest $B_s \to \mu\mu$ the latest results can be implemented easily but generating and analysing the new MCMC chain requires considerable effort. In this section we analyse the effect that the latest results from the LHC could have on the model using the existing MCMC chain.

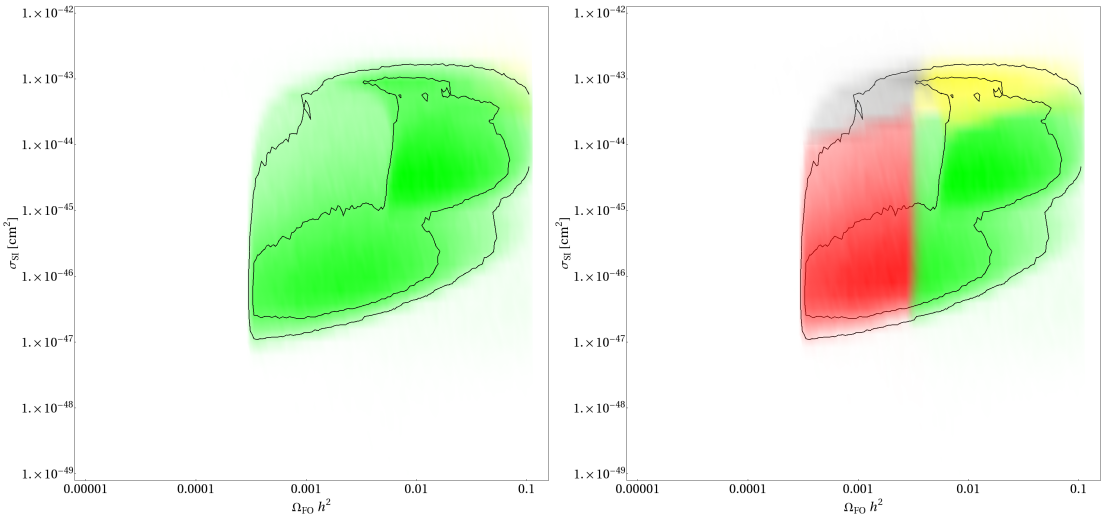

Figure 6.17: Spin-independent cross section versus the neutralino relic density with $m_{\tilde{\chi}_1^0} > 100$ GeV. The right panel shows the case with the regeneration of the DM relic density to the correct value, the left panel shows the case without. Colour coding is the same as in figure 6.11.

6.9.1 Observation of the Higgs boson

The latest results from the search for the Higgs boson at Atlas and CMS [195, 196, 197, 198, 199, 200] have lead to the discovery of a particle compatible with the SM (or MSSM) Higgs boson with mass 127GeV. The impact of these results to the MSSM have been studied [216, 217, 218, 219, 220, 221, 222, 223, 224, 225] and the results are compatible with the MSSM Higgs sector although with a mass heavier than would be preferred in the MSSM in the absence of the data.

Figures 6.19 and 6.18 show the posterior distributions of the Higgs sector for the two scans. For the heavy and charged Higgs particles large masses are favoured which are generally beyond the reach of the Higgs searches. Both scans favour a light Higgs boson which is considerably lighter than is compatible with the current observation. The tail of the posterior distribution is still compatible such that at least some of the regions found in the scan remain viable.

Figure 6.20 shows the posterior distribution of the lightest Higgs boson and relic abundance of neutralinos. For scan A there appears to be some correlation between the Higgs mass and the relic abundance suggesting that dedicated scans in the low neutralino mass region may find that the most under-abundant scenarios are disfavoured by the Higgs result. In scan B there is no indication of correlation between the Higgs mass and the relic abundance suggesting that the

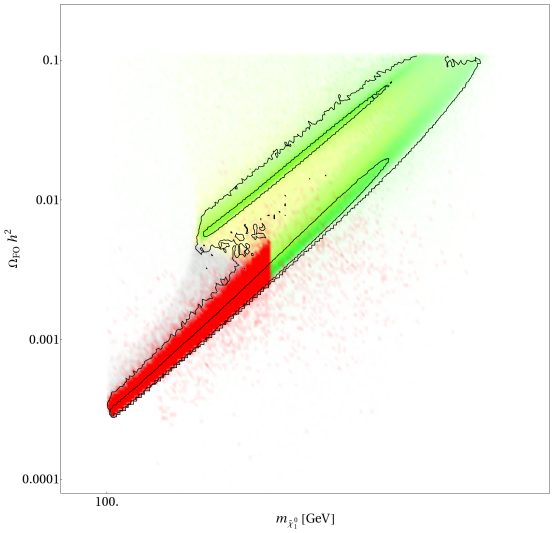

Figure 6.18: Neutralino mass versus the freeze-out neutralino relic density where the regeneration of the DM density is assumed. Colour coding is the same as in figure 6.11.

Higgs mass will not impact the most under-abundant scenarios in this region.

6.9.2 Evidence of $B_s \to \mu\mu$

The LHCb experiment has published evidence for the observation of the rare decay $B_s \to \mu\mu$ with a significance of 3.5σ . The observed branching fraction is [192]

$$\mathrm{BR}(B_s \to \mu^+\mu^-) = (3.2^{+1.5}_{-1.2}) \times 10^{-9}. \tag{6.36}$$

This result is compatible with the SM prediction and thus constrains any contribution to the rate coming from SUSY. The effect of this result on the allowed MSSM parameter space has been extensively investigated [226, 227, 222, 218].

Figure 6.21 shows the posterior distribution of $B_s \to \mu\mu$ and $\Omega_{FO}h^2$ with the observed branching fraction indicated. The observed value is broadly compatible with the points found in the scan. In terms of the relic abundance there is little correlation and so $B_s \to \mu\mu$ will have little effect on the regeneration aspect of the scans.

6.9.3 SUSY searches at the LHC

Both the ATLAS and CMS experiments have performed many searches for supersymmetric particles at the LHC. For many spectrums the strongest limits are obtained by searches for gluino

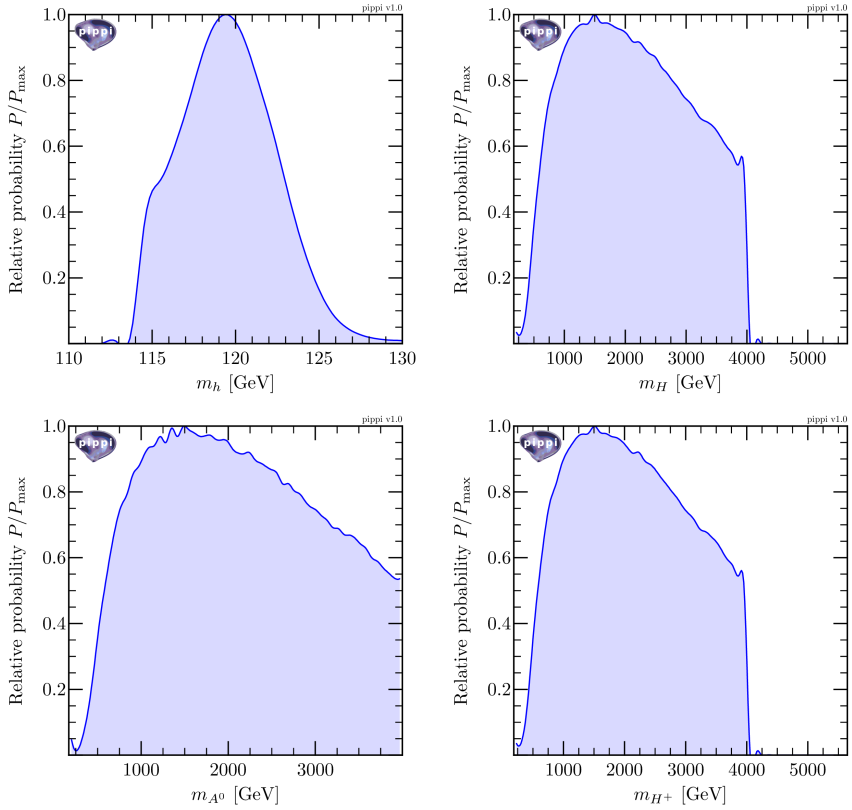

Figure 6.19: Marginalised posterior distributions of the masses of the Higgs sector for scan A $m_{\tilde{\chi}_1^0} <$ 100GeV.

and squark production in final states involving jets and missing energy [228, 229, 230, 231, 232, 233, 234, 235]. These searches are normally analysed in the context of the CMSSM and translated into limits in terms of the input parameters m_0 and $m_{1/2}$. This has allowed the LHC searches to be used in global fits of the CMSSM [216, 220, 219, 218, 227]. In the pMSSM the interpretation of the limits from ATLAS and CMS is more difficult. One method of analysing the effect of the searches on fits in the pMSSM is to perform the scan and then compare a selection of points from the Markov chain directly to the LHC limits by generating collider events and reproducing the event selection cuts and detector effects by fast simulation and then comparing the number of events predicted in the pMSSM to limits obtained at the LHC [125, 126, 127, 128].

Another method of comparing a pMSSM point to the LHC results is via simplified models [236, 237]. Simplified models characterise the new physics as an effective Lagrangian describing the interactions of a small number of the new particles. The model is then specified by only a few masses, cross sections and branching fractions. ATLAS and CMS searches are then interpreted

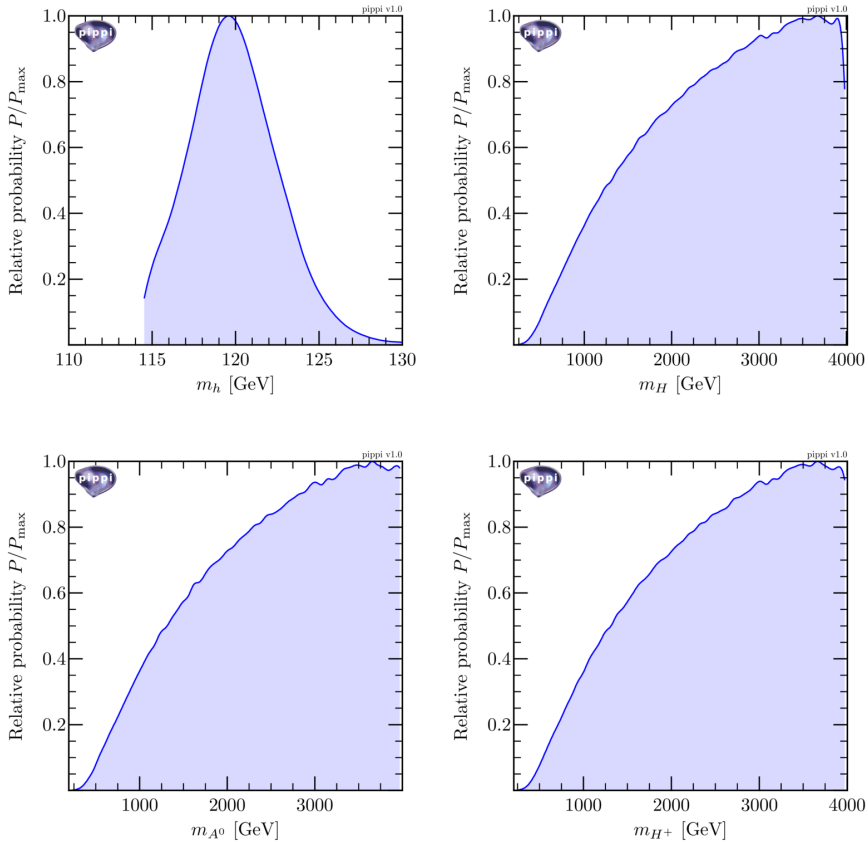

Figure 6.20: Marginalised posterior distributions of the masses of the Higgs sector for scan B $m_{\tilde{\chi}_1^0} >$ 100GeV.

in terms of these simplified models giving a limit on the production cross-section as a function of the masses of the particles that make up the simplified model. These limits can then be applied to the pMSSM when the spectrum of particles in the pMSSM leads to collider signatures that are similar to the simplified model, rather than simulating events only the cross-section needs to be calculated making comparison much faster. This method has been applied to the pMSSM see [221].

A missing energy signature is required for many of the supersymmetry search strategies. Missing energy is expected in SUSY events because the lightest SUSY particle is stable (for R-parity conserving SUSY models) and is normally required to be either the neutralino or sneutrino in order to be a viable DM candidate. When SUSY states are created at the LHC the decay chain will then always terminate at an invisible SUSY particle which escapes the detector undetected. This typically leads to large amounts of missing transverse momentum in the event which is used

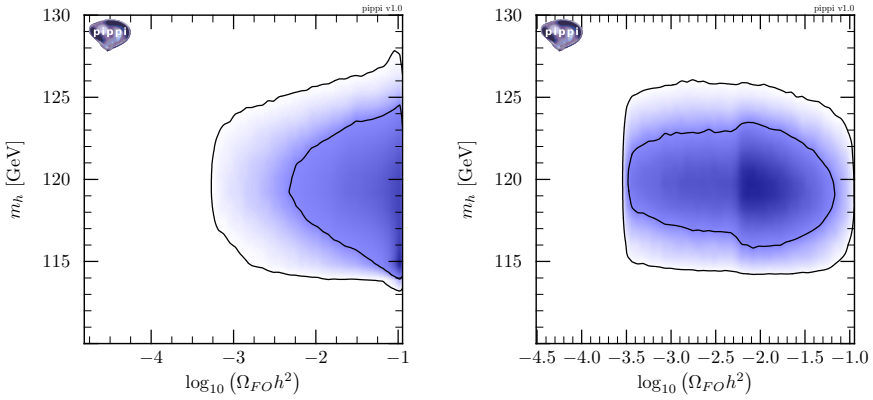

(a) Scan A (b) Scan B

Figure 6.21: 2D Posterior distribution of m_h and $\Omega_{FO}h^2$ for both scans.

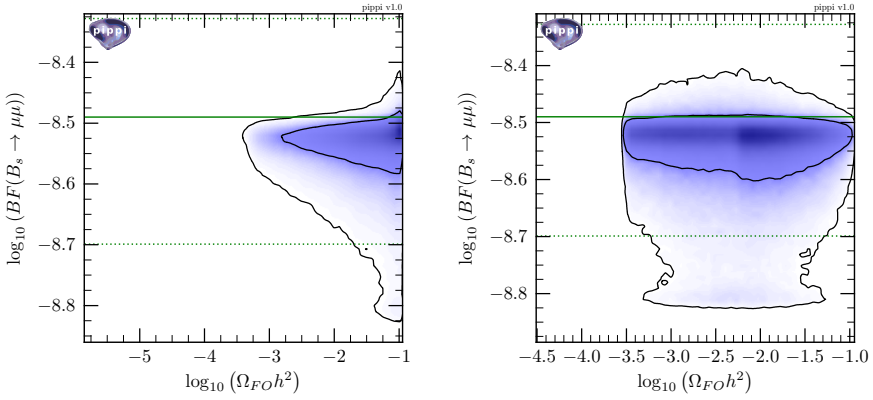

(a) Scan A (b) Scan B

Figure 6.22: 2D Posterior distribution of $B_s \to \mu\mu$ and $\Omega_{FO}h^2$ for both scans. The solid green line indicates the observed value of $B_s \to \mu\mu$ and the dotted lines indicate the experimental uncertainty.

to discriminate SUSY events from the standard model background. This has the consequence that when the SUSY spectrum is sufficiently compressed with a small mass-splitting between the LSP and the produced SUSY particles then momentum carried by the visible decay products will be small and leading to softer leptons and jets which will not pass the cuts. For this reason typical SUSY searches that make cuts on missing energy and hard jets or leptons rapidly lose sensitivity as the masses of the LSP and NLSP become degenerate. Conversely theses searches are at their most sensitive when the approximation that the LSP is massless compared to the other SUSY particles can be made.

To compare the points found by our MCMC to the LHC searches we can consider the latest limits from ATLAS on the masses of SUSY particles based on simplified models. For the gluino and squarks we use the limit coming from the zero lepton jets plus missing transverse energy final state [238]. This represents a very conservative limit particularly for the case of squark and gluino co-annihilation points where a search relying on large amounts missing energy will have poor sensitivity. In the case of limits on the stop mass we can consider the search with the final state of 6 jets including 2 b-jets and missing energy [239]. Where again this limit will be weakened considerably if the stop and neutralino are close in mass. Finally we consider the limit on the chargino in the case where the other SUSY particles except the neutralino and chargino are decoupled. Searches for direct chargino production are typically less sensitive than searches for the production of coloured states due to the smaller cross-section to produce the weakly interacting chargino compared to the strongly interacting squarks and gluinos. However if the coloured states are beyond the reach of the squark and gluino searches then chargino searches can become relevant. We take the limit on direct chargino production coming from the 3-lepton + missing energy signal where a degenerate chargino and χ_2^0 are produced [240]. Again this limit will not be relevant when the mass splitting between chargino and neutralino becomes very small as is the case for the chargino co-annihilation regions.

To asses the impact of these limits on the regeneration scenario we plot the 2D posterior distributions of the sparticle mass and freeze-out relic abundance of the neutralino. Figure 6.22 shows the results for scan A while figure 6.23 shows the results for scan B. In these plots the lightest sparticle of the type indicated is used to plot the distribution. The red line indicates the ATLAS mass limit on the sparticle and points below the line may be ruled out by the LHC searches. It is important to recall that the assumptions under which the limits are made will not

in general be satisfied by the spectrum present in the pMSSM and that this is will weaken the limits.

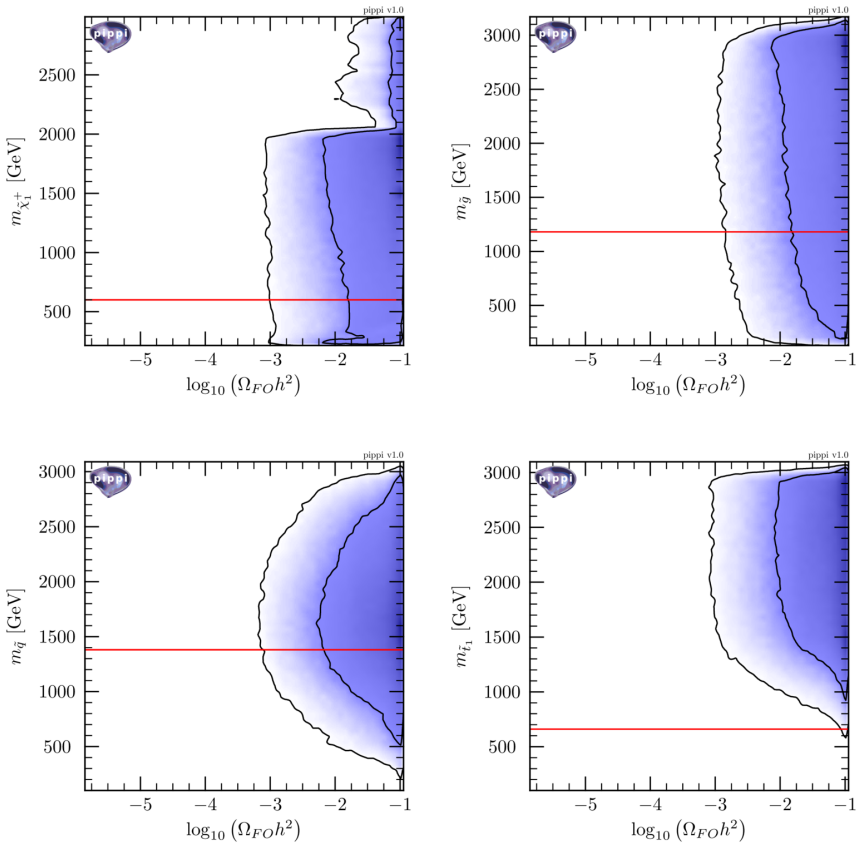

Figure 6.23: Marginalised posterior distributions of the masses of the sparticles and $\Omega_{FO}h^2$ for scan A $m_{\tilde{\chi}_1^0} < 100$GeV. The red line indicates the ATLAS mass limit on the lightest sparticle of that type under the assumptions stated.

From the plots it can be seen that the correlation between sparticle masses and neutralino relic abundance does not tend to rule out under abundant scenarios. Applying the limits will push up the sparticle masses but points with a small relic abundance will still be available. In general the limits are not very constraining in scan B where a heavier mass spectrum is already favoured. Applied naively the limit on chargino mass would eliminate the chargino co-annihilation regions in scan A and the lower mass chargino co-annihilation regions in scan B however since these regions are characterised by a small mass splitting between the chargino and neutralino such that co-annihilation is effective the limits are likely to be weakened in this region requiring a dedicated study.

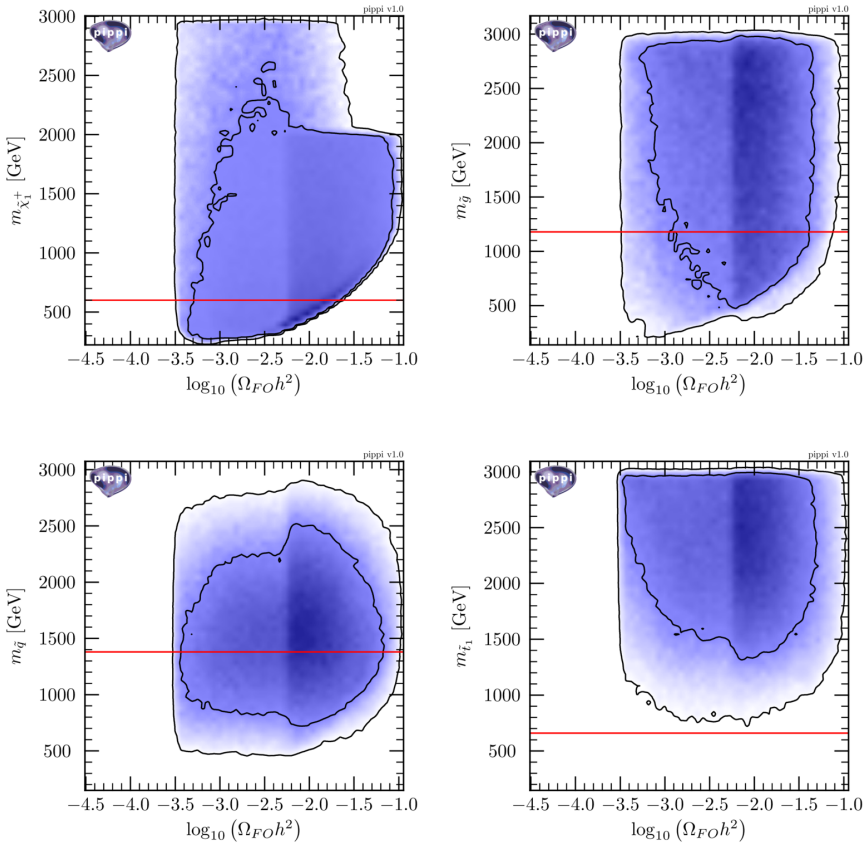

Figure 6.24: Marginalised posterior distributions of the masses of the sparticles and $\Omega_{FO}h^2$ for scan B $m_{\tilde{\chi}_1^0} > 100$GeV. The red line indicates the ATLAS mass limit on the lightest sparticle of that type under the assumptions stated.

6.10 Conclusion

Using a familiar framework (neutralinos in the MSSM), we have investigated the configurations for which the expected freeze-out relic density could be much smaller than the upper limit of the WMAP observed value. We have found many configurations where $\Omega_{\rm FO}h^2$ could be down to $10^{-5}\Omega_{\rm WMAP}h^2$. In particular, for low neutralino masses, resonant annihilation through Higgs or Z boson appear to be very efficient.

However, we have demonstrated that if a mechanism is capable of regenerating the candidate DM number density to the present observed value, the combination of FERMI-LAT gamma ray observations in dSph and DM direct detection limits from XENON100 make such scenarios difficult to realise, thereby suggesting that candidates with very small freeze-out relic density (less than a percent of the WMAP upper limit) cannot be the sole explanation to the DM problem

even if one assumes that after freeze-out the DM density is regenerated.

One of the central points of this study is the link between the DM annihilation process at freeze-out and the predicted direct detection rate. Essentially, as is already known in the MSSM scenario a light Higgs or Z exchange is needed in order for light neutralinos to become extremely under-abundant. Small neutralino freeze-out abundances correspond to scenarios which are close to the Higgs resonance and thus typically predict large neutralino-nucleon elastic scattering cross sections since one is close to the minimal Higgs mass value that is possible in the MSSM (given collider constraints) and the neutralino-Higgs couplings are constrained by the requirement of a large annihilation cross section which is itself bounded by the Higgs decay width[3].

In scenarios without regeneration, such a large neutralino-nucleon elastic scattering cross section (or large annihilation cross section) is not necessarily excluded. Indeed, the very small freeze-out abundance actually induces a 'η' suppression factor and reduces the elastic scattering rate in nuclear recoil direct detection experiments as well as the indirect detection rate. However in scenarios where one allows regeneration of the relic density to happen, there is no 'η' suppression factor and these scenarios can be ruled out by direct and indirect detection experiments.

The heavy neutralino scenarios which are under-abundant (less than 3% of the observed relic density) also benefit from the 'η' factor suppression if there is no regeneration mechanism involved, so they cannot be ruled out. However, when we assume regeneration, we find that the indirect detection constraint set by the FERMI-LAT experiment actually rule out these candidates and complement the constraint set by XENON100.

Our conclusion is based on the combination of astrophysics, astroparticle and particle physics data. Any more constraints in, at least, one of these fields will enable stronger constraints to be set, thus restricting the types of mechanisms that could give the DM the relic density it has today.

[3]For scenarios which lie very close to the resonance the couplings cannot be arbitrarily small since the decay width will dominate over a very small mass degeneracy between the Higgs and the neutralino.

Chapter 7

Dark matter and black holes

7.1 Introduction

Intermediate mass black holes may be associated with a density spike of dark matter [241] that can provide a enhancement in the annihilation of DM particles to gamma rays or neutrinos. The indirect detection of DM through its annihilations could provide information about the nature of the DM in the galaxy and its distribution. The physics of particle collisions in the gravitational field of a black hole has been extensively studied, see e.g. [242] [8] [243] [244] [245] [246] [247] [248]. In the case of rotating black holes collisions between DM particles can yield large centre of mass energies [8] and inside the ergosphere particles produced via the Penrose process could carry high energies [245].

The collision of DM around a black hole could therefore provide an opportunity to probe the nature of the DM in the universe and its distribution and also provide a window to high energy physics not accessible to particle colliders. It is important then to study both the properties of the collision that can occur close to a black hole and also the properties of the flux of radiation that is produced by the collisions that may be detected. The main results of this chapter were originally presented as [249].

7.2 Kerr black holes as particle accelerators

In order to investigate the possibility of using rotating black holes as particle accelerators we will first reproduce the work of [8] by calculating the center of mass energy available to colliding

particles close to the horizon. The general set-up is that of two particles in free fall approaching the horizon of the black hole. If the particles have different angular momentum, l, then they may collide. To an observer at the horizon the particles will appear blue shifted as they accelerate towards the black hole however the center of mass frame of the two particles is itself a free falling frame and the energy should be bounded.

The center of mass energy for two particles of mass m_0 colliding in a curved background has the form[8],

$$E_{cm} = m_0\sqrt{2}\sqrt{1 - g_{\nu\mu}u^{\nu}_{(1)}u^{\mu}_{(2)}}, \tag{7.1}$$

where $u^{\nu}_{(1)}$ and $u^{\mu}_{(2)}$ are the 4-velocities of the particles. Eq. 7.1 can be derived from the special relativity case as follows [8]. First we introduce the set of orthonormal vectors that define a local frame in which special relativity holds [250]. The physical quantities in the coordinate basis described by the metric are projected onto this set of basis vectors. The physical quantities in a local observers frame are obtained and the standard formula from special relativity for the center of mass energy can be used. The basis vectors at a given point $\hat{e}_a$ are defined such that $\hat{e}_a.\hat{e}_b = \Sigma_{ab}$. Translation between the coordinate basis $\vec{e}_\mu$ and the orthonormal frame is carried out by an invertible matrix e^a_μ such that $\vec{e}_\mu = e^a_\mu \hat{e}_a$. The local flat metric is then related to the curved metric by $g_{\mu\nu} = e^a_\mu e^b_\nu \Sigma_{ab}$ so that for a given point in space time if the metric is known then e^a_μ will be uniquely defined. The frames of physical observers can then be obtained by a Lorentz transformation from the local frame. Using the matrix e^a_μ to transform from the coordinate basis to the orthonormal then allows E_{cm} to the calculated using Eq. 7.1 using Σ_{ab} as the metric.

The 4-velocities are constructed from the trajectories of the particles by $u^\mu = \frac{dx^\mu}{d\tau}$. The 3-velocity of the particle in the orthonormal frame is then [8],

$$v^{(i)} = \frac{e^{(i)}_\mu u^\mu}{e^{(0)}_\mu u_\mu}. \tag{7.2}$$

Since special relativity holds in this frame the 4-momentum of the particle can be written using the standard formula.

$$p^a = m_0\gamma(v)\left(1, v^{(i)}\right), \tag{7.3}$$

where $\gamma(v)$ is the usual Lorentz factor $\left(1-v^2\right)^{-\frac{1}{2}}$. This method can be applied to any curved metric $g_{\mu\nu}$ which is stationary, axisymmetric and asymptotically flat such that the orthonormal

basis can be defined [250].

We now apply this to the Schwarzschild and Kerr metrics. The Schwarzschild metric describes a non-rotating black hole and is defined as.

$$ds^2 = -\left(1-\frac{2}{r}\right)dt^2\left(1-\frac{2}{r}\right)^{-1}dr^2 + r^2\left(d\theta^2+\sin^2\theta d\phi^2\right). \tag{7.4}$$

The geodesic equation gives the solutions

$$\begin{aligned}\frac{dt}{d\tau} &= \left(1-\frac{2}{r}\right)^{-1},\\ \frac{dr}{d\tau} &= -\frac{1}{r^2}\sqrt{r(2r^2+2l^2-rl^2)},\\ \frac{d\phi}{d\tau} &= \frac{l}{r^2}.\end{aligned} \tag{7.5}$$

The resulting collision energy is given by [242]

$$\frac{1}{2m_0^2}\left(E_{cm}^{Schw}\right)^2 = \frac{2r^2(r-1)-l_1l_2(r-2)-\sqrt{2r^2-l_1^2(r-2)}\sqrt{2r^2-l_2^2(r-2)}}{r^2(r-2)}, \tag{7.6}$$

where l_1 and l_2 are the angular momenta of the colliding particles. There appears to be a pole at $r=2$ so that the energy would diverge at the horizon however the numerator also disappears at the horizon. Taking the limit correctly the collision energy is found to be.

$$E_{cm}^{Schw}(r\to 2) = \frac{m_0}{2}\sqrt{(l_2-l_1)^2+16}. \tag{7.7}$$

The energy is maximized by taking l_1 and l_2 to have opposite maximum values. For the collision to occur both particles must reach the horizon the maximal values of l for this to occur at $l=\pm 4$ giving a value of $E_{cm}^{Schw} = 2\sqrt{5}m_0$ as found in [242].

The Kerr metric describing a rotating black hole can be written in in Boyer-Lindquist coordinates by the metric[250].

$$\begin{aligned}ds^2 = &-\left(1-\frac{2r}{\Sigma}\right)dt^2 - \left(\frac{4ar\sin^2\theta}{\Sigma}\right)dtd\varphi\\ &+\left(\frac{\Sigma}{\Delta}\right)dr^2+\Sigma d\theta^2+\left(r^2+a^2+\frac{2a^2r\sin^2\theta}{\Sigma}\right)\sin^2\theta d\varphi^2,\end{aligned} \tag{7.8}$$

where the mass of the black hole has been set to 1. a is the angular momentum of the black hole per unit mass so that $0 \leq a \leq 1$. The functions Δ, Σ, A have the following definitions.

$$\begin{aligned} \Delta &\equiv r^2 - 2r + a^2, \\ \Sigma &\equiv r^2 + a^2 \cos^2\theta, \\ A &\equiv \left(r^2 + a^2\right)^2 - a^2 \Delta \sin^2\theta. \end{aligned} \tag{7.9}$$

The Kerr metric has two boundaries, the event horizon, r_+, which is located at $\Delta = 0$ and the outer boundary of the ergosphere located at $\Sigma - 2r = 0$. For a maximally rotating black hole ($a = 1$) these occur at $r = 1$ for the event horizon and $r = 1 + \sqrt{1 - \cos^2\theta}$.

Orbits of particles in the Kerr metric conserve three constants of motion. These can be written in terms of the particles 4-momentum as [250]

$$\begin{aligned} E &= -p_t, \\ L &= p_\phi, \\ Q &= p_\theta^2 + cos^2\theta \left(a^2 \left(\mu^2 - p_t^2\right) + \frac{p_\phi^2}{sin^2\theta} \right), \end{aligned} \tag{7.10}$$

where E is the total energy of the particle and L is the angular momentum parallel to the axis of symmetry of the black hole. It can be seen from the third line that if $Q = 0$ and the particle is initially in the equatorial plane then $p_\theta = 0$ and will remain so. This makes it simple to construct orbits that are constrained to the equatorial plane. Q is equal to the total angular momentum squared when $a = 0$.

The trajectories of particles are given by [250],

$$\Sigma \frac{dr}{d\lambda} = \pm\sqrt{V_r}, \tag{7.11}$$

$$\Sigma \frac{d\theta}{d\lambda} = \pm\sqrt{V_\theta}, \tag{7.12}$$

$$\Sigma \frac{d\phi}{d\lambda} = -\left(aE - \frac{L}{\sin^2\theta} \right) + \frac{aT}{\Delta}, \tag{7.13}$$

$$\Sigma \frac{dt}{d\lambda} = -a\left(aE\sin^2\theta - L\right) + \frac{\left(r^2 + a^2\right)T}{\Delta}, \tag{7.14}$$

where λ is related to the particle's proper time by $\lambda = \tau/\mu$, when $\mu \to 0$ λ becomes an affine

parameter. The functions V_r, V_θ and T are defined as.

$$\begin{aligned} T &\equiv E\left(r^2+a^2\right)-La, \\ V_r &\equiv T^2-\Delta\left(\mu^2 r^2+(L-aE)^2+Q\right), \\ V_\theta &\equiv Q-\cos^2\theta\left(a^2\left(\mu^2-E^2\right)+\frac{L^2}{\sin^2\theta}\right). \end{aligned} \tag{7.15}$$

Consider two particles constrained to the equatorial plane with $Q=0$ and angular momenta l_1 and l_2, initially at rest at infinity with total energies $E_1=E_2=m_0$. The collision energy is found to be [8]

$$\begin{aligned} \left(E_{cm}^{Kerr}\right)^2 = \frac{2m_0^2}{r(r^2-2r+a^2)}\Big(&2a^2(1+r)-2a(l_2+l_1)-l_2l_1(-2+r)+2(-1+r)r^2 \\ &-\sqrt{2(a-l_2)^2-l_2^2r+2r^2}\sqrt{2(a-l_1)^2-l_1^2r+2r^2}\Big). \end{aligned} \tag{7.16}$$

The denominator appears to vanish at the horizon when $r^2-2r+a^2=0$ as in the Schwarzschild case however the numerator vanishes as well and the limit is finite. This is not true when $a=1$ however, in this case the limit as $r\to r_+$ is [8]

$$E_{cm}^{Kerr}(r\to r_+)=\sqrt{2}m_0\sqrt{\frac{l_2-2}{l_1-2}+\frac{l_1-2}{l_2-2}}. \quad (a=1) \tag{7.17}$$

Written like this it is clear that if either l_1 or l_2 is equal to 2 then the center of mass energy with diverge at the horizon. $l=2$ corresponds to the critical angular momentum however only one of the particles needs to have maximal angular momenta for the collision energy to blow up. Figure 7.1[8] shows the behaviour of the center of mass energy for different values of l_1. When $l_1=2$ the energy diverges at the horizon while for other values of l_1 the collision energy remains finite.

Such a result suggests that the region around rotating black holes could contain extremely energetic collisions. Particles produced in the collisions that escape the black hole will necessarily be red shifted however these could still function as a probe of the high energy scale physics.

This result has attracted much discussion as to whether a physical black hole would ever produce such collisions and if the resulting radiation could be observed [243, 244, 9, 245, 249, 251,

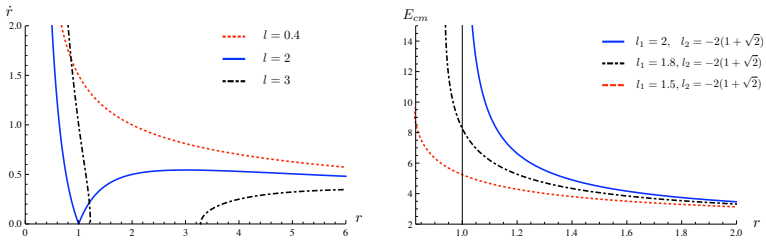

(a) (b)

Figure 7.1: From [8]. For a Kerr Black hole with $a = 1$ (a) shows the variation of $\dot{r}$ with radius for three different values of angular momentum $l = 0.4, 2$ and 3. (b) shows the variation of E_{cm} with radius for three combinations of l_1 and l_2. For $l_1 = 2$ we see that E_{cm} blows up at the horizon.

252, 253, 254]. As well as numerous calculations of related effects and the energy associated with collisions in the non-extremal case, particles in different orbits and multiple scatterings [255, 247, 248, 256, 257, 258, 259, 260, 261, 262, 263, 264]. As well as calculations of the center of mass energy associated with different black hole geometries [246, 265, 266, 267]. The possibility of extracting energy from black hole in the collisions has also been considered [268, 269].

7.3 Calculating the escape fraction

In the previous section we reviewed the calculation of the collision energy of particles falling into a rotating black hole. We now address the question of the possibility of observing the particles produced in these collisions. In particular we want to find out if particles produced close to the black hole horizon can escape to infinity so that we are able to observe them and what the energy spectrum of the escaping particles will be. To do this it is useful to define the escape fraction as the probability that the products of the annihilation will escape to infinity. The escape fraction will depend on the coordinates of the collision as well as the momenta of the colliding particles. As a function of r escape fraction should tend towards zero at the horizon where all the products of the collisions will be captured by the black hole and rise to one at infinity.

The collisions that we will consider are annihilations of pairs of DM particles to a pair of massless particles either photons or neutrinos (Although neutrinos have mass they are light enough to be considered massless for the purposes here.). Massive charged particles such as protons or electrons could also be produced but would be diffused by magnetic fields while

photons or neutrinos would point back to the location of the black hole and appear as a point source in the sky. Annihilation to a pair of massless particles also makes the kinematics in the center of mass frame particularly simple since each particle will carry exactly half the center of mass energy and the particles will be emitted back to back.

To understand how the escape fraction can be constructed we review the case of the Schwarzschild black hole. The derivation of the escape condition for a massless particle in the Schwarzschild metric can be found in [270]. The conserved quantities for a particle in the Schwarzschild metric are energy $E \equiv -p_0$ and angular momentum $L \equiv p_\phi$. For a particle of mass μ the conserved quantities can be recast as the energy and angular momentum per unit mass defined as.

$$\begin{aligned} \tilde{E} &\equiv \frac{E}{\mu}, \\ \tilde{L} &\equiv \frac{L}{\mu}. \end{aligned} \tag{7.18}$$

The equations of motion can be written in terms of these quantities as

$$\begin{aligned} \left(\frac{dr}{d\tau}\right)^2 &= \tilde{E}^2 - \tilde{V}^2(r), \\ \tilde{V}(r) &= \left(\left(1-\frac{2M}{r}\right)\left(1+\frac{\tilde{L}^2}{r^2}\right)\right)^{1/2}, \\ \frac{d\phi}{d\tau} &= \frac{\tilde{L}}{r^2}, \end{aligned} \tag{7.19}$$

where τ is the proper time. Combining these gives the shape of the orbit as the variation of r with ϕ.

$$\left(\frac{\tilde{L}}{r^2}\frac{dr}{d\phi}\right)^2 + \tilde{V}^2(r) = \tilde{E}^2. \tag{7.20}$$

Which defines the trajectory of the particle. For a massless particle the quantities $\tilde{L}$ and $\tilde{E}$ are not well defined instead it is useful to define the impact parameter b as the ratio of the angular to linear momentum.

$$b = \frac{L}{\sqrt{E^2-\mu^2}} = \frac{\tilde{L}}{\sqrt{\tilde{E}^2-1}}. \tag{7.21}$$

In the limit that $\mu \to 0$ we have.

$$\lim_{\mu\to 0}\frac{\tilde{L}}{\tilde{E}} = b. \tag{7.22}$$

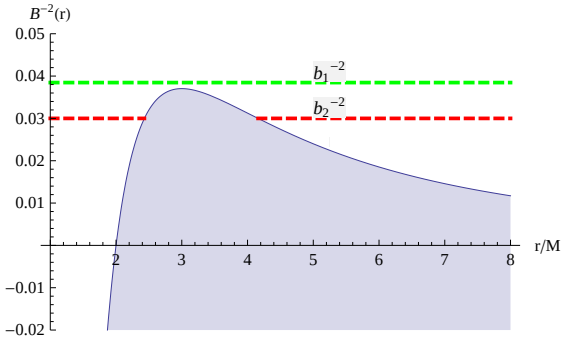

Figure 7.2: Effective potential $B^{-2}(r)$ for the Schwarzchild metric

The equation of motion governing the trajectory for a massless particle can then be rewritten as,

$$\begin{aligned} \left(\frac{1}{r^2}\frac{dr}{d\phi}\right)^2 + B^{-2}(r) &= \frac{1}{b^2}, \\ B^{-2}(r) &\equiv \frac{1-2M/r}{r^2}, \end{aligned} \tag{7.23}$$

where $B^{-2}(r)$ will play the role of an effective potential. We can write the equations of motion in terms of the affine parameter λ without reference to the mass of the particle this gives.

$$\frac{d\phi}{d\lambda} = \frac{L}{r^2}, \frac{dt}{d\lambda} = \frac{E}{1-2M/r}. \tag{7.24}$$

By making the replacement $\lambda \to L\lambda$ the equations of motion take the form.

$$\frac{d\phi}{d\lambda} = \frac{1}{r^2}, \frac{dt}{d\lambda} = \frac{1}{b(1-2M/r)}. \tag{7.25}$$

Which makes clear that the trajectory only depends on the impact parameter b and not E and L independently. For a null geodesic the radial equation is then given by,

$$\left(\frac{dr}{d\lambda}\right)^2 + B^{-2}(r) = b^{-2}. \tag{7.26}$$

The shape of $B^{-2}(r)$ determines the behaviour of the massless particle for a given impact factor. Figure 7.2 shows the effective potential $B^{-2}(r)$ as a function of r. For reference two possible values of the impact parameter are also shown. The behaviour of the particle can be deduced from this plot. For a massless particle with $r < 3M$ it can only escape if it is emitted away from the black hole and b^{-2} is greater than the maximum of the potential barrier $B^{-2}(r)$ as is the case

for b_1 in figure 7.2, if b^{-2} is less than the maximum of $B^{-2}(r)$ then the particle will reach a turning point and be reflected back to the horizon. For a particle at $r > 3M$ if it is emitted away from the black hole it will escape, if it is emitted towards the horizon it will escape only if it is reflected by the potential barrier. To see if a massless particle will escape we just need to know where it is emitted and its impact parameter along with the initial sign of its trajectory in r. By inspection of $B^{-2}(r)$ we see that it has a maximum at $r = 3M$ of $B^{-2}(3M) = 1/27M^2$.

More useful is to write the criteria for escaping in terms of the initial direction of the particle. To do this we define the velocity of the particle relative to the orthonormal frame. Using our previous definition of the 3 velocity of the particle Eq.7.2 and taking the orthonormal basis vectors for the Schwarzschild geometry we get.

$$\begin{aligned} v^{(r)} &= \frac{|g_{rr}|^{1/2}\frac{dr}{d\lambda}}{|g_{00}|^{1/2}\frac{dt}{d\lambda}} = \pm\left(1-\frac{b^2}{B^2}\right)^{1/2}, \\ v^{(\phi)} &= \frac{|g_{\phi\phi}|^{1/2}\frac{d\phi}{d\lambda}}{|g_{00}|^{1/2}\frac{dt}{d\lambda}} = \frac{b}{B}. \end{aligned} \tag{7.27}$$

In this basis special relativity hold and we have $\left(v^{(r)}\right)^2 + \left(v^{(\phi)}\right)^2 = 1$. We define the direction δ as the angle between the direction of travel and the radial direction. Now we recall from figure.7.2 and the definition of $B^{-2}(r)$ that to cross the potential barrier we must have that $b^{-2} > \frac{1}{27M^2}$. Substituting this into the equation for $v^{(\phi)}$ we have the criteria that

$$\left(v^{(\phi)}\right)^2 < \frac{27M^2}{B^2}. \tag{7.28}$$

This can be related to the direction by $\sin\delta = v^{(\phi)}$. This yields the result that a massless particle is able to cross the potential barrier if and only if,

$$\sin\delta < \frac{3\sqrt{3}M}{B(r)}. \tag{7.29}$$

We can now summarize the criteria for a particle to escape the black hole in terms of its direction of emission and radial position. For particles emitted at $r < 3M$ particles emitted towards the black hole, $v^{(r)}$ is negative and the particle will be captured. Particles emitted with $v^{(r)}$ positive will escape if $\sin\delta < \frac{3\sqrt{3}M}{B(r)}$. For particles emitted at $r > 3M$ particles with positive $v^{(r)}$ will always escape. Particles with negative $v^{(r)}$ will only escape if reflected by the potential barrier

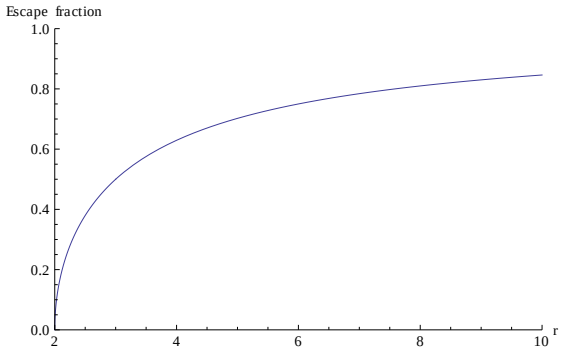

Figure 7.3: Escape fraction for a Schwarzschild black hole in the stationary orthonormal frame. M normalised to 1

i.e if $\sin\delta > \frac{3\sqrt{3}M}{B(r)}$.

This simple set of rules allows the escape fraction for any r to be written down by taking the fraction of the solid angle that satisfies the above criteria for escaping. Figure 7.3 shows the escape fraction as a function of r in the stationary orthonormal frame. The behaviour is as expected with the escape fraction approaching zero at the horizon and tending towards one as the distance from the black hole increases. The escape fraction reaches $1/2$ at $r = 3M$ where the effective potential has its maximum at this point the only allowed values b are larger than the potential barrier and the criteria for escape depends only on the initial sign of $v^{(r)}$.

This method outlines how the escape fraction can be calculated in general. Firstly the equations of motion in the coordinate frame must be found and the solved to get trajectories of the particles. The criteria to escape the black hole should then be found in terms of the constants of motion in this frame. For the Schwarzschild case this was reduced to a requirement on the impact parameter b but could be more complicated for Kerr black hole. By transforming to the orthonormal frame the constants of motion can be expressed in terms of the initial direction of the massless particle leading allowing the escape fraction to be calculated. For the case of particles produced in collisions there is another step that needs to be taken. In general the orthonormal frame will not be the center of mass frame of a collision. The escape fraction will then depend on the Lorentz boost between the orthonormal and collision frames this boost depends on the momentum of the colliding particles in the orthonormal frame. This in turn leads to a dependence on the angular momentum of the colliding particles.

A similar method has been applied to the case of the extremal Kerr black hole [9]. To calculate the escape fraction the problem is reduced to the equatorial plane by restricting the

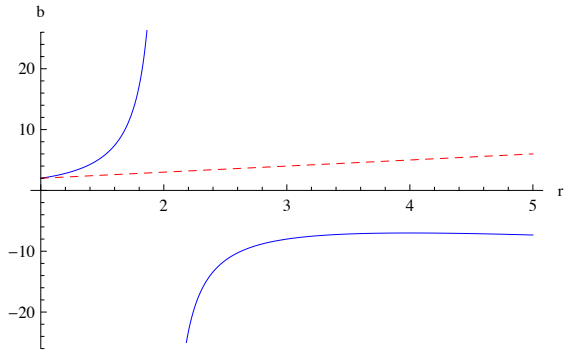

Figure 7.4: From [9] Plot of turning points for an extremal Kerr black hole in terms of b as a function of r. The dashed (red) line is $b_+^{a=1}(r)$ whereas the solid (blue) curve is $b_-^{a=1}(r)$.

motion of both the colliding particles and the particles produced in the collision to have $Q = 0$. The direction of the massless particles produced in the collision can again be expressed in terms of the impact parameter and the turning points in $\frac{dr}{d\lambda}$ were found. Figure **??** shows the turning points of the r solution. The two lines represent the location of the turning points in r as a function of the impact parameter b. The two solutions that give the turning points are [9].

$$\begin{aligned} b_+^{a=1}(r) &= 1+r, \\ b_-^{a=1}(r) &= -\frac{r^2-r+2}{r-2}. \end{aligned} \tag{7.30}$$

As in the Schwarzschild case we can read from Fig **??** the requirements that a particle is able to escape. These are summarised as [9].

$$r<4:\sigma = +1 \quad \text{and} \quad -7<b<b_+(r); \tag{7.31}$$

$$\sigma = -1 \quad \text{and} \quad 2<b<b_+(r), \tag{7.32}$$

and for

$$r>4:\sigma = +1 \quad \text{and} \quad b_-(r)<b<b_+(r); \tag{7.33}$$

$$\sigma = -1 \quad \text{and} \quad 2<b<b_+(r); \tag{7.34}$$

$$\sigma = -1 \quad \text{and} \quad b_-(r)<b<-7, \tag{7.35}$$

where $\sigma = +1$ denotes motion initially away from the horizon and $\sigma = -1$ means that the particle is initially moving towards the horizon. Note that the two regimes occur due to the

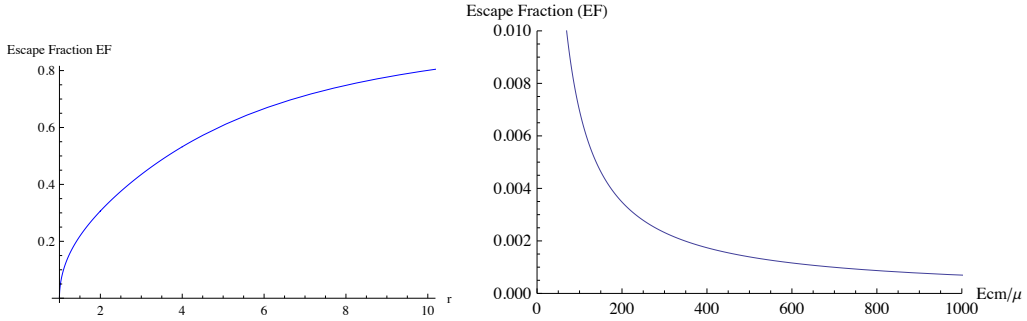

(a) Escape fraction as a function of r (b) Escape fraction as a function of E_{cm}

Figure 7.5: From [9]. Escape fraction for a maximal Kerr black hole. Trajectories of incoming and outgoing particles are restricted to the equatorial plane. Colliding particles have mass μ and angular momenta $l_1 = 2$ and $l_2 = -2$.

maximum of $b_-^{a=1}(r)$ which occurs at $r = 4$. There are two key differences between the Kerr and Schwarzschild cases. Firstly in the Kerr case the event horizon is located at $r = M$ in the equatorial plane rather than $r = 2M$ this means that the escape fraction is larger in the Kerr case when measured from the origin. Secondly there is different behaviour depending on the sign of b in the Kerr case. For in the Schwarzschild metric the turning points depend only on the value of b^2 and so there is a symmetry between the positive and negative values of the impact parameter. In the Kerr metric this symmetry is broken by the direction of rotation of the black hole and particles with angular momentum of the same sign as the black hole will have very different trajectories than those with angular momentum of the same sign.

The escape fraction is then calculated by mapping the angle at which the massless particle is emitted in the center of mass frame to the impact parameter in the coordinate frame. This has to be done for a specific collision frame specified by the angular momenta of the colliding particles. Specifying the angular momenta of the colliding particles also specifies the center of mass energy of the collision as a function of r.

Figure 7.4 shows the escape fraction as a function of both r and E_{cm} for a pair of colliding particles with angular momenta $l_1 = 2$, $l_2 = -2$. Since one of the particles as maximal angular momentum $l = 2$ the center of mass energy will be unbounded at the horizon. The escape fraction will fall rapidly at the horizon however leading to the shape of Figure 7.4b. The escape fraction is non-zero however so there is a possible flux of outgoing particles from collisions with center of mass energy orders of magnitude larger than the rest mass of the colliding particles.

7.4 Numerical solution of the geodesic equation

A calculation of the escape fraction for particles allowed to move away from the equatorial plane is not known analytically. The trajectory depends on another constant of motion Q and makes the definition of an escape criteria in terms of the solid angle more complicated. Boosting between the center of mass frame and the locally non-rotating frame and the conversion to the Boyer-Lindquist coordinate system also becomes more difficult. We now consider the estimation of the full escape fraction and related energy spectrum numerically as presented in [249]. The first ingredient of the numerical calculation is solving the geodesic equation. The goal here is to develop a numerical method of determining if a massless particle will escape the black hole based on its constants of motion. To do this we will solve the geodesic equation for motion in the Kerr metric numerically and find the behaviour as $t \to \infty$.

We recall here the equations of motion in the Boyer-Lindquist coordinates given in the previous section 7.2. We work in units where the black hole is set to $M = 1$ as a result a ranges between 0 and 1 in units where $\frac{M_{BH}G}{c^2} = 1$ such that the Schwarzchild radius $r_s = 2$. The trajectories of a particle are then defined by 3 constants of motion which are conserved,

$$\begin{aligned} E &= -p_t, \qquad L = p_\phi, \\ Q &= p_\theta^2 + \cos^2\theta \left(a^2 \left(\mu^2 - p_t^2\right) + \frac{p_\phi^2}{\sin^2\theta} \right), \end{aligned} \tag{7.36}$$

where μ is the mass of the particle, E is the energy, L is the component of the angular momentum parallel to symmetry axis of the black hole and $Q + p_\phi^2$ is the total angular momentum squared when $a = 0$. Q characterises the motion in the θ direction and for $Q = 0$ particles in the equatorial plane will remain restricted to that plane. The equations of motion for the particles can now be written in terms of λ, which will become an affine parameter for massless particles, and are written here in the form given by Ref. [250],

$$\begin{aligned} \Sigma \frac{dr}{d\lambda} &= \pm V_r = \pm \sqrt{T^2 - \Delta \left(\mu^2 r^2 + (L - aE)^2 + Q \right)}, \\ \Sigma \frac{d\theta}{d\lambda} &= \pm V_\theta = \pm \sqrt{Q - \cos^2\theta \left(a^2 \left(\mu^2 - E^2\right) + \frac{L^2}{\sin^2\theta} \right)}, \\ T &= E\left(r^2 + a^2\right) - La. \end{aligned} \tag{7.37}$$

The final state particles of the collisions are assumed to be massless allowing the equations to be simplified by setting $\mu = 0$ (For massive particles the approximation $\mu = 0$ is good provided $\mu \ll E$ and E is generally of the order of the DM mass. The results therefore remain unchanged if a small mass is introduced. We require only the equation for r and θ since we are only concerned as to whether the particle can escape or not.

In order to calculate the escape function numerically the equations of motion for r and θ were integrated numerically until the particle either crossed the horizon or escaped to some large value of r. The algorithm employed was based on an embedded adaptive step size Runge-Kutta formula as outlined in Ref [271]. The general idea behind the Runge-Kutta algorithm is to take a series of trial steps to refine the estimate of value of the function at the end point of the next step. The simplest example is the midpoint method which uses one trial step to refine the solution. Consider a function $y(x)$ for which we can evaluate the derivative $\frac{dy}{dx} = f(x,y)$. We want to advance the solution from x_n to $x_{n+1} = x_n + h$ where h is the step size. The midpoint method achieves this by evaluating.

$$\begin{aligned} k_1 &= hf(x_n, y_n), \\ k_2 &= hf(x_n + 1/2h, y_n + 1/2k_1), \\ y_{n+1} &= y_n + k_2 + O(h^3), \end{aligned} \tag{7.38}$$

where k_2 is calculated by the trial step to $x_n + 1/2h$. Higher order Runge-Kutta methods use more trial steps to calculate more k values these can then be combined to eliminate higher order errors. The Runge-Kutta-Fehlberg method of embedded Runge-Kutta methods takes advantage of the fact that the function calls of $f(x,y)$ required 5th order Runge-Kutta method can be reused to calculate the 4th order Runge-Kutta method. This means that when the 5th order method is used to calculate the next step the 4th order estimate for that step can be constructed without any further calls to the derivative function $f(x,y)$. The uncertainty can then be calculated by taking the difference between the 5th and 4th order methods. The step size for the next step is then adjusted according to the equation [271]

$$h_0 = h_1 \left| \frac{\Delta_0}{\Delta_1} \right|^{0.2}, \tag{7.39}$$

where h_1 is the size of the previous step, Δ_1 is the difference between two estimates and Δ_0 is

the desired accuracy of the solution. If $h_0 < h_1$ then the required accuracy was not met in this case the previous step is repeated with step size h_0. If $h_0 > h_1$ then the accuracy was greater than required and the step size can be safely increased to h_0 for the next step. Such a method ensures each step has the required accuracy however the real uncertainty in the solution will be greater since errors can accumulate from one step to the next. The Δ values need not be a single variable but can be a vector of quantities such that h is adjusted to keep the worst behaving quantity within its desired accuracy.

The equation of motion for the r coordinate has 2 solutions with opposite sign corresponding the particle travelling towards or away from the black hole the sign is chosen based on the initial conditions and turning points in the r solution must be detected and the sign changed. In particular for the escape fraction it will be of interest when the two solutions must be interchanged since only outgoing solutions correspond to escaping particles. A numerical check was used to determine when the derivative of r became very small, when this occurs the sign of the r solution as changed. It was important that this cut off was performed at the right time so rather than measure the uncertainty in r the error in $\frac{dr}{d\lambda}$ was measured and the difference in the two estimates required to be less than the minimum value required to change the sign. Originally both accuracy in θ and r was required however it was found that even specifying a very high accuracy in θ the step size was still driven by the r solution and the specifying an accuracy for the θ solution is not important. One issue with a variable step size algorithm in this case is that after taking a step the algorithm then checks to see if the sign of the solution needs to be changed, after changing the sign the solution the next step in λ may be smaller than the last and the value of $\frac{dr}{d\lambda}$ still be smaller than the cut off value. If this process repeats then the solution will get stuck at the turning point changing between the two solutions. To alleviate this the algorithm kept track of whether the sign was changed on the last step and the sign was kept from changing until the next time the solution took a step that was above the cut off value of $\frac{dr}{d\lambda}$.

The integration was ended whenever the photon crossed the horizon or achieved some maximum distance from the black hole for example $r_{max} \approx 100$ for collisions close to the horizon. This was increased for collisions further from the black hole. In some cases the photon remained bound by the black hole in a stable orbit in this situation the integration would end only when some maximum value of λ was reached. If λ_{max} is set too high then solutions with several turning points are computationally intensive since the step size is smallest at those points so integrations

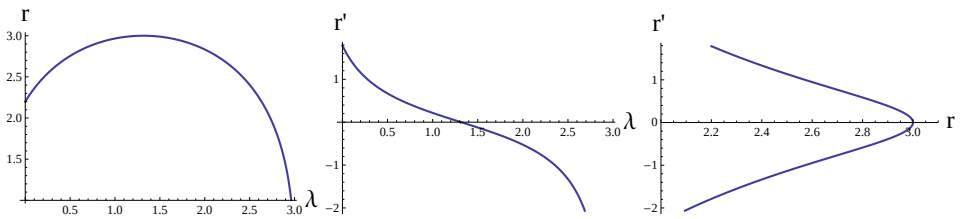

(a) r as a function of λ (b) $\frac{dr}{d\lambda}$ as a function of λ (c) $\frac{dr}{d\lambda}$ as a function of r

Figure 7.6: Trajectory of massless particle emitted at $r = 1.2$ with $E = 1$, $L = -8$, $Q = 0$ in the equatorial plane. $a = 1$

of bound orbits would slow down the computation, However setting a low value of λ_{max} is not suitable since some escaping photons do so only for large values of λ. The integration for these can be rapid since the step size can be large and therefore the actual number of integration steps small. To avoid these problems bound orbits were detected by tracking the number of turning points encountered by a solution when this became large, more than 100, the photon was assumed to be trapped and the integration ended. In practise the parameters of the algorithm, the minimum step size, λ_{max}, r_{max} and the value of $\frac{dr}{d\lambda}$ that indicates a turning point were varied to find optimal values that did not introduce errors in the final result based on comparison to the known cases.

Figure **??** shows the trajectory of a massless particle generated by the numerical method in the equatorial plane for impact parameter $b = -8$. The particle is initially travelling away from the horizon but is reflected by the potential barrier at $r = 3$. This behaviour is in agreement with figure **??**.

7.5 Locally non-rotating frames

The previous section provides a method for determining the escape criteria in terms of the momentum of the particle in the Boyer-Lindquist coordinate system. The momentum of the particle in this system is not initially known and must be calculated from the momentum in the center of mass frame of the collision. The center of mass frame is a local frame related to the locally non-rotating frame by a Lorentz transformation. In these frames special relativity holds and the direction and momenta of the particles produced in the collision are easy to calculate due to the diagonal metric. The global trajectory of the particle is not simple in this frame and so we need to translate the momentum of the particle from the LNRF to the Boyer-Lindquist frame. This is

analogous to the calculation of the escape fraction in the Schwarzschild case where the emission of particles was assumed to be isotropic in the orthonormal frame.

The LNRF basis vectors for one-forms is given by [250].

$$\begin{aligned}
\hat{e}^t &= \sqrt{\frac{\Sigma\Delta}{A}}\,\overline{e}^t, \\
\hat{e}^r &= \sqrt{\frac{\Sigma}{\Delta}}\,\overline{e}^r, \\
\hat{e}^\theta &= \sqrt{\Sigma}\,\overline{e}^\theta, \\
\hat{e}^\phi &= -\frac{2Mar\sin(\theta)}{\sqrt{\Sigma A}}\,\overline{e}^t + \sqrt{\frac{A}{\Sigma}}\sin(\theta)\,\overline{e}^\phi,
\end{aligned} \tag{7.40}$$

where $\hat{e}$ are the basis vectors for the LNRF and $\overline{e}$ is the basis in the Boyer-Lindquist frame. The components of the momentum in the LNRF can be found from the momentum in the Boyer-Lindquist (BL) frame by projecting onto each of the LNRF basis vectors. The momentum in the BL frame can be written as.

$$P^{BL} = \overline{e}^t P_t + \overline{e}^r P_r + \overline{e}^\theta P_\theta + \overline{e}^\phi P_\phi. \tag{7.41}$$

The components of the momentum in the LNRF P'_μ are then given by.

$$P'_\mu = P^{BL}\hat{e}^\mu. \tag{7.42}$$

The end result is achieved by substituting Eq. 7.29 into Eq. 7.31 and contracting the BL basis vectors using the contravariant form of the metric given by.

$$\begin{aligned}
\left(\frac{\partial}{\partial s}\right)^2 &= -\frac{A}{\Sigma\Delta}\left(\frac{\partial}{\partial t}\right)^2 - \frac{4Mar}{\Sigma\Delta}\left(\frac{\partial}{\partial t}\right)\left(\frac{\partial}{\partial\phi}\right) + \frac{\Delta}{\Sigma}\left(\frac{\partial}{\partial r}\right)^2 \\
&\quad + \frac{1}{\Sigma}\left(\frac{\partial}{\partial\theta}\right)^2 + \frac{\Delta - a^2\sin^2\theta}{\Sigma\Delta\sin^2\theta}\left(\frac{\partial}{\partial\phi}\right)^2.
\end{aligned} \tag{7.43}$$

This gives a linear transformation depending on r, a and θ between P^{BL} and P^{LNRF}. Inverting the transformation gives P^{BL} in terms of P^{LNRF}. We note that this transformation does not depend on the mass of the particle and also gives all of the components of the momentum in the BL frame. To calculate the escape fraction for a massless particle it would be enough to find the direction of the momentum in the BL frame as the trajectory would not depend on E but rather

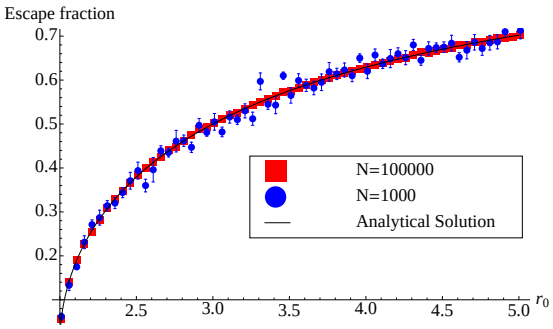

Figure 7.7: The escape fraction for a = 0, where N is the number of Monte Carlo iterations. The solid line shows the escape fraction constructed from the analytical conditions of escape

the impact parameter b only. However by finding the energy directly by this transformation we can construct the energy spectrum of the escaping particles in addition to the escape fraction.

As previously noted the LNRF is equivalent to the orthonormal frame in the Schwarzschild metric we can use the above transformation taking $a \to 0$ to test the numerical solution against the escape fraction calculated analytically for the Schwarzschild metric. The escape fraction is calculated numerically via a simple Monte-Carlo integration as follows. The emitted particles are assumed to be isotropic in the orthonormal frame and the energy is fixed to $E = 1$ (we are free to fix the energy to any value since the trajectory depends only on the direction for a massless particle. The direction is defined by two angles θ the angle from the radial axis parallel to the polar angle of the black hole coordinate system and ϕ the azimuthal angle about the radial axis. For the integration a flat distribution of these angles was randomly generated and for each direction the momentum in the BL frame was calculated and the the geodesic equation was solved numerically as above. The massless particle was recorded as either escaping or becoming trapped by the black hole. The escape fraction was then taken as the number of massless particles recorded as escaping divided by the total number generated.

The uncertainty in the escape fraction due to the statistical effects of the Monte Carlo integration was found by separating the massless particles into discrete bins, the escape fraction for each bin was determined then the average escape fraction taken. The variance in the escape fraction for each bin then gave an estimate for the uncertainty in the averaged escape fraction. This uncertainty does not account for any error in the numerical solution for the geodesic equations but since the escape fraction only depends on the general behaviour of each massless particle this was neglected.

Figure 7.5 shows the behaviour of the escape fraction when the massless particle is emitted isotropically in the orthonormal frame. The escape fraction matches the function determined from [270] with some variation due to the Monte Carlo integration. The effect of the number of Monte Carlo iterations on the error in the escape fraction can be seen and gives an indication of the number of iterations required to give a good agreement with the analytical solution. A Monte Carlo method is chosen here since this will allow the construction of the energy spectrum in some distant observers frame of escaping particles later.

7.6 Lorentz boosted frame

For particles emitted from collisions around the black hole the emission will not be isotropic in the LNRF. We assume here that the particles are emitted isotropically in the center of mass frame of the collision and this frame is related to the LNRF by a Lorentz boost. The isotropic distribution must therefore be boosted to the LNRF before transforming to the BL frame.

The Lorentz boost between the LNRF and center of mass frame depends on the trajectories of the colliding particles. The calculation follows the method for calculating the center of mass energy of the collision [8]. The 4-velocity of the colliding particles is found from the equations of motion in the BL frame and the corresponding 4-velocities in the LNRF are used to calculate the momentum of the colliding particles in the LNRF. The center of mass energy and Lorentz boost is then given by the normal special relativity form for the boost.

Firstly the 4-velocity of the particles was calculated in the Boyer-Lindquist coordinate system by evaluating $\frac{dt}{d\tau}$, $\frac{dt}{d\tau}$, $\frac{d\theta}{d\tau}$ and $\frac{d\phi}{d\tau}$ using the equations of motion given by Eq. 7.14. The transformation between the BL frame and LNRF is given by projecting onto the LNRF basis vectors [250].

$$\begin{aligned}
\hat{e}_t &= \sqrt{\frac{A}{\Sigma\Delta}}\bar{e}_t + \frac{2Mar}{\sqrt{A\Sigma\Delta}}\bar{e}_\phi, \\
\hat{e}_r &= \sqrt{\frac{\Delta}{\Sigma}}\bar{e}_r, \\
\hat{e}_\theta &= \frac{1}{\sqrt{\Sigma}}\bar{e}_\theta, \\
\hat{e}_\phi &= \sqrt{\frac{\Sigma}{A}}\frac{1}{\sin\theta}\bar{e}_\phi.
\end{aligned} \tag{7.44}$$

The basis vectors in the BL frame are then contracted using the usual Kerr metric. In the LNRF the 4-velocity is related to the particle 3-velocity and momentum by Eq. 7.2 and Eq. 7.3. This defines the momentum of the two colliding particles in the LNRF in terms of the 3 constants of motion in BL frame.

We consider the collision of 2 particles with momenta in the LNRF $P = (P_a, P_b, P_c, P_d)$ and $Q = (Q_a, Q_b, Q_c, Q_d)$. The Lorentz boost between the LNRF and the center of mass frame of collision is given by.

$$\Lambda = \begin{pmatrix} \gamma & -C_\chi\beta\gamma & -S_\chi\beta\gamma & -T_\chi\beta\gamma \\ -C_\chi\beta\gamma & 1+C_\chi^2(-1+\gamma) & C_\chi S_\chi(-1+\gamma) & C_\chi T_\chi(-1+\gamma) \\ -S_\chi\beta\gamma & C_\chi S_\chi(-1+\gamma) & 1+S_\chi^2(-1+\gamma) & S_\chi T_\chi(-1+\gamma) \\ -T_\chi\beta\gamma & C_\chi T_\chi(-1+\gamma) & S_\chi T_\chi(-1+\gamma) & 1+T_\chi^2(-1+\gamma) \end{pmatrix}, \tag{7.45}$$

where the components are defined by

$$\begin{aligned} \beta &= \frac{\left((P_b+Q_b)^2+(P_c+Q_c)^2+(P_d+Q_d)^2\right)^{1/2}}{(P_a+Q_a)}, \\ \gamma &= \frac{1}{\sqrt{1-\beta^2}}, \qquad C_\chi = \frac{P_b+Q_b}{\beta^2\left(P_a+Q_a\right)^2}, \\ S_\chi &= \frac{P_c+Q_c}{\beta^2\left(P_a+Q_a\right)^2}, \quad T_\chi = \frac{P_d+Q_d}{\beta^2\left(P_a+Q_a\right)^2}. \end{aligned}$$

Note that in the center of mass frame the energy of the collision is just the sum of the energies of the two components which can be read off the first row of the boost matrix.

$$\begin{aligned} E_{cm} &= Q_a\gamma - C_\chi\beta\gamma Q_b - S_\chi\beta\gamma Q_c - T_\chi\beta\gamma Q_d \\ &\quad + P_a\gamma - C_\chi\beta\gamma P_b - S_\chi\beta\gamma P_c - T_\chi\beta\gamma P_d. \end{aligned} \tag{7.46}$$

The momentum of the massless particle emitted in the center of mass frame is given by.

$$P_{CM} = (E_{CM}, E_{CM}\cos\theta_{CM}\sin\phi_{CM}, E_{CM}\sin\theta_{CM}, E_{CM}\cos\theta_{CM}\cos\phi_{CM}). \tag{7.47}$$

Which is then converted to the BL frame to find the trajectory.

The steps carried out by the numerical code are; Firstly the constants of motion for the colliding particles in the BL frame are set to some values, l_1, l_2, q_1, q_2. The energy at infinity

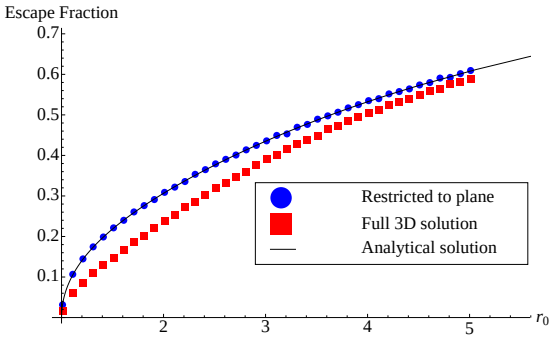

Figure 7.8: Escape fraction for a=1 with momenta of colliding particles fixed: Analytic solution in equatorial plane (Black line) [9], Numerical result in equatorial plane (blue circles) and full numerical result allowing propagation in all directions (red squares).

of the particles are normalised to 1 setting the units of energy to the rest mass of the colliding particles. The specific coordinates of the collision in the BL are chosen given by r_0 and θ_0. The 4-velocities of the particles at these coordinates are calculated from the equations of motion. The transformation between the BL and LNRF is performed and the momentum in the LNRF calculated from Eq. 7.3. The momentum of the two particles in the LNRF is used to define the Lorentz boost, Λ, between the LNRF and center of mass frame and the center of mass energy. A distribution of directions is generated in the center of mass frame for the Monte-Carlo integration. For each direction the momentum in the center of mass frame is transformed to the LNRF by Λ^{-1} and the momentum in the LNRF is transformed to the BL as described above. The momentum in the BL frame is sufficient to define the constants of motion E, L, Q and the trajectory of the particle calculated via the Runge-Kutta method. The particle is then recorded as either escaping or being trapped by the black hole.

We can test all of the steps together by calculating the escape fraction as a function of r to the result from [9] by setting the incoming angular momentum of the colliding particles to $l_1 = 2$, $l_2 = -2$ and $q_1 = q_2 = 0$. The emitted particles are restricted to the equatorial plane by setting $\theta_{CM} = 0$.

Figure 7.6 shows the result from the numerical solution (blue circles) compared to the analytic result. The numerical result matches the exact solution when the particles are confined to the equatorial plane. The result found when θ_{CM} is allowed to vary is also shown. In this case the escape fraction is reduced compared to the result confined to the equatorial plane at small r but remains comparable in size.

7.7 Distribution of colliding particles

The previous section considered massless particles produced in collisions of massive particles with fixed incoming momenta. However the escape fraction depends on the Lorentz boost from the LNRF to the centre of mass frame given above. The Lorentz boost is derived from the constants of motion E, L and Q of the incoming particles. In general these constants are not fixed and the momenta of the colliding particles will have some distribution. This distribution will also affect the centre of mass energy of the collision and the energy of the produced massless particles. In order to calculate the energy distribution of escaping particles and the general escape fraction it will therefore be important to consider incoming particles with some distribution of momenta.

The form of this distribution is not known so as a first approximation we assume a flat distribution in the constants L and Q. The allowed range of L and Q was fixed by considering only particles with geodesics that would allow the particle to fall from some large r to the radius r_0 at which the collision takes place. This means close to the horizon collisions will occur only from particles on plunge geodesics while for collisions further from the horizon a wider range of incoming particles are allowed. The constant of motion E was set to the mass of the DM which in turn is set to 1. The distribution of allowed momenta was sampled by Monte Carlo integration. Figure **??** shows the allowed range in L and Q for collisions occurring at $r_0 = 1.1$ as an example. This is characterised (for $a = 1$) by a maximum value of Q which occurs for $L = -1$ as well as a maximum and minimum value of L with the largest range corresponding to $Q = 0$. Figure **??** shows the escape fraction when the momenta of the colliding particles is averaged over all allowed values of L and Q. The escape fraction has only a weak dependence on the Lorentz boost and hence L and Q, of the colliding particles so the full escape fraction is only a slight shift from the result found for a particular fixed boost shown in figure 7.6. The uncertainty in the calculated escape fraction is larger due to the integration over the colliding particles initial angular momenta, as the dimensions of the integration increase a greater number of Monte Carlo samples are needed.

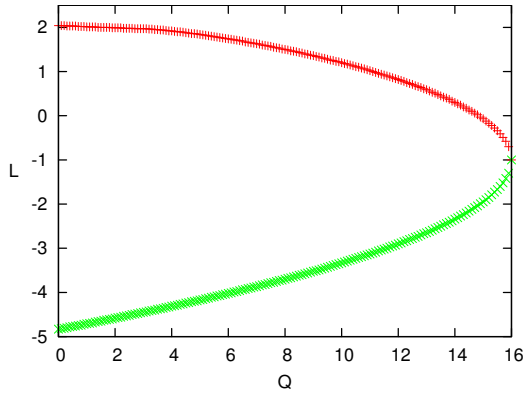

Figure 7.9: Allowed range in Q and L for incoming particles that reach $r_0 = 1.1$ with $a = 1$. The red line show L_{max} and the green line L_{min}.

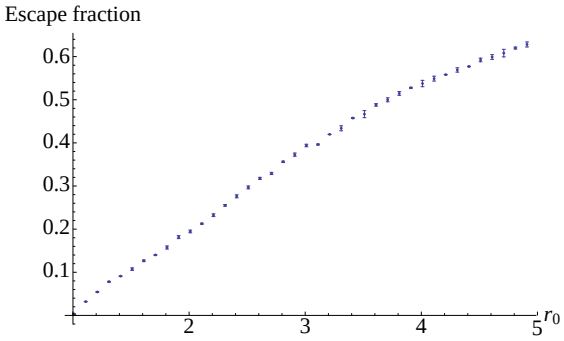

Figure 7.10: Escape fraction for $a = 1$ with integration over momenta of the colliding particles including the effect of the Lorentz boost.

7.8 Spectrum of emergent massless particles

In order to calculate the energy spectrum of emergent particles we must integrate the effect of collisions over the distribution of DM surrounding the black hole. The flux arriving at some distance D, from the black hole reads [9],

$$\Phi \approx \frac{\sigma v r_s^3}{4\pi m_\chi^2 D^2} \int_{r_h}^{r_\infty} \rho^2(r)\, e(r)\, dV, \tag{7.48}$$

where σv is the cross-section for annihilation to massless particles which we assume to be energy independent, m_χ is the mass of the DM particles, r_s is the Schwarzschild radius, r_h is the event horizon, $e(r)$ is the escape fraction shown in figure **??** and $\rho(r)$ is the DM density around the black hole, which is assumed to be a function of r only. It is assumed that the escape fraction is spherically symmetric. The calculation is performed for collisions occurring in the equatorial

plane only, to simplify the integration. By writing

$$\rho(r) = \rho_{\rm pl}\rho_0(r), \tag{7.49}$$

where $\rho_0(r)$ is a dimensionless function giving the shape of the density profile. The flux can be written in terms of a dimensionless integral containing all the of the dependence on the rotation of the black hole and the shape of the density profile as [9],

$$\Phi \approx \frac{\sigma v r_s^3 \rho_{\rm pl}^2}{m_\chi^2 D^2} I(a), \tag{7.50}$$

$$I(a) = \int_{r_h}^{r_\infty} r^2 \rho_0^2(r)\, e(r)\, dr. \tag{7.51}$$

In order to calculate the spectrum of the emergent massless particles we need to know $\Phi(E)$ which depends on the convolution of the escape fraction and spectrum of massless particles produced in the collisions. To find this we define $p(r,E_1,E_2)$ as the fraction of massless particles that escape with energy between E_1 and E_2 per collision. This was found numerically by separating the escaped massless particles into bins of energy and dividing by the total number of collisions. The integral can then be rewritten as

$$\Phi(E_1,E_2) \propto I(a,E_1,E_2) = \int_{r_h}^{r_\infty} r^2 \rho_0^2(r)\, p(r,E_1,E_2)\, dr, \tag{7.52}$$

where summing over all the energy bins gives the total flux.

We want to calculate $p(r,E_1,E_2)$ numerically. $p(r,E_1,E_2)$ consists of two pieces the first is the energy spectrum of particles produced in the collision averaged over the momenta of the colliding particles. The second part is the convolution of this energy spectrum with the escape fraction so that only those particles that escape the black hole are counted. The energy spectrum of particles produced in the collisions as a function of r_0 and θ_0 the coordinates of the collision is found as follows. A Monte Carlo integration is performed over the allowed constants of motion for infalling particles to r_0 and over the direction of the emitted particle. The energy at infinity, E, in the BL frame is recorded for each collision. The particles are placed in energy bins and divided by the total number of particles sampled. This gives the fraction of particles produced in each energy bin per collision. This processes does not depend on whether the particle will ultimately escape the black hole or not so the produced spectrum is not what will be seen by an

observer far from the black hole. Instead this spectrum is total spectrum that would be locally observed at the point of collision but transformed to the BL coordinate system so the energy for each particle is the energy at infinity if the particle were able to escape to infinity.

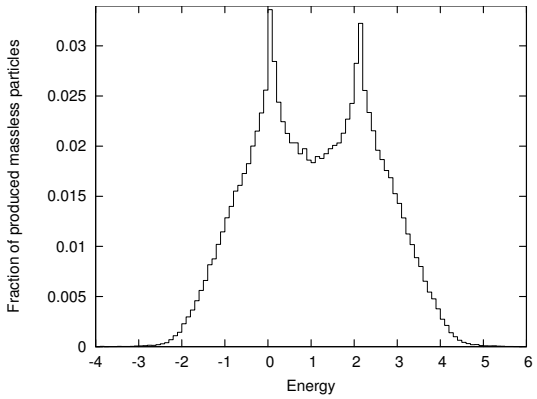

(a) $r_0 = 1.1$

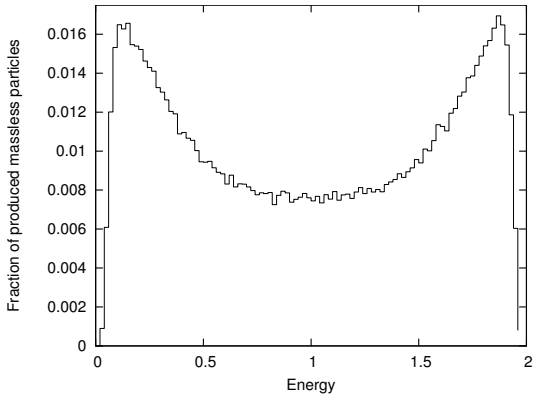

(b) $r_0 = 2.1$

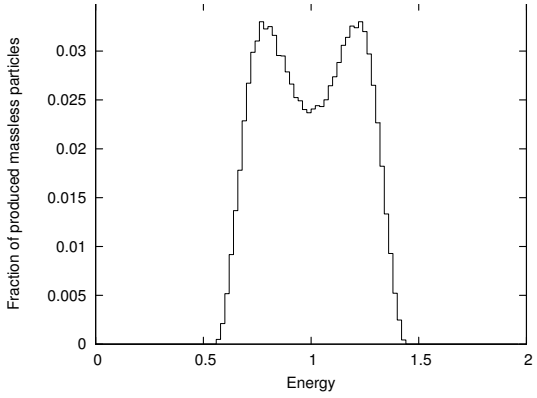

(c) $r_0 = 10$

Figure 7.11: Energy spectrum that would be observed at infinity of all massless particles produced in collisions at varying r_0 if all particles escaped the black hole. ($a = 1$)

Figure 7.7 shows the energy spectrum of the massless particles produced in collisions for

three different values of r_0. We start with figure 7.7a at $r_0 = 1.1$ this shows the spectrum produced by collisions close to the horizon of the black hole within the ergosphere. The most prominent features of the spectrum are the two peaks. The peaks are located at $E \approx 0$ and $E \approx 2$. This structure arises due to several effects. Firstly there is a balance between the centre of mass energy and the gravitational red shift as suggested in Ref. [242], this is expected from energy conservation considerations that the energy available to the collision as measured far from the black hole will be $2m_\chi$.

The result is that the spectrum is not shifted to higher energies by the increasing centre of mass energy close to the black hole horizon or red shifted by increasing gravitational potential. There is a shift of the peaks that arises from the Lorentz boost, since the centre of mass frame is in general boosted towards the horizon, massless particles emitted away from the black hole are red shifted to lower energies. Particles emitted towards the horizon are correspondingly shifted to higher energies. The effect of this is to split the spectrum of escaping particles into two peaks, a red shifted peak with energy below the DM mass and a blue shifted peak with energy above the DM mass. Close to the horizon the Lorentz boost between center of mass frame and LNRF is very large. In the LNRF particles that are emitted towards the black hole have a large blue-shift and carry nearly all the energy from the collision, particles emitted away from the black hole have a large red-shift and will carry very little energy in that frame. When transformed to the BL frame the total energy should be twice the DM mass so the blue-shifted particles have $E \approx 2$ and the red-shifted particles $E \approx 0$.

This explains the two peaks in the spectrum but there are also tails extending to $E > 2$ and $E < 0$. These can be explained via the Penrose process [245], [272]. Inside the ergrosphere some collisions will produce pairs of particles where one particle has energy greater than the total energy of the in-falling particles and the other particle has negative energy. The negative energy particle will always be trapped by the black hole. Such processes extract energy from the black hole by reducing its mass and angular momentum.

Figures. 7.7b and 7.7c show how the spectrum changes as r_0 increases. The first change is that for $r_0 > 2$ the collisions are no longer occurring in the ergosphere the Penrose process can no longer occur and the energy of the particles produced in the collision is bounded by the masses of the colliding particles. As r_0 increases the Lorentz boost between the center of mass and LNRF becomes smaller and the Lorentzs shift of the particles is reduced. The separation of

the beaks reduces and they converge around $E = 1$.

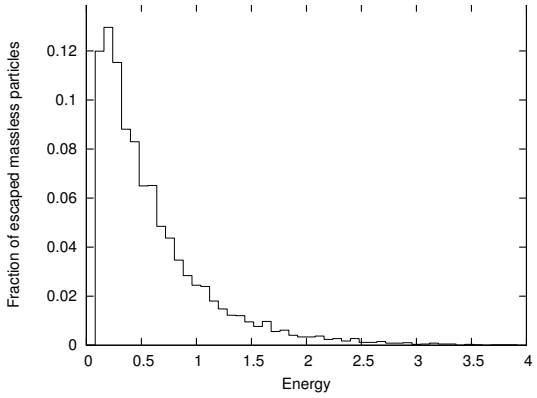

(a) $r_0 = 1.1$

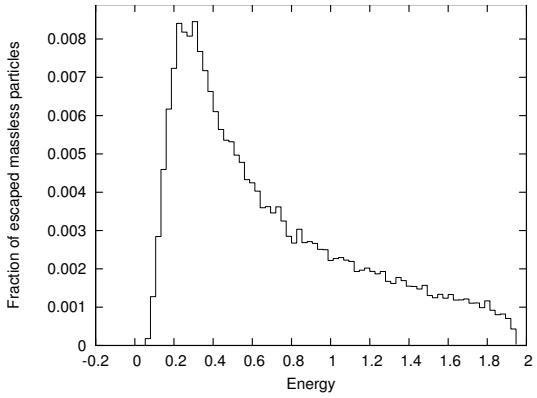

(b) $r_0 = 2.1$

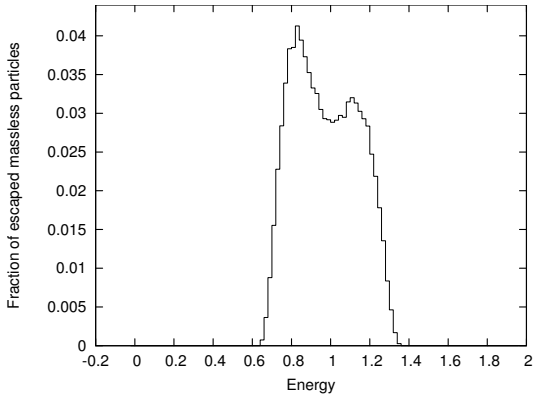

(c) $r_0 = 15$

Figure 7.12: $p(r_0, E_1, E_2)$ as a function of r_0. The fraction of massless particles that escape with energy between E_1 and E_2 per collision. ($a = 1$)

We now consider the convolution of the spectrum produced in the collisions with the escape fraction. Figure 7.8 shows the shape of the spectrum observed at infinity for collisions occurring at different values of r_0. In contrast with figure 7.7 only those particles that escape the black

hole contribute to the spectrum now. Figure 7.8a shows the spectrum of escaping particles for collisions close to the horizon (compare with figure 7.7a). It is clear that once the escape fraction has been taken into account most of the particles emitted towards the black hole that previously made up the peak at $E \approx 2$ have been captured by the black hole. This leaves only the peak at $E \approx 0$. From this it can be seen that the escape fraction is generally smaller for particles with larger energy. Another key difference is that the spectrum is now strictly positive since all the negative energy particles produced by the Penrose process are unable to escape the ergosphere. Some particles with $E > 2$ are able to escape contributing to the tail of the spectrum.

As r_0 is increased the escape fraction increases. More particles are able to escape including those initially emitted towards the black hole. At $r_0 = 2.1$ shown in figure 7.8b the spectrum has a flat tail extending to $E \approx 2$. The flatness of the distribution is because although the escape fraction is getting smaller as E increases, the fraction of particles produced in the collisions are increasing with E due to the blue-shifted peak in figure 7.7b. As r_0 is increased further the escape fraction becomes larger still and the blue-shifted peak emerges in the spectrum. Although the second peak is still smaller than the red-shifted peak due to the escape fraction. As before the two peaks are converging towards $E = 1$ as r_0 becomes larger.

7.9 The flux of escaping particles

In the previous section we described the shape of $p(r_0, E_1, E_2)$ we now want to relate this to the flux of particles escaping from black hole. We recall the definition of $I(a, E_1, E_2)$.

$$\Phi(E_1, E_2) \propto I(a, E_1, E_2) = \int_{r_h}^{r_\infty} r^2 \, \rho_0^2(r) \; p(r, E_1, E_2) \, dr. \tag{7.53}$$

So to derive the flux we must now integrate $p(r_0, E_1, E_2)$ and choose a suitable density distribution of DM $\rho_0^2(r)$. The density distribution of DM around black holes has been extensively studied for non-rotating black holes see [241] [273] [274]. Considering the case of an intermediate mass black hole the density distribution can be described as follows [241]; close to the black hole there is an annihilation plateau with constant density $\rho_{\rm pl} = m_\chi/(\sigma v t)$ where t is the formation time of the black hole. This holds out to a radius r_{cut} from which point the density falls off with a power law $\rho \propto r^{-\frac{7}{3}}$. The distribution here is assumed to be spherically symmetric (For a rotating black hole this may no longer be true but serves as a first approximation.). The

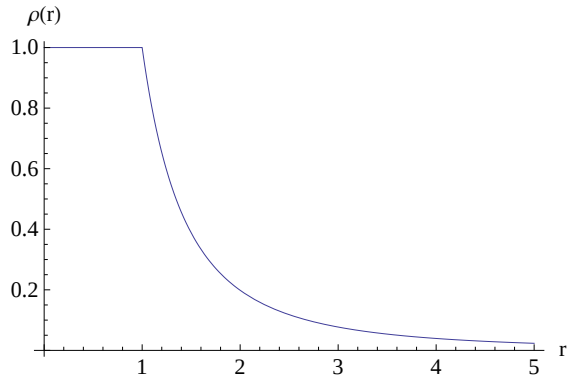

Figure 7.13: Density of dark matter as a function of r. With $\rho_{\rm pl} = 1$ and $r_{cut} = 1$.

flux will be dominated by contributions from the annihilation plateau and density spike since the escape fraction is only small for radii much smaller than the annihilation plateau. It is now clear that if $\rho_{\rm pl}$ given in Eq. **??** is taken to be the density of the annihilation plateau, $\rho_0(r)$ will take the form [241],

$$\rho_0(r) = \begin{cases} 1 & \text{if } r < r_{cut} \\ \left(\frac{r}{r_{cut}}\right)^{-\frac{7}{3}} & \text{if } r > r_{cut}. \end{cases} \tag{7.54}$$

Figure **??** shows the shape of the density distribution of the DM when $\rho_{\rm pl}$ and r_{cut} are normalised to 1. It is clear from this that since $\frac{dI(a,E_1,E_2)}{dr} \propto r^2 \rho_0^2(r)$ it will be increasing with r so long as $r < r_{cut}$ above r_{cut} the density drops off faster than r^{-2} so $\frac{dI(a,E_1,E_2)}{dr}$ will start to decrease. The flux is then expected to be dominated by the collisions occurring at $r \approx r_{cut}$.

To calculate the value of I for a particular set of black hole parameters the value of r_{cut} needs to be specified. In general this depends on the mass of the black hole and on the annihilation cross-section of the DM. For the super massive black hole at the centre of the galaxy this was estimated to be $r_{cut} \approx 4 \times 10^{-5} pc$ from Ref. [273] which is $r_{cut} \approx 137 r_s$ in terms of the Schwarzschild radius.

The exact value is not important since the shape of the spectrum remains distinctive over a large range of r_{cut} and a measurement of the spectrum should in principle allow r_{cut} to be determined. To show this, the spectrum produced for a number of different values of r_{cut} are shown in figure 7.9. The energy is expressed in units of the DM mass.

figure 7.9a shows the spectrum for a small value of $r_{cut} = 5$ (in units where $r_s = 2$), and hence is dominated by collisions close to $r_0 = 5$. Here the spectrum is characterised by a single asymmetric peak below the DM mass. The peak itself is broad and the mass of the DM is found

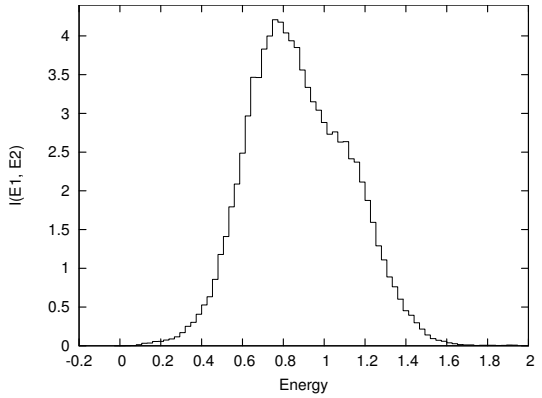

(a) $r_{cut} = 5$

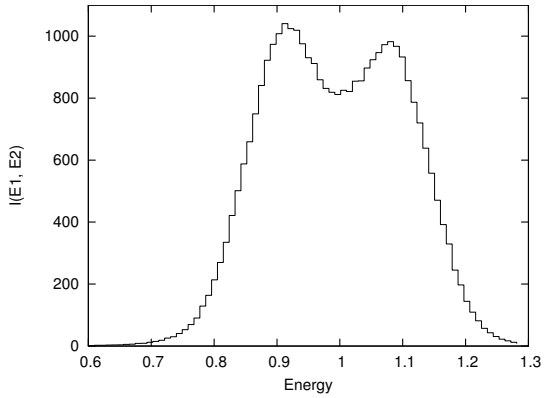

(b) $r_{cut} = 34$

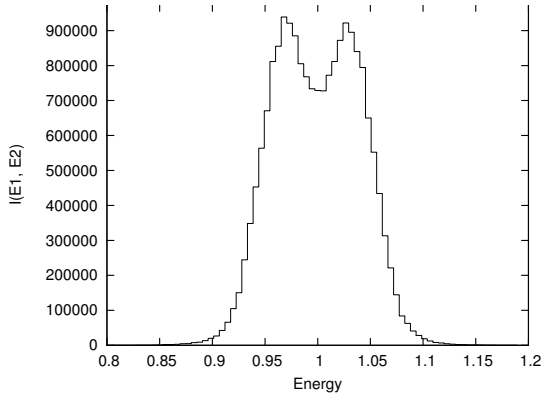

(c) $r_{cut} = 274$

Figure 7.14: Spectrum of massless particles escaping to infinity with a cut off in dark matter density at various values of r_{cut}. ($a = 1$)

to be roughly equidistant from the peak and the edge of the shoulder in the distribution. This structure arises due to effects of the Lorentz boost and escape factor discussed earlier. The peak is broadened slightly by the integration over r. The blue-shifted peak appears as a shoulder in the spectrum for this value of r_{cut}.

As r_{cut} in figure 7.9b increases to 34, both peaks become clearly visible and the spectrum becomes less broad. The height difference between the peaks also decreases as they get closer together. The peaks in the spectrum move towards the DM mass since the Lorentz boost to the centre of mass frame becomes smaller. It is still more likely that a massless particles emitted away from the horizon will escape than one emitted towards it so the blue shifted peak is generally smaller than the red shifted one. It also becomes clear that the spectrum is indeed roughly symmetric around the DM mass which could be useful in determining the mass from the spectrum. The similarity of the spectrum to figure 7.8 is due to the fact the the flux is dominated by collisions at the edge of the annihilation plateau and so will look like $p(r_0, E_1, E_2)$ at $r_0 = r_{cut}$.

In figure 7.9c the spectrum is shown for $r_{cut} = 274 = 137 r_s$ the collisions responsible for the majority of the flux are now occurring far from the horizon. The escape fraction becomes even less important and nearly all of the massless particles produced in the collisions will now escape. This can be seen in the spectrum by noting that the red shifted and blue shifted peaks are now very nearly the same height. Comparing the spectrum with that in figure 7.9b it can be seen that the red shifted and blue shifted peaks continue to move towards the DM mass as the effect of the Lorentz boost diminishes.

The spectrum could potentially be used to infer some of the quantities in the system. The DM mass is indicated by the minimum between the peaks and the value of r_{cut} can be estimated from the separation of the peaks as a fraction of the DM mass.

The value of r_{cut} can be estimated as follows; the DM mass must be found first by locating the minimum of the spectrum, the energy at which the first peak occurs as a fraction of the mass of the DM then decreases as a function of r_{cut}. By plotting the peak location as a function of r_{cut} from simulation the expected value of r_{cut} can be found for a given peak separation. It should be noted that the distribution is not exactly symmetric and that the higher energy peak is located closer to the DM mass than the lower energy peak. However both could be used to find an estimate of r_{cut} and the ratio of the height of the peaks could also be utilised in this way. One problem with this analysis is that it assumes that the angular momentum of the black hole is known and varying a shifts the separation of the peaks. However this effect is much smaller than changing r_{cut} but would still introduce uncertainty in the estimation. The ability to resolve the peaks depends on the total flux available and the energy resolution around the DM mass of a particular measurement. In terms of the annihilation plateau the separation of the peaks

was found up to $r_{cut} = 10^5$ with a separation of $\Delta_E \sim 0.001 m_\chi$. For $r_{cut} = 10^3$ a separation of $\Delta_E \sim 0.03 m_\chi$ was found. In the case that the peaks can not be resolved then the spectrum can be approximated as a single peak with a width comparable to the peak separation centred at the DM mass.

The total flux can be estimated by choosing some suitable values for the parameters in Eq. **??**. Setting the mass of the black hole to $M = 40 \times 10^5 M_\odot$, the annihilation cross-section of the DM as $\sigma v = 10^{-28}\text{cm}^2\text{s}^{-1}$, the distance from the black hole $D = 10$pc and the time-scale for the growth of the black hole as $t_0 = 10^{10}$years the flux can be written as [9],

$$\Phi = \Phi_0 I, \tag{7.55}$$

where $\Phi_0 = 3.41\text{km}^{-2}\text{year}^{-1}$. Integrating over r for $r_{cut} = 274$ gives a total value of $I \approx 2 \times 10^7$ which gives a total flux of $\Phi \approx 7 \times 10^7 \text{km}^{-2}\text{year}^{-1}$. For 10TeV DM annihilating to high energy gamma rays the HESS experiment could be sensitive to such a large flux however the energy resolution would be smaller than the separation of the peaks [275]. For smaller values of r_{cut} resolution of the peaks becomes easier but the total flux is reduced. At $r_{cut} = 34$ the separation is potentially large enough to be observed but $I \approx 10^4$ requiring greater sensitivity or observation time.

7.10 More general cases

So far we have made three assumptions in calculating the flux, firstly that the rotating black hole is maximally rotating ($a = 1$), Secondly we considered only massless particles produced in collisions and thirdly we performed the calculation only for collisions in the equatorial plane.

The shape of the spectrum can also be considered for a non-rotating black hole and for a reasonable value of r_{cut} gives a flux very similar to the Kerr case. Figure 7.10 shows the spectrum for a non-rotating black hole with $r_{cut} = 34$ and differs from figure 7.9b by having a slightly larger flux and the peaks closer to $E = 1$. This is due to the smaller Lorentz boosts associated with the Schwarzschild black hole and a faster growing escape fraction. This is found in contrast to the spectrum in Ref. [242] where the spectrum was found to have a narrow single peak. In considering the incoming DM particles to have momenta distributed over the whole range of allowed in falling geodesics the Lorentz shifting of the peak is found to have a splitting

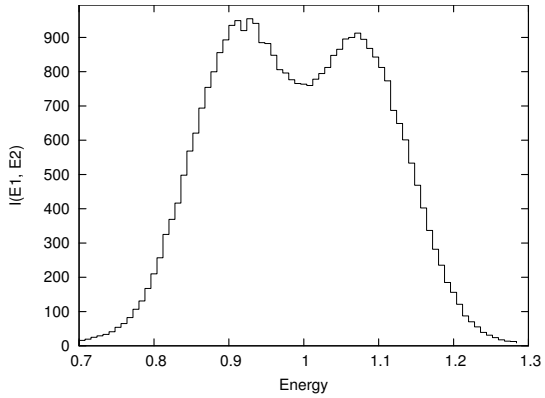

Figure 7.15: $I(r_{cut} = 34, E_1, E_2)$ for $a = 0$

effect giving rise to two peaks that accounts for this difference.

In the analysis presented here the final state particles are assumed to be massless, however the final result is not changed for massive particles so long as the mass is small compared to the mass of the colliding particles. This will certainly be true for neutrinos in models where the DM mass is of the order of few GeV and above. The numerical calculation can be trivially expanded to include a mass term for the escaping particles and we find little change in the resulting spectrum even for final state particles with a mass up to half that of the DM particle.

In the numerical analysis carried out the collisions were assumed to take place in the equatorial plane and the escape fraction and spectrum were taken to be independent of the initial polar angle θ_0 at which the collision takes place. The results were checked for collisions at $\theta_0 = 0.6$ for $r_{cut} = 34$ and the spectrum retains the same structure with a lower total flux but the same separation between peaks. It would therefore appear that the radial dependence of the energy spectrum dominates over any θ_0 dependence. For small r the spectrum will differ due to the dependence of the radius of the ergosphere on θ however for reasonable value of r_{cut} the spectrum is dominated by collisions far beyond the ergosphere.

In calculating the energy spectrum we assumed that the annihilation cross-section of the DM was independent of the centre of mass energy, for a particular DM model the energy dependence of the cross section could modify the shape of the spectrum. The cross-section would need to be found for each Monte-Carlo generated collision as the centre of mass energy changes for each pair of colliding particles.

Chapter 8

Conclusions and future outlook

In this thesis we have shown that the problem of dark matter is a major motivation for beyond the standard model physics. The production of DM in the early universe is a key component to any model of DM. We have seen that freeze-in presents an alternative to the standard freeze-out production and that this introduced new signals for DM, some of which we have explored here.

We have shown that the freeze-in production of FIMP DM can lead to a long lived LOSP particle that produces displaced vertices when it decays at the LHC. The lifetime of the LOSP is governed by the small coupling of the FIMP which links the production mechanism to of the FIMP in the early universe to the phenomenology of the visible decay of a long lived particle that can be produced at the LHC. It was shown that existing searches can be sensitive to these models but that the signals generated by LOSP decays at the LHC can evade standard BSM searches and may not show up as deviations in the standard model analyses. It was shown that displaced muons can be a very powerful discriminator from standard model backgrounds but that cuts on the angular separation of displaced muon pairs used to reject contamination from cosmic rays can reduce the sensitivity to these signals. Overall we see that the LOSP decays require their own search strategies as the events deviate from the normal SUSY signals and the type of search that will be most sensitive to the FIMP models depends on the form of the FIMP coupling to the visible particles. There is a large scope for future work in this area, the searches were applied to direct chargino production which has the cleanest signals but is the dominant SUSY particle production mechanism for only a small region of the parameter space. A more realistic search strategy could be to look at gluino or squark production and subsequent decay chains. There are many different couplings that the FIMP could have and it would be useful to

compare the signals created by these.

We have also explored another area of freeze-in phenomenology in the form of the regeneration of a WIMP abundance through the decays of a FIMP. We saw that this mechanism can indeed rescue areas of parameter space where the freeze-out production of the WIMP is insufficient to explain the DM abundance. We showed that such regions are easily found in the pMSSM while satisfying other experimental bounds. When applying the limits from indirect and direct DM searches it was shown that the two methods are quite complimentary probing different regions of parameter space. Direct detection proves most constraining when resonance annihilation through the Z and Higgs boson dominates the freeze-out abundance and indirect detection constrains WIMPs that freeze-out with a low abundance due to co-annihilations with charginos. In both cases we saw that the most under-abundant scenarios are the first to be ruled out by the DM searches due to the larger WIMP cross sections and that in these scenarios there is already a minimum limit of around 1% to the amount of DM produced by freeze-out ruling out an entirely freeze-in dominated scenario. This work investigated the regeneration scenario for the MSSM but future work could expand on this by analysing regeneration scenarios in other models such as the NMSSM or non-SUSY models. The effect of the LHC limits on sparticles was not fully addressed and these should also be included in future work. A final consideration for regeneration models is that while the free parameters of the freeze-in sector are generally enough to fix the relic abundance to the correct value we did not consider any limits that could arise from freeze-in. For example the effect of the late FIMP decays to the WIMP may perturb BBN or face limits from structure formation by producing a hot DM relic and specific models may face their own limits on the FIMP coupling.

We have also presented an alternative area of DM phenomenology in the form of collisions close to rotating black holes. The idea that collisions between DM particles close to a rotating black hole can have a very large centre of mass energy was introduced and the numerical calculation of the flux of escaping particles presented. The resulting escape fraction and energy spectrum showed that photons or neutrinos produced in these collisions can indeed escape from the black hole and that the resulting energy spectrum produces a distinctive shape. It was demonstrated how this shape depends on the profile of the DM density around the black hole. If observed the escaping particles from these collisions would present both a striking signal for the evidence of DM and its mass as well allowing the distribution of DM around black holes to be

probed. So far no evidence for DM annihilation around an intermediate mass black hole have been found and the distribution of DM around such an object is not known. Future work should then address what effect different types of DM distribution functions have on these signals. We employed a minimal model for the particle physics input assuming that the DM annihilates to a pair of photons or neutrinos with a constant cross section. One possible extension is to consider a cross section for DM annihilation that is energy dependent in which case the very high energy collisions close to the horizon could become the dominant source of the flux despite the smaller volume and escape fraction. This would require analysing how the annihilation plateau responds to the change in annihilation rate as the DM approaches the black hole.

Appendices

Appendix A

Plotting procedure for posterior probabilities

In this section the plotting procedure for the various plots found in Chapter. 6 is described.

The "blue" one and two dimensional posterior distributions are generated by the plotting routine `pippi` [206] and are the usual way of presenting these distributions. The one dimensional plots are generated in the usual way by marginalising over all the parameters the histogram is then normalised and an interpolating function used to generate a smooth distribution. The two dimensional plots are generated in a similar fashion but in this case the 95% and 64% confidence level intervals are calculated and plotted as contours.

For Figures. **??** and 6.7 a different procedure is used. For these plots the posterior density is indicated by plotting all of the points found by the MCMC in the appropriate plane using semi-transparent dots. The colour of the dots indicates the main annihilation channel that contributes the freeze-out abundance. In this way in areas of high posterior density the dots stack on top of each other creating a more solid colour while low probability regions remain faint. The main issue with such a method is that the high probability regions can quickly become opaque and the relative differences between the high probability regions can not be seen. The order in which the points are plotted is also important since points plotted first can become masked by the later points. For this reason the annihilation channels with the smallest probability are plotted last.

The coloured figures for comparing the regeneration with no-regeneration scenarios are probability density plots. To generate these first all of the points in the MCMC are used to calculate the confidence level intervals which are plotted as black contours. A colour map is

defined by interpolating function between the bin with maximum occupancy and the bin levels corresponding to the 64% and 95% levels. This function maps each colour to a corresponding transparency. The colour function is then used to generate density plots for each set of points corresponding to the grey, red, yellow and green regions and these plots are overlaid with the confidence level contours. In this way the transparency of the regions corresponds to the posterior density in the same fashion as the plots generated with `pippi` while still allowing the effect of the limits to be seen by the colours.

Bibliography

[1] K. Begeman, A. Broeils, R. Sanders, Extended rotation curves of spiral galaxies: Dark haloes and modified dynamics, Mon.Not.Roy.Astron.Soc. 249 (1991) 523.

[2] P. Ade, et al., Planck 2013 results. XV. CMB power spectra and likelihoodarXiv:1303.5075.

[3] K. Garrett, G. Duda, Dark Matter: A Primer, Adv.Astron. 2011 (2011) 968283. arXiv:1006.2483, doi:10.1155/2011/968283.

[4] L. J. Hall, K. Jedamzik, J. March-Russell, S. M. West, Freeze-In Production of FIMP Dark Matter, JHEP 1003 (2010) 080. arXiv:0911.1120, doi:10.1007/JHEP03(2010)080.

[5] S. P. Martin, A Supersymmetry primerarXiv:hep-ph/9709356.

[6] E. Aprile, et al., Dark Matter Results from 100 Live Days of XENON100 Data, Phys.Rev.Lett. 107 (2011) 131302. arXiv:1104.2549, doi:10.1103/PhysRevLett.107.131302.

[7] A. Geringer-Sameth, S. M. Koushiappas, Exclusion of canonical WIMPs by the joint analysis of Milky Way dwarfs with Fermi, Phys. Rev. Lett. 107 (2011) 241303. arXiv:1108.2914, doi:10.1103/PhysRevLett.107.241303.

[8] M. Banados, J. Silk, S. M. West, Kerr Black Holes as Particle Accelerators to Arbitrarily High Energy, Phys.Rev.Lett. 103 (2009) 111102. arXiv:0909.0169, doi:10.1103/PhysRevLett.103.111102.

[9] M. Banados, B. Hassanain, J. Silk, S. M. West, Emergent Flux from Particle Collisions Near a Kerr Black Hole, Phys.Rev. D83 (2011) 023004. arXiv:1010.2724, doi:10.1103/PhysRevD.83.023004.

[10] K. Nakamura, et al., Review of particle physics, J. Phys. G37 (2010) 075021. doi:10.1088/0954-3899/37/7A/075021.

[11] D. Clowe, M. Bradac, A. H. Gonzalez, M. Markevitch, S. W. Randall, et al., A direct empirical proof of the existence of dark matter, Astrophys.J. 648 (2006) L109–L113. arXiv:astro-ph/0608407, doi:10.1086/508162.

[12] P. Ade, et al., Planck 2013 results. XVI. Cosmological parametersarXiv:1303.5076.

[13] E. W. Kolb, M. S. Turner, The Early universe, Front.Phys. 69 (1990) 1–547.

[14] G. Bertone, D. Hooper, J. Silk, Particle dark matter: Evidence, candidates and constraints, Phys.Rept. 405 (2005) 279–390. arXiv:hep-ph/0404175, doi:10.1016/j.physrep.2004.08.031.

[15] V. C. Rubin, J. Ford, W. Kent, Rotation of the Andromeda Nebula from a Spectroscopic Survey of Emission Regions, Astrophys.J. 159 (1970) 379–403. doi:10.1086/150317.

[16] V. Rubin, N. Thonnard, J. Ford, W.K., Rotational properties of 21 SC galaxies with a large range of luminosities and radii, from NGC 4605 /R = 4kpc/ to UGC 2885 /R = 122 kpc/, Astrophys.J. 238 (1980) 471. doi:10.1086/158003.

[17] W. de Blok, S. S. McGaugh, A. Bosma, V. C. Rubin, Mass density profiles of LSB galaxies, Astrophys.J. 552 (2001) L23–L26. arXiv:astro-ph/0103102, doi:10.1086/320262.

[18] P. Salucci, A. Borriello, The intriguing distribution of dark matter in galaxies, Lect.Notes Phys. 616 (2003) 66–77. arXiv:astro-ph/0203457.

[19] D. Reed, F. Governato, L. Verde, J. Gardner, T. R. Quinn, et al., Evolution of the density profiles of dark matter halos, Mon.Not.Roy.Astron.Soc. 357 (2005) 82–96. arXiv:astro-ph/0312544, doi:10.1111/j.1365-2966.2005.08612.x/abs/.

[20] J. Bovy, S. Tremaine, On the local dark matter density, Astrophys.J. 756 (2012) 89. arXiv:1205.4033, doi:10.1088/0004-637X/756/1/89.

[21] R. Catena, P. Ullio, A novel determination of the local dark matter density, JCAP 1008 (2010) 004. arXiv:0907.0018, doi:10.1088/1475-7516/2010/08/004.

[22] L. A. Moustakas, R. B. Metcalf, Detecting dark matter substructure spectroscopically in strong gravitational lenses, Mon.Not.Roy.Astron.Soc. 339 (2003) 607. arXiv:astro-ph/0206176, doi:10.1046/j.1365-8711.2003.06055.x.

[23] R. B. Metcalf, L. A. Moustakas, A. J. Bunker, I. R. Parry, Spectroscopic gravitational lensing and limits on the dark matter substructure in Q2237+0305, Astrophys.J. 607 (2004) 43–59. arXiv:astro-ph/0309738, doi:10.1086/383243.

[24] A. More, J. P. McKean, S. More, R. W. Porcas, L. V. E. Koopmans, M. A. Garrett, The role of luminous substructure in the gravitational lens system mg 2016+112, Monthly Notices of the Royal Astronomical Society 394 (1) (2009) 174–190. arXiv:http://mnras.oxfordjournals.org/content/394/1/174.full.pdf+html, doi:10.1111/j.1365-2966.2008.14342.x.

[25] H. Hoekstra, H. Yee, M. Gladders, Current status of weak gravitational lensing, New Astron.Rev. 46 (2002) 767–781. arXiv:astro-ph/0205205, doi:10.1016/S1387-6473(02)00245-2.

[26] M. Mateo, E. W. Olszewski, S. S. Vogt, M. J. Keane, The internal kinematics of the leo I dwarf spheroidal galaxy: dark matter at the fringe of the milky way, Astron.J. 116 (1998) 2315–2327. arXiv:astro-ph/9807296, doi:10.1086/300618.

[27] M. Mateo, Dwarf galaxies of the Local Group, Ann.Rev.Astron.Astrophys. 36 (1998) 435–506. arXiv:astro-ph/9810070, doi:10.1146/annurev.astro.36.1.435.

[28] F. Zwicky, Spectral displacement of extra galactic nebulae, Helv.Phys.Acta 6 (1933) 110–127.

[29] N. A. Bahcall, X.-h. Fan, The Most massive distant clusters: Determining omega and sigma_8, Astrophys.J. 504 (1998) 1. arXiv:astro-ph/9803277, doi:10.1086/306088.

[30] A. Kashlinsky, Determining Omega from cluster correlation function, Phys.Rept. 307 (1998) 67–73. arXiv:astro-ph/9806236, doi:10.1016/S0370-1573(98)00050-7.

[31] M. Birkinshaw, The Sunyaev-Zel'dovich effect, Phys.Rept. 310 (1999) 97–195. arXiv:astro-ph/9808050, doi:10.1016/S0370-1573(98)00080-5.

[32] C. L. Bennett, et al., Seven-Year Wilkinson Microwave Anisotropy Probe (WMAP) Observations: Are There Cosmic Microwave Background Anomalies?, Astrophys. J. Suppl. 192 (2011) 17. arXiv:1001.4758, doi:10.1088/0067-0049/192/2/17.

[33] P. Ade, et al., Planck 2013 results. I. Overview of products and scientific resultsarXiv:1303.5062.

[34] N. Jarosik, C. Bennett, J. Dunkley, B. Gold, M. Greason, et al., Seven-Year Wilkinson Microwave Anisotropy Probe (WMAP) Observations: Sky Maps, Systematic Errors, and Basic Results, Astrophys.J.Suppl. 192 (2011) 14. arXiv:1001.4744, doi:10.1088/0067-0049/192/2/14.

[35] A. Lewis, S. Bridle, Cosmological parameters from CMB and other data: A Monte Carlo approach, Phys.Rev. D66 (2002) 103511. arXiv:astro-ph/0205436, doi:10.1103/PhysRevD.66.103511.

[36] M. Tegmark, et al., Cosmological parameters from SDSS and WMAP, Phys.Rev. D69 (2004) 103501. arXiv:astro-ph/0310723, doi:10.1103/PhysRevD.69.103501.

[37] R. Mandelbaum, A. Slosar, T. Baldauf, U. Seljak, C. M. Hirata, et al., Cosmological parameter constraints from galaxy-galaxy lensing and galaxy clustering with the SDSS DR7arXiv:1207.1120.

[38] C. P. Ahn, et al., The Ninth Data Release of the Sloan Digital Sky Survey: First Spectroscopic Data from the SDSS-III Baryon Oscillation Spectroscopic Survey, Astrophys.J.Suppl. 203 (2012) 21. arXiv:1207.7137, doi:10.1088/0067-0049/203/2/21.

[39] M. Boylan-Kolchin, V. Springel, S. D. White, A. Jenkins, G. Lemson, Resolving Cosmic Structure Formation with the Millennium-II Simulation, Mon.Not.Roy.Astron.Soc. 398 (2009) 1150. arXiv:0903.3041, doi:10.1111/j.1365-2966.2009.15191.x.

[40] P. Peebles, Large scale background temperature and mass fluctuations due to scale invariant primeval perturbations, Astrophys.J. 263 (1982) L1–L5.

[41] A. Jenkins, C. S. Frenk, F. R. Pearce, P. A. Thomas, J. M. Colberg, S. D. M. White, H. M. P. Couchman, J. A. Peacock, G. Efstathiou, A. H. Nelson, Evolution of structure in

cold dark matter universes, The Astrophysical Journal 499 (1) (1998) 20.
URL http://stacks.iop.org/0004-637X/499/i=1/a=20

[42] G. Bertone, Particle dark matter: Observations, models and searches.

[43] T. Appelquist, H.-C. Cheng, B. A. Dobrescu, Bounds on universal extra dimensions, Phys.Rev. D64 (2001) 035002. arXiv:hep-ph/0012100, doi:10.1103/PhysRevD.64.035002.

[44] G. Servant, T. M. Tait, Is the lightest Kaluza-Klein particle a viable dark matter candidate?, Nucl.Phys. B650 (2003) 391–419. arXiv:hep-ph/0206071, doi:10.1016/S0550-3213(02)01012-X.

[45] H.-C. Cheng, J. L. Feng, K. T. Matchev, Kaluza-Klein dark matter, Phys.Rev.Lett. 89 (2002) 211301. arXiv:hep-ph/0207125, doi:10.1103/PhysRevLett.89.211301.

[46] M. Kakizaki, S. Matsumoto, M. Senami, Relic abundance of dark matter in the minimal universal extra dimension model, Phys.Rev. D74 (2006) 023504. arXiv:hep-ph/0605280, doi:10.1103/PhysRevD.74.023504.

[47] N. Arkani-Hamed, A. G. Cohen, H. Georgi, Electroweak symmetry breaking from dimensional deconstruction, Phys.Lett. B513 (2001) 232–240. arXiv:hep-ph/0105239, doi:10.1016/S0370-2693(01)00741-9.

[48] N. Arkani-Hamed, A. G. Cohen, T. Gregoire, J. G. Wacker, Phenomenology of electroweak symmetry breaking from theory space, JHEP 0208 (2002) 020. arXiv:hep-ph/0202089.

[49] M. Schmaltz, D. Tucker-Smith, Little Higgs review, Ann.Rev.Nucl.Part.Sci. 55 (2005) 229–270. arXiv:hep-ph/0502182, doi:10.1146/annurev.nucl.55.090704.151502.

[50] H.-C. Cheng, I. Low, TeV symmetry and the little hierarchy problem, JHEP 0309 (2003) 051. arXiv:hep-ph/0308199.

[51] H.-C. Cheng, I. Low, Little hierarchy, little Higgses, and a little symmetry, JHEP 0408 (2004) 061. arXiv:hep-ph/0405243, doi:10.1088/1126-6708/2004/08/061.

[52] A. Birkedal, A. Noble, M. Perelstein, A. Spray, Little Higgs dark matter, Phys.Rev. D74 (2006) 035002. arXiv:hep-ph/0603077, doi:10.1103/PhysRevD.74.035002.

[53] J. L. Feng, A. Rajaraman, F. Takayama, Superweakly interacting massive particles, Phys.Rev.Lett. 91 (2003) 011302. arXiv:hep-ph/0302215, doi:10.1103/PhysRevLett.91.011302.

[54] J. R. Ellis, K. A. Olive, Y. Santoso, V. C. Spanos, Gravitino dark matter in the CMSSM, Phys.Lett. B588 (2004) 7–16. arXiv:hep-ph/0312262, doi:10.1016/j.physletb.2004.03.021.

[55] J. L. Feng, A. Rajaraman, F. Takayama, SuperWIMP dark matter signals from the early universe, Phys.Rev. D68 (2003) 063504. arXiv:hep-ph/0306024, doi:10.1103/PhysRevD.68.063504.

[56] W. Buchmuller, K. Hamaguchi, M. Ratz, T. Yanagida, Supergravity at colliders, Phys.Lett. B588 (2004) 90–98. arXiv:hep-ph/0402179, doi:10.1016/j.physletb.2004.03.016.

[57] J. L. Feng, S. Su, F. Takayama, Supergravity with a gravitino LSP, Phys.Rev. D70 (2004) 075019. arXiv:hep-ph/0404231, doi:10.1103/PhysRevD.70.075019.

[58] F. Wang, J. M. Yang, SuperWIMP dark matter scenario in light of WMAP, Eur.Phys.J. C38 (2004) 129–133. arXiv:hep-ph/0405186, doi:10.1140/epjc/s2004-02029-6.

[59] L. Roszkowski, R. Ruiz de Austri, K.-Y. Choi, Gravitino dark matter in the CMSSM and implications for leptogenesis and the LHC, JHEP 0508 (2005) 080. arXiv:hep-ph/0408227, doi:10.1088/1126-6708/2005/08/080.

[60] J. L. Feng, A. Rajaraman, F. Takayama, Graviton cosmology in universal extra dimensions, Phys.Rev. D68 (2003) 085018. arXiv:hep-ph/0307375, doi:10.1103/PhysRevD.68.085018.

[61] J. L. Feng, J. Kumar, The WIMPless Miracle: Dark-Matter Particles without Weak-Scale Masses or Weak Interactions, Phys.Rev.Lett. 101 (2008) 231301. arXiv:0803.4196, doi:10.1103/PhysRevLett.101.231301.

[62] M. Dine, A. E. Nelson, Y. Shirman, Low-energy dynamical supersymmetry breaking simplified, Phys.Rev. D51 (1995) 1362–1370. arXiv:hep-ph/9408384, doi:10.1103/PhysRevD.51.1362.

[63] M. Dine, A. E. Nelson, Y. Nir, Y. Shirman, New tools for low-energy dynamical supersymmetry breaking, Phys.Rev. D53 (1996) 2658–2669. arXiv:hep-ph/9507378, doi:10.1103/PhysRevD.53.2658.

[64] D. Hooper, K. M. Zurek, A Natural Supersymmetric Model with MeV Dark Matter, Phys.Rev. D77 (2008) 087302. arXiv:0801.3686, doi:10.1103/PhysRevD.77.087302.

[65] R. Peccei, H. R. Quinn, Constraints Imposed by CP Conservation in the Presence of Instantons, Phys.Rev. D16 (1977) 1791–1797. doi:10.1103/PhysRevD.16.1791.

[66] R. Peccei, H. R. Quinn, CP Conservation in the Presence of Instantons, Phys.Rev.Lett. 38 (1977) 1440–1443. doi:10.1103/PhysRevLett.38.1440.

[67] S. Weinberg, A New Light Boson?, Phys.Rev.Lett. 40 (1978) 223–226. doi:10.1103/PhysRevLett.40.223.

[68] F. Wilczek, Problem of Strong p and t Invariance in the Presence of Instantons, Phys.Rev.Lett. 40 (1978) 279–282. doi:10.1103/PhysRevLett.40.279.

[69] M. S. Turner, Windows on the Axion, Phys.Rept. 197 (1990) 67–97. doi:10.1016/0370-1573(90)90172-X.

[70] G. G. Raffelt, D. S. P. Dearborn, Bounds on hadronic axions from stellar evolution, Phys. Rev. D 36 (1987) 2211–2225. doi:10.1103/PhysRevD.36.2211.
URL http://link.aps.org/doi/10.1103/PhysRevD.36.2211

[71] G. G. Raffelt, Astrophysical methods to constrain axions and other novel particle phenomena, Phys.Rept. 198 (1990) 1–113. doi:10.1016/0370-1573(90)90054-6.

[72] D. A. Dicus, E. W. Kolb, V. L. Teplitz, R. V. Wagoner, Astrophysical bounds on very-low-mass axions, Phys. Rev. D 22 (1980) 839–845. doi:10.1103/PhysRevD.22.839.
URL http://link.aps.org/doi/10.1103/PhysRevD.22.839

[73] Y. Wong, S. Hannestad, A. Mirizzi, G. Raffelt, Cosmological limits on axions, AIP Conf.Proc. 1115 (2009) 303–307. doi:10.1063/1.3131516.

[74] R. A. Battye, E. P. S. Shellard, Axion string constraints, Phys. Rev. Lett. 73 (1994) 2954–2957. doi:10.1103/PhysRevLett.73.2954.
URL http://link.aps.org/doi/10.1103/PhysRevLett.73.2954

[75] M. Yamaguchi, M. Kawasaki, J. Yokoyama, Evolution of axionic strings and spectrum of axions radiated from them, Phys. Rev. Lett. 82 (1999) 4578–4581. doi:10.1103/PhysRevLett.82.4578.
URL http://link.aps.org/doi/10.1103/PhysRevLett.82.4578

[76] S. Chang, C. Hagmann, P. Sikivie, Studies of the motion and decay of axion walls bounded by strings, Phys. Rev. D 59 (1998) 023505. doi:10.1103/PhysRevD.59.023505.
URL http://link.aps.org/doi/10.1103/PhysRevD.59.023505

[77] C. Hagmann, S. Chang, P. Sikivie, Axion radiation from strings, Phys. Rev. D 63 (2001) 125018. doi:10.1103/PhysRevD.63.125018.
URL http://link.aps.org/doi/10.1103/PhysRevD.63.125018

[78] K. J. Bae, J.-H. Huh, J. E. Kim, Update of axion CDM energy, JCAP 0809 (2008) 005. arXiv:0806.0497, doi:10.1088/1475-7516/2008/09/005.

[79] S. Dodelson, L. M. Widrow, Sterile neutrinos as dark matter, Phys. Rev. Lett. 72 (1994) 17–20. doi:10.1103/PhysRevLett.72.17.
URL http://link.aps.org/doi/10.1103/PhysRevLett.72.17

[80] T. Asaka, M. Shaposhnikov, M. Laine, Lightest sterile neutrino abundance within the msm, Journal of High Energy Physics 2007 (01) (2007) 091.
URL http://stacks.iop.org/1126-6708/2007/i=01/a=091

[81] A. Kusenko, Sterile neutrinos, dark matter, and pulsar velocities in models with a higgs singlet, Phys. Rev. Lett. 97 (2006) 241301. doi:10.1103/PhysRevLett.97.241301.
URL http://link.aps.org/doi/10.1103/PhysRevLett.97.241301

[82] M. Shaposhnikov, I. Tkachev, The msm, inflation, and dark matter, Physics Letters B 639 (5) (2006) 414 – 417. doi:10.1016/j.physletb.2006.06.063.
URL http://www.sciencedirect.com/science/article/pii/S0370269306008124

[83] K. Petraki, A. Kusenko, Dark-matter sterile neutrinos in models with a gauge singlet in the higgs sector, Phys. Rev. D 77 (2008) 065014. doi:10.1103/PhysRevD.77.065014.
URL http://link.aps.org/doi/10.1103/PhysRevD.77.065014

[84] K. N. Abazajian, Detection of Dark Matter Decay in the X-rayarXiv:0903.2040.

[85] E. Farhi, L. Susskind, Technicolor, Phys.Rept. 74 (1981) 277. doi:10.1016/0370-1573(81)90173-3.

[86] B. Holdom, Techniodor, Phys.Lett. B150 (1985) 301. doi:10.1016/0370-2693(85)91015-9.

[87] K. Yamawaki, M. Bando, K.-i. Matumoto, Scale Invariant Technicolor Model and a Technidilaton, Phys.Rev.Lett. 56 (1986) 1335. doi:10.1103/PhysRevLett.56.1335.

[88] C. T. Hill, Topcolor assisted technicolor, Phys.Lett. B345 (1995) 483–489. arXiv:hep-ph/9411426, doi:10.1016/0370-2693(94)01660-5.

[89] S. Nussinov, Technocosmology could a technibaryon excess provide a natural missing mass candidate?, Physics Letters B 165 (13) (1985) 55 – 58. doi:http://dx.doi.org/10.1016/0370-2693(85)90689-6.
URL http://www.sciencedirect.com/science/article/pii/0370269385906896

[90] R. Chivukula, T. P. Walker, Technicolor cosmology, Nuclear Physics B 329 (2) (1990) 445 – 463. doi:http://dx.doi.org/10.1016/0550-3213(90)90151-3.
URL http://www.sciencedirect.com/science/article/pii/0550321390901513

[91] J. Bagnasco, M. Dine, S. D. Thomas, Detecting technibaryon dark matter, Phys.Lett. B320 (1994) 99–104. arXiv:hep-ph/9310290, doi:10.1016/0370-2693(94)90830-3.

[92] S. B. Gudnason, C. Kouvaris, F. Sannino, Dark Matter from new Technicolor Theories, Phys.Rev. D74 (2006) 095008. arXiv:hep-ph/0608055, doi:10.1103/PhysRevD.74.095008.

[93] S. B. Gudnason, C. Kouvaris, F. Sannino, Towards working technicolor: Effective theories and dark matter, Phys.Rev. D73 (2006) 115003. arXiv:hep-ph/0603014, doi:10.1103/PhysRevD.73.115003.

[94] J. Edsjo, P. Gondolo, Neutralino relic density including coannihilations, Phys.Rev. D56 (1997) 1879–1894. arXiv:hep-ph/9704361, doi:10.1103/PhysRevD.56.1879.

[95] G. Bertone, D. Hooper, J. Silk, Particle dark matter: evidence, candidates and constraints, Physics Reports 405 (56) (2005) 279 – 390. doi:10.1016/j.physrep.2004.08.031.
URL http://www.sciencedirect.com/science/article/pii/S0370157304003515

[96] G. Belanger, F. Boudjema, A. Pukhov, A. Semenov, Micromegas, Comput.Phys.Commun. 149 (2002) 103–120. arXiv:hep-ph/0112278, doi:10.1016/S0010-4655(02)00596-9.

[97] G. Belanger, F. Boudjema, A. Pukhov, A. Semenov, micrOMEGAs2.0: A program to calculate the relic density of dark matter in a generic model, Comput. Phys. Commun. 176 (2007) 367–382. arXiv:hep-ph/0607059, doi:10.1016/j.cpc.2006.11.008.

[98] G. Belanger, F. Boudjema, A. Pukhov, A. Semenov, micrOMEGAs : a tool for dark matter studiesarXiv:1005.4133.

[99] P. Gondolo, J. Edsj, P. Ullio, L. Bergstrm, M. Schelke, E. A. Baltz, Darksusy: computing supersymmetric dark matter properties numerically, Journal of Cosmology and Astroparticle Physics 2004 (07) (2004) 008.
URL http://stacks.iop.org/1475-7516/2004/i=07/a=008

[100] S. Chatrchyan, et al., Search for Dark Matter and Large Extra Dimensions in pp Collisions Yielding a Photon and Missing Transverse Energy, Phys.Rev.Lett. 108 (2012) 261803. arXiv:1204.0821, doi:10.1103/PhysRevLett.108.261803.

[101] M. T. Frandsen, F. Kahlhoefer, A. Preston, S. Sarkar, K. Schmidt-Hoberg, LHC and Tevatron Bounds on the Dark Matter Direct Detection Cross-Section for Vector Mediators, JHEP 1207 (2012) 123. arXiv:1204.3839, doi:10.1007/JHEP07(2012)123.

[102] M. Martinez, f. t. A. Collaboration, Search for new phenomena in events with a monojet and large missing transverse momentum at the LHC using the ATLAS detector, EPJ Web Conf. 28 (2012) 12015. arXiv:1202.0158, doi:10.1051/epjconf/20122812015.

[103] H.-C. Tsai, K.-C. Yang, Dark Matter Mass Constrained by the Relic Abundance, Direct Detections, and ColliderarXiv:1301.4186.

[104] A. Barr, C. Lester, P. Stephens, m(T2): The Truth behind the glamour, J.Phys. G29 (2003) 2343–2363. arXiv:hep-ph/0304226, doi:10.1088/0954-3899/29/10/304.

[105] C. Lester, A. Barr, MTGEN: Mass scale measurements in pair-production at colliders, JHEP 0712 (2007) 102. arXiv:0708.1028, doi:10.1088/1126-6708/2007/12/102.

[106] M. Serna, A short comparison between m t 2 and m ct, Journal of High Energy Physics 2008 (06) (2008) 004.
URL http://stacks.iop.org/1126-6708/2008/i=06/a=004

[107] M. Burns, K. Kong, K. T. Matchev, M. Park, Using Subsystem MT2 for Complete Mass Determinations in Decay Chains with Missing Energy at Hadron Colliders, JHEP 0903 (2009) 143. arXiv:0810.5576, doi:10.1088/1126-6708/2009/03/143.

[108] Y. B. Zel'dovich, Zh. Eksp. Teor. Fiz 48 (1965) 986.

[109] Y. B. Zel'dovich, L. B. Okun, P. S. B., Usp. Fiz. Nauk 84 (1965) 113.

[110] H. Y. Chiu, Phys. Rev. Lett. 17 (1966) 712.

[111] G. Brooijmans, B. Gripaios, F. Moortgat, J. Santiago, P. Skands, et al., Les Houches 2011: Physics at TeV Colliders New Physics Working Group ReportarXiv:1203.1488.

[112] C. Cheung, G. Elor, L. J. Hall, P. Kumar, Origins of Hidden Sector Dark Matter II: Collider Physics, JHEP 1103 (2011) 085. arXiv:1010.0024, doi:10.1007/JHEP03(2011)085.

[113] A. J. Williams, C. Boehm, S. M. West, D. A. Vasquez, Regenerating WIMPs in the Light of Direct and Indirect Detection, Phys.Rev. D86 (2012) 055018. arXiv:1204.3727, doi:10.1103/PhysRevD.86.055018.

[114] K. Jedamzik, Big bang nucleosynthesis constraints on hadronically and electromagnetically decaying relic neutral particles, Phys. Rev. D74 (2006) 103509. arXiv:hep-ph/0604251, doi:10.1103/PhysRevD.74.103509.

[115] M. Drewes, On the Role of Quasiparticles and thermal Masses in Nonequilibrium Processes in a PlasmaarXiv:1012.5380.

[116] K. Hamaguchi, T. Moroi, K. Mukaida, Boltzmann equation for non-equilibrium particles and its application to non-thermal dark matter production, JHEP 1201 (2012) 083. arXiv:1111.4594, doi:10.1007/JHEP01(2012)083.

[117] K. Jedamzik, S. M. West, A. J. Williams, In preperation.

[118] U. Amaldi, W. de Boer, H. Furstenau, Comparison of grand unified theories with electroweak and strong coupling constants measured at LEP, Phys.Lett. B260 (1991) 447–455. doi:10.1016/0370-2693(91)91641-8.

[119] R. Haag, J. T. Lopuszanski, M. Sohnius, All Possible Generators of Supersymmetries of the s Matrix, Nucl.Phys. B88 (1975) 257. doi:10.1016/0550-3213(75)90279-5.

[120] S. R. Coleman, J. Mandula, ALL POSSIBLE SYMMETRIES OF THE S MATRIX, Phys.Rev. 159 (1967) 1251–1256. doi:10.1103/PhysRev.159.1251.

[121] S. Dimopoulos, D. W. Sutter, The Supersymmetric flavor problem, Nucl.Phys. B452 (1995) 496–512. arXiv:hep-ph/9504415, doi:10.1016/0550-3213(95)00421-N.

[122] G. L. Kane, C. F. Kolda, L. Roszkowski, J. D. Wells, Study of constrained minimal supersymmetry, Phys.Rev. D49 (1994) 6173–6210. arXiv:hep-ph/9312272, doi:10.1103/PhysRevD.49.6173.

[123] V. Bertin, E. Nezri, J. Orloff, Neutralino dark matter beyond CMSSM universality, JHEP 0302 (2003) 046. arXiv:hep-ph/0210034.

[124] A. Birkedal-Hansen, B. D. Nelson, Relic neutralino densities and detection rates with nonuniversal gaugino masses, Phys.Rev. D67 (2003) 095006. arXiv:hep-ph/0211071, doi:10.1103/PhysRevD.67.095006.

[125] S. Sekmen, S. Kraml, J. Lykken, F. Moortgat, S. Padhi, et al., Interpreting LHC SUSY searches in the phenomenological MSSMarXiv:1109.5119.

[126] A. Arbey, M. Battaglia, F. Mahmoudi, Implications of LHC Searches on SUSY Particle Spectra: The pMSSM Parameter Space with Neutralino Dark Matter, Eur.Phys.J. C72 (2012) 1847. arXiv:1110.3726, doi:10.1140/epjc/s10052-011-1847-3.

[127] S. S. AbdusSalam, LHC-7 supersymmetry search interpretation within the pMSSMarXiv:1211.0999.

[128] M. W. Cahill-Rowley, J. L. Hewett, S. Hoeche, A. Ismail, T. G. Rizzo, The New Look pMSSM with Neutralino and Gravitino LSPs, Eur.Phys.J. C72 (2012) 2156. arXiv:1206.4321, doi:10.1140/epjc/s10052-012-2156-1.

[129] E. Komatsu, et al., Seven-Year Wilkinson Microwave Anisotropy Probe (WMAP) Observations: Cosmological Interpretation, Astrophys.J.Suppl. 192 (2011) 18. arXiv:1001.4538, doi:10.1088/0067-0049/192/2/18.

[130] D. Hooper, J. March-Russell, S. M. West, Asymmetric sneutrino dark matter and the Omega(b) / Omega(DM) puzzle, Phys.Lett. B605 (2005) 228–236. arXiv:hep-ph/0410114, doi:10.1016/j.physletb.2004.11.047.

[131] D. E. Kaplan, M. A. Luty, K. M. Zurek, Asymmetric Dark Matter, Phys.Rev. D79 (2009) 115016. arXiv:0901.4117, doi:10.1103/PhysRevD.79.115016.

[132] S. Chang, M. A. Luty, Displaced Dark Matter at CollidersarXiv:0906.5013.

[133] S. P. Martin, Collider signals from slow decays in supersymmetric models with an intermediate scale solution to the mu problem, Phys.Rev. D62 (2000) 095008. arXiv:hep-ph/0005116, doi:10.1103/PhysRevD.62.095008.

[134] G. Aad, et al., Search for displaced muonic lepton jets from light Higgs boson decay in proton-proton collisions at $\sqrt{s} = 7$ TeV with the ATLAS detector, Phys.Lett. B721 (2013) 32–50. arXiv:1210.0435, doi:10.1016/j.physletb.2013.02.058.

[135] S. Chatrchyan, et al., Search in leptonic channels for heavy resonances decaying to long-lived neutral particles, JHEP 1302 (2013) 085. arXiv:1211.2472, doi:10.1007/JHEP02(2013)085.

[136] J. Alwall, M. Herquet, F. Maltoni, O. Mattelaer, T. Stelzer, MadGraph 5 : Going Beyond, JHEP 1106 (2011) 128. arXiv:1106.0522, doi:10.1007/JHEP06(2011)128.

[137] A. Pukhov, CalcHEP 2.3: MSSM, structure functions, event generation, batchs, and generation of matrix elements for other packagesarXiv:hep-ph/0412191.

[138] G. D. Kribs, A. Martin, T. S. Roy, Supersymmetry with a Chargino NLSP and Gravitino LSP, JHEP 0901 (2009) 023. arXiv:0807.4936, doi:10.1088/1126-6708/2009/01/023.

[139] N. D. Christensen, C. Duhr, FeynRules - Feynman rules made easy, Comput.Phys.Commun. 180 (2009) 1614–1641. arXiv:0806.4194, doi:10.1016/j.cpc.2009.02.018.

[140] C. Duhr, B. Fuks, A superspace module for the FeynRules package, Comput. Phys. Commun. 182 (2011) 2404–2426. arXiv:1102.4191, doi:10.1016/j.cpc.2011.06.009.

[141] P. Meade, M. Reece, BRIDGE: Branching ratio inquiry / decay generated eventsarXiv:hep-ph/0703031.

[142] T. Sjostrand, S. Mrenna, P. Z. Skands, PYTHIA 6.4 Physics and Manual, JHEP 0605 (2006) 026. arXiv:hep-ph/0603175, doi:10.1088/1126-6708/2006/05/026.

[143] T. Sjostrand, S. Mrenna, P. Z. Skands, A Brief Introduction to PYTHIA 8.1, Comput.Phys.Commun. 178 (2008) 852–867. arXiv:0710.3820, doi:10.1016/j.cpc.2008.01.036.

[144] P. Z. Skands, et al., SUSY Les Houches Accord: Interfacing SUSY Spectrum Calculators, Decay Packages, and Event Generators, JHEP 07 (2004) 036. arXiv:hep-ph/0311123, doi:10.1088/1126-6708/2004/07/036.

[145] J. Alwall, A. Ballestrero, P. Bartalini, S. Belov, E. Boos, et al., A Standard format for Les Houches event files, Comput.Phys.Commun. 176 (2007) 300–304. arXiv:hep-ph/0609017, doi:10.1016/j.cpc.2006.11.010.

[146] M. Dobbs, J. B. Hansen, The HepMC C++ Monte Carlo event record for High Energy Physics, Comput.Phys.Commun. 134 (2001) 41–46. doi:10.1016/S0010-4655(00)00189-2.

[147] T. C. Collaboration, Search for long-lived exotica decaying to displaced leptonsarXiv:CMSPASEXO-11-004.

[148] A. L. Scott, Search for long-lived parents of the Z^0 boson, Int.J.Mod.Phys. A20 (2005) 3263–3266. arXiv:hep-ex/0410019, doi:10.1142/S0217751X05026297.

[149] V. Abazov, et al., Search for neutral, long-lived particles decaying into two muons in $p\overline{p}$ collisions at $\sqrt{s}$ = 1.96-TeV, Phys.Rev.Lett. 97 (2006) 161802. arXiv:hep-ex/0607028, doi:10.1103/PhysRevLett.97.161802.

[150] G. Aad, et al., Measurement of the inclusive W+- and Z/gamma cross sections in the electron and muon decay channels in pp collisions at sqrt(s) = 7 TeV with the ATLAS detectorarXiv:1109.5141.

[151] E. Komatsu, et al., Seven-Year Wilkinson Microwave Anisotropy Probe (WMAP) Observations: Cosmological Interpretation, Astrophys.J.Suppl. 192 (2011) 18. arXiv:1001.4538, doi:10.1088/0067-0049/192/2/18.

[152] K. Griest, D. Seckel, Three exceptions in the calculation of relic abundances, Phys.Rev. D43 (1991) 3191–3203. doi:10.1103/PhysRevD.43.3191.

[153] P. Binetruy, G. Girardi, P. Salati, CONSTRAINTS ON A SYSTEM OF TWO NEUTRAL FERMIONS FROM COSMOLOGY, Nucl.Phys. B237 (1984) 285. doi:10.1016/0550-3213(84)90161-5.

[154] A. Abdo, M. Ackermann, M. Ajello, W. Atwood, L. Baldini, et al., Observations of Milky Way Dwarf Spheroidal galaxies with the Fermi-LAT detector and constraints on Dark Matter models, Astrophys.J. 712 (2010) 147–158, * Temporary entry *. arXiv:1001.4531, doi:10.1088/0004-637X/712/1/147.

[155] K. Griest, L. Roszkowski, Effect of relaxing grand unification assumptions on neutralinos in the minimal supersymmetric model, Phys.Rev. D46 (1992) 3309–3317. doi:10.1103/PhysRevD.46.3309.

[156] K. Griest, M. Kamionkowski, M. S. Turner, Supersymmetric Dark Matter Above the W Mass, Phys.Rev. D41 (1990) 3565–3582. doi:10.1103/PhysRevD.41.3565.

[157] M. Drees, M. M. Nojiri, The Neutralino relic density in minimal $N = 1$ supergravity, Phys.Rev. D47 (1993) 376–408. arXiv:hep-ph/9207234, doi:10.1103/PhysRevD.47.376.

[158] L. Roszkowski, R. Ruiz de Austri, T. Nihei, New cosmological and experimental constraints on the CMSSM, JHEP 0108 (2001) 024. arXiv:hep-ph/0106334.

[159] O. Buchmueller, R. Cavanaugh, D. Colling, A. De Roeck, M. Dolan, et al., Supersymmetry and Dark Matter in Light of LHC 2010 and Xenon100 Data, Eur.Phys.J. C71 (2011) 1722. arXiv:1106.2529, doi:10.1140/epjc/s10052-011-1722-2.

[160] J. Ellis, T. Hahn, S. Heinemeyer, K. Olive, G. Weiglein, WMAP-Compliant Benchmark Surfaces for MSSM Higgs Bosons, JHEP 0710 (2007) 092. arXiv:0709.0098, doi:10.1088/1126-6708/2007/10/092.

[161] V. D. Barger, C. Kao, Implications of new CMB data for neutralino dark matter, Phys.Lett. B518 (2001) 117–122. arXiv:hep-ph/0106189, doi:10.1016/S0370-2693(01)01046-2.

[162] J. Ellis, K. A. Olive, Revisiting the Higgs Mass and Dark Matter in the CMSSMarXiv:1202.3262.

[163] N. Bhattacharyya, A. Choudhury, A. Datta, Low mass neutralino dark matter in mSUGRA and more general models in the light of LHC data, Phys.Rev. D84 (2011) 095006. arXiv:1107.1997, doi:10.1103/PhysRevD.84.095006.

[164] A. Choudhury, A. Datta, Many faces of low mass neutralino dark matter in the unconstrained MSSM and new signals at the LHC26 pages, 1 figure. arXiv:1203.4106.

[165] D. A. Vasquez, G. Belanger, C. Boehm, A. Pukhov, J. Silk, Can neutralinos in the MSSM and NMSSM scenarios still be light?arXiv:1009.4380.

[166] D. Albornoz Vasquez, G. Belanger, C. Boehm, Revisiting light neutralino scenarios in the MSSM, Phys.Rev. D84 (2011) 095015. arXiv:1108.1338, doi:10.1103/PhysRevD.84.095015.

[167] D. Sivia, Data Analysis: A Bayesian Tutorial, Oxford Science Publications, Clarendon Press, 1996.
URL http://books.google.co.uk/books?id=wR5yljKasLsC

[168] P. Gregory, Bayesian logical data analysis for the physical sciences, Vol. 10, Cambridge University Press Cambridge, UK, 2005.

[169] R. Trotta, Bayes in the sky: Bayesian inference and model selection in cosmology, Contemp.Phys. 49 (2008) 71–104. arXiv:0803.4089, doi:10.1080/00107510802066753.

[170] R. R. de Austri, R. Trotta, L. Roszkowski, A Markov chain Monte Carlo analysis of the CMSSM, JHEP 0605 (2006) 002. arXiv:hep-ph/0602028, doi:10.1088/1126-6708/2006/05/002.

[171] R. Neal, Technical report crg-tr-93-1, University of Toronto (ftp://ftp. utoronto. ca/pub/radford/review. ps).

[172] R. M. Neal, Slice sampling, Annals of statistics (2003) 705–741.

[173] J. Skilling, Nested sampling, in: AIP Conference Proceedings, Vol. 735, 2004, p. 395.

[174] F. Feroz, K. Cranmer, M. Hobson, R. Ruiz de Austri, R. Trotta, Challenges of Profile Likelihood Evaluation in Multi-Dimensional SUSY Scans, JHEP 1106 (2011) 042. arXiv:1101.3296, doi:10.1007/JHEP06(2011)042.

[175] A. Gelman, D. B. Rubin, Inference from Iterative Simulation Using Multiple Sequences, Statist.Sci. 7 (1992) 457–472.

[176] S. S. AbdusSalam, B. C. Allanach, F. Quevedo, F. Feroz, M. Hobson, Fitting the Phenomenological MSSM, Phys.Rev. D81 (2010) 095012. arXiv:0904.2548, doi:10.1103/PhysRevD.81.095012.

[177] C. Boehm, A. Djouadi, M. Drees, Light scalar top quarks and supersymmetric dark matter, Phys.Rev. D62 (2000) 035012. arXiv:hep-ph/9911496, doi:10.1103/PhysRevD.62.035012.

[178] J. R. Ellis, T. Falk, K. A. Olive, Neutralino - Stau coannihilation and the cosmological upper limit on the mass of the lightest supersymmetric particle, Phys.Lett. B444 (1998) 367–372. arXiv:hep-ph/9810360, doi:10.1016/S0370-2693(98)01392-6.

[179] J. R. Ellis, T. Falk, K. A. Olive, M. Srednicki, Calculations of neutralino-stau coannihilation channels and the cosmologically relevant region of MSSM parameter space, Astropart.Phys. 13 (2000) 181–213. arXiv:hep-ph/9905481, doi:10.1016/S0927-6505(99)00104-8,10.1016/S0927-6505(99)00104-8.

[180] N. Jarosik, C. Bennett, J. Dunkley, B. Gold, M. Greason, et al., Seven-Year Wilkinson Microwave Anisotropy Probe (WMAP) Observations: Sky Maps, Systematic Errors, and Basic Results, Astrophys.J.Suppl. 192 (2011) 14. arXiv:1001.4744, doi:10.1088/0067-0049/192/2/14.

[181] D. Asner, et al., Averages of b-hadron, c-hadron, and τ-lepton PropertiesarXiv:1010.1589.

[182] R. Aaij, et al., Strong constraints on the rare decays $B_s \to \mu^+\mu^-$ and $B^0 \to \mu^+\mu^-$arXiv:1203.4493.

[183] G. Abbiendi, et al., Search for chargino and neutralino production at s**(1/2) = 192-GeV to 209-GeV at LEP, Eur. Phys. J. C35 (2004) 1–20. arXiv:hep-ex/0401026, doi:10.1140/epjc/s2004-01780-x.

[184] P. Ade, et al., Planck 2013 results. XVI. Cosmological parametersarXiv:1303.5076.

[185] G. Bennett, et al., Final Report of the Muon E821 Anomalous Magnetic Moment Measurement at BNL, Phys.Rev. D73 (2006) 072003. arXiv:hep-ex/0602035, doi:10.1103/PhysRevD.73.072003.

[186] J. P. Miller, E. de Rafael, B. L. Roberts, Muon (g-2): Experiment and theory, Rept.Prog.Phys. 70 (2007) 795. arXiv:hep-ph/0703049, doi:10.1088/0034-4885/70/5/R03.

[187] G. Belanger, F. Boudjema, A. Pukhov, A. Semenov, micrOMEGAs: Version 1.3, Comput.Phys.Commun. 174 (2006) 577–604. arXiv:hep-ph/0405253, doi:10.1016/j.cpc.2005.12.005.

[188] A. Djouadi, Supersymmetry effects on high precision electroweak observablesarXiv:hep-ph/9911468.

[189] A. Djouadi, J.-L. Kneur, G. Moultaka, SuSpect: A Fortran code for the supersymmetric and Higgs particle spectrum in the MSSM, Comput. Phys. Commun. 176 (2007) 426–455. arXiv:hep-ph/0211331, doi:10.1016/j.cpc.2006.11.009.

[190] T. Hurth, M. Nakao, Radiative and Electroweak Penguin Decays of B Mesons, Ann.Rev.Nucl.Part.Sci. 60 (2010) 645–677. arXiv:1005.1224, doi:10.1146/annurev.nucl.012809.104424.

[191] P. Gambino, M. Misiak, Quark mass effects in anti-B $\to$ X(s gamma), Nucl.Phys. B611 (2001) 338–366. arXiv:hep-ph/0104034, doi:10.1016/S0550-3213(01)00347-9.

[192] R. Aaij, et al., First evidence for the decay Bs $\to$ mu+ mu-, Phys.Rev.Lett. 110 (2013) 021801. arXiv:1211.2674, doi:10.1103/PhysRevLett.110.021801.

[193] P. Bechtle, O. Brein, S. Heinemeyer, G. Weiglein, K. E. Williams, HiggsBounds: Confronting Arbitrary Higgs Sectors with Exclusion Bounds from LEP and the Tevatron, Comput.Phys.Commun. 181 (2010) 138–167. arXiv:0811.4169, doi:10.1016/j.cpc.2009.09.003.

[194] P. Bechtle, O. Brein, S. Heinemeyer, G. Weiglein, K. E. Williams, HiggsBounds 2.0.0: Confronting Neutral and Charged Higgs Sector Predictions with Exclusion Bounds from LEP and the Tevatron, Comput.Phys.Commun. 182 (2011) 2605–2631. arXiv:1102.1898, doi:10.1016/j.cpc.2011.07.015.

[195] S. Chatrchyan, et al., Combined results of searches for the standard model Higgs boson in pp collisions at $\sqrt{s} = 7$ TeV, Phys.Lett. B710 (2012) 26–48. arXiv:1202.1488, doi:10.1016/j.physletb.2012.02.064.

[196] G. Aad, et al., Combined search for the Standard Model Higgs boson in pp collisions at $\sqrt{s} = 7$ TeV with the ATLAS detector, Phys.Rev. D86 (2012) 032003. arXiv:1207.0319, doi:10.1103/PhysRevD.86.032003.

[197] S. Chatrchyan, et al., Observation of a new boson at a mass of 125 GeV with the CMS experiment at the LHC, Phys.Lett. B716 (2012) 30–61. arXiv:1207.7235, doi:10.1016/j.physletb.2012.08.021.

[198] G. Aad, et al., Observation of a new particle in the search for the Standard Model Higgs boson with the ATLAS detector at the LHC, Phys.Lett. B716 (2012) 1–29. arXiv:1207.7214, doi:10.1016/j.physletb.2012.08.020.

[199] Combined measurements of the mass and signal strength of the higgs-like boson with the atlas detector using up to 25 fb^{-1} of proton-proton collision data, Tech. Rep. ATLAS-CONF-2013-014, CERN, Geneva (Mar 2013).

[200] S. Chatrchyan, et al., Observation of a new boson with mass near 125 GeV in pp collisions at sqrt(s) = 7 and 8 TeVarXiv:1303.4571.

[201] P. Bechtle, O. Brein, S. Heinemeyer, O. Stal, T. Stefaniak, et al., Recent Developments in HiggsBounds and a Preview of HiggsSignalsarXiv:1301.2345.

[202] B. Allanach, C. Balazs, G. Belanger, M. Bernhardt, F. Boudjema, et al., SUSY Les Houches Accord 2, Comput.Phys.Commun. 180 (2009) 8–25. arXiv:0801.0045, doi:10.1016/j.cpc.2008.08.004.

[203] G. Belanger, F. Boudjema, A. Pukhov, A. Semenov, Dark matter direct detection rate in a generic model with micrOMEGAs2.1, Comput. Phys. Commun. 180 (2009) 747–767. arXiv:0803.2360, doi:10.1016/j.cpc.2008.11.019.

[204] G. Belanger, F. Boudjema, P. Brun, A. Pukhov, S. Rosier-Lees, et al., Indirect search for dark matter with micrOMEGAs2.4, Comput.Phys.Commun. 182 (2011) 842–856. arXiv:1004.1092, doi:10.1016/j.cpc.2010.11.033.

[205] B. Allanach, SOFTSUSY: a program for calculating supersymmetric spectra, Comput.Phys.Commun. 143 (2002) 305–331. arXiv:hep-ph/0104145, doi:10.1016/S0010-4655(01)00460-X.

[206] P. Scott, Pippi - Painless parsing, post-processing and plotting of posterior and likelihood samples, European Physical Journal Plus 127 (2012) 138. arXiv:1206.2245, doi:10.1140/epjp/i2012-12138-3.

[207] J. L. Feng, K. T. Matchev, F. Wilczek, Neutralino dark matter in focus point supersymmetry, Phys.Lett. B482 (2000) 388–399. arXiv:hep-ph/0004043, doi:10.1016/S0370-2693(00)00512-8.

[208] J. L. Feng, K. T. Matchev, D. Sanford, Focus Point Supersymmetry ReduxarXiv:1112.3021.

[209] G. J. Feldman, R. D. Cousins, A Unified approach to the classical statistical analysis of small signals, Phys.Rev. D57 (1998) 3873–3889. arXiv:physics/9711021, doi:10.1103/PhysRevD.57.3873.

[210] J. Neyman, , Royal Society of London Philosophical Trans- actions Series A 236 (1937) 333.

[211] J. R. Ellis, K. A. Olive, C. Savage, Hadronic Uncertainties in the Elastic Scattering of Supersymmetric Dark Matter, Phys.Rev. D77 (2008) 065026. arXiv:0801.3656, doi:10.1103/PhysRevD.77.065026.

[212] J. Giedt, A. W. Thomas, R. D. Young, Dark matter, the CMSSM and lattice QCD, Phys.Rev.Lett. 103 (2009) 201802. arXiv:0907.4177, doi:10.1103/PhysRevLett.103.201802.

[213] A. M. Green, Extracting Information about WIMP Properties from Direct Detection Experiments: Astrophysical UncertaintiesarXiv:1004.2383.

[214] C. McCabe, The Astrophysical Uncertainties Of Dark Matter Direct Detection Experiments, Phys. Rev. D82 (2010) 023530. arXiv:1005.0579, doi:10.1103/PhysRevD.82.023530.

[215] J. H. Davis, C. Boehm, N. Oppermann, T. Ensslin, T. Lacroix, The XENON100 exclusion limit without considering Leff as a nuisance parameterarXiv:1203.6823.

[216] C. Strege, G. Bertone, D. Cerdeno, M. Fornasa, R. Ruiz de Austri, et al., Updated global fits of the cMSSM including the latest LHC SUSY and Higgs searches and XENON100 data, JCAP 1203 (2012) 030. arXiv:1112.4192, doi:10.1088/1475-7516/2012/03/030.

[217] O. Buchmueller, R. Cavanaugh, A. De Roeck, M. Dolan, J. Ellis, et al., Higgs and Supersymmetry, Eur.Phys.J. C72 (2012) 2020. arXiv:1112.3564, doi:10.1140/epjc/s10052-012-2020-3.

[218] C. Strege, G. Bertone, F. Feroz, M. Fornasa, R. R. de Austri, et al., Global Fits of the cMSSM and NUHM including the LHC Higgs discovery and new XENON100 constraints, JCAP 1304 (2013) 013. arXiv:1212.2636, doi:10.1088/1475-7516/2013/04/013.

[219] O. Buchmueller, R. Cavanaugh, M. Citron, A. De Roeck, M. Dolan, et al., The CMSSM and NUHM1 in Light of 7 TeV LHC, Bs to mu+mu- and XENON100 Data, Eur.Phys.J. C72 (2012) 2243. arXiv:1207.7315, doi:10.1140/epjc/s10052-012-2243-3.

[220] A. Fowlie, M. Kazana, K. Kowalska, S. Munir, L. Roszkowski, et al., The CMSSM Favoring New Territories: The Impact of New LHC Limits and a 125 GeV Higgs, Phys.Rev. D86 (2012) 075010. arXiv:1206.0264, doi:10.1103/PhysRevD.86.075010.

[221] S. Antusch, L. Calibbi, V. Maurer, M. Monaco, M. Spinrath, Naturalness of the Non-Universal MSSM in the Light of the Recent Higgs Results, JHEP 01 (2013) 187. arXiv:1207.7236, doi:10.1007/JHEP01(2013)187.

[222] A. Arbey, M. Battaglia, A. Djouadi, F. Mahmoudi, An update on the constraints on the phenomenological MSSM from the new LHC Higgs results, Phys.Lett. B720 (2013) 153–160. arXiv:1211.4004, doi:10.1016/j.physletb.2013.02.001.

[223] P. Bechtle, S. Heinemeyer, O. Stal, T. Stefaniak, G. Weiglein, et al., MSSM Interpretations of the LHC Discovery: Light or Heavy Higgs?arXiv:1211.1955.

[224] U. Haisch, F. Mahmoudi, MSSM: Cornered and Correlated, JHEP 1301 (2013) 061. arXiv:1210.7806, doi:10.1007/JHEP01(2013)061.

[225] M. Carena, S. Heinemeyer, O. Stl, C. Wagner, G. Weiglein, MSSM Higgs Boson Searches at the LHC: Benchmark Scenarios after the Discovery of a Higgs-like ParticlearXiv:1302.7033.

[226] W. Altmannshofer, M. Carena, N. R. Shah, F. Yu, Indirect Probes of the MSSM after the Higgs Discovery, JHEP 1301 (2013) 160. arXiv:1211.1976, doi:10.1007/JHEP01(2013)160.

[227] H. Baer, V. Barger, P. Huang, D. Mickelson, A. Mustafayev, et al., Post-LHC7 fine-tuning in the mSUGRA/CMSSM model with a 125 GeV Higgs bosonarXiv:1210.3019.

[228] G. Aad, et al., Search for squarks and gluinos with the ATLAS detector in final states with jets and missing transverse momentum using $4.7 fb^{-1}$ of $\sqrt{s} = 7$ TeV proton-proton collision data, Phys.Rev. D87 (2013) 012008. arXiv:1208.0949, doi:10.1103/PhysRevD.87.012008.

[229] G. Aad, et al., Search for a supersymmetric partner to the top quark in final states with jets and missing transverse momentum at $\sqrt{s} = 7$ TeV with the ATLAS detector, Phys.Rev.Lett. 109 (2012) 211802. arXiv:1208.1447, doi:10.1103/PhysRevLett.109.211802.

[230] G. Aad, et al., Hunt for new phenomena using large jet multiplicities and missing transverse momentum with ATLAS in 4.7 fb^{-1} of $\sqrt{s} = 7$ TeV proton-proton collisions, JHEP 1207 (2012) 167. arXiv:1206.1760, doi:10.1007/JHEP07(2012)167.

[231] G. Aad, et al., Search for top and bottom squarks from gluino pair production in final states with missing transverse energy and at least three b-jets with the ATLAS detector, Eur.Phys.J. C72 (2012) 2174. arXiv:1207.4686, doi:10.1140/epjc/s10052-012-2174-z.

[232] S. Chatrchyan, et al., Search for new physics in the multijet and missing transverse momentum final state in proton-proton collisions at $\sqrt{s} = 7$ TeV, Phys.Rev.Lett. 109 (2012) 171803. arXiv:1207.1898, doi:10.1103/PhysRevLett.109.171803.

[233] S. Chatrchyan, et al., Search for Supersymmetry at the LHC in Events with Jets and Missing Transverse Energy, Phys.Rev.Lett. 107 (2011) 221804. arXiv:1109.2352, doi:10.1103/PhysRevLett.107.221804.

[234] S. Chatrchyan, et al., Search for supersymmetry in hadronic final states using MT2 in pp collisions at $\sqrt{s} = 7$ TeV, JHEP 1210 (2012) 018. arXiv:1207.1798, doi:10.1007/JHEP10(2012)018.

[235] S. Chatrchyan, et al., Search for supersymmetry in events with b-quark jets and missing transverse energy in pp collisions at 7 TeV, Phys.Rev. D86 (2012) 072010. arXiv:1208.4859, doi:10.1103/PhysRevD.86.072010.

[236] J. Alwall, P. Schuster, N. Toro, Simplified Models for a First Characterization of New Physics at the LHC, Phys.Rev. D79 (2009) 075020. arXiv:0810.3921, doi:10.1103/PhysRevD.79.075020.

[237] D. Alves, et al., Simplified Models for LHC New Physics Searches, J.Phys. G39 (2012) 105005. arXiv:1105.2838, doi:10.1088/0954-3899/39/10/105005.

[238] Search for squarks and gluinos with the atlas detector using final states with jets and missing transverse momentum and 5.8 fb^{-1} of $\sqrt{s}$=8 tev proton-proton collision data, Tech. Rep. ATLAS-CONF-2012-109, CERN, Geneva (Aug 2012).

[239] Search for direct production of the top squark in the all-hadronic ttbar + etmiss final state in 21 fb-1 of p-pcollisions at sqrt(s)=8 tev with the atlas detector, Tech. Rep. ATLAS-CONF-2013-024, CERN, Geneva (Mar 2013).

[240] Search for direct production of charginos and neutralinos in events with three leptons and missing transverse momentum in 21 fb^{-1} of pp collisions at $\sqrt{s} = 8$ tev with the atlas detector, Tech. Rep. ATLAS-CONF-2013-035, CERN, Geneva (Mar 2013).

[241] G. Bertone, M. Fornasa, M. Taoso, A. R. Zentner, Dark Matter Annihilation around Intermediate Mass Black Holes: an update, New J.Phys. 11 (2009) 105016. arXiv:0905.4736, doi:10.1088/1367-2630/11/10/105016.

[242] A. Baushev, Dark matter annihilation in the gravitational field of a black holearXiv:0805.0124.

[243] E. Berti, V. Cardoso, L. Gualtieri, F. Pretorius, U. Sperhake, Comment on 'Kerr Black Holes as Particle Accelerators to Arbitrarily High Energy', Phys.Rev.Lett. 103 (2009) 239001. arXiv:0911.2243, doi:10.1103/PhysRevLett.103.239001.

[244] T. Jacobson, T. P. Sotiriou, Spinning Black Holes as Particle Accelerators, Phys.Rev.Lett. 104 (2010) 021101. arXiv:0911.3363, doi:10.1103/PhysRevLett.104.021101.

[245] A. Grib, Y. Pavlov, On particle collisions in the gravitational field of the Kerr black hole, Astropart.Phys. 34 (2011) 581–586. arXiv:1001.0756, doi:10.1016/j.astropartphys.2010.12.005.

[246] S.-W. Wei, Y.-X. Liu, H. Guo, C.-E. Fu, Charged spinning black holes as Particle Accelerators, Phys.Rev. D82 (2010) 103005. arXiv:1006.1056, doi:10.1103/PhysRevD.82.103005.

[247] O. B. Zaslavskii, Acceleration of particles as universal property of rotating black holes, Phys.Rev. D82 (2010) 083004. arXiv:1007.3678, doi:10.1103/PhysRevD.82.083004.

[248] T. Harada, M. Kimura, Collision of an innermost stable circular orbit particle around a Kerr black hole, Phys.Rev. D83 (2011) 024002. arXiv:1010.0962, doi:10.1103/PhysRevD.83.024002.

[249] A. J. Williams, Numerical estimation of the escaping flux of massless particles created in collisions around a Kerr black hole, Phys.Rev. D83 (2011) 123004. arXiv:1101.4819, doi:10.1103/PhysRevD.83.123004.

[250] J. M. Bardeen, W. H. Press, S. A. Teukolsky, Rotating black holes: Locally nonrotating frames, energy extraction, and scalar synchrotron radiation, Astrophys.J. 178 (1972) 347. doi:10.1086/151796.

[251] M. Cannoni, M. Gomez, M. Perez-Garcia, J. Vergados, New gamma ray signal from gravitationally boosted neutralinos at the galactic center, Phys.Rev. D85 (2012) 115015. arXiv:1205.1709, doi:10.1103/PhysRevD.85.115015.

[252] S. T. McWilliams, Black Holes are neither Particle Accelerators nor Dark Matter Probes, Phys.Rev.Lett. 110 (2013) 011102. arXiv:1212.1235, doi:10.1103/PhysRevLett.110.011102.

[253] O. Zaslavskii, Comment on 'Black Holes are Neither Particle Accelerators Nor Dark Matter Probes'arXiv:1301.3429.

[254] S. T. McWilliams, Reply to "Comment on 'Black Holes are neither Particle Accelerators nor Dark Matter Probes' "arXiv:1302.5950.

[255] K. Lake, Particle Accelerators inside Spinning Black Holes, Phys.Rev.Lett. 104 (2010) 211102. arXiv:1001.5463, doi:10.1103/PhysRevLett.104.259903,10.1103/PhysRevLett.104.211102.

[256] A. Grib, Y. Pavlov, On particles collisions near rotating black holes, Grav.Cosmol. 17 (2011) 42–46. arXiv:1010.2052.

[257] M. Kimura, K.-i. Nakao, H. Tagoshi, Acceleration of colliding shells around a black hole: Validity of the test particle approximation in the Banados-Silk-West process, Phys.Rev. D83 (2011) 044013. arXiv:1010.5438, doi:10.1103/PhysRevD.83.044013.

[258] O. B. Zaslavskii, Acceleration of particles by black holes: general explanation, Class.Quant.Grav. 28 (2011) 105010. arXiv:1011.0167, doi:10.1088/0264-9381/28/10/105010.

[259] A. Grib, Y. Pavlov, O. Piattella, O. Piattella, High energy processes in the vicinity of the Kerr's black hole horizon, Int.J.Mod.Phys. A26 (2011) 3856–3867. arXiv:1105.1540, doi:10.1142/S0217751X11054310,10.1142/S2010194511001449.

[260] S. Gao, C. Zhong, Non-extremal Kerr black holes as particle accelerators, Phys.Rev. D84 (2011) 044006. arXiv:1106.2852, doi:10.1103/PhysRevD.84.044006.

[261] O. Zaslavsky, Acceleration of particles by rotating black holes: near-horizon geometry and kinematics, Grav.Cosmol. 18 (2012) 139–142. arXiv:1107.3964, doi:10.1134/S0202289312020144.

[262] O. Zaslavskii, Acceleration of particles near the inner black hole horizon, Phys.Rev. D85 (2012) 024029. arXiv:1110.5838, doi:10.1103/PhysRevD.85.024029.

[263] O. Zaslavskii, Ultra-high energy collisions of nonequatorial geodesic particles near dirty black holes, JHEP 1212 (2012) 032. arXiv:1209.4987, doi:10.1007/JHEP12(2012)032.

[264] A. Grib, Y. Pavlov, On the energy of particle collisions in the ergosphere of the rotating black holes, Europhys.Lett. 101 (2013) 20004. arXiv:1301.0698, doi:10.1209/0295-5075/101/20004.

[265] O. B. Zaslavskii, Acceleration of particles by nonrotating charged black holes, JETP Lett. 92 (2010) 571–574. arXiv:1007.4598, doi:10.1134/S0021364010210010.

[266] M. Patil, P. S. Joshi, Naked singularities as particle accelerators, Phys.Rev. D82 (2010) 104049. arXiv:1011.5550, doi:10.1103/PhysRevD.82.104049.

[267] I. Hussain, Collision energy in the center-of-mass frame for rotating and accelerating black holes, Mod.Phys.Lett. A27 (2012) 1250017. doi:10.1142/S0217732312500174.

[268] M. Bejger, T. Piran, M. Abramowicz, F. Hakanson, Collisional Penrose process near the horizon of extreme Kerr black holes, Phys.Rev.Lett. 109 (2012) 121101. arXiv:1205.4350, doi:10.1103/PhysRevLett.109.121101.

[269] O. Zaslavskii, On energetics of particle collisions near black holes: BSW effect versus Penrose process, Phys.Rev. D86 (2012) 084030. arXiv:1205.4410, doi:10.1103/PhysRevD.86.084030.

[270] C. W. Misner, K. Thorne, J. Wheeler, Gravitation.

[271] W. H. Press, S. A. Teukolsky, W. T. Vetterling, B. P. Flannery, Numerical recipes in C (2nd ed.): the art of scientific computing, Cambridge University Press, New York, NY, USA, 1992.

[272] J. Gariel, M. A. MacCallum, G. Marcilhacy, N. Santos, Kerr Geodesics, the Penrose Process and Jet Collimation by a Black HolearXiv:gr-qc/0702123.

[273] G. Bertone, D. Merritt, Dark matter dynamics and indirect detection, Mod.Phys.Lett. A20 (2005) 1021. arXiv:astro-ph/0504422, doi:10.1142/S0217732305017391.

[274] G. Bertone, A. R. Zentner, J. Silk, A new signature of dark matter annihilations: gamma-rays from intermediate-mass black holes, Phys.Rev. D72 (2005) 103517. arXiv:astro-ph/0509565, doi:10.1103/PhysRevD.72.103517.

[275] F. Aharonian, et al., Observations of the Crab Nebula with H.E.S.S, Astron.Astrophys. 457 (2006) 899–915. arXiv:astro-ph/0607333, doi:10.1051/0004-6361:20065351.